Extending Eikonal-based Models in Cardiac Electrophysiology Research

Balancing Accuracy and Speed

Zur Erlangung des akademischen Grades eines

DOKTORS DER INGENIEURWISSENSCHAFTEN (Dr.-Ing.)

von der KIT-Fakultät für
Elektrotechnik und Informationstechnik
des Karlsruher Instituts für Technologie (KIT)
genehmigte

DISSERTATION

von

Cristian Alberto Barrios Espinosa, M.Sc.
geb. in Bogota, Kolumbien

Tag der mündlichen Prüfung:	23. Januar 2025
Referent:	PD Dr-Ing. Axel Loewe
1. Korreferent:	Prof. Dr. Simone Pezzuto
2. Korreferent:	Prof. Dr. rer. nat. Olaf Dössel

Abstract

Cardiac arrhythmias are a leading cause of morbidity and mortality, with atrial fibrillation (AF) being the most prevalent sustained arrhythmia, significantly impacting global public health. Despite its importance, AF treatment strategies remain insufficient due to an incomplete understanding of the underlying mechanisms. Computational models are valuable tools for advancing research in cardiac electrophysiology and enhancing patient diagnostics and treatment. While reaction diffusion (RD) models are widely used, they are computationally intensive. In contrast, the eikonal model is computationally less demanding, making it attractive for large-scale simulations and clinical scenarios where faster computation times are critical. However, several limitations hinder its application in realistic settings. This work aims to explore how the eikonal model can be better understood and expanded to improve research, diagnosis, and treatment of atrial arrhythmias.

To investigate the standard eikonal model, it was first compared to RD models by simulating single beats under sinus rhythm, both with and without fibrosis. Then, the standard eikonal model was modified to provide additional outputs, including conduction velocity (CV) magnitude and wavefront propagation direction under anisotropic conditions, alongside activation times. These outputs served as ground truth to evaluate the radial basis function method, which estimates CV based on activation times while ignoring anisotropy.

The eikonal model was then extended by combining it with the RD model, forming the diffusion-reaction eikonal alternant model (DREAM). A new cyclical fast iterative method (cycFIM) was introduced to solve the anisotropic eikonal equation while enabling reactivations, a complex challenge for iterative methods.

To address the eikonal model's limitations, particularly its inability to account for source-sink mismatch, regression models were developed. Bidomain simulations examined the effects of wall thickness and tissue curvature on CV. Moreover, monodomain simulations investigated pacing frequency and source-sink mismatch effects on diffusion current (DC) amplitude. These findings were integrated into regression models for the eikonal model. To facilitate the regression, a new method was introduced to quantify source-sink mismatch based solely on activation times and node coordinates.

Comparison with RD models showed that the eikonal model reasonably simulates sinus rhythm in non-fibrotic atrial geometry but significantly declines in performance with fibrosis due to its inability to capture source-sink mismatches. Additionally, when assessing the radial basis function it was found that neglecting anisotropic propagation when estimating CV can lead to significant errors up to 700 mm/s.

DREAM simulations maintained low computational costs while effectively simulating action potentials, node reactivations, and reentries. Investigating CV restitution revealed that the steepness of restitution curves can modulate the dynamics of the vulnerable window and the average duration of reentry. Regression models based on RD simulations successfully predicted key factors in cardiac electrophysiology, such as CV and DC amplitude, using data available during eikonal simulations, including activation times and geometric factors like wall thickness and tissue curvature.

This research highlights the eikonal model's potential in advancing the understanding and clinical management of cardiac arrhythmias. As a computationally efficient alternative to more complex models, it provides valuable insights into arrhythmia mechanisms, diagnosis, and treatment, making it ideal for large-scale simulations and clinical settings with limited computing resources. The DREAM was applied to explore the role of personalized CV restitution curves in reentry dynamics. This study paves the way for broader applications of eikonal-based models in cardiac electrophysiology, ultimately improving patient outcomes. Additionally, the new cycFIM, embedded in the DREAM, could be used to simulate cyclical wave propagation in other fields beyond medical applications.

Zusammenfassung

Herzrhythmusstörungen zählen zu den wesentlichen Ursachen für Morbidität und Mortalität. Dabei ist Vorhofflimmern die häufigste persistierende Arrhythmie, welche die Gesundheit einer Vielzahl von Menschen weltweit erheblich beeinträchtigt. Trotz ihrer Relevanz sind Behandlungsstrategien für Vorhofflimmern aufgrund eines unvollständigen Verständnisses der zugrunde liegenden Mechanismen jedoch oft nicht ausreichend effektiv. Computermodelle sind wertvolle Werkzeuge in der Forschung auf dem Gebiet der kardialen Elektrophysiologie, sowie der Verbesserung von Diagnostik und Therapieentscheidungen. Reaktions-Diffusionsmodelle gehören zu den häufig verwendeten, jedoch sehr rechenintensiven Modellierungsansätzen. Im Vergleich dazu zeichnet sich das Eikonalmodell durch eine geringere Rechenintensität aus, was es für großangelegte Simulationen und in klinischen Anwendungen prädestiniert. Dennoch verhindern diverse Modellbeschränkungen bislang den Einsatz in realistischen Szenarien. Diese Arbeit untersucht das Eikonalmodell im Detail und erweitert es gezielt, um es für die Erforschung, Diagnose und Therapie von Vorhofarrhythmien zu optimieren.

Zunächst wurde das Eikonalmodell im Vergleich zu Reaktions-Diffusionsmodellen untersucht, indem Herzschläge im Sinusrhythmus mit und ohne Fibrose simuliert wurden. Das Eikonalmodell wurde modifiziert, um zusätzliche Parameter wie die Ausbreitungsgeschwindigkeit sowie die Ausbreitungsrichtung der Wellenfront unter anisotropen Bedingungen, und Aktivierungszeiten zu erfassen. Diese Ausgaben dienten als Referenz für die Evaluation der Radialbasisfunktionsmethode, welche die Leitungsgeschwindigkeit anhand der Aktivierungszeiten schätzt, jedoch Anisotropie zunächst außer Acht lässt.

Das Eikonalmodell wurde durch Integration des Reaktions-Diffusionsmodells zum Diffusion-Reaction-Eikonal-Alternant-Modell (DREAM) erweitert. Dabei wurde eine schnelle iterative Methode entwickelt, die das Lösen der anisotropen Eikonal-Gleichung unter Berücksichtigung von Reaktivierungen ermöglicht. DREAM wurde verwendet, um die Rolle personalisierter Restitutionskurven der Ausbreitungsgeschwindigkeit in Reentry-Dynamiken zu untersuchen.

Um die Einschränkungen des Eikonalmodells insbesondere hinsichtlich seiner Inkompatibilität bezüglich der Berücksichtigung der Quellen-Senken-Diskrepanz zu adressieren, wurden Regressionsmodelle basierend auf Mono- und Bidomain-Simulationen entwickelt. Mit den Bidomain-Simulationen wurden die Auswirkungen der Wanddicke und der Gewebeanordnung auf die Ausbreitungsgeschwindigkeit untersucht, wohingegen Monodomain-Simulationen die Auswirkungen der Stimulationsfrequenz und der Quellen-Senken-Diskrepanz auf die Amplitude des Diffusionsstroms untersuchten. Die Erkenntnisse wurden in Regressionsmodelle für das Eikonalmodell integriert. Eine neue Methode zur Quantifizierung der Quellen-Senken-Diskrepanz, basierend ausschließlich auf Aktivierungszeiten und Knotenkoordinaten, wurde entwickelt.

Der Vergleich mit Reaktions-Diffusionsmodellen zeigte, dass das Eikonalmodell den Sinusrhythmus in nicht-fibrotischen Vorhofgeometrien hinreichend genau simuliert. Unter Berücksichtigung von Fibrose sank die Modellleistung jedoch signifikant, bedingt durch die unzureichende Berücksichtigung von Quellen-Senken-Diskrepanzen. Zudem ergab die Evaluierung der Radialbasisfunktion, dass eine Vernachlässigung des anisotropen Ausbreitungsverhaltens bei der Schätzung der Ausbreitungsgeschwindigkeit zu Fehlern von bis zu 700 mm/s führt.

Die DREAM-Simulationen zeichneten sich durch eine geringere Rechenintensität aus, während sie effektiv Aktionspotentiale, Knotenreaktivierungen und Reentries simulierten. Die Analyse des Restitutionsverhaltens der Ausbreitungsgeschwindigkeit ergab, dass deren Steilheit das für die Reentry-Initiierung anfällige Zeitfenster sowie die durchschnittliche Reentry-Dauer beeinflusst. Regressionsmodelle, die auf Reaktions-Diffusionssimulationen basierten und Informationen wie Aktivierungszeiten sowie geometrische Faktoren wie Wanddicke und Gewebeanordnung nutzten, konnten erfolgreich zentrale Parameter der kardialen Elektrophysiologie, wie die Ausbreitungsgeschwindigkeit und die Amplitude des Diffusionsstroms, voraussagen.

Diese Arbeit demonstriert das Potential des Eikonalmodells, das Verständnis und die Behandlung von Herzrhythmusstörungen entscheidend zu verbessern. Als rechnerisch effiziente Alternative zu komplexeren Modellen erlaubt es wertvolle Einblicke in die Mechanismen, Diagnose, und Therapie von Arrhythmien. Aufgrund seiner geringen Rechenintensität ist es besonders geeignet für großangelegte Simulationen und klinische Anwendungen mit begrenzten Ressourcen. Ergebnisse dieser Studie eröffnen Perspektiven für eine breitere Anwendung eikonal-basierter Modelle zur Optimierung der Patientenbehandlung.

Acknowledgments

I am endlessly grateful for the support of everyone who accompanied me on my PhD path.

I would like to express my deepest gratitude to my primary supervisor, **PD Dr.-Ing. Axel Loewe**, for his exceptional guidance and unwavering support throughout my PhD journey. His close supervision allowed me the independence to explore my research interests while providing a flexible environment that nurtured my growth as a researcher. I greatly appreciate the supportive and collaborative culture he has fostered within our team, which encouraged me to embrace open science and develop my skills confidently.

I am truly honored and thankful to **Prof. Dr. rer. nat. Olaf Dössel** for allowing me to be part of his esteemed group, opening the door to the fascinating world of cardiac modeling. It was a privilege to share academic environments with him and to benefit from his extensive knowledge in diverse fields, including physics, electromagnetics, and cardiac research. His insights and engaging anecdotes about science and even history made my experience not only educational but also enjoyable. It has been an honor to learn from such a respected authority in the field.

I would like to extend my heartfelt thanks to my master thesis supervisor, **Univ.-Prof. Dr. Jordi Heijman**, whom I met during my master's in Maastricht. He introduced me to the fascinating world of cardiac modeling, and his passion for the subject was truly contagious. His support was fundamental for my transition from a master's student to a PhD candidate, and I consider him one of the most talented researchers I know.

I would also like to extend my heartfelt thanks to my fellow PhD students and VT employes at the Institute of Biomedical Technology (IBT) for creating such a supportive and collaborative environment. The camaraderie among us made it possible not only to work closely with colleagues but also to form lasting friendships that became vital, especially as I was far from home. This network of support was invaluable during my journey.

I want to particularly acknowledge **Jorge** for being a remarkable mentor—capable, kind, and humble. Your endless support for my countless requests has inspired me to strive to be the kind of scientist I aspire to be: knowledgeable yet approachable. Thank you for being such a positive influence.

I also want to express my gratitude to **Laura**; collaborating with you was always a pleasure. Your unique ability to translate our engineering research into clinical applications taught me the importance of maintaining a close connection to the clinical world.

To my officemate **Joni**, thank you for your patience during my moments of crisis and for our endless discussions about science and life. Your perspectives and support in helping

me navigate my own challenges have been invaluable. I also appreciate your willingness to satiate my curiosity about mechanics and for the generous supply of protein and proof-reading you provided!

I would like to thank **Paty** and **Carmen**, my partners in adventure who joined the program at the same time as I did with PersonalizeAF. It was comforting to share our experiences, especially during the tougher moments of PhD life, and to hear a bit of Spanish—my native language—even so far from home.

I am grateful to **Stephanie** for being an excellent mentee and for carrying forward my work. I have no doubt that you will make significant contributions to our field, and I appreciate your support while I was writing my thesis in more ways than one.

A special thank you goes to **Marie** for her invaluable IT support. Whenever I faced challenges, she was quick to provide effective solutions, making what could have been overwhelming situations manageable. Coming from a different field, I can confidently say that much of my work would not have been possible without her expertise and assistance—she truly saved my ass in many ways!

To my colleagues and supervisors from the PersonalizeAF consortium, thank you for the enriching experiences and the enlightening insights gained through our shared work. Learning from the multidisciplinary backgrounds of researchers from various countries was not only educational but also enjoyable. I want to especially thank **Victor**, **Ozan**, and **Eric** for graciously hosting me during my secondments in Maastricht and Barcelona; your hospitality made my time away from Karlsruhe truly memorable. Special thanks to **Dr. Maria Guillem** and **Arantxa** for all the effort you put into organizing the consortium activities. Of course, I must also thank the **European Commission** for funding most of my research. This work was supported by the European Union's Horizon research and Innovation programme under the Marie Skłodowska-Curie grant agreement No. 860974 and the European High-Performance Computing Joint Undertaking EuroHPC under grant agreement No 955495 (MICROCARD).

I would also like to thank the students I had the pleasure of supervising: **Silvia** (now my colleague), **Hanish**, **Lisa**, **Nils**, and **Guillaume**. Guiding you and sharing my knowledge was a rewarding experience, and I also learned so much from each of you. Additionally, I want to acknowledge other talented students with whom I had the opportunity to interact, such as **Leonie**, **Jule**, **Sara**, **Franzi**, and **Jan-Erik**. It has been thrilling to witness your progress, and I am confident that you all have brilliant futures ahead.

I would also like to take a moment to remember the colleagues who were instrumental in creating a warm and supportive environment when I first joined. My former officemate, **Luca**, offered invaluable help during those early days, and I am grateful for **Claudia**, with whom I had the privilege of collaborating and who exemplified the dedication of a talented researcher. I would also like to acknowledge **Eki**, **Tobi**, **Jochen**, **Debbie**, **Rebe**, and **Giorgio**, whose presence made the institute a much more welcoming place when I arrived. l. Additionally, I appreciate the newer members **Moritz**, **Ciro**, **Dominico**, **Mark**, and **Clarence** who helped maintain the continuity of this positive environment."

Assessing the quality of my work, I would like to extend my heartfelt gratitude to **PD Dr.-Ing. Axel Loewe** for serving as my referee, and to **Prof. Dr. Simone Pezzuto** and

Prof. Dr. rer. nat. Olaf Dössel for kindly agreeing to serve as my co-referees. I am deeply grateful to **Lori**, **Paty**, **Joni**, **Laura**, **Silvia**, **Jorge** and **Stephanie** for their invaluable help in proofreading my thesis; your feedback was essential in improving the quality of this manuscript. Additionally, I am thankful to my colleagues in the Pacemakers group: **Miri**, **Julian**, and **Stephanie**, for the enjoyable running sessions that helped me clear my mind during the final months of intense work.

I would like to thank my old friends who have been a continuous source of support, even if it was just a call now and then to vent about life. A special shoutout goes to **Laura** and **Vanessa**, my oldest and closest friends; I know I can always count on you both.

To my dearest former housemates from Maastricht, **Hannah**, **Pia**, **Lottie**, and **Nesli**, thank you for being my go-to confidants and for the gossip sessions that helped me unwind when research became overwhelming.

I also want to express my gratitude to my friends in Karlsruhe, who made my time here more enjoyable and, at times, bearable during challenging moments. The dancing community has been my true support throughout this journey. To my teachers, **Carsten** and **Jenny**, your classes and the wonderful people I met through your courses helped me navigate these tough years. I am also thankful to my many friends within the dancing community: **Martina**, **David**, **Vicky**, **Elena**, **Juan Fer**, **Giulia**, **Salo**, and many others; your presence brought joy and relief during stressful times. Other friends that I met in Karsruhe worth mentioning are **Tania**, **Lena**.

Gracias a **Sofi** por tu tiempo y tu amistad cuando las cosas estaban difíciles y cuando me sentía solo. Tu compañía siempre fue bastante importante para mí en momentos muy duros. Gracias, **Nici**, por ser mi alemanalatina favorita del mundo mundial, por compartir nuestro sentido del humor absurdo, aun si el último año haciendo esta tesis no tuve mucho tiempo para nuestras chocoaventuras.

Finalmente, quisiera agradecer a mi familia, a mis hermanos **Simon Camilo** y **Paola Katerine**, por enseñarme el valor de la resiliencia y salir adelante a pesar de las adversidades sin abandonar nuestros sueños. Especiales gracias a mi hermanita por venir a vivir a Europa y poder estar más cerquita, dándonos apoyo mutuamente en nuestras adversidades y celebrando los momentos más felices. Especial agradecimiento a mis papitos **Simon** y **Cristina** por todo el apoyo, la paciencia, los valores inculcados, y por toda la atención que me han brindado desde la infancia hasta la fecha. Aun ahora, aun a la distancia, por siempre estar pendientes de mí; su apoyo constante ha sido una gran base para volverme la persona que soy ahora. Finalmente, quisiera agradecerle a **Karla** por todo el amor que me diste en este último año, por el apoyo incondicional, por siempre salirte de tu camino para hacer cosas para que yo estuviera bien, por toda la comida, por los platos veganizados, por las risas, los viajecitos y las noches de películas. Toda la tranquilidad que me brindaste fue invaluable para terminar este proyecto. Espero que podamos seguir apoyándonos mucho más en muchos proyectos en el futuro.

As I conclude this acknowledgment, I am filled with immense gratitude for all the incredible people who have been part of my PhD journey. Each of you has played a unique role in shaping my experience, and I carry with me the lessons, memories, and friendships

we have forged together. This thesis is not just a culmination of my research but a testament to the unwavering support and love from my academic and personal circles. I look forward to the future with excitement, knowing that I am surrounded by such inspiring individuals. Thank you all for being part of this remarkable journey.

Contents

III Diffusion Reaction Eikonal Alternant Model 57

Abbreviations

AF	atrial fibrillation	i, 1 f., 7, 14–19, 107 ff., 111 ff., 115, 119, 123, 128, 139, 144
AP	action potential	1 f., 12–15, 19, 135, 138, 152
APD	action potential duration	19 f., 108, 142, 152
AT	activation time	2, 23 ff., 29, 44–49, 53 f., 109, 112, 115, 134 f., 137, 141 f., 144 ff., 148, 151, 159, 161
AV	atrioventricular	8–13, 17
CT	computed tomography	17
CV	conduction velocity	i f., 2 f., 15 ff., 24, 43–55, 59, 107–116, 118–123, 127–130, 132–140, 142 ff., 151 f., 155 ff., 159–162
cycFIM	cyclical FIM	i f., 59, 150, 160 f.
DC	diffusion current	i f., 13, 141–148, 150 ff., 155
DI	diastolic interval	110, 122 f., 142, 144, 147
DREAM	diffusion reaction eikonal alternant model	i–iv, 3, 59 f., 62, 64, 66, 68, 70, 72, 74, 76, 78, 80, 82, 84, 86, 88, 90, 92, 94, 96, 98, 100, 102, 104, 107 f., 110, 112 ff., 116, 118–123, 141, 150, 152, 155, 159–162
ECG	electrocardiogram	16 f.
ECGI	electrocardiographic imaging	17
ERP	effective refractory period	44
FIM	fast iterative method	24, 47 f., 52 ff., 134
FMM	fast marching method	2
MRI	magnetic resonance imaging	17
PCL	pacing cycle length	109–116, 120, 122 f., 144
PPI	post pacing interval	109, 113
PT	propagation time	145
RBF	radial basis function	43, 45–54
RD	reaction diffusion	i f., 1 ff., 21, 29 f., 32, 34, 36, 38, 40, 42, 59, 152, 159 ff.
RE	reaction-eikonal	141
RMSE	root mean square error	49 ff., 113 f., 116, 133 f., 136
SAN	sinoatrial node	8, 10, 13

Chapter 1

Introduction

1.1 Motivation

Cardiovascular diseases are a great affliction for humankind. They are the leading cause of mortality worldwide, affecting patients from diverse socioeconomic backgrounds and geographical locations, which places a significant load on global public health [1]. The economic cost associated with the treatment of these diseases and the morbidity of patients unable to work is an additional source of stress [2]. Moreover, the quality of life and mental health of these individuals are also significantly worsened [3, 4]. Optimizing strategies to reduce risk factors and improve healthcare interventions is essential for improving the quality of life for cardiovascular disease patients and for alleviating the substantial economic burden on health systems across the globe.

The most common sustained arrhythmia in humans is atrial fibrillation (AF) [5, 6]. It is characterized by irregular and often rapid atrial activity, which increases the risk of heart failure and stroke, thereby raising the mortality risk [7]. Given the complex nature and the incomplete understanding of AF's causes, current treatments are still ineffective [8]. Therefore, improving AF diagnosis and treatment, along with enhancing our understanding of AF mechanisms, is a top priority in cardiac research.

Given the complexity of AF and the limitations of current treatments, advancing both diagnosis and therapeutic approaches is a pressing priority. One promising strategy in this effort is the use of computer models, which have assured applications in basic research and growing potential in clinical settings. In basic research, they provide new insights into the complex mechanisms of AF [9]. In clinical settings, these models could aid in patient stratification and optimize ablation and drug therapies [10–13].

These models can replicate phenomena across different spatial scales. At the cellular level, ionic models use ordinary differential equations to simulate the action potential (AP) of a single cell [14]. At the tissue level, models simulate the propagation of electrical depolarization waves through interconnected cells [15]. Two key tissue-level models are reaction diffusion (RD) models and eikonal-based models. RD models are based on physical laws like the Ohm's law and the Kirchhoff's law. They integrate ionic models for each cell and use parabolic and elliptical partial differential equations to represent interactions between neighboring cells in both intracellular and extracellular domains [16–18]. These models simulate APs across all cells and accurately capture phenomena such as source-sink mismatch, but they are computationally burdensome [19, 20].

On the other hand, the standard eikonal model focuses on calculating activation times (ATs) with lower computational cost. However, it has significant limitations, such as lack of reactivations, conduction velocity (CV) restitution, and inability to capture source-sink mismatch phenomena [19, 21]. Different eikonal-based models have been developed to enhance its capabilities [22]. Neic et al.'s reaction eikonal model combines RD models with activation times obtained from the eikonal equation, enabling simulations on low-resolution meshes and reducing computing times. However, it does not simulate reactivations [20]. The multifrontal fast marching method (FMM) allows for reactivations by solving the eikonal equation but can introduce numerical errors, especially in anisotropic propagation [21, 22]. Gassa et al. developed a method incorporating CV restitution, producing spiral waves in realistic geometries without structural changes, yet it also inherits FMM's limitations in anisotropic propagation [22, 23]. These advancements show the eikonal model's potential in cardiac electrophysiology. However, further development is necessary to address some of its more relevant limitations and fully exploit its capabilities in the field of cardiac arrhythmias.

1.2 Objective of the Thesis

General Objective:

The aim of this thesis is to compare and integrate the eikonal model with other mathematical models to identify its limitations, gain a deeper understanding of the mechanisms underlying cardiac arrhythmias, particularly AF, and enhance its capabilities for patient stratification and treatment recommendations. To accomplish this aim, several specific objectives have been established.

Specific Objectives:

1. To evaluate the current characteristics of the standard eikonal model compared to RD models.
2. To utilize the standard eikonal model to assess methods for estimating atrial CVs from ATs data obtained from patients.
3. To enhance the eikonal model by extending it and integrating it with other models to broaden the scope of its applications.
4. To reduce the limitations arising from the lack of source-sink mismatch representation in the eikonal model by employing regression models fed with small RD simulations.

1.3 Structure of the Thesis

Part I: Fundamentals presents the required fundamentals which are introduced at a medical and a technical level.

- **Chapter 2** introduces the medical fundamentals of cardiac electrophysiology with focus on the atria at cellular and tissue level.
- **Chapter 3** presents the basic theory of computer models of cardiac electrophysiology at cellular and tissue level.

Part II: Analysis and Applications of the Standard Eikonal Model presents two projects related to the analysis and use of the standard eikonal models in cardiac electrophysiology.

- **Chapter 4** provides a comparison of the bidomain, monodomain and eikonal-based models.
- **Chapter 5** introduces a new application of the standard eikonal model to assess methods to estimate CV of the wavefront propagation in cardiac tissue.

Part III: Diffusion reaction eikonal alternant model (DREAM) presents an extended version of the eikonal model, the DREAM. It alternates the eikonal model with an approximated version of the RD model to take advantage of the capabilities of both models.

- **Chapter 6** introduces the mathematical fundamentals of the DREAM comparing it with the monodomain model.
- **Chapter 7** shows an application of the DREAM model to assess personalized CV restitution properties in reentry vulnerability.

Part IV: Source-Sink Mismatch Implementation in the Eikonal Model provides different methods to decrease the error coming from the lack of source-sink match representation in the eikonal model.

- **Chapter 8** explores the effects of wall thickness and tissue curvature in the CV of the excitation wave and propose methods to reduce the error from neglecting these phenomena in the eikonal model.
- **Chapter 9** explores the effect of source-sink mismatch and frequency activation in the morphology of the diffusion current.

In the final chapters future work is suggested in **Chapter 10** and the conclusion is drawn in **Chapter 11**.

PART I

FUNDAMENTALS

Chapter 2

Medical Fundamentals

This chapter presents the fundamental medical concepts necessary for understanding this thesis. It begins with an exploration of heart morphology, covering its histological and anatomical features. Following this, the chapter offers a brief explanation of heart physiology, focusing on its mechanical and electrophysiological properties. Finally, it provides a concise overview of atrial fibrillation (AF), discussing its epidemiology, pathophysiology, diagnosis, and treatment.

2.1 Morphology of the Heart

2.1.1 Anatomy

The heart is a muscular, cone-shaped, hollow organ with four chambers: the left and right atria, and the left and right ventricles (Figure 2.1) [24, 25]. It weighs approximately 361.6±95.9 g [26]. The heart is well protected within the thorax, situated between the lungs. It is positioned posterior to the rib cage, the intercostal muscles, and the sternum; and anterior to the esophagus, trachea, bronchi, descending aorta, inferior vena cava, and thoracic vertebrae. Superiorly, the heart is connected to the pulmonary trunk, pulmonary veins, superior vena cava, and ascending aorta. Inferiorly, it rests on the central tendon of the diaphragm. The human heart has an oblique orientation, with two-thirds of its mass to the left of the midline. The base, which is the superior part, is directed superiorly, to the right of the midline, and posteriorly. The apex, located opposite to the base, points downward and towards the left of the midline [24, 25, 27, 28]. The heart is supported and enclosed by the pericardium, a sac with two layers. The outer fibrous layer provides mechanical support and anchors the heart to the thoracic cavity, while the inner serous layer produces a lubricant to reduce friction during contractions [25].

Right Atrium The right atrium is a roughly quadrangular chamber. The left atrium is situated to the left, superior, and posterior to the right atrium. The right atrium consists of

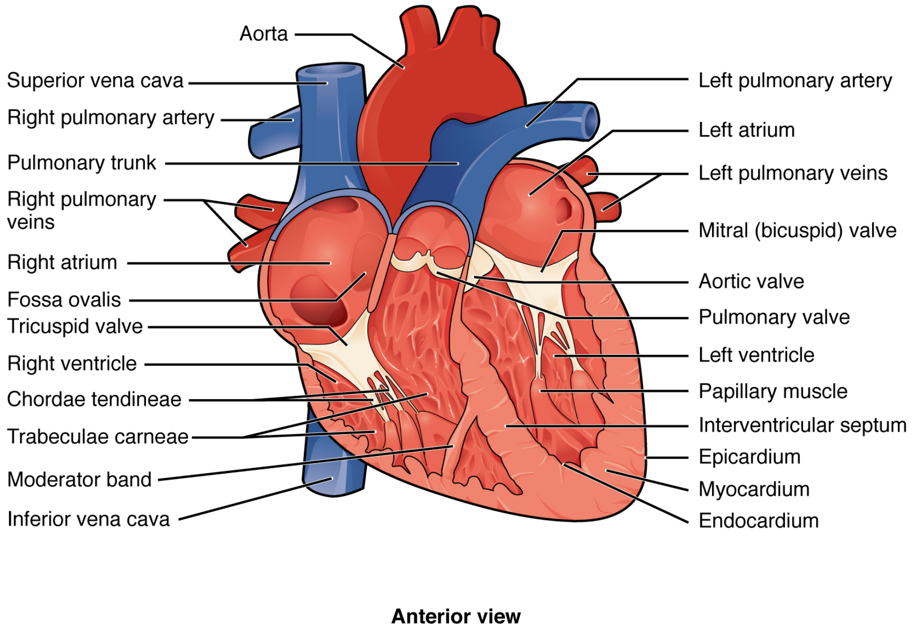

Figure 2.1: Diagram of the anatomy of the heart. Taken from [29] and licensed under the Creative Commons Attribution 3.0 unported license

three parts, each with distinct embryological origins. The posterior part, where the superior and inferior vena cava and the coronary sinus open, has a smooth internal surface and houses the sinoatrial node (SAN). The anterior part contains the pectinate muscles, which are parallel muscle bundles, as well as the right atrial appendage with a similar wall structure. The septum, which is a shared wall with the left atrium, contains the atrioventricular (AV) node. Additionally, on the inferior and left side of the septal wall of the right atrium, there is the AV septum, which borders the left ventricle [24, 25, 28, 30].

Right Ventricle The right ventricle is typically the most anterior chamber of the heart and has an irregular pyramidal shape. Its major axis is oriented inferiorly, anteriorly, and to the left. The walls of the right ventricle are covered by abundant, coarse trabeculae carneae, similar to the pectinate muscles. The right ventricle can be divided into two portions: the outflow tract and the base. The free wall of the right ventricle is thinner than that of the left ventricle. The right ventricle is separated from the right atrium by the tricuspid valve. The outflow tract is distinguished from the rest of the right ventricle by the supraventricular crest and is directed anterosuperiorly to the left, leading to the pulmonary trunk, which is separated by the pulmonary semilunar valve [24, 25, 28].

Left Atrium The left atrium is typically the most posterior chamber of the heart, with its major axis oriented transversely. The pulmonary veins enter the left atrium posteriorly and laterally on each side, usually in two pairs, one on each side. The left atrium is positioned posteriorly and to the left of the right atrium, as well as superiorly and posteriorly to the left ventricle. The left atrial appendage is located anterolaterally and has pectinate walls, unlike the rest of the left atrium, which has a smooth surface [24, 25, 28, 31, 32].

Left Ventricle The left ventricle is the most inferior chamber of the heart. It has a half-bullet shape due to the interventricular septum bulging into the right ventricle, resulting in a narrower apex compared to its base. Unlike the right ventricle, the left ventricle's walls have finer muscular ridges, and its free wall is significantly thicker. The entry and exit orifices of the left ventricle are closer to each other. The left ventricle is separated from the left atrium by the mitral valve and from the aorta by the aortic semilunar valve, with the outflow tract oriented superiorly and posteriorly to the right [24, 25, 28].

Irrigation The heart is supplied by the coronary arteries, which provide oxygen-rich blood and originate from the ostia above the aortic valve. The right coronary artery travels through the right anterior AV groove. It bifurcates into two branches: one descends along the posterior interventricular groove, while the other extends to the left AV groove. This artery supplies the right atrium, right ventricle, and the posterior part of the interventricular septum.

The left coronary artery divides shortly after its origin into two main branches: the left anterior descending (LAD) coronary artery and the left circumflex coronary artery. The LAD artery provides branches to the free wall of the left ventricle and the interventricular septum, continues to the apex, and then turns into the posterior interventricular groove. The left circumflex artery travels along the AV groove, supplying the left atrium, as well as the lateral and posterior walls of the left ventricle.

The coronary venous system is twice as abundant as the arterial system. It drains the myocardium and is divided into two groups: the greater and smaller cardiac venous systems. The greater cardiac venous system drains into the coronary sinus and includes the anterior cardiac veins, atrial veins, and veins of the ventricular septum. The smaller cardiac venous system, also known as the Thebesian vessels, originates in the endocardial layer of the myocardium and drains directly into the heart chambers, including the left chambers. These vessels do not reach the external surface of the heart. The Thebesian vessels are more numerous in the atria compared to the ventricles and are more frequent in the right ventricle than in the left ventricle [24, 25, 28].

Innervation The heart's innervation is involuntary and primarily controlled by the autonomic nervous system, which includes both the sympathetic and parasympathetic branches. Both systems originate in the hypothalamus and involve two neurons: the first neuron synapses in a ganglion (a group of neuron cell bodies), and the second neuron's axon extends to various components of the heart.

The parasympathetic nervous system is mediated through the vagus nerve, also known as the X cranial nerve. The sympathetic nervous system arises from the 8 cervical segments and the first 5 thoracic nerves, with synapses occurring in the stellate ganglia. The cardiac nerves from both the sympathetic and parasympathetic systems converge in the cardiac plexuses: the dorsal cardiac plexus and the ventral cardiac plexus, located posterior and anterior to the aorta, respectively. Nerves from these plexuses innervate the SAN, the AV node, the coronary arteries, the great vessels, and the myocardium itself [25, 28].

2.1.2 Histology

The cardiac wall consists of three layers: the endocardium (inner layer), the myocardium (middle layer), and the epicardium (outer layer). The majority of the heart's mass is within the myocardium. The endocardium lines the inner surfaces of all four chambers and covers both surfaces of the heart valves [25]. It continues with the endothelium of the arteries and veins connected to the heart. The endocardium has a single layer of polygonal endothelial cells. Beneath this layer, there is a dense connective tissue layer rich in elastic and collagen fibers [33, 34]. The myocardium is composed of cardiomyocytes interconnected through dense connective tissue. These cardiomyocytes are arranged in networks oriented either circularly or spirally around the heart [34]. Cardiomyocytes are special muscle cells with short branch projections that connect to other cardiomyocytes through intercalated discs [25]. The epicardium is the outside layer of the heart walls and the inner layer of the pericardium.

Cardiomyocytes are cylindrical cells with a diameter of 10-20 µm and lengths between 50 and 100 µm [35]. Internally, they contain all the usual organelles found in other cells, but most of their volume is dedicated to cytoskeletal structures. Unlike skeletal muscle cells, which are multinucleated, cardiomyocytes typically have only one or two nuclei. Like other cells, cardiomyocytes are enclosed by a bilayer phospholipid membrane with embedded ion channels, pumps, and receptor proteins. This membrane features invaginations filled with extracellular fluid, known as T-tubules, which are more numerous in the ventricular than in the atrial cardiomyocytes. T-tubules are closely associated with the sarcoplasmic reticulum, which stores calcium. Within the sarcoplasm, myofibrils, contractile organelles, are densely packed and extend from one end of the cell to the other, with diameters of 1-2 µm [36]. Each myofibril is composed of a series of sarcomeres, which are delineated by Z-discs, dense arrays of actin proteins perpendicular to the cell's longitudinal axis (Figure 2.2). Inside each sarcomere, thick and thin filaments intertwine. Thick filaments are primarily composed of myosin, while thin filaments consist of actin surrounded by regulatory proteins, troponin and tropomyosin. Thick filaments are connected to the Z-discs by the protein titin [25, 37].

Although atrial and ventricular cardiomyocytes share many structural features, there are notable differences. Atrial cardiomyocytes typically have a single, elongated nucleus, whereas ventricular cardiomyocytes might have up to two nuclei. T-tubules are less frequent and less pronounced in atrial cardiomyocytes compared to ventricular cardiomyocytes. Atrial cardiomyocytes also exhibit a denser packing of mitochondria compared to those in the ventricles. Additionally, atrial cardiomyocytes contain dense secretory granules, which are not present in ventricular cardiomyocytes. Finally, atrial cardiomyocytes generally have a higher density of other organelles, such as Golgi complexes [39, 40].

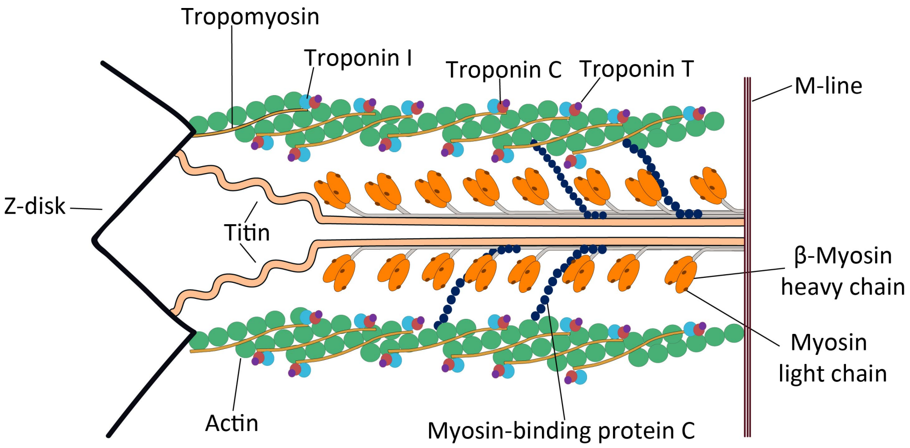

Figure 2.2: A diagram illustrating various components of the cardiac sarcomere structure, including myosin-binding protein C. Taken from [38] and licensed under the Creative Commons Attribution-Share Alike 4.0 International license

2.2 Physiology of the Heart

2.2.1 Mechanical Function

The heart's main function is to generate the necessary pressure gradient for blood flow between different compartments of the body, including the lungs and the systemic circulation. This pressure gradient enables the supply of nutrients to tissues, removal of metabolic byproducts, transport of hormones and immune components, and oxygenation of blood in the lungs, among other functions. To create this gradient, the cardiac muscle in the four chambers contracts cyclically, moving deoxygenated blood from the veins to the right atrium, then to the right ventricle, and finally to the lungs via the pulmonary arteries for oxygenation. Oxygenated blood returns from the lungs back to the heart in the left atrium and is then pumped out to the systemic circulation through the left ventricle and the aorta. The efficiency of this process is enhanced by the coordinated electrical excitation of cardiomyocytes, ensuring the atria contract before the ventricles [25, 37, 41].

In the first phase of the cardiac cycle, the atria undergo electrical activation, leading to their contraction. As the atria contract, the pressure inside these chambers increases, creating a greater pressure gradient between the atria and the ventricles. This increased gradient facilitates the flow of blood from the atria to the ventricles through the open AV valves. Once atrial contraction concludes, the atrial muscle begins to relax, causing a decrease in pressure and a temporary reversal of the pressure gradient, with higher pressure now in the ventricles. This reversed gradient triggers an attempt by the blood to flow back into the atria, which results in the closure of the AV valves [25, 37, 41].

Once the AV valves close, the ventricles begin to contract while the semilunar valves remain closed, as the pressure in the arteries is still higher than in the ventricles. This marks the onset of the systole. During this phase, known as isovolumetric contraction, the ventricles contract without a change in volume, causing a significant rise in ventricular pressure. Meanwhile, the atria are filling with blood from the veins, steadily increasing their pressure due to venous return. When the pressure in the ventricles surpasses the pressure in the aorta and pulmonary artery, the semilunar valves open, allowing rapid ejection of blood, initially at a high rate, followed by a slower ejection phase. Simultaneously, the atria continue to fill with blood, which increases their volume but temporarily reduces their pressure as the atrial base is pulled downward.

As ventricular contraction concludes, ventricular repolarization leads to relaxation, and the pressure in the ventricles drops. This pressure reduction reverses the pressure gradient between the ventricles and arteries, although blood does not immediately flow backward due to its inertia, marking the end of systole.

Once blood attempts to reenter the ventricles, the semilunar valves close. During this time, the ventricles continue to relax, resulting in isovolumetric relaxation, where the pressure decreases without a change in volume. Because the elastic walls of the aorta and pulmonary artery slow and moderate the decrease in arterial pressure, the drop is slower and less pronounced than in the ventricles. Finally, when ventricular pressure falls below atrial pressure, the AV valves open, allowing rapid ventricular filling. Ventricular pressure continues to decrease despite the filling, as the ventricles continue to relax.

Once ventricular relaxation ends and filling continues, ventricular pressure gradually rises. After most of the blood has left the atria, the pressure and volume in the ventricles begin to increase while compliance decreases. This leads to a period of ventricular diastasis, characterized by reduced ventricular filling. Just before atrial contraction, atrial pressure is lower than ventricular pressure, but blood flow into the ventricles continues due to the inertia of the blood. Atrial contraction, together with rapid and reduced ventricular filling, marks the diastolic phase of the cardiac cycle. When atrial contraction starts again, it initiates a new cycle [25, 37, 41].

For the heart to generate contracting force, cardiomyocytes must shorten their length to create active tension. This process occurs through the interaction of proteins within the sarcomere, the functional unit of contraction in the sarcoplasm. In the resting state, actin is bounded to tropomyosin, which prevents it from interacting with myosin. This inhibition is regulated by troponin, a protein complex associated with tropomyosin. Troponin has three subunits: troponin I, which inhibits the actin-myosin interaction; troponin C, which binds to calcium; and troponin T, which binds to tropomyosin. During diastole, calcium concentrations in the sarcoplasm are kept very low to maintain the separation between myosin and actin, controlled by the conformation of troponin and tropomyosin. However, during the action potential (AP), when calcium enters the sarcoplasm from the extracellular space and sarcoplasmic reticulum, troponin C binds to calcium. This binding causes a conformational change that allows actin to interact with myosin. The interaction between these two proteins causes the thick and thin filaments to slide over each other, shortening the sarcomere and, consequently, the cardiomyocyte. When calcium levels decrease during the repolarization phase of the cardiac cycle, troponin C releases calcium, returning the complex to its previous state where myosin detaches from actin and tropomyosin once again blocks the actin binding sites. Both contraction and relaxation require adenosine triphosphate (i.e., ATP) to facilitate the binding and release of the myosin head from the actin filament. Consequently, mitochondria are abundant around the myofibrils and the sarcoplasmic reticulum to meet the high energy demands of this process [25, 37, 41].

2.2.2 Electrical Function

The SAN, with its spontaneous depolarization occurring at a frequency of 60-100 cycles per minute at rest, sets the heart rate. This depolarization stimulates the atrial tissue, initiating an excitation wave followed by atrial contraction. Subsequently, the AV node, delays the excitation wave, allowing the ventricles to depolarize and contract after the atria. The impulse then progresses through the His bundle and the Purkinje fibers, facilitating rapid and complete depolarization of both ventricles [25, 37, 41].

When a cardiomyocyte is excited, ions exchange across the membrane resulting in changes in transmembrane voltage, creating an AP. The AP of a cardiomyocyte consists of 5 phases. The cell membrane, or sarcolemma, functions as a capacitor, separating net negative charges inside the cell from positive charges outside. The resting state is known as phase 4, and is characterized by a transmembrane voltage of approximately -85 mV. The net intracellular negativity is due to proteins and nucleic acids with negative charges, while extracellular positivity comes from having more possitive ions like calcium and sodium than negative ions like chlorine.

At the beginning of the cycle, activation from neighboring cells causes a diffusion current (DC) that increases the transmembrane voltage to a threshold level. This partial depolarization, corresponding to phase 0, activates fast sodium channels, allowing sodium to enter the cell and producing the fast inward sodium current, I_{Na}, which quickly raises the transmembrane voltage. Once the voltage peak is reached, sodium channels close and potassium channels open, allowing potassium to exit the cell, slightly decreasing the transmembrane voltage and producing the transient outward potassium current, I_{to}, which corresponds to phase 1, or early repolarization. Concurrently, slower calcium channels open, permitting calcium to enter the intracellular space through the L-type calcium current, $I_{\mathrm{Ca,L}}$. The increase in calcium in the cytosol triggers the release of much more calcium from the sarcoplasmic reticulum via ryanodine receptor type 2. This increase in intracellular calcium concentration leads to the mechanical contraction of the cardiomyocyte and delays repolarization, creating the plateau phase, or phase 2. During phase 2, the outward movement of potassium continues through the ultra-rapid potassium current, I_{Kur}.

Repolarization occurs when additional potassium channels open, producing the rapid delayed rectifier potassium current (I_{Kr}) and slow delayed rectifier potassium current (I_{Ks}), while calcium channels close, marking phase 3. Once potassium currents return the cell to its resting state, the inward rectifier potassium current (I_{K1}) stabilizes the resting membrane potential, and the sodium-potassium ATPase pump restores the ion gradient until the next AP. During phases 0 to 3, the cardiomyocyte is in a refractory state, preventing a second

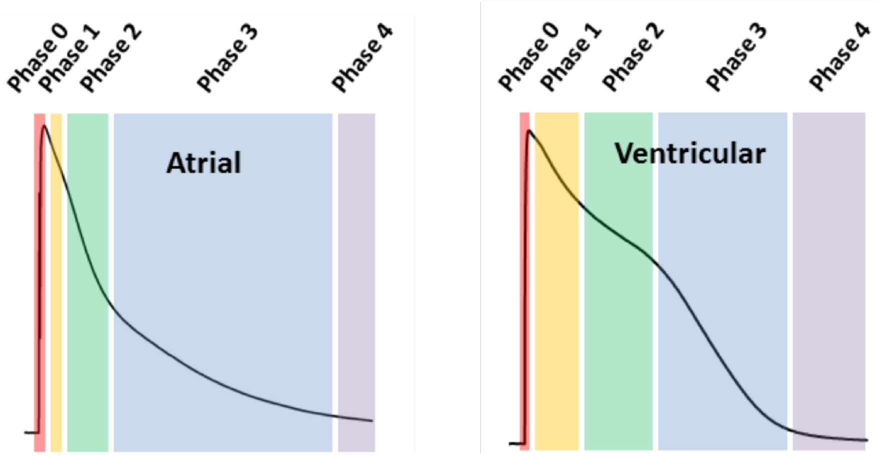

Figure 2.3: Ventricular and atrial action potentials with their phases. Adapted from [43] licensed under the Creative Commons Attribution-Share Alike 4.0 International license.

AP, a period known as the effective refractory period, which protects against arrhythmia initiation. [25, 37, 41].

The electrophysiology of atrial and ventricular cardiomyocytes differs in several key aspects. Figure 2.3 shows atrial and ventricular action potential with their respective phases. One major difference is that the $I_{\mathrm{Ca,L}}$ current in atrial cells is closely regulated by serotonin and phosphodiesterases, which reduce this current in the atria, resulting in a significantly shorter AP compared to ventricular cells. Additionally, I_{Kur} current plays a prominent role in atrial repolarization, whereas it is less significant in the ventricles further contributing to shorter APs. In contrast, ventricular cardiomyocytes exhibit higher activity of the I_{K1} current which translate to more negative resting potential. Lastly, atrial cells are rich in stretch-sensitive ion channels, which act as mechanosensors and can induce depolarizations in response to mechanical stimuli [42].

2.3 Atrial Fibrillation

AF is the most common sustained arrhythmia. It is characterized by irregular electrical activation in atria. It increases the risk of mortality and impairs quality of life due to associated complications such as stroke or heart failure. On the other hand, other diseases such as diabetes mellitus or hypertension are risk factors for AF. Mechanisms of physiopathology are still poorly understood. The treatment alternatives are not quite optimal yet. Consequently, AF still represents a big burden for society in terms of health and economic cost.

2.3.1 Epidemiology

In 2019 the prevalence of AF and atrial flutter, another supraventricular arrhythmia, was 59.7 millions patients worldwide. This value has doubled since 1990 probably due to the increased life expectancy [1]. Multiple modifiable risk factors are related to AF such as hypertension, obesity, obstructive sleep apnea, diabetes mellitus [44]. Advancing age is a significant risk factor for AF, probably due to a decrease in conduction velocity (CV) and increase of heterogeneity of the cardiac tissue with age [44]. The lifetime cumulative risk of developing AF is lower in women compared to men, but tends to have similar values at old age. Mortality seems to increase equally in both sexes [45]. Regarding ethnicity, lower prevalence rates have been reported among Black, Hispanic, and Asian individuals compared to Caucasians [44].

2.3.2 Mechanisms of Pathophysiology

The mechanisms of AF pathophysiology are not completely understood. Nonetheless there has been significant amount of research and discoveries on this topic. Studies in patients, animals, in-vitro and computer models have been used to gain new insights about the changes in cardiac tissue that lead to AF. Some of these mechanisms include the presence of ectopic foci, structural and functional remodelling of the cardiac tissue. The weight of those mechanisms very likely vary from patient to patient [46].

Automaticity and triggered activity are some of the most important mechanisms linked to the initiation of AF. These mechanisms include enhanced automaticity, abnormal automaticity and triggered activity. Enhanced automaticity happens when pacemaker myocytes increase their activity due to various reasons such as a decreased threshold of AP upstroke or a less negative diastolic potential. Abnormal automaticity can happen when any kind of current depolarize the cell, normally driven by calcium inward currents. Triggered activities are related to the membrane oscillations happening during or after a normal AP. These oscillations might lead to new APs during phase 2 or 3 of the previous AP (early afterdepolarizations) or after full repolarization from the previous AP (delayed afterdepolarizations) [46].

Reentry, which is defined as a self perpetuating wavefront, is another one of the main mechanisms of AF. An important requirement for reentry is the presence of an excitable gap so that the tissue ends the refractory period before the wavefront reaches it again. Conditions such as shorter refractory period or slow CV increase the probability for the occurrence of reentry. Among the main theories of reentry there are the circle movement reentry, the leading circle concept, the spiral wave reentry, and the multiple wavelet hypothesis. The circle movement reentry consist of an excitation wavefront that moves around an anatomical obstacle and reactivate cells previously excited by the same wavefront (Figure 2.4A). The leading circle concept is a similar phenomena but without an anatomical structure, the reentry travels around potentially excitable tissue that is not fully activated but receives electrotonic depolarizations that hinders its full activation (Figure 2.4B). The spiral wave reentry occurs

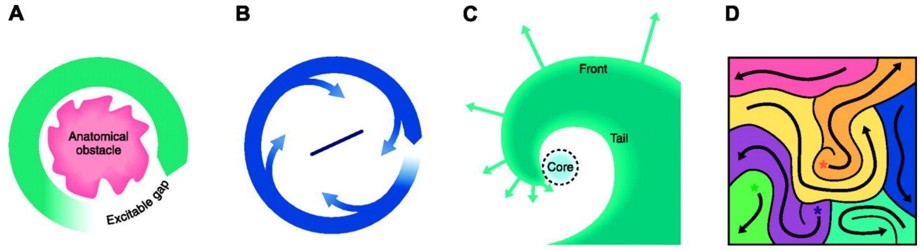

Figure 2.4: Mechanisms of reentry. A: circus movement reentry. B: leading circle concept. C: rotor theory reentry. D: chaotic activation pattern caused by multiple wavelets. Taken from [46] with permission from the publisher.

when a wavefront collides perpendicularly with the tail of another wavefront. This collision with refractory tissue in the tail creates a block of the second wavefront which must turn behind the tail of first wavefront. An important phenomenon taking place during the spiral wave reentry is the source sink mismatch: in the center of the spiral when the curvature of the wavefront is higher the CV is slower. On the other hand, in the outer area of the spiral the curvature is lower and the CV higher (Figure 2.4C). Finally, the multiple wavelet hypothesis states of the existence of multiple wavefronts constantly interacting with each other colliding and creating new wavefronts in a chaotic manner. Shortening of the refractory period and slow CV also contribute to the stability of this process (Figure 2.4D) [46].

Another relatively recent mechanism identified is epi-endocardial dissociation, which is promoted by epicardial fibrosis and the complex structure of the left atrium. This creates a larger three-dimensional substrate for the arrhythmia to sustain itself via transmural breakthroughs, making it difficult to map AF from either the endocardium or epicardium alone. As a result, identifying the main mechanism of AF becomes more challenging [47–50].

2.3.3 Diagnostic, Imaging and Mapping Techniques

Clinical presentation Although up to one third of patients with AF can be asymptomatic, patients can present various symptoms of diverse severity. The most common symptoms are palpitations, dizziness, chest pain, shortness of breath, fatigue [7]. In some complications such as stroke there can be also neurological deficit such as muscular weakness, speech impediments, headaches, lost of balance [51]. Another common complication is heart failure that can be accompanied by swelling, reduced tolerance to exercise, and shortness of breath while lying flat [52].

Electrophysiological Mapping The electrocardiogram (ECG) is one of the most fundamental tools for assessing the heart's electrophysiological activity. It is non-invasive, cost-effective, and widely accessible. The ECG typically uses a set of 12 leads, configured from the electrical potentials recorded by electrodes placed on the skin's surface. Each wave and segment of the ECG corresponds to a crucial part of the cardiac cycle: the P-wave reflects atrial depolarization, the QRS complex represents ventricular depolarization, and the T-wave signifies ventricular repolarization, while atrial repolarization is masked by the

QRS complex. An ECG is essential for diagnosing AF, which is identified by at least 30 seconds of electrical activity without distinct P-waves, irregular RR intervals, and intact AV conduction [7, 53].

Electrocardiographic imaging (ECGI) builds upon the ECG concept by significantly increasing the number of electrodes on the patient's torso. This advanced technique reconstructs 3D maps of the heart's electrical pathways, offering potential for localizing sources of AF and quantifying regional CV. However, its clinical application in AF is still under development and validation [54, 55].

Finally, electroanatomical mapping is an invasive technique that involves inserting catheters into the cardiac chambers. These catheters are equipped with electrodes arranged in various geometrical configurations, depending on the catheter's type and purpose. The catheter's location can be tracked over time, allowing for the reconstruction of atrial geometry. The electrodes measure the extracellular potential relative to a distant reference electrode, generating a unipolar electrogram. When signals from two different electrodes are subtracted, the result is a bipolar electrogram, which is less affected by ventricular activity and respiratory noise compared to unipolar electrograms. Electroanatomical data is crucial for guiding ablation treatments for AF [56].

Tomographic Imaging Methods Tomographic imaging of the heart is a powerful technique for assessing its anatomical structure. Both computed tomography (CT) and magnetic resonance imaging (MRI) use different types of waves to penetrate cardiac tissue and reconstruct the heart's 3D geometry. CT employs X-rays, which are directed at the patient from various angles. Sensors measure the attenuation of these X-rays as they pass through the body, enabling the reconstruction of a detailed 3D map of the heart [57]. MRI, on the other hand, uses strong magnetic fields and radio waves to align hydrogen atoms within the body. The energy released as the atoms return to their original states is captured and used to create a 3D map of the heart [58–61].

CT scans generally offer better spatial resolution, providing a more precise view of the patient's anatomical structures [62]. However, a significant drawback of CT is the exposure to ionizing radiation, which can have adverse side effects. In contrast, MRI does not involve ionizing radiation, making it a safer alternative in terms of radiation exposure. Additionally, when combined with gadolinium contrast, MRI can more effectively identify myocardial tissue abnormalities [59–61].

2.3.4 Treatment

The management of AF focuses on alleviating symptoms, reducing mortality, and preventing complications. The cornerstone of AF treatment includes anticoagulation therapy, rate control, and rhythm control. Anticoagulation therapy is primarily aimed at reducing the risk of stroke and is recommended for most patients, except those with a very low risk of stroke. Although anticoagulants increase the risk of bleeding, this should not preclude their use but rather be carefully monitored during follow-up. Rate control is aimed at managing symptoms and is usually achieved with medications; however, node ablation combined with ventricular pacing may be considered in selected cases where medication is ineffective. Rhythm control, which not only improves symptoms but also may reduce the progression of AF, can be accomplished with antiarrhythmic drugs, electrical cardioversion, or catheter ablation [7].

Chapter **3**

Mathematical Fundamentals

This chapter explores the mathematical models in cardiac electrophysiology that are essential for understanding the context of this work. The chapter is divided into two sections: the first section focuses on ionic models, which describe electrophysiology at the cellular level, while the second section examines models that simulate the propagation of excitation waves in cardiac tissue. These mathematical models are particularly relevant for advancing cardiac research, as they help to unravel the mechanisms underlying the pathophysiology of atrial fibrillation (AF) and have the potential to contribute to the development of improved diagnostic tools and treatments.

The content of this chapter is taken and adapted from previous work [19, 22]. Most passages have been rephrased or quoted verbatim from these publications.

3.1 Ionic Models

Ionic models simulate changes in transmembrane voltage of a single cardiomyocyte during the action potential (AP) based on ionic currents flowing through its sarcolemma. These models are crucial for studying how drugs or channel mutations affect the AP of single cardiomyocytes. These in silico studies can reduce preclinical trial costs by evaluating cardiotoxic risks early, identifying drugs that alter action potential duration (APD) and increase arrhythmia risk [63, 64]. Additionally, these models are essential for building more complex simulations of multiple coupled cardiomyocytes.

To simulate single-cell electrophysiology, the sarcolemma (i.e., cell membrane) is modeled as a capacitor that separates negative intracellular net charges from positive extracellular net charges in the resting state. The relationship between transmembrane voltage (V_m), membrane capacitance (C_m), and ionic current (I_ion) is derived from Kirchhoff's current law:

$$C_\mathrm{m}\frac{\mathrm{d}V_\mathrm{m}}{\mathrm{d}t} = -I_\mathrm{ion}. \tag{3.1}$$

The ionic current I_ion is defined as the sum of all currents facilitating ionic exchanges between the intracellular and extracellular spaces:

$$I_{\text{ion}} = \sum_X I_X \tag{3.2}$$

where for a single type of channel, the current I_X that allows the passage of ion X through the cell membrane depends on several factors:

$$I_X = g_X p(O)(V_{\text{m}} - E_X) \tag{3.3}$$

- **Channel Conductance (g_X):** This conductance is proportional to the number of channels of this type in the sarcolemma.
- **Driving Force ($V_{\text{m}} - E_X$):** The difference between the transmembrane voltage V_{m} and the equilibrium potential E_X for X. The equilibrium potential is the transmembrane voltage at which there is zero net exchange of X through the cell membrane. If $V_{\text{m}} > E_X$, the current is positive and X moves out of the cell and vice versa if $V_{\text{m}} < E_X$, then X moves into the cell.
- **Open Probability ($p(O)$):** This probability represents the ratio of channels that are open over the total number of channels of X. This depends on factors such as the transmembrane voltage, ion concentrations, and drug interactions. It can be represented with more simple ordinary differential equations like in the Hodgkin-Huxley models or more sophisticated systems like the Markov models [65].

Ionic models can be adapted to replicate properties of cardiomyocytes in different species such as rabbits, or humans. They can represent atrial or ventricular electrophysiology. Due to the lack of experimental human data, animal studies were used to fit some of the parameters of the human models. Depending on the level of complexity they can represent more detailed ion currents or physiological phenomena such as alternans of APD [66]. Other more simple models with less level of detail can be more appealing due to computing speed [67]. The efficiency to perform single cell simulations relies not only on the used ionic model but also on the time integrator. The most used time integrator in these cell models is the Rush-Larsen method. The Rush-Larsen method is a partitioned method, using an exponential Euler method for gating variables (i.e., variables related to the dynamics of the ion channels) and forward Euler method for the rest of the variables such as ion concentrations [68]. The popularity of this method is due to its stability balanced with an easy implementation, however other methods might be better suited when the stiffness of the model is not captured by the gating variables [69].

The Courtemanche et al. model is the most used in this work [66]. This ionic model was one of the first to represent the human atria. In this particular case, the ionic current is the sum of the following currents:

$$I_{\text{ion}} = I_{\text{Na}} + I_{\text{K1}} + I_{\text{to}} + I_{\text{Kur}} + I_{\text{Kr}} + I_{\text{Ks}} + I_{\text{Ca,L}} + I_{\text{p,Ca}} + I_{NaK} + I_{\text{b,Na}} + I_{\text{b,Ca}}, \tag{3.4}$$

The sodium current (I_{Na}) is responsible for rapid depolarization, while the inward rectifier potassium current (I_{K1}) stabilizes the resting potential and aids in repolarization. The transient outward potassium current (I_{to}) contributes to early repolarization, and the ultrarapid delayed rectifier potassium current (I_{Kur}) facilitates rapid repolarization in atrial cells. The rapid delayed rectifier potassium current (I_{Kr}) supports repolarization with fast kinetics, and the slow delayed rectifier potassium current (I_{Ks}) helps with slower repolarization. The L-type calcium current ($I_{\text{Ca,L}}$) is crucial for the action potential plateau and calcium-induced calcium release. The plasma membrane calcium pump current ($I_{\text{p,Ca}}$) removes excess calcium from the cell, while the sodium-potassium pump current (I_{NaK}) maintains ionic gradients by exchanging sodium and potassium ions. Additionally, the background sodium current ($I_{\text{b,Na}}$) and the background calcium current ($I_{\text{b,Ca}}$) provide persistent ionic flows across the membrane.

3.2 Propagation Models

This section explores the most commonly used mathematical models to simulate electrical excitation waves in cardiac tissue. These models simulate propagation of the excitation wave at the tissue or organ level and there are two kinds analyzed in this work: the reaction diffusion (RD) models and the eikonal model. RD models, based on Ohm's law and the conservation of charge, provide an accurate representation of several important physical phenomena. While eikonal models offer a computationally faster alternative, they have significant limitations. Standard eikonal models cannot accurately capture reactivations and reentry, and fail to account for diffusion and curvature effects.

3.2.1 Bidomain Model

The bidomain model is widely recognized for accurately representing the propagation of electrical depolarization and repolarization wavefronts through cardiac tissue [16–18]. This model couples the intracellular and extracellular domains through a system of partial differential equations. Solving these equations yields the intracellular (Φ_{i}) and extracellular (Φ_{e}) electrical potentials at each point within the cardiac tissue:

$$-\nabla \cdot ((\sigma_{\text{i}} + \sigma_{\text{e}})\nabla\Phi_{\text{e}}) = \nabla \cdot (\sigma_{\text{i}}\nabla V_{\text{m}}) \tag{3.5}$$

$$\nabla \cdot (\sigma_{\text{i}}\nabla V_{\text{m}}) + \nabla \cdot (\sigma_{\text{i}}\nabla\Phi_{\text{e}}) = \beta\left(C_{\text{m}}\frac{\partial V_{\text{m}}}{\partial t} + I_{\text{ion}}(V_{\text{m}}, \overrightarrow{\eta}) - I_{\text{s}}\right) \tag{3.6}$$

Here, $V_{\text{m}} = \Phi_{\text{i}} - \Phi_{\text{e}}$ represents the transmembrane potential, while σ_{i} and σ_{e} denote the intracellular and extracellular conductivity tensors:

$$\sigma_{\text{i}} = \sigma_{\text{i,l}}\overrightarrow{l} \otimes \overrightarrow{l} + \sigma_{\text{i,t}}\overrightarrow{t} \otimes \overrightarrow{t} + \sigma_{\text{i,n}}\overrightarrow{n} \otimes \overrightarrow{n} \quad \text{on } \Omega \subset \mathbb{R}^3, \tag{3.7}$$

$$\sigma_{\text{e}} = \sigma_{\text{e,l}}\overrightarrow{l} \otimes \overrightarrow{l} + \sigma_{\text{e,t}}\overrightarrow{t} \otimes \overrightarrow{t} + \sigma_{\text{e,n}}\overrightarrow{n} \otimes \overrightarrow{n} \quad \text{on } \Omega \subset \mathbb{R}^3, \tag{3.8}$$

where $\sigma_{\text{i},\xi}$ is the scalar value for the intracellular conductivity in the longitudinal, transversal, or sheet-normal directions, and $\sigma_{\text{e},\xi}$ is the scalar values for the extracellular conductivities in the same directions with $\xi = \mathrm{l/t/n}$. Moreover, $\overrightarrow{l}$, $\overrightarrow{t}$, and $\overrightarrow{n}$ form an orthonormal system of vectors in the longitudinal, transversal, and sheet-normal directions, respectively. $\overrightarrow{l}$ is aligned with the local preferential myocyte orientation. Additionally, β is the surface-to-volume ratio of the membrane, and C_m is the membrane capacitance per unit surface area. The terms I_s and I_ion are the optional transmembrane stimulus current and ionic current, respectively. The ionic current I_ion depends on state variables $\overrightarrow{\eta}$, which are calculated using a nonlinear system of ordinary differential equations.

Depending on the simulation setup, boundary conditions can be enforced in different ways. For instance, a simulation where the myocardium is embedded in a torso and filled with blood, specific conditions are required. Homogeneous Neumann boundary conditions must be applied at the boundaries of both the myocardial tissue (intra- and extracellular domains) and the torso (extracellular domain). At the interface between the myocardial tissue and the torso, the potential Φ_e is constrained to be continuous, while a no-flux condition is enforced in the normal direction $\overrightarrow{n}$ for Φ_i:

$$\overrightarrow{n} \cdot \sigma_\mathrm{i} \nabla \Phi_\mathrm{i} = 0 \tag{3.9}$$

Additionally, a no-flux boundary condition for Φ_e is imposed on the torso boundary not in contact with the myocardial tissue:

$$\overrightarrow{n} \cdot \sigma_\mathrm{b} \nabla \Phi_\mathrm{e} = 0 \tag{3.10}$$

where σ_b is the conductivity of the bath (torso or blood). Continuity of the normal component of the extracellular current and the potential Φ_e at the tissue-bath interface is enforced by the following conditions:

$$\sigma_\mathrm{e} \nabla \Phi_\mathrm{e} \cdot \overrightarrow{n} = \sigma_\mathrm{b} \nabla \Phi_\mathrm{e} \cdot \overrightarrow{n} \tag{3.11}$$

$$\Phi_\mathrm{e}\big|_\mathrm{e} = \Phi_\mathrm{e}\big|_\mathrm{b} \tag{3.12}$$

The initial conditions for the model are set using the state variables of the cell models paced to a limit cycle at 1 Hz. Numerical methods used to solve the bidomain model equations require high-resolution meshes, contributing to the model's high computational cost [70]. Nonetheless, the bidomain model is regarded as the most accurate among cardiac tissue-level electrophysiology models.

3.2.2 Monodomain Model

The monodomain model, derived from the bidomain equations, assumes equal intracellular and extracellular anisotropy ratios, making it computationally more efficient. The assumption of equal anisotropy does not fully hold in reality, e.g. defibrillation simulations where extracellular dynamics are crucial. However, this model still offers a close approximation of wave propagation. For a planar wave moving along the fiber directions, monodomain and bidomain models are exactly equivalent. The extracellular potential field Φ_e can be approximated from the monodomain transmembrane potentials as a source model by solving the elliptic bidomain equation at a temporally coarser scale. However, in this approach, the volume conductor cannot influence the transmembrane voltage distribution, and bath loading effects are ignored. This concept, referred to as the pseudo-bidomain approach, is computationally only marginally more expensive than a standard monodomain simulation [71].

The monodomain model has proven adequate for most cardiac electrophysiology simulations due to its ability to capture various electrophysiological mechanisms accurately, such as source-sink mismatch, curvature and collission effects [19, 72]. Nevertheless, numerical methods used to solve the monodomain equations require high-resolution meshes, contributing to their computational cost. In this thesis, we utilized the finite element method [73] for spatial discretization, as it faithfully represents the propagation of the electrical wavefront through cardiac tissue. The equations of the monodomain model are expressed as follows:

$$\beta C_\mathrm{m} \frac{\partial V_\mathrm{m}}{\partial t} = \nabla \cdot (\sigma_\mathrm{m} \nabla V_\mathrm{m}) - \beta (I_\mathrm{ion}(V_\mathrm{m}, \overrightarrow{\eta}) - I_\mathrm{s}) \qquad \text{on } \Omega \subset \mathbb{R}^3 \tag{3.13}$$

$$(\sigma_\mathrm{m} \nabla V_\mathrm{m}) \cdot \overrightarrow{n}_\mathrm{surf} = 0 \qquad \text{on } \delta\Omega \tag{3.14}$$

$$\sigma_\mathrm{m} = \frac{\sigma_\mathrm{i,l}\sigma_\mathrm{e,l}}{\sigma_\mathrm{i,l} + \sigma_\mathrm{e,l}} \overrightarrow{l} \otimes \overrightarrow{l} + \frac{\sigma_\mathrm{i,t}\sigma_\mathrm{e,t}}{\sigma_\mathrm{i,t} + \sigma_\mathrm{e,t}} \overrightarrow{t} \otimes \overrightarrow{t} + \frac{\sigma_\mathrm{i,n}\sigma_\mathrm{e,n}}{\sigma_\mathrm{i,n} + \sigma_\mathrm{e,n}} \overrightarrow{n} \otimes \overrightarrow{n} \qquad \text{on } \Omega \subset \mathbb{R}^3 \tag{3.15}$$

Here, β is the surface-to-volume ratio, C_m is the membrane capacitance, V_m is the transmembrane voltage, and σ_m is the tissue conductivity tensor. I_ion is the ionic transmembrane current density, which depends on V_m and the state variables $\overrightarrow{\eta}$ that govern the ion channels' behavior. I_s is the transmembrane stimulus current density. The domain Ω represents the myocardium, and $\overrightarrow{n}_\mathrm{surf}$ is the outward surface normal vector. The boundary condition at $\delta\Omega$ is a non-flux condition.

3.2.3 Eikonal Model

The anisotropic eikonal model, based on the macroscopic kinetics of wavefront propagation, seeks to determine the activation time (AT) of points within the myocardium through the following equation: [17, 18]:

$$\sqrt{\nabla T(X)^\top \mathbf{M}(X) \nabla T(X)} = 1 \qquad \forall X \in \Omega \tag{3.16}$$

$$T(X) = T_i \qquad \forall X \in \Gamma_i \subset \Omega \tag{3.17}$$

where $T : \Omega \to \mathbb{R}_{\geq 0} \cup \{\infty\}$, maps every point in the myocardium to its corresponding AT. Γ_i denotes the subset of points in the myocardium where the i-th stimulus is applied at time $T_i \in \mathbb{R}_{\geq 0}$, for $i = 1,\dots,n_\mathrm{s}$, with $n_\mathrm{s} \in \mathbb{N}$ representing the total number of stimuli. $\mathbf{M} : \Omega \to \mathbb{R}^{3\times 3}$ maps points in the myocardium to their tensor of squared conduction velocity (CV) defined as:

$$\mathbf{M}(X) = (v_\mathrm{l}^2(X))\,\overrightarrow{l} \otimes \overrightarrow{l} + (v_\mathrm{t}^2(X))\,\overrightarrow{t} \otimes \overrightarrow{t} + (v_\mathrm{n}^2(X))\,\overrightarrow{n} \otimes \overrightarrow{n}. \tag{3.18}$$

where $v_\mathrm{l}, v_\mathrm{t}, v_\mathrm{n} : \Omega \to \mathbb{R}_{\geq 0}$ assign the CV values in their respective directions at X.

The fast iterative method (FIM) is an effective approach for solving the anisotropic eikonal equation as this algorithm is particularly suited for unstructured meshes and anisotropic local CV functions [74]. The single-thread version of the FIM is outlined in the following Algorithm 3.1. Let Ω be considered to be a 2D manifold embedded in $\mathbb{R}^3$. For this reason, it is assumed that $v_\mathrm{n} = v_\mathrm{t}$, however the effect of the normal component is small since most of the characteristic directions (i.e., optimal trajectories) are almost perpendicular to $\overrightarrow{n}$. To numerically approximate the viscosity solution of the eikonal equation, a triangulation $\mathscr{T} \subset \mathscr{P}(\Omega_\mathscr{T})$ is defined over a finite set of points $\Omega_\mathscr{T} \subset \Omega$, such that the convex hull of $\Omega_\mathscr{T}$ (i.e., the union of all triangles in $\mathscr{T}$) approximates Ω. The FIM approximates the viscosity solution of the eikonal equation only at the vertices of the triangles in $\mathscr{T}$ (i.e., points in $\Omega_\mathscr{T}$).

In the first step of the FIM, the boundary conditions of the system are defined by the AT of the source nodes (Eq. 3.17). Then, the neighbors of the nodes that belong to any Γ_i (for $i = 1,\dots,n_\mathrm{s}$) are included in a set of active nodes $L \subset \Omega_\mathscr{T}$, that is initialized as $\emptyset$, which contains the list of nodes that are being updated by the local solver. This local solver is referred to as the UPDATE() function. As soon as L is not empty, the list iteration begins. For each iteration, every node X in L is updated and the previous solution for its AT is replaced. If the difference between the old and the new solution is smaller than a certain threshold ε, the node is then removed from L and each of its neighbors, that are not currently in L, is analyzed. For each neighbor, a potential new solution is calculated and only replaces the old solution if the new solution is smaller (i.e., earlier) than the old solution. If this condition is fulfilled, this neighbor is added to L. This process is repeated until L is empty.

When solving the eikonal equation on a triangular mesh, the local solver aims to determine the smallest AT that fits the eikonal equation at a specific node X. For this purpose, a potential AT is calculated for every triangle containing X. Figure 3.1 shows (X,Y,Z) a triangle in $\mathscr{T}$, with vertices $X,Y,Z \in \Omega_\mathscr{T}$:

$$\begin{aligned} T_{Y,Z}(X) &= \min_{\lambda\in[0,1]} \left(\lambda T(Y) + (1-\lambda)T(Z) + \frac{\sqrt{\overrightarrow{X_\lambda X}^\top \mathbf{D}(X)^{-1} \overrightarrow{X_\lambda X}}}{v_\mathrm{l}(X)} \right), \\ \overrightarrow{X_\lambda X} &= \lambda \overrightarrow{YX} + (1-\lambda)\overrightarrow{ZX}, \\ \mathbf{D}(X) &= \mathbf{M}(X) \cdot v_\mathrm{l}(X)^{-2}, \end{aligned} \tag{3.19}$$

where $T_{Y,Z}(X)$ is the potential AT that is obtained if the characteristic direction lies within the triangle (X,Y,Z). Additionally, $\mathbf{D}(X)$ is a tensor that holds information about the anisotropy of conduction, and $v_\mathrm{l}(X)$ is the CV along the longitudinal direction at node X.

Algorithm 3.1 Fast Iterative Method

```
$L = \emptyset$
for $X \in \Omega_{\mathscr{T}}$ do
    $T(X) \leftarrow \infty$
    for $i \in 1,\ldots,n_s$ do
        if $X \in \Gamma_i$ then
            $T(X) \leftarrow T_i$
            for adjacent neighbor $X_{NB}$ of $X$ do
                add $X_{NB}$ to $L$
            end for
        end if
    end for
end for
while $L \neq \emptyset$ do
    for $X \in L$ do
        $p \leftarrow T(X)$
        $q \leftarrow \mathrm{UPDATE}(X)$
        $T(X) \leftarrow q$
        if $|p - q| < \varepsilon$ then
            for adjacent neighbor $X_{NB}$ of $X$ do
                if $X_{NB}$ is not in $L$ then
                    $p \leftarrow T(X_{NB})$
                    $q \leftarrow \mathrm{UPDATE}(X_{NB})$
                    if $p > q$ then
                        $T(X_{NB}) \leftarrow q$
                        add $X_{NB}$ to $L$
                    end if
                end if
            end for
            remove $X$ from $L$
        end if
    end for
end while
```

Finally, UPDATE(X) is set as the minimum AT among all the potential ATs calculated from each triangle containing X:

$$\mathrm{UPDATE}(X) = \min_{(X,Y,Z)\in\mathscr{T}} T_{Y,Z}(X). \tag{3.20}$$

It's essential to understand that the final outcome of the UPDATE() function represents the definitive result from a given local solver application. However, it is not necessarily the definitive AT for X, as it may still change in subsequent updates and iterations.

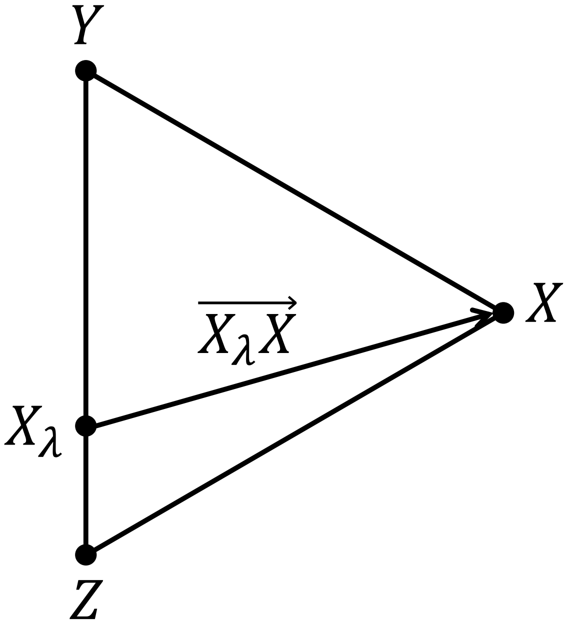

Figure 3.1: Triangle (X,Y,Z) illustrating the calculation of activation time(AT) at node X. The AT at the intermediate node X_λ, positioned between neighboring nodes Y and Z, is interpolated to minimize the AT at X.

PART II

ANALYSIS AND APPLICATIONS OF THE STANDARD EIKONAL MODEL

Chapter 4

Comparison of Eikonal-Based and Reaction-Diffusion Models in Atrial Electrophysiology

The use of computer models to study cardiac electrophysiology has significantly increased in recent years [11]. They can be applied to investigate new therapies and to gain new insights about the mechanisms of arrhythmia. The main advantages of using computer models come from the feasibility of doing in-silico experiments, having perfect control over the parameters and total observability over the variables that are being simulated. The most popular models of electrical propagation are the reaction diffusion methods, which come from the Ohm's law and Kirchhoff's law [17, 18]. They solve for transmembrane voltage at each node in the cardiac tissue over each time step. Their popularity stems from their ability to faithfully represent many important phenomena in cardiac electrophysiology such as source-sink mismatch, bath-loading effects, reactivation, and reentries etc. Their caveat is that they usually require high resolution meshes, and relatively complicated equations, demanding substantial computational effort [19, 20]. On the other hand, standard eikonal models offer an important advantage since they are capable of computing faster simulations. However, they only solve for one activation time (AT) per node without accounting for repolarization or reactivation [22]. Moreover, they neglect the important phenomena mentioned before that are reproduced in reaction diffusion (RD) models. New extensions of the eikonal model have been developed such as the reaction-eikonal model which combines both models in order to take advantage of the computational speed of the eikonal model in coarse meshes and the additional mechanisms accounted for in the RD models [20]. Despite not being able to reproduce reactivation and reentries, it incorporates calculation of transmembrane voltages which allows to investigate repolarization phenomena and calculate body surface potentials.

In this chapter, a comparison between RD models and eikonal-based models is performed. In the context of this work a single beat was simulated with different models with and without fibrosis. Resulting ATs and atrial signals were then compared between models.

In the manuscript presented below [19], the author of this thesis made substantial contributions, specifically by writing the methods section related to the propagation models. The author ran the pure eikonal simulations and collaborated closely with the first author in deciding on the simulation setups to benchmark the different propagation models. Additionally, the author helped interpret the results, identifying the main differences in activation sequences in both the healthy and fibrotic cases across simulations. The author also contributed to the discussion, providing key explanations for the observed differences in activation patterns between the models. Furthermore, the author reviewed, edited, and provided feedback on the entire manuscript alongside the other co-authors.

IEEE TRANSACTIONS ON BIOMEDICAL ENGINEERING, VOL. 70, NO. 2, FEBRUARY 2023 511

Comparison of Propagation Models and Forward Calculation Methods on Cellular, Tissue and Organ Scale Atrial Electrophysiology

Claudia Nagel, Cristian Barrios Espinosa, Karli Gillette, Matthias A.F. Gsell, Jorge Sánchez, Gernot Plank, Olaf Dössel, and Axel Loewe, *Senior Member, IEEE*

Abstract*—*Objective: **The bidomain model and the finite element method are an established standard to mathematically describe cardiac electrophysiology, but are both suboptimal choices for fast and large-scale simulations due to high computational costs. We investigate to what extent simplified approaches for propagation models (monodomain, reaction-Eikonal and Eikonal) and forward calculation (boundary element and infinite volume conductor) deliver markedly accelerated, yet physiologically accurate simulation results in atrial electrophysiology. *Methods:* We compared action potential durations, local activation times (LATs), and electrocardiograms (ECGs) for sinus rhythm simulations on healthy and fibrotically infiltrated atrial models. *Results:* All simplified model solutions yielded LATs and P waves in accurate accordance with the bidomain results. Only for the Eikonal model with pre-computed action potential templates shifted in time to derive transmembrane voltages, repolarization behavior notably deviated from the bidomain results. ECGs calculated with the boundary element method were characterized by correlation coefficients $>$0.9 compared to the finite element method. The infinite volume conductor method led to lower correlation coefficients caused predominantly by systematic overestimations of P wave amplitudes in the precordial leads. *Conclusion:* Our results demonstrate that the Eikonal model yields accurate LATs and combined with the boundary element method precise ECGs compared to markedly more expensive full bidomain simulations. However, for an accurate representation of atrial repolarization dynamics, diffusion terms must be accounted for in simplified models. *Significance:* Simulations of atrial LATs and ECGs can be notably accelerated to clinically feasible time frames at high accuracy by resorting to the Eikonal and boundary element methods.**

***Index Terms*—Atrial electrophysiology, bidomain, eikonal, electrocardiograms, finite element method, local activation times, monodomain, P waves.**

I. INTRODUCTION

In COMPUTATIONAL cardiac modeling, the bidomain model is the most biophysically detailed formulation to compute the spread of the de- and repolarization wavefront and the electrical source distribution throughout the cardiac tissue. Furthermore, the finite element method is considered the gold standard for computing the body surface potentials from a given distribution of the electrical sources in the heart to extract electrocardiograms (ECG) at standardized electrode positions. However, both methods are computationally expensive and are thus suboptimal for generating large *in silico* datasets of cardiac signals for machine learning applications [1], [2], or for efficiently simulating excitation propagation in cardiac digital twin for certain clinical applications such as to guide ablation therapy [3]. Hence, simplified models with fast solution times are needed to speed up the generation of *in silico* datasets of cardiac signals, such as local activation times (LATs), electrograms or ECGs by several orders of magnitude [4]–[6]. Yet, the signals obtained with these simplified methods need to be physiologically accurate and resemble the results obtained with the bidomain and finite element method. In this work, we therefore aim to quantify the inaccuracies arising in simulated atrial signals when resorting to simplified computational methods. While comparisons of this type have already been performed for the ventricles [5], [7] and partly also for four chamber heart models [8], a study focusing on atrial electrophysiology is lacking to the best of our knowledge. However, this is substantial since the atria stand out by a highly complex myocardial fiber structure, locally heterogeneous properties regarding ion channel and tissue conductivities and higher anisotropy ratios as compared to the ventricles.

Manuscript received 9 March 2022; revised 27 June 2022; accepted 24 July 2022. Date of publication 3 August 2022; date of current version 20 January 2023. This work was supported in part by the EMPIR programme co-financed by the participating states and from the European Union's Horizon 2020 research and innovation programme under Grant MedalCare 18HLT07, in part by the Deutsche Forschungsgemeinschaft (DFG, German Research Foundation) under Grant 2093/6-1, in part by the State of Baden-Württemberg through bwHPC, and in part by European Union's Horizon 2020 Research and Innovation Programme under the Marie Sklodowska- Curie Grant 860974. *(Corresponding author: Claudia Nagel.)*

Claudia Nagel is with the Institute of Biomedical Engineering, Karlsruhe Institute of Technology, 76131 Karlsruhe, Germany (e-mail: publications@ibt.kit.edu).

Cristian Barrios Espinosa, Jorge Sánchez, Olaf Dössel, and Axel Loewe are with the Institute of Biomedical Engineering, Karlsruhe Institute of Technology, Germany.

Karli Gillette and Gernot Plank are with the Division of Biophysics, Medical University of Graz, Austria.

Matthias A.F. Gsell is with the Division of Biophysics, Medical University of Graz, Austria, and also with the Institute of Mathematics and Scientific Computing, University of Graz, Austria.

This article has supplementary downloadable material available at https://doi.org/10.1109/TBME.2022.3196144, provided by the authors.

Digital Object Identifier 10.1109/TBME.2022.3196144

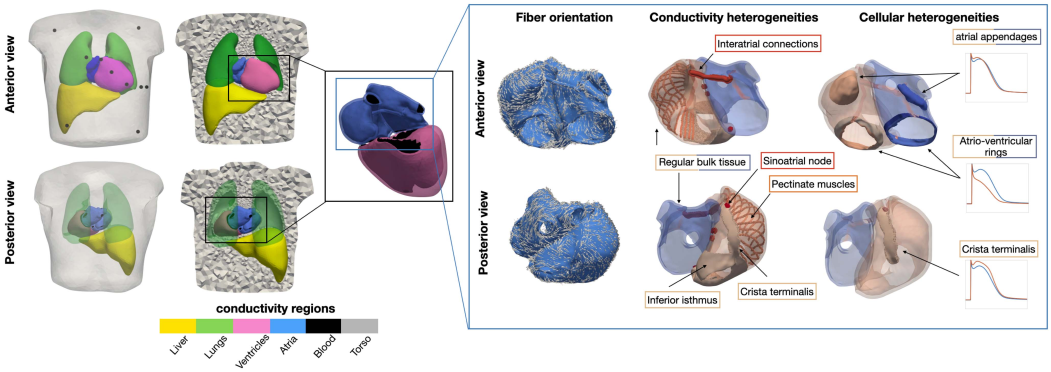

Fig. 1. Torso model with the segmented organs and electrode positions (transparent and clipped views) from the anterior and posterior view in the top and bottom row, respectively. The right panel shows the anatomically detailed atrial model that was augmented with fiber orientation and labels for anatomical structures. Heterogeneous conductivity and ionic properties were assigned to spatially distinct regions in the mesh. Resulting APs featuring ionic heterogeneity are depicted on the right side in red together with the baseline Courtemanche et al. cellular model in blue.

The monodomain, reaction-Eikonal (RE), and the Eikonal model solved by the fast iterative method constitute the simplified propagation models investigated in this work. Forward calculation techniques applied in this study comprise the boundary element and the infinite volume conductor methods. Simulations were carried out in sinus rhythm with and without the inclusion of fibrotic tissue modeled as passive conduction barriers [9], slow conducting tissue patches and rescaled ion channel conductivities representing cytokine effects [10], [11]. We assess the errors between simplified propagation models and forward calculation methods to the gold standard bidomain and finite element formulations with metrics extracted from the simulation results on cellular, tissue and organ scale comprising APDs, LATs, and ECGs, respectively.

II. METHODS

A. Model Generation

An anatomically detailed model of the torso was obtained by multi-label magnetic resonance image segmentation as described in [12]. The contours of atria, ventricles, lungs, liver and torso were exported as triangular surface meshes. These were smoothed and resampled with an average edge length of 0.5 mm, 5 mm, 5 mm, 7 mm and 15 mm, respectively, using *Meshmixer* (Autodesk, San Rafael, CA, USA) and *InstantMeshes* [13] whereby details were corrected manually in *Blender* (Blender Foundation, Amsterdam, The Netherlands) to avoid intersecting segments and ensure a sufficient mesh quality and topology. The segmented atrial endocardial surfaces were fed into the pipeline described in [10], [14], [15] to obtain a volumetric tetrahedral bi-atrial geometry with a homogeneous wall thickness of 3 mm and an average edge length of 523 μm augmented with inter-atrial connections, labels for anatomical structures and myocardial fiber orientation. In contrast to fully personalized approaches where fiber orientation can be defined based on information extracted from diffusion tensor imaging data, we defined myocardial fiber architecture in a rule-based way as described in [14] building on the solution of Laplace's [16], [17]. *Meshtool* [18] was used to generate a tetrahedral model of the full torso while preserving the surfaces of the considered organs. Tags for the atrial and ventricular blood pools were allocated to all elements in the volumetric torso model located inside the surfaces bounded by the atrial and ventricular endocardial walls with closed valve and vein orifices. A detailed view of the torso and atrial model is depicted in Fig. 1.

Isotropic extracellular conductivity of 0.0389 S/m, 0.028 S/m, 0.06 S/m, 0.7 S/m and 0.22 S/m was assigned to lungs, liver, ventricles, atrial and ventricular blood pools and the remaining torso tissue, respectively, as reported in previous work [19]–[21].

In order to conduct comparable experiments with the mono- or bidomain model that require conductivities, and the Eikonal-based models that resort instead to conduction velocities (CVs), it is crucial to consistently associate conductivities and CVs for all heterogeneous tissue regions in the atria. Therefore, anisotropic and locally heterogeneous conductivities were assigned to five different regions in the atria comprising regular bulk tissue, crista terminalis, pectinate muscles, inferior isthmus, and inter-atrial connections. CVs corresponding to the monodomain conductivities reported in [22] for 0.33 mm resolution voxel models were therefore first calculated as described in [23]. Using *tuneCV* [24], [25], intra- (σ_i) and extracellular (σ_e) conductivities as well as the monodomain conductivities (σ_m) were iteratively optimized for the tetrahedral mesh setup described above while keeping the σ_i/σ_e ratio fixed. For this purpose, five strand geometries with a length of 10 cm were generated each characterized by a resolution corresponding to the average edge length of one of the heterogeneous conductivity regions in the atria. Intra- and extracellular conductivities in longitudinal and transversal fiber direction as reported by Clerc et al. [26] as well as by Roberts et al. [27] were initially assigned to the elements in the slab meshes. In an iterative optimization procedure, the conductivities were adjusted until the CV converged to the target value derived from [22]. In this way, the originally reported intra- and extracellular conductivity values were scaled while the ratios between them were kept constant along the eigenaxes [25]. In the following, we refer to the tuned conductivities obtained by initially assigning the values reported by Clerc [26] and Roberts et al. [27] to the slab meshes as Clerc and Roberts conductivities, respectively. The resulting heterogeneous and anisotropic conductivity setup for each atrial region is summarized in Table SI in the supplementary material. For the monodomain simulations, we considered two different cases which we refer to as "monodomain with and without explicit conductivity tuning". For the first one, we repeated the *tuneCV* optimization using the monodomain propagation model and obtained the monodomain conductivities listed in Table SI in the supplementary material. In the second case, we directly computed the monodomain conductivities from the tuned intra- and extracellular bidomain conductivities as half of their harmonic mean.

The Courtemanche et al. cell model [28] was used in the simulations described in Section II-B. To reflect regionally heterogeneous electrophysiology, maximum ion channel conductances were rescaled compared to the baseline model as reported in previous work [22], [29] and are summarized in Table SII in the supplementary material. The final CV values in longitudinal and transversal fiber direction as used for the Eikonal and RE simulations described in Section II-B were subsequently calculated with *tuneCV* [24] based on the tissue and ion channel conductivity settings in each atrial region.

B. Propagation Models

1) Bidomain Model: The bidomain model represents the propagation of the electrical de- and repolarization wavefront through the cardiac tissue [30]–[32]. Here, the intracellular and extracelullar domains are coupled and intertwined in a system of partial differential equations. Solving this system provides at each point in the cardiac tissue the intracellular Φ_i and extracellular Φ_e electrical potentials:

$$-\nabla \cdot ((\sigma_i + \sigma_e)\nabla \Phi_e) = \nabla \cdot (\sigma_i \nabla V_m) \tag{1}$$

$$\nabla \cdot (\sigma_i \nabla V_m) + \nabla \cdot (\sigma_i \nabla \Phi_e) = \beta \left(C_m \frac{\partial V_m}{\partial t} + I_{ion} - I_s \right) \tag{2}$$

where $V_m = \phi_i - \phi_e$ is the transmembrane potential σ_i and σ_e are the intracellular and extracellular conductivity tensors, respectively, β is the surface to volume ratio of the membrane, and C_m is the membrane capacitance per unit surface. Additionally, I_s and I_{ion} are the transmembrane stimulus and ionic currents, respectively. The ionic current I_{ion} depends on the state variables η that are calculated with a non-linear system of ordinary differential equations. To solve the bidomain equation, we defined a reference electrode on the anterior, lower left hand side of the torso. Homogeneous Neumann boundary conditions were imposed at the boundaries of the myocardial tissue (intra- and extracellular domains) and the torso (extracellular domain). At the myocardial tissue to torso interface, ϕ_e is constrained to be continuous and no-flux is enforced in the normal direction $\vec{n}$ for ϕ_i:

$$\vec{n} \cdot \sigma_i \nabla \phi_i = 0 \tag{3}$$

Also at the boundary of the torso that is not in contact with the myocardial tissue, a no-flux boundary condition for ϕ_e is imposed:

$$\vec{n} \cdot \sigma_b \nabla \phi_e = 0 \tag{4}$$

where σ_b is the conductivity of the bath (torso). Additionally, the continuity of the normal component of the extracellular current (5) and ϕ_e at the tissue-bath interface (6) is enforced:

$$\sigma_e \nabla \phi_e \cdot \vec{n} = \sigma_b \nabla \phi_e \cdot \vec{n} \tag{5}$$

$$\phi_e|_e = \phi_e|_b \tag{6}$$

Initial conditions of the model were defined by the state variables of the cell models paced to a limit cycle at 1 Hz. Numerical methods used to solve the bidomain model equations rely on high resolution meshes which is the main cause of the model's high computational cost [33]. Nonetheless, the bidomain model is considered the most accurate of the available cardiac models for tissue level electrophysiology.

2) Monodomain Model: Assuming that the intra- and extracellular conductivity tensors are proportional, i.e. their anisotropic ratios are equal, the bidomain model can be significantly reduced to the monodomain model [31]–[33]:

$$\beta C_m \frac{\partial V_m}{\partial t} = \nabla \cdot (\sigma_m \nabla V_m) - \beta (I_{ion}(V_m, \eta) - I_s) \tag{7}$$

where σ_m is the monodomain conductivity tensor. This tensor can be expressed in terms of half the harmonic mean of intra- and extracellular conductivity tensors:

$$\sigma_m = \frac{\sigma_i \sigma_e}{\sigma_i + \sigma_e} \tag{8}$$

The assumption of equal anisotropy does not fully hold in reality. However, this model still offers a close approximation of the wave propagation. [8]. For a planar wave moving along the fiber directions monodomain and bidomain models are exactly equivalent. The extracellular potential field Φ_e can be approximated from the monodomain transmembrane potentials as a source model by solving the elliptic bidomain (1) at a temporally coarser scale. However, the volume conductor cannot influence the transmembrane voltage distribution in this approach and bath loading effects are ignored. This concept is referred to as pseudo-bidomain approach [7] and is computationally only marginally more expensive than a standard monodomain simulation. The monodomain and bidomain models can be discretized in space using different approaches [34]. For this study, we used the finite element method [24].

3) Eikonal Model: The Eikonal model is based on the macroscopic kinetics of the wavefront propagation [5], [31], [32], [35]. Solving the Eikonal equation seeks to find the activation times T for each node x based on a local speed function:

$$\sqrt{\nabla T(x)^{\top} M \nabla T(x)} = 1, \tag{9}$$

$$T(x) = T_0 \text{ for } x \in \Gamma, \tag{10}$$

where M is the squared CV tensor and T_0 are the initial conditions for the activation sites Γ. Although V_m is not directly calculated in this model, it can be inferred from the activation times:

$$V_m(x,t) = U(x, t - T(x)) \tag{11}$$

where U is an AP timecourse. It was obtained based on a simulation of a planar wavefront propagating in a tissue block from which the transmembrane potential V_m was extracted at a node in the center of the mesh. Specific AP timecourse were used in different anatomical regions. Numerical simulations are significantly faster because of the simplicity of the equation and lower resolution meshes that are required. Unfortunately, the Eikonal model fails to accurately represent the influence of bath loading effects, high wavefront curvatures, reentry, and wave-collisions on CV. [5], [36]. In the case of complex patterns of activation that occur for example during atrial fibrillation, these limitations become more significant. Nonetheless, these simulations still provide a decent approximation of wave propagation under healthy conditions. In these case, the shortcomings of the Eikonal model are still present but their effects are less pronounced.

4) Reaction-Eikonal Model: When applied to coarse meshes, the mono- and bidomain models both exhibit slowed CV for a given tissue conductivity [5], [34]. The general RE model uses the activation times obtained by the Eikonal model to enable biophysical models to calculate the transmembrane potential in coarse meshes [5]. The resolution requirement is relaxed because the thin wavefront does not need to be explicitly represented. The RE model calculates an I_{foot} current to replicate the activating effect of the diffusion term on neighboring cells and applies it to the reaction model at the time given by the Eikonal solution. In this work, only the RE$^+$ version of the model is considered (12), in which the I_{foot} current is added to the diffusion term instead of replacing it.

$$\beta C_m \frac{\partial V_m}{\partial t} = \nabla \cdot (\sigma_m \nabla V_m) + I_{foot} - \beta(I_{ion}(V_m, \eta)) \tag{12}$$

Thus, the activation of the nodes can be achieved by either the diffusion term or the I_{foot} current and neighboring nodes also interact during repolarization. The RE$^+$ variant is more accurate when comparing to the monodomain model in coarse meshes and the repolarization gradients are significantly smoother. However, RE models are unable to activate the same node several times (as for example required for simulations of reentry) and share the limitations of the standard Eikonal model regarding the influences of wavefront curvature, source sink mismatch and bath loading on CV.

C. Forward Calculation Methods

When modeling the torso as a passive volume conductor, the bidomain formulation can be reduced to its parabolic part to solve the forward problem of electrocardiography for a given distribution of V_m. The Poisson equation in (1) can be solved numerically by discretizing the full torso domain with finite elements (finite element method). To comply with the terminology in related work [37], we use the term finite element method (FEM) in the following when referring to solving Poisson's (1) numerically using a finite element discretization scheme even though this discretization scheme was also used to solve for example the bidomain equations. Standard extracellular conductivities were hereby assigned to different organs as described in Section II-A. By assuming isotropic myocardial properties in the extracellular space, a reduced set of dipole sources can be mapped onto the surfaces bounding the organs with different conductivity properties. Then, the boundary element method can be used for computing the body surface potentials and the ECG. In the latter case, applying Green formulas and boundary conditions as well as assuming equal anisotropy ratios in the intra- and extracellular domain allow for reformulating (1) as a surface integral to compute the extracellular potential Φ at any point $\vec{r}$ on the torso surface:

$$\Phi(\vec{r}) \approx 2 \cdot \Phi^{\infty}(\vec{r}) - \frac{1}{2\pi} \sum_{k=1}^{K} \frac{\sigma_-^k - \sigma_+^k}{\sigma_T} \int_{S^k} \Phi(\vec{r'}) \frac{(\vec{r} - \vec{r'})}{|\vec{r} - \vec{r'}|^3} d\vec{S}', \tag{13}$$

whereby the minuend describes the potentials attributable to the sources in an unbounded medium with conductivity σ_T. The subtrahend in (13) accounts for secondary sources introduced by the bounded volume conductor. σ_-^k and σ_+^k characterize the conductivities inside and outside the respective surface S^k. The potential Φ^{∞} can be expressed either using the transmembrane voltage distribution on the cardiac surface [38] or the primary impressed currents $\vec{J_p}$ [39] as volumetric sources inside the bounded volume conductor V_h:

$$\Phi^{\infty}(\vec{r}) = \frac{1}{4\pi\sigma_T} \int_{V_h} \frac{\vec{J_p} \cdot (\vec{r} - \vec{r'})}{|\vec{r} - \vec{r'}|^3} dV_h \tag{14}$$

When computing the ECG using the infinite volume conductor method (IVC), the heart is assumed to be immersed in a medium of infinite spatial extent with a homogeneous conductivity σ_T. This reflects in the sum over the surface integrals in (13) being neglected for calculating extracellular potentials on the torso surface:

$$\Phi(\vec{r}) \approx \Phi^{\infty}(\vec{r}) \tag{15}$$

D. Simulation Scenarios

Simulations were carried out on the bi-atrial volumetric model described in Section II-A in sinus rhythm with and without the inclusion of fibrotic tissue patches. For the former case, several elliptically shaped patches with their principal axis aligned to the macroscopic atrial fiber orientation were manually defined predominantly on the posterior wall of the left atrium and the left pulmonary vein antrum as reported by Highuchi et al. [40]. These regions extended transmurally and are shown in Fig. 2. To not only account for the patchiness of atrial fibrosis but also for its diffuse deposition, 80% of the cells within the elliptical patches were defined as fibrotic. In this way, the volume fraction of left atrial fibrosis quantified to 22 % of the total left atrial tissue volume. Remodeled conduction properties were assigned the fibrotic regions in three different ways: In the first case, fibrotic elements were removed from the atrial mesh and instead assigned to the extracellular domain following the concept of percolation [9]. In this way, we introduced passive conduction barriers that do not have a transmembrane voltage and thus do not

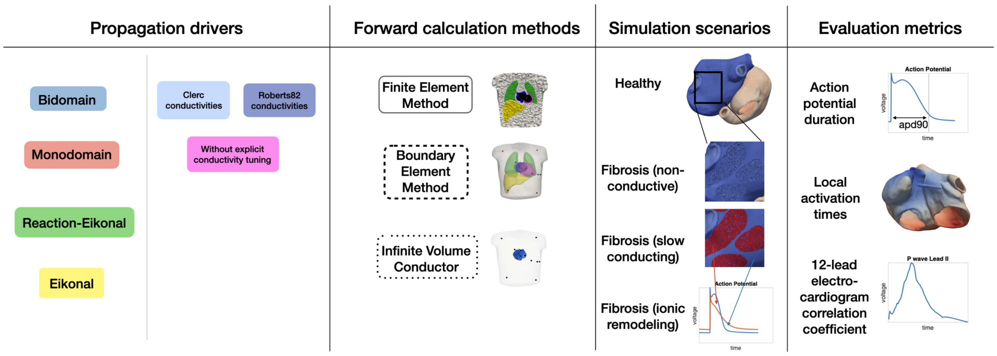

Fig. 2. Overview of the different propagation models, forward calculation methods, simulation scenarios and evaluation metrics used in this work.

contribute to the electrical source distribution on the myocardial tissue surface. In the second case, fibrotic regions were characterized as slow conducting patches with CVs reduced by 80 % in transversal and 50 % in longitudinal fiber direction compared to the healthy baseline case. Conductivities in these regions were obtained as described in Section I. In this way, anisotropy ratios were increased by a factor of 2.5 in fibrotic areas promoting wave propagation along myocardial fiber orientation and thus forming the basis for functional reentry circuits. In the third case, ionic properties of the fibrotic cells were remodeled by rescaling the conductances of the sodium (g_{Na}), the L-type calcium (g_{CaL}) and the inward rectifier potassium current (g_{K1}) by a factor of 0.6, 0.5 and 0.5, respectively, compared to the baseline conductances of the Courtemanche et al. cell model to account for cytokine remodeling effects [11].

Sinus rhythm simulations were initiated at a sinus node exit site located at the junction of crista terminalis and the superior vena cava. We obtain the transmembrane voltage distribution for the LATs computed with the Eikonal model as described in (11), whereby the respective ionic model parameters in each region as listed in Table SII in the supplementary material were taken into account for calculating the AP templates.

The Cardiac Arrhythmia Research Package (*CARP*) [41] and *openCARP* [24] were used for computing the spread of the depolarization wave with different propagation models as well as ECGs with the finite element and the infinite volume conductor method. The algorithms described by Stenroos et al. [39] were used for calculating ECGs with the boundary element method. As recommended by Schuler et al. [42], we downsampled the surface mesh bounding the atria to a resolution of 2.5 mm for computing the transfer matrix. Furthermore, we applied Laplacian smoothing to the transmembrane voltage sources to ensure a continuous wave propagation on the coarse mesh.

E. Evaluation Metrics

From the source distribution obtained from simulations using different propagation models, we calculated APDs at 90 % repolarization (APD_{90}) for each node in the mesh. Also at each vertex in the geometry, we extracted LATs defined as the timestep with the steepest AP upstroke. For both, APDs and LATs, the accuracy of each propagation model simulation was quantified as the absolute difference to the respective value for each metric obtained from the bidomain simulation with the Clerc conductivities.

To assess fidelity of simplified forward calculation methods along with different propagation models, we evaluated the Pearson correlation coefficient of the respective ECG results with the ECGs obtained by solving the forward problem with the finite element method based on the bidomain source model computed with the Clerc conductivities.

III. RESULTS

A. Propagation Models

The effect of different propagation models on the activation sequence (LATs) is visualized in Fig. 3. The total activation time in the healthy reference scenario solved with the bidomain model was 102 ms. In the top panel, the distributions of the signed differences between the examined propagation models' LATs and the bidomain results obtained with Clerc conductivity ratios evaluated at all mesh nodes are visualized as violin plots. In the bottom panel, the difference to the bidomain results are mapped onto the atrial geometry. The mismatch in LATs was most pronounced for the bidomain scenario with Roberts conductivities and much smaller for the simplified propagation models. For the Roberts conductivity ratios, the LATs were systematically smaller than the ones resulting from the reference bidomain simulation with the Clerc conductivity settings. Furthermore, the error increased with the spread of the depolarization wave front leading to small deviations close to the sinus node exit site, but errors of up to -14 ms at the latest activated areas at the posterior wall of the left atrium and the coronary sinus in the right atrium. The mean and standard deviation of the absolute errors between the bidomain and monodomain LATs with and without explicit conductivitiy tuning were 0.93 ± 0.61 ms and 1.02 ± 0.64 ms. With the temporal resolution of the sampled simulated myocyte APs being 1 ms and the LATs being calculated as the point in time marking the steepest AP upstroke, in particular the LAT results for the monodomain simulation

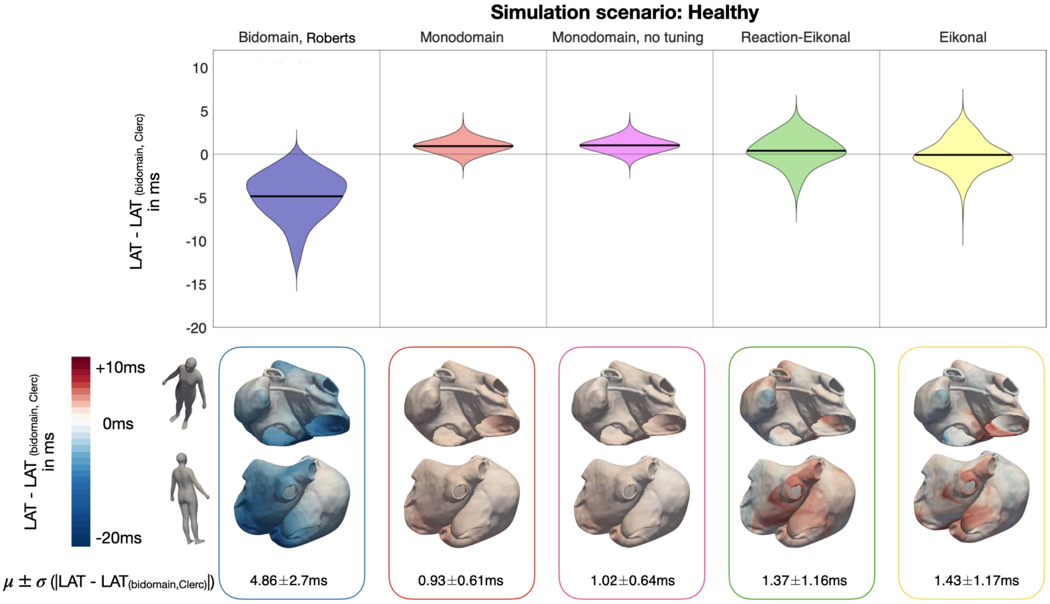

Fig. 3. Local activation time (LAT) results in sinus rhythm for healthy (non-fibrotic) tissue for different propagation models. The top panel shows the distribution of the signed LAT differences taking the bidomain simulations executed with the Clerc conductivity ratios as a reference. From left to right, the violin plots show the results for the bidomain (Roberts conductivities), the monodomain (with and without explicit conductivity tuning), the RE^+ and the Eikonal simulations. The bottom panel shows the signed LAT differences mapped on the atrial geometry for each propagation model in the above order. Mean and standard deviation of the absolute LAT differences are shown in the bottom row for each case.

with additional conductivity tuning were below the accuracy with which the LATs were determined. RE^+ and Eikonal LAT differences quantified to 1.37 ± 1.16 ms and 1.43 ± 1.17 ms, respectively. The signed LAT error to the bidomain results was distributed similarly across the atrial tissue among these two propagation models (see Fig. 3 bottom panel). The LAT results in the simulation scenarios involving fibrosis remodeling were only slightly different compared to the sinus rhythm results depicted in Fig. 3. The largest differences occurred for the Eikonal propagation model in the simulation scenario where fibrosis was modeled as slow conducting tissue. There, the absolute error to the bidomain results quantified to 1.71 ± 1.46 ms compared to 1.43 ± 1.17 ms in sinus rhythm without the inclusion of fibrosis.

APD_{90} results are visualized for the simulation scenario with fibrosis modeled as ionic conductance rescaling in Fig. 4. For the monodomain simulations, the mean and standard deviation of the absolute APD_{90} discrepancies to the bidomain results obtained with Clerc conductivity ratios were below the temporal resolution of the AP time course of 1 ms. Absolute errors to the bidomain simulation with Roberts conductivity ratios and the RE^+ results quantified to 2.92 ± 3.07 ms and 1.13 ± 1.69 ms, respectively. In both cases, the highest errors occurred in regions around the fibrotic tissue patches. APD_{90} results for the Eikonal simulation were characterized by an absolute error to the bidomain simulation results of 25.1 ± 20.72 ms. Furthermore, the AP signal trace obtained from a tissue strand simulation and used as a template to infer the transmembrane voltage distribution for the Eikonal LATs is visually clearly distinguishable from the bidomain AP especially in fibrotic regions (see Fig. 4 bottom panel).

ECGs obtained from the transmembrane voltage distributions from the simulation scenario with fibrosis modeled as ionic rescaling as depicted in Fig. 4 and using the boundary element forward calculation method are visualized in Fig. 5. The 12-lead ECG is displayed for a duration of 650 ms whereby the signal sections in the interval [0 ms, 150 ms] and [150 ms, 650 ms] represent the P wave and the atrial repolarization, respectively. The latter is typically not visible in the ECG of a full heartbeat since the repolarization phase of the atria temporally coincides with the ventricular activation and the respective signal parts are thus buried within the QRS complex.

The observed discrepancies in the AP signal course between the bidomain and Eikonal simulation also reflects in the ECG. As can be seen in Fig. 5, the repolarization signal obtained with the Eikonal and bidomain propagation model differ. In lead aVL, the polarity of the repolarization wave was even inverted. Apart from the atrial repolarization ECG signal obtained with the Eikonal model and precomputed AP templates, the choice of the propagation model did not markedly influence the ECG as the remaining signals in Fig. 5 show only minor differences. Furthermore, the correlation coefficients between the bidomain ECG obtained with the Clerc conductivity ratios and the other examined propagation models are summarized in Table I for the

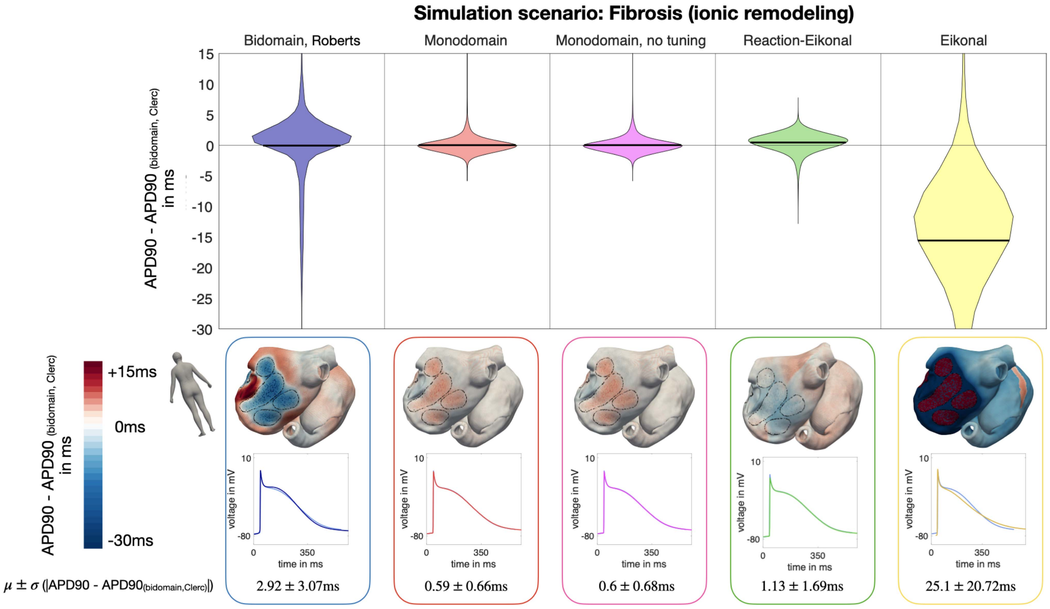

Fig. 4. APD_{90} results in sinus rhythm with fibrotic substrate replacing 22% of the left atrial myocardial tissue modeled as rescaled ionic conductances. The violin plots in the top panel represent the distribution of APD_{90} discrepancies to the bidomain results for all investigated propagation models. In the bottom panel, the signed APD_{90} differences are mapped onto the atrial geometry. Fibrotic regions are encircled with black dashed lines. The APs are shown for one node within the fibrotic area on the posterior left atrial wall. Bidomain APs are visualized in light blue, the other signal trace was obtained with the respective propagation model. The numbers in the bottom line show the mean and standard deviation of absolute APD_{90} differences with respect to the bidomain simulation results.

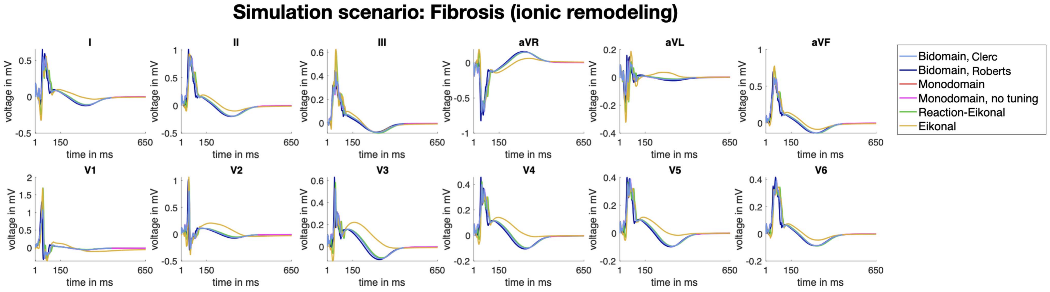

Fig. 5. ECGs calculated with the same forward calculation method (BEM) but different propagation models (color coded) with the transmembrane voltages resulting from the simulation scenario with fibrosis modeled as ionic conductivity rescaling.

TABLE I

CORRELATION COEFFICIENTS BETWEEN THE ECGS OBTAINED WITH THE BIDOMAIN AND SIMPLIFIED PROPAGATION MODELS WHEN SOLVING THE FORWARD PROBLEM WITH BEM. COLUMNS REPRESENT DEPOLARIZATION (P WAVE), REPOLARIZATION AND THE ENTIRE SIGNAL

	[0 ms, 150 ms]	[150 ms, 650 ms]	[0 ms, 650 ms]
Bidomain, Clerc	1	1	1
Bidomain, Roberts	0.8590	0.9904	0.9028
Monodomain	0.9942	0.9998	0.9961
Monodomain, no tuning	0.9931	0.9998	0.9954
Reaction-Eikonal	0.9211	0.9953	0.9428
Eikonal	0.9203	0.6233	0.8791

intervals [0 ms, 150 ms] (P wave), [150 ms, 650 ms] (repolarization) and [0 ms, 650 ms]. The lowest correlation coefficient for the P wave occurred for the bidomain simulation with Roberts conductivity ratios. For all simplified propagation models, the P wave correlation coefficients were above 0.92. Except for the Eikonal model, the correlation coefficient of the ECG signal sections representing the repolarization phase wave was above 0.99. ECG and APD_{90} results only marginally differed for the remaining fibrosis remodeling scenarios as detailed and visualized in the figures S6-S10 in the supplementary material.

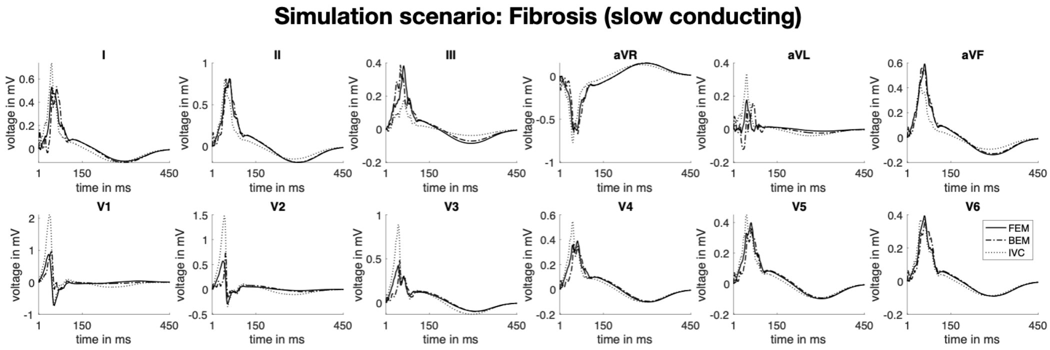

Fig. 6. ECGs calculated the same source distribution resulting from a bidomain simulation with Clerc conductivity ratios and with different forward calculation methods in the simulation scenario with fibrosis modeled as slow conducting tissue. ECGs calculated with the finite element method (FEM), the boundary element method (BEM) and the infinite volume conductor method (IVC) are visualized with the solid, dash-dotted and dotted lines, respectively.

B. Forward Calculation Methods

ECGs calculated with different forward calculation methods based on the same source distribution stemming from the bidomain simulation with Clerc conductivity ratios are depicted in Fig. 6 for the simulation scenario with fibrosis modeled as slow conducting tissue. The correlation coefficients covering the ECG signal parts of the P wave between the gold standard FEM approach and each of the BEM and IVC method quantified to 0.94 and 0.83 for fibrosis modeled as slow conducting tissue. Especially the IVC method yielded too high ECGs amplitudes in the precordial leads and inaccurately captured atrial repolarization in the inferior leads II, III and aVF.

IV. DISCUSSION

A. Main Findings

In this work, we compared atrial APD_{90}, LATs and ECGs computed with the bidomain, monodomain, RE^+ and the Eikonal propagation models as well as with the finite element, the boundary element and the infinite volume conductor forward calculation methods. The largest deviations in LATs were observed between the bidomain simulations with Clerc and Roberts conductivity ratios. As the absolute LAT errors increase with the propagating wavefront, discrepancies in LATs can be traced back to more pronounced bath loading effects occurring in the Roberts conductivity settings. With a higher ratio between extracellular bulk and isotropic bath conductivities, the depolarization wave propagates faster in close vicinity to the interface between blood pool and endocardial wall leading to earlier LATs throughout the cardiac tissue. Due to the thin atrial wall, the bathloading effect is visible transmurally and thus leads to globally faster conduction velocities in the bidomain simulation with the Roberts conductivity setup. However, in this work, conductivities were tuned as described in Section II-A without a bath attached to one face of the strand meshes. Incorporating the bath already in the tuning process would have led to more similar results between the bidomain simulation results obtained with tuned Clerc and Roberts conductivities. This systematic underestimation of LATs also reflects in the ECG. The bidomain simulation with the Roberts conductivity settings yielded the smallest P wave correlation to the bidomain ECGs with the Clerc conductivity ratios and markedly shorter P wave duration. Also Sebastian et al. [43] found that the choice of conductivity ratios in the intra- and extracellular domain as well as in longitudinal and transversal fiber direction had a marked effect on CV and LATs. Intra- and extracellular conductivity values were derived by Clerc and Roberts et al. in animal experiments on specimen from excised trabecular cardiac bundles. Measuring intra- and extracellular current flow using microelectrodes allowed for a computation of the resistance and in turn the conductivity in longitudinal and transversal fiber direction in both, the extra- and intracellular space. Considering the complex and cumbersome in and ex vivo experiments to derive these parameters, fixed ratios between σ_i and σ_e along and perpendicular to the myocardial fiber orientation need to be assumed when personalizing computer models. As a consequence, the high uncertainty of the ratio between σ_i and σ_e which cannot be measured patient-specifically with reasonable efforts further justifies the application of simplified models that do not involve uncertainties in non-measurable entities and only cause minor differences in LATs, ECGs and APD_{90}. Among all investigated simplified model solutions, the monodomain model yielded the most accurate results regarding activation times, repolarization behavior and ECGs. However, explicit conductivity tuning for the monodomain model neither had a notable effect on LATs, nor APD_{90}, nor on the 12-lead ECG. With mean and standard deviation of the absolute LAT differences to the bidomain results quantifying to 1.37 ± 1.16 ms and 1.43 ± 1.17 ms for the RE^+ and the Eikonal model, respectively, which differed only slightly due to numerical jitter. The distribution of LAT discrepancies to the bidomain results mapped on the atrial geometry was similar for the Eikonal and the RE^+ model. The LATs of the simplified propagation models were especially higher compared to the bidomain results in regions on the posterior left atrial wall. In these areas, different wavefronts collided causing an acceleration of the wave in the bidomain model, which is not captured in the (reaction-) Eikonal model. Source-sink mismatch effects caused by convex wavefronts entailing conduction slowing in the bidomain model cause smaller LATs in the Eikonal simulation results. This effect is especially visible in the area where Bachmann's bundle connects to the anterior wall of the left atrium, i.e. where a small source (Bachmann's bundle) meets a large sink (the left atrium). At the apex of the right atrial appendage, two convex wavefronts traversing the tissue from the lateral and the septal right atrial wall collide and cause Eikonal LATs to be smaller than the ones resulting from the bidomain simulation. The P waves computed with the reaction-Eikonal and the Eikonal source distribution showed similar correlation coefficients of 0.921 and 0.920 to the bidomain results. However, when evaluating repolarization dynamics, the RE^+ model clearly led to more precise results. This reflects on the one side in smaller APD_{90} discrepancies to the bidomain simulation results. The small APD_{90} discrepancies between the monodomain and RE^+ simulation results might have occurred due to differences in the activation pattern or a mismatch between the diffusion term and the I_{foot} current in the case of curved wavefronts or wave collisions causing different AP upstrokes and amplitudes which subsequently lead to subtle APD changes. On the other hand, the RE^+ model is capable of faithfully replicating both the P wave as well as the atrial repolarization phase in the ECG, whereas with the Eikonal model, only the P wave highly resembles the bidomain results. Using precomputed AP templates to obtain the transmembrane voltage source distribution for the Eikonal LAT results, APD_{90} results were systematically smaller compared to the bidomain results in regular bulk tissue regions and systematically higher in fibrotic regions. The more precise representation of repolarization behavior in simulation results using the RE^+ model is due to local APD balancing caused by the diffusion term. Consequently, also the repolarization signal in the ECG obtained with the source distribution derived from the Eikonal results only showed a correlation coefficient of 0.62 to the bidomain ECG.

ECGs calculated with the BEM highly resembled the ECGs obtained with the FEM. P wave correlation coefficients to the FEM approach quantified to 0.94 and 0.93 for the simulation scenario with fibrosis modeled as slow conducting and non-conductive patches, respectively. In the former scenario, transmembrane voltages can be used as a source model for the forward calculation, whereas in the latter, volumetric sources such as primary impressed currents were necessary to model the effect of passive conduction barrier not contributing to the electrical source distribution in the heart. If the surface transmembrane voltages had been used as sources for the forward calculation in this case as well, an offset in the isoelectric line in the P wave would have been induced. The infinite volume conductor method instead yielded more inaccurate ECG results. Especially in the septal and anterior leads, the ECG amplitudes were overestimated by a factor of >2 compared to the FEM results. On the one side, this observation can be traced back to the method's assumption that the atria are immersed in an infinite medium of a homogeneous conductivity, which does not allow considering a heterogeneous conductivity setup in the torso. On the other hand, the high ECG errors occurred predominantly in leads measured at electrode locations on the body surface in close proximity to the cardiac sources. Thus, neglecting the attenuating effect that the bounded torso volume conductor introduces causes a more pronounced effect on the resulting ECGs in V1-V3.

Simulations were run on a 16 core CPU machine (Intel Xeon Gold 6230, 2.1 GHz). The full bidomain and the pseudo-bidomain simulation for a duration of 450 ms were completed in 25 and 1.5 hours, respectively. Computation time for the RE^+ setup was 1.4 hours on a 6 core machine. The computation of the transfer matrix for the BEM approach in the case of a heterogeneous torso volume conductor with seven surfaces bounding the atria, the torso and other organs took 2 hours on a 4 core CPU machine (Intel Core i5, 2.4 GHz). The speed-up in computation times when using simplified propagation models is comparable to a ventricular setup. Computational performance improved by one order of magnitude when using the monodomain model [7] and up to three orders of magnitude when using the Eikonal or RE^+ model [4], [5] compared to bidomain. However, increasing the number of cores the simulations are ran on could change the results regarding algorithmic efficiency as different models might exhibit different scalability properties when parallelized to multiple threads or processes [44]. Solvers with strong scaling capabilities have been shown to provide the basis for fast simulation runs of the biophysically detailed monodomain model without any cutbacks on anatomical and electrophysiological properties [45]. In the simulations in our study, the degrees of freedom in terms of number of nodes and elements in the mesh was the same for all propagation models. High resolutions in time and space are required for numerical convergence of the bi- and monodomain solution [46]. As described by Woodworth et al. [47], a high mesh resolution is a necessary requirement for CV convergence, especially for low conductivities (see also Fig. S3 in the supplementary material). On the other side, (reaction-)Eikonal models are capable of faithfully estimating activation time sequences on coarser meshes [5], [48]. The computational complexity of the Eikonal model depends on the method used to solve it [49], but is approximately $\mathcal{O}(n\log(n))$ with n being the number of nodes in the mesh. These properties could be taken advantage of to further reduce computational cost when running simulations based on these simplified models.

Computational savings using the BEM approach are on the one hand due to the decreased problem complexity when discretizing the domain with surface instead of volume elements [37]. On the other hand, coarser resolution meshes can be applied which is the key influencing factor for an improved computational efficiency over FEM [50].

B. Related Work

In our work, we studied the differences in activation and repolarization times when using different propagation models in atrial electrophysiology, which, to the best of our knowledge, has not been done before in a comprehensive way. However, comparable studies have partly already been conducted for the ventricles and four-chamber heart models. Potse et al. [8] found that activation using bidomain was 2 % faster compared to the monodomain approach for a complete cardiac cycle. Also in our study, the monodomain activation times were on average 1 ms higher than those obtained from the bidomain simulation. Pashaei et al. [51], [52] as well as Wallman et al. [4] found that the differences in activation times are small for a ventricular simulation setup when comparing biophysically detailed approaches and the Eikonal model. Neic et al. [5] compared extracellular potential fields, electrograms and ECGs calculated with the RE and the bidomain model for the ventricles and concluded that the simplified model can replicate the gold standard results with high fidelity. Gassa et al. [53] investigated the suitability of an RE model to generate re-entrant activity on a bi-atrial geometry and succeeded in replicating the wave patterns resulting from a monodomain simulation. We have also recently shown that the Eikonal-based models can produce activation times and ECGs resembling full bidomain simulation results with high fidelity in an atrial model without cellular remodeling placed in a homogeneous torso volume conductor [54]. Here, we extended the setup to heterogeneous scenarios covering cellular and conductivity heterogeneity in both the torso and the atria and observed similar results. This work confirms the findings from previous studies mainly conducted for ventricular simulation setups.

Previous studies have also investigated the application of simplified forward calculation methods to computed ECGs. Schuler et al. [42] suggest the calculation of ECGs based on the BEM with coarse resolution surface meshes bounding the heart and the torso whereby parameters to blur the cardiac sources are optimized beforehand to avoid discontinuous wave propagation. In this way, they obtained body surface potentials in accurate accordance with the bidomain simulation results for a ventricular setup. However, one major drawback of the BEM approach is the impossibility of accounting for anisotropic conductivity in the myocardium [37]. However, we found that P wave correlation coefficients still quantified to >0.93 showing that the isotropic assumption yields similar ECGs compared to the bidomain results. For the infinite volume conductor method instead, not only the assumption of isotropic myocardial conductivities but also of a homogeneous torso volume conductor has to be made. Moreover, the simplified assumption that the atria is immersed in a medium of infinite spatial extent holds. Although the general P wave morphology was preserved, the ECG still substantially differs regarding peak-to-peak amplitudes in the precordial leads and atrial repolarization in the inferior leads as it reflects in our results and was reported in previous work [55]. For the application field of computing intracardiac electrograms, the reader is referred to the review by SÃ¡nchez et al. [6].

C. Limitations

In this work, we investigated 4 different simulation scenarios comprising a healthy baseline case and three atrial models infiltrated with fibrosis, which was modeled either as slow conducting patches, non-conductive conduction barriers or ionic conductance rescaling. For the spatially distributed fibrotic areas (patchy and diffuse), none of the fibrosis remodeling scenarios had a marked effect on the ECG compared to the healthy baseline case. Ionic conductance rescaling, slow conducting fibrotic patches and percolation reflect in the ECG as a slight prolongation of the repolarization phase and an offset in the isoelectric line, a marginal prolongation of the P wave and a decrease in peak-to-peak P wave amplitudes, respectively. However, all these effects on the ECG are small and would show up in a more pronounced way if different fibrosis remodeling approaches were combined [1]. However, we intentionally decided to investigate the effect of different propagation models and forward calculation methods in each of these simulation scenarios separately to shed light on which fibrosis remodeling aspects can be accurately captured by the simplified model solutions.

In our simulation setup, we did not consider motion and contraction of the atria for the sake of reducing model complexity and computational cost. Moss et al. showed that a fully coupled electro-mechanical model does not have any influence on simulation results regarding atrial activation and that resulting P waves exhibit negligible differences to the ones computed on a non-deforming model [56]. However, the atrial repolarization results of our study might be affected to a larger extent by the lack of a coupled model as previous studies reported a substantial impact of mechanical feedback on electrophysiological behavior in the ventricles [57], [58], especially during the repolarization phase [56], [59].

CVs were derived from the values reported in [22]. Based on them, conductivities were computed using *tuneCV* [25] as described in Section II-A using strand meshes. However, no bath loading effects, mesh and wavefront curvature were considered when tuning the CVs, which might lead to mismatching CVs and conductivities assigned to different regions in the more complex atrial geometry. Adding a bath in the experiments set up for the tuning process, could lead to more similar LAT and ECG results between the bidomain results with Clerc and Roberts conductivities on the bi-atrial geometry. Moreover, performing the tuning with a bath attached to the strand geometries would lead to different monodomain conductivities for the setups without explicit conductivity tuning while the conductivity values in case of explicit conductivity tuning for the monodomain simulation would remain unchanged. Conductivities in transverse and longitudinal direction needed to be scaled by a factor of 54 and 12, respectively. The tuning procedure caused the original transversal vs. longitudinal conductivity ratios reported by Clerc and Roberts et al. to change while keeping intra- vs. extracellular conductivity ratios constant.

The average edge length of the atrial geometry was 523 μm. To quantify the numerical error arising due to the mesh resolution, we conducted experiments on a 5 cm $\times$ 2 cm $\times$ 2.8 mm block mesh with a resolution of 528 μm and a refined resolution of 265 μm by linearly subdividing the elements (see Fig. S2 in the supplementary material). Using the same numerical settings as for the experiments on the bi-atrial geometry, we ran a simulation of a planar wave passing through an isthmus and then propagating with a curved wavefront. Conductivities were adjusted using *tuneCV* [25] as described in Section I to the CV in the regular atrial bulk tissue region. Maximum LAT differences between the experiments on the coarse and the fine mesh were 1.2 ms. Considering the total activation time in the block of 43 ms, the error introduced by the coarse mesh resolution was 2%. The root mean squared errors between two APs resulting from the simulations on the coarse and the fine mesh were 0.0186 mV and 0.0491 mV for the two nodes marked in Fig. 2 in the supplementary material. When adding a fibrotic region to the block, the maximum absolute LAT error between the experiments on the fine and the coarse mesh was 1.2 ms ($\sim$2 %) as well (see Fig. 3 in the supplementary material) for planar wave propagating along fiber direction. The latter is approximately also the case in our bi-atrial simulation setup where the depolarization wavefront traverses the elliptically shaped fibrotic patches growing predominantly in fiber direction. However, if a notable transverse wave propagation had to be represented, our chosen mesh resolution of 523 μm would have been too coarse to capture the wave propagation at a velocity of 0.15 m/s. Thus, the mesh resolution chosen for the atrial model in this study might introduce an error of 2 %, which is equivalent to an absolute LAT error of $\sim$2 ms on the bi-atrial mesh. Due to the small root mean squared error between the APs of the coarse and the fine mesh, no additional discretization error affecting APD_{90} is expected.

V. CONCLUSION

The results presented here show that the Eikonal model is capable of faithfully producing LATs and P waves compared to full bidomain simulations with a reduction of computation times by a factor of up to three orders of magnitude. However, propagation models neglecting diffusion terms lack the fidelity in terms of repolarization as shown by APD_{90} deviations. Thus, RE models are needed e.g. in cases where repolarization dynamics are of significant importance such as e.g. for re-entry mechanism studies. ECGs calculated with the BEM accurately resemble the FEM results for both P waves and the ECG in the repolarization phase. When computing ECGs with the infinite volume conductor method, the systematic overestimation of peak-to-peak P wave amplitudes especially in the precordial leads should be taken into account when evaluating P wave features.

REFERENCES

[1] C. Nagel et al., "Non-invasive and quantitative estimation of left atrial fibrosis based on P waves of the 12-lead ECG-a large-scale computational study covering anatomical variability," *J. Clin. Med.*, vol. 10, 2021, Art. no. 1797.

[2] G. Luongo et al., "Hybrid machine learning to localize atrial flutter substrates using the surface 12-lead electrocardiogram," *EP Europace*, vol. 24, no. 7, pp. 1186–1194, 2022.

[3] L. Azzolin et al., "A reproducible protocol to assess arrhythmia vulnerability: Pacing at the end of the effective refractory period," *Front. Physiol.*, vol. 12, 2021, Art. no. 656411.

[4] M. Wallman, N. P. Smith, and B. Rodriguez, "A comparative study of graph-based, eikonal, and monodomain simulations for the estimation of cardiac activation times," *IEEE Trans. Biomed. Eng.*, vol. 59, no. 6, pp. 1739–1748, Jun. 2012.

[5] A. Neic et al., "Efficient computation of electrograms and ECGs in human whole heart simulations using a reaction-eikonal model," *J. Comput. Phys.*, vol. 346, pp. 191–211, 2017.

[6] J. Sánchez and A. Loewe, "A review of healthy and fibrotic myocardium microstructure modeling and corresponding intracardiac electrograms," *Front. Physiol.*, vol. 13, 2022, Art. no. 908069.

[7] M. J. Bishop and G. Plank, "Bidomain ECG simulations using an augmented monodomain model for the cardiac source," *IEEE Trans. Bio-Med. Eng.*, vol. 58, no. 8, pp. 2297–2307, Aug. 2011.

[8] M. Potse et al., "A comparison of monodomain and bidomain propagation models for the human heart," in *Proc. IEEE Annu. Int. Conf. Eng. Med. Biol. Soc.*, 2006, pp. 3895–3898.

[9] E. Vigmond et al., "Percolation as a mechanism to explain atrial fractionated electrograms and reentry in a fibrosis model based on imaging data," *Heart Rhythm*, vol. 13, pp. 1536–1543, 2016.

[10] L. Azzolin et al., "Automated framework for the augmentation of missing anatomical structures and generation of personalized atrial models from clinical data," in *Proc. Comput. Cardiol. Conf.*, 2021, pp. 1–4.

[11] C. H. Roney et al., "Modelling methodology of atrial fibrosis affects rotor dynamics and electrograms," *EP Europace*, vol. 18, pp. iv146–iv155, 2016.

[12] M. W. Krueger et al., "Personalization of atrial anatomy and electrophysiology as a basis for clinical modeling of radio-frequency ablation of atrial fibrillation," *IEEE Trans. Med. Imag.*, vol. 32, no. 1, pp. 73–84, Jan. 2013.

[13] W. Jakob et al., "Instant field-aligned meshes," *ACM Trans. Graph.*, vol. 34, pp. 1–15, 2015.

[14] L. Azzolin et al., "AugmentA: Patient-specific augmented atrial model generation tool," *medRxiv*, 2022, doi: 10.1101/2022.02.13.22270835.

[15] T. Zheng et al., "An automate pipeline for generating fiber orientation and region annotation in patient specific atrial models," *Curr. Directions Biomed. Eng.*, vol. 7, pp. 136–139, 2021.

[16] R. Piersanti et al., "Modeling cardiac muscle fibers in ventricular and atrial electrophysiology simulations," *Comput. Methods Appl. Mechanics Eng.*, vol. 373, 2021, Art. no. 113468.

[17] P. C. Africa et al., "life^x - heart module: A high-performance simulator for the cardiac function. package 1: Fiber generation," 2022, *arXiv:2201.03303*.

[18] A. Neic et al., "Automating image-based mesh generation and manipulation tasks in cardiac modeling workflows using meshtool," *SoftwareX*, vol. 11, 2020, Art. no. 100454.

[19] K. Gillette et al., "A framework for the generation of digital twins of cardiac electrophysiology from clinical 12-leads ECGs," *Med. Image Anal.*, vol. 71, 2021, Art. no. 102080.

[20] A. Reinke et al., "Geometrical model and corresponding conductivities for solving the inverse problem of ECG," in *Biomedizinische Technik / Biomed. Eng.*, vol. 59, pp. 937–940, 2014.

[21] D. Keller et al., "Ranking the influence of tissue conductivities on forward-calculated ECGs," *IEEE Trans. Biomed. Eng.*, vol. 57, no. 7, pp. 1568–1576, Jul. 2010.

[22] A. Loewe et al., "Left and right atrial contribution to the p-wave in realistic computational models," in *Proc. Int. Conf. Funct. Imag. Model. Heart*, pp. 439–447, 2015.

[23] M. W. Krüger, "Personalized multi-scale modeling of the atria : Heterogeneities, fiber architecture, hemodialysis and ablation therapy," Ph.D. dissertation, KIT Scientific Publishing, Karlsruhe, Germany, 2013.

[24] G. Plank et al., "The openCARP simulation environment for cardiac electrophysiology," *Comput. Methods Programs Biomed.*, vol. 208, 2021, Art. no. 106223.

[25] C. Costa et al., "Automatic parameterization strategy for cardiac electrophysiology simulations," in *Proc. Conf. Comput. Cardiol.*, 2013, pp. 373–376.

[26] L. Clerc, "Directional differences of impulse spread in trabecular muscle from mammalian heart," *J. Physiol.*, vol. 255, pp. 335–346, 1976.

[27] D. E. Roberts and A. M. Scher, "Effect of tissue anisotropy on extracellular potential fields in canine myocardium in situ," *Circulation Res.*, vol. 50, pp. 342–351, 1982.

[28] M. Courtemanche, R. J. Ramirez, and S. Nattel, "Ionic mechanisms underlying human atrial action potential properties: Insights from a mathematical model," *Amer. J. Physiol.-Heart Circulatory Physiol.*, vol. 275, no. 1, pp. H301–H321, 1998.

[29] M. W. Krueger et al., "In-silico modeling of atrial repolarization in normal and atrial fibrillation remodeled state," *Med. Biol. Eng. Comput.*, vol. 51, pp. 1105–1119, 2013.

[30] L. Tung, *A Bi-domain Model for Describing Ischemic Myocardial DC Potentials*. Ph.D. Dissertation, Massachusetts Inst. Technol., Cambridge, MA, USA, 1978.

[31] P. C. Franzone, L. F. Pavarino, and S. Scacchi, *Mathematical Cardiac Electrophysiology*, vol. 13, Berlin, Germany: Springer, 2014.

[32] J. Keener and J. Sneyd, *Mathematical Physiology 1: Cellular Physiology*. Berlin, Germany: Springer, 2009.

[33] E. Vigmond et al., “Solvers for the cardiac bidomain equations,” *Prog. Biophys. Mol. Biol.*, vol. 96, no. 1–3, pp. 3–18, 2008.

[34] S. A. Niederer et al., “Verification of cardiac tissue electrophysiology simulators using an n-version benchmark,” *Philos. Trans. Roy. Soc. A Math. Phys. Eng. Sci.*, vol. 369, no. 1954, pp. 4331–4351, 2011.

[35] E. Pernod et al., “A multi-front eikonal model of cardiac electrophysiology for interactive simulation of radio-frequency ablation,” *Comput. Graph.*, vol. 35, no. 2, pp. 431–440, 2011.

[36] A. J. Pullan, K. A. Tomlinson, and P. J. Hunter, “A finite element method for an eikonal equation model of myocardial excitation wavefront propagation,” *SIAM J. Appl. Math.*, vol. 63, no. 1, pp. 324–350, 2002.

[37] M. Potse, B. Dube, and A. Vinet, “Cardiac anisotropy in boundary-element models for the electrocardiogram,” *Med. Biol. Eng. Comput.*, vol. 47, pp. 719–729, 2009.

[38] D. B. Geselowitz and T. W. Miller, “A bidomain model for anisotropic cardiac muscle,” *Ann. Biomed. Eng.*, vol. 11, pp. 191–206, 1983.

[39] M. Stenroos, V. Mäntynen, and J. Nenonen, “A Matlab library for solving quasi-static volume conduction problems using the boundary element method,” *Comput. Methods Programs Biomed.*, vol. 88, pp. 256–263, 2007.

[40] K. Higuchi et al., “The spatial distribution of late gadolinium enhancement of left atrial magnetic resonance imaging in patients with atrial fibrillation,” *JACC: Clin. Electrophysiol.*, vol. 4, pp. 49–58, 2018.

[41] E. J. Vigmond et al., “Computational tools for modeling electrical activity in cardiac tissue,” *J. Electrocardiol.*, vol. 36, pp. 69–74, 2003.

[42] S. Schuler et al., “Spatial downsampling of surface sources in the forward problem of electrocardiography,” in *Funct. Imaging and Modeling of the Heart*, Y. Coudière et al., Eds., vol. 11504, Berlin, Germany: Springer, 2019, pp. 29–36.

[43] R. Sebastian et al., “Assessing influence of conductivity in heart modelling with the aim of studying cardiovascular diseases,” *Med. Imag.*, vol. 6916, 2008, Art. no. 691627.

[44] T. Cojean, F. Goebel, and M. Houillon, “Porting the OpenCARP cardiac electrophysiology simulation framework to GPU architectures,” in *Proc. 5th ISC Workshop HPC Appl. Precis. Med.*, 2022, Art. no. 956.

[45] C. M. Augustin et al., “Anatomically accurate high resolution modeling of human whole heart electromechanics: A strongly scalable algebraic multigrid solver method for nonlinear deformation,” *J. Comput. Phys.*, vol. 305, pp. 622–646, 2016.

[46] P. Pathmanathan et al., “A numerical guide to the solution of the bidomain equations of cardiac electrophysiology,” *Prog. Biophys. Mol. Biol.*, vol. 102, pp. 136–155, 2010.

[47] L. A. Woodworth, B. Cansız, and M. Kaliske, “A numerical study on the effects of spatial and temporal discretization in cardiac electrophysiology,” *Int. J. Numer. Method Biomed. Eng.*, vol. 37, 2021, Art. no. e3443.

[48] Z. Fu, R. M. Kirby, and R. T. Whitaker, “A fast iterative method for solving the eikonal equation on tetrahedral domains,” *SIAM J. Sci. Comput.*, vol. 35, pp. c473–c494, 2013.

[49] A. Capozzoli et al., “A comparison of fast marching, fast sweeping and fast iterative methods for the solution of the Eikonal equation,” in *Proc. 21st Telecommun. Forum Telfor*, 2013, pp. 685–688.

[50] S. Mukherjee and M. Morjaria, “On the efficiency and accuracy of the boundary element method and the finite element method,” *Int. J. Numer. Methods Eng.*, vol. 20, pp. 515–522, 1984.

[51] A. Pashaei et al., “Comparison of phenomenological and biophysical cardiac models coupled with heterogenous structures for prediction of electrical activation sequence,” in *Proc. Comput. Cardiol.*, 2010, pp. 871–874.

[52] A. Pashaei et al., “Fast multiscale modeling of cardiac electrophysiology including purkinje system,” *IEEE Trans. Biomed. Eng.*, vol. 58, no. 10, pp. 2956–2960, Oct. 2011.

[53] N. Gassa et al., “Spiral waves generation using an eikonal-reaction cardiac electrophysiology model,” in *Proc. Int. Conf. Functional Imag. Model. Heart*, 2021, pp. 523–530.

[54] C. Nagel et al., “Comparison of source models and forward calculation methods for atrial electrophysiology regarding activation times and electrocardiograms,” in *Proc. iHEART Congr. Modelling Cardiac Function*, 2021, p. 48.

[55] L. R. Bear et al., “Forward problem of electrocardiography: Is it solved ?,” *Circulation Arrhythmia Electrophysiol.*, vol. 8, pp. 677–684, 2015.

[56] R. Moss et al., “A fully-coupled electro-mechanical whole-heart computational model: Influence of cardiac contraction on the ECG,” *Front. Physiol.*, vol. 12, 2021, Art. no. 778872.

[57] M. Salvador et al., “Electromechanical modeling of human ventricles with ischemic cardiomyopathy: Numerical simulations in sinus rhythm and under arrhythmia,” *Comput. Biol. Med.*, vol. 6, 2021, Art. no. 104674.

[58] M. Salvador et al., “The role of mechano-electric feedbacks and hemodynamic coupling in scar-related ventricular tachycardia,” *Comput. Biol. Med.*, vol. 142, 2021, Art. no. 105203.

[59] T. Gerach et al., “Electro-mechanical whole-heart digital twins: A fully coupled multi-physics approach,” *Mathematics*, vol. 9, 2021, Art. no. 1247.

Chapter 5

Estimation of Conduction Velocity Using the Standard Eikonal Model

This chapter focuses on the process of estimating conduction velocity (CV) in cardiac tissue and how the eikonal model can enhance the accuracy of these estimations. It begins by discussing the significance of accurate CV estimation, emphasizing its importance for clinical applications and why it is crucial to assess the reliability of different estimation methods. Following this, the radial basis function (RBF) method is introduced as an example of a technique to be evaluated. Next, the chapter outlines the necessary modifications made to the standard eikonal model to provide CV ground truth values and ultimately assess and improve the accuracy of CV estimation methods, particularly in accounting for tissue anisotropy. These adjustments are aimed at providing a more realistic representation of how electrical signals propagate through cardiac tissue. Lastly, the chapter presents a comparative analysis between the CV values estimated using the RBF method and the ground truth derived from the modified eikonal model. This comparison reveals discrepancies and identifies the conditions under which the RBF method may introduce errors in estimating CV.

The specific adaptations of the RBF method for this context were developed by Laura Unger, Nicolas Pilia, Claudia Nagel, Jeanne Koch and Leonie Schicketanz. Since some of their adaptations are still unpublished work, their contributions to this method are only briefly outlined here. The author's contributions to this project involved extending the eikonal model to evaluate CV estimation methods, conducting the eikonal simulations, applying the RBF method to estimate CV, and analyzing the comparison between the estimated values and the ground truth.

5.1 Introduction

One important metric for cardiac tissue characterization is CV. This metric refers to both the speed and direction of the electrical excitation wave as it propagates through myocardial tissue [75]. When the propagation is assumed to be isotropic, the CV direction is perpendicular to the wavefront (i.e., parallel to the gradient of activation time (AT)), and only one speed is associated with this propagation [76].

However, due to the geometric arrangement of cardiomyocytes, the preferential alignment of gap junctions along the longitudinal axis, and the distribution of collagen fibers within the tissue, electrical propagation in the heart becomes anisotropic [77–81]. In this case, the propagation direction is no longer perpendicular to the wavefront (see Figure 5.1), and the speed of propagation is no longer the inverse of the magnitude of the AT gradient [76].

In this work, the speed of propagation is referred to as CV magnitude, and the direction of propagation as CV direction. When the wavefront propagates along the preferential orientation of the cardiomyocytes (i.e., parallel to their longitudinal axis), the CV magnitude reaches its maximum value, which is referred to as longitudinal CV. Conversely, when the propagation occurs perpendicular to the cardiomyocyte orientation, the CV magnitude is lower and is referred to as transversal CV. The anisotropy ratio is defined as the ratio between longitudinal and transversal CV. In this chapter, CV in the normal direction, though physiologically relevant, either is neglected or assumed to be equal to the transversal CV.

CV can be reduced for various physiological or anatomical reasons. For instance, when source-sink mismatch effects occur with the activated tissue area being smaller than the excitable tissue, it can lead to reduced CV, as observed in a concave wavefront [82]. This mismatch can also occur due to branching of cardiac tissue, channels within scar tissue, or interatrial bridges [83]. Reduced excitability and fewer available fast sodium channels, such as during acute myocardial ischemia, tachycardia, or with class I anti-arrhythmic drugs, further slow conduction. In the absence of fast sodium channels, L-type calcium channels may also play a role in this reduction [84]. Moreover, decreased intracellular conductivity from gap junction remodeling [85] and reduced extracellular conductivity due to scar tissue also contribute to slower CV [86].

Slow and heterogeneous CV, combined with a short effective refractory period (ERP), are closely linked to reentry and self-activation mechanisms in cardiac tissue, as they create a vulnerable substrate. For reentry to occur, the tissue must complete its refractory phase by the time the wavefront reactivates a specific area. This can happen if either the CV is reduced or the effective refractory period is shortened. Both decreased ERP and reduced CV lead to a shorter wavelength, which is defined as the distance covered by the depolarization wave during the time it takes for the tissue to recover its excitability enough to propagate a new impulse. The smaller the wavelength, the easier it becomes for reentry patterns to form and coexist [87, 88].

Accurately measuring CV is crucial for several reasons. Characterizing CV aids in risk stratification by helping to identify patients who are more susceptible to arrhythmias. It also enables the detection of reentry pathways, including the identification of the critical isthmus, which is a key mechanism in atrial flutter and essential for therapy planning in arrhythmias [89]. By pinpointing these pathways, clinicians can better understand the underlying causes of abnormal heart rhythms and personalize treatment strategies, such as targeted ablation therapy, improving patient outcomes and reducing the likelihood of recurrent arrhythmias. Additionally, CV measurements can be used to personalize computer models for in silico simulations, allowing for more accurate predictions of arrhythmic behavior and treatment responses in individual patients [75, 87, 90].

Coveney et al. reviewed various methods for estimating CV from AT obtained through electroanatomical mapping with different types of catheters [75]. They categorize these methods into three types: local, global, and inverse. Local methods focus on the AT from small areas, making them better suited for analyzing heterogeneous AT but more prone to measurement errors. Global methods, on the other hand, interpolate all AT data simultaneously. While these methods are more robust against errors, they disregard physical constraints since they rely purely on data-driven approaches. Inverse methods take physical phenomena into account when modeling electrical propagation and consider all AT data at once but tend to require longer computation times.

A common challenge across all methods is the absence of a ground truth for accurately assessing CV estimations. In some cases, eikonal simulations have been used to fit the AT data [91]. However, discrepancies in the fit of AT data do not always correspond to small differences in CV estimations. Additionally, propagation is often assumed to be isotropic, which can lead to substantial errors [75, 91]. The goal of this chapter is to demonstrate how the eikonal model can be adapted to improve the evaluation of CV estimation methods. Furthermore, it highlights that errors resulting from assuming isotropic propagation in the presence of anisotropic conditions are not always negligible.

In this study, the RBF method is applied to estimate CV and evaluated against ground truth values derived from the eikonal model. First, the core principles of the RBF method are briefly explained. Subsequently, necessary modifications to the eikonal model are implemented to enable the assessment of CV estimation techniques and provide accurate ground truth values for CV. Simulated data is then generated to provide AT as well as ground truth for CV magnitude and direction. Finally, the RBF method is used to estimate CV from the simulated ATs. The CV estimates are compared to the CV ground truth obtained from the eikonal model.

5.2 Methods

5.2.1 Radial Basis Function Method

The method proposed by Mase and Ravelli utilizes RBF to interpolate AT sequences obtained from electroanatomical mapping [92]. These AT values, initially available at a limited number of points on the atrial surface, are extended to a more detailed set of coordinates that better represent the atrial geometry. The CV magnitude is then analytically calculated as the inverse of the AT gradient, with the assumption that CV direction vectors are orthogonal to the isochrones of the interpolated wavefront.

This method can be particularly helpful for scattered data, as it does not rely on assumptions about the spacing or density of mapping points. Since the lack of appropriate AT measurements often poses challenges in calculating accurate CV maps, this technique may assist in addressing that limitation [75, 92].

The coordinates of each point in the set of N mapped points are denoted as $X_p = [x_p, y_p, z_p]$, where $p = 1, \ldots, N$ is the index of the point. For each point X_p, an associated known AT is denoted by T_p. A function $T : \Omega \to \mathbb{R}_{\geq 0}$ is defined to assign an AT denoted as $T(x, y, z)$ to each coordinate $X = [x, y, z]$ on the atrial surface. For the mapped points, the coordinates $X_p = [x_p, y_p, z_p]$ and their ATs are known for $1 \leq p \leq N$.

The ATs for other points on the surface can be interpolated using RBF. The interpolation is expressed as:

$$T(X) = \sum_{i=1}^{N} \alpha_i R(\|X - X_p\|) + \phi, \tag{5.1}$$

where $R(\|X - X_p\|)$ are the RBF centered at the mapped points, and it depends on the Euclidean distances between X (the point to be interpolated) and the known points X_p. The coefficients α_i are determined by solving a linear system with interpolation constraints. For simplicity, the polynomial term ϕ is neglected, as it does not significantly affect the results in this work.

Once the ATs are interpolated, CV is calculated based on the gradient of the AT function T. The gradient ∇T is given by:

$$\nabla T = \left[\frac{\partial T}{\partial x}, \frac{\partial T}{\partial y}, \frac{\partial T}{\partial z}\right] = [t_x, t_y, t_z]. \tag{5.2}$$

The gradient vector ∇T is normal to the excitation wavefront, which is assumed to be the direction of propagation. To calculate the CV, the approach from Bayly et al. [93] is used, which expresses the velocity vector $\overrightarrow{v} = [v_x, v_y, v_z]$ as:

$$\overrightarrow{v} = \frac{\nabla T}{|\nabla T|^2} = \frac{1}{t_x^2 + t_y^2 + t_z^2}[t_x, t_y, t_z]. \tag{5.3}$$

Thus, the components of the CV are given by:

$$v_x(x, y, z) = \frac{t_x}{t_x^2 + t_y^2 + t_z^2}, \tag{5.4}$$

$$v_y(x, y, z) = \frac{t_y}{t_x^2 + t_y^2 + t_z^2}, \tag{5.5}$$

$$v_z(x, y, z) = \frac{t_z}{t_x^2 + t_y^2 + t_z^2}. \tag{5.6}$$

These equations describe the components of the CV vector, indicating both the direction and magnitude of the wavefront propagation at each point on the surface.

5.2.2 Eikonal Model Modifications

Eikonal simulations can serve as ground truth for evaluating methods used to estimate CV. In the standard eikonal model, solving the eikonal equation results in a single AT value for each node, with the CV provided as input. It is important to note that in the isotropic scenario, the magnitude of CV as well as the longitudinal and transversal CV are identical since there is no preferred propagation direction. Additionally, the CV magnitude is easily known a priori, as it corresponds to the same CV value used to solve the eikonal equation. The direction of propagation can also be easily determined by normalizing the AT gradient. In-silico simulations based on the eikonal equation have been utilized to evaluate the RBF approach in the context of isotropic propagation, yielding satisfactory results [91].

In the anisotropic case, the process becomes more intricate, as solving the anisotropic eikonal equations yields ATs but does not directly provide the CV directions and magnitudes. Additionally, it is no longer possible to calculate the direction as the gradient of AT, since the propagation may not always be normal to the wavefront. Moreover, the longitudinal CV can vary significantly from the CV magnitude, depending on the anisotropy ratio. Consequently, obtaining ground truth values for CV direction and magnitude poses a challenge in anisotropic propagation. To address this, the local solver of the anisotropic eikonal equation was extended to provide both the CV magnitude and direction as ground truth, without affecting the standard output of ATs.

Let $\lambda^* \in [0,1]$ represent the value that minimizes equation 3.19 in the final iteration of the fast iterative method (FIM) for a given node. The final AT for a node $X \in \Omega$ is then defined as:

$$T(X) = \lambda^* T(Y) + (1-\lambda^*)T(Z) + \frac{\sqrt{\overrightarrow{X_{\lambda^*}X}^\top \mathbf{D}(X)^{-1}\overrightarrow{X_{\lambda^*}X}}}{v_1(X)}, \tag{5.7}$$

where the triangle XYZ is the one with the smallest possible AT for X among all triangles containing X. Here,

$$\overrightarrow{X_{\lambda^*}X} = \lambda^* \overrightarrow{YX} + (1-\lambda^*)\overrightarrow{ZX}, \tag{5.8}$$

represents a vector aligned with the wavefront propagation. Using this, the direction of the CV can be defined as:

$$\frac{\overrightarrow{X_{\lambda^*}X}}{\|\overrightarrow{X_{\lambda^*}X}\|}. \tag{5.9}$$

Furthermore, the CV magnitude is given by:

$$\frac{\|\overrightarrow{X_{\lambda^*}X}\|}{\frac{\sqrt{\overrightarrow{X_{\lambda^*}X}^\top \mathbf{D}(X)^{-1}\overrightarrow{X_{\lambda^*}X}}}{v_1(X)}}, \tag{5.10}$$

where the numerator represents the distance traveled by the wavefront across the triangle XYZ, from edge YZ to node X, and the denominator represents the time required to travel this distance.

5.2.3 Simulated Conduction Velocity and Activation Time Data Generation

Two geometries were utilized for simulation: a simple 2D sheet and a 2D manifold derived from electroanatomical mapping (Figure 5.1a and Figure 5.3a). Boundary conditions were applied at a single point, with predefined preferential cardiomyocyte orientations. The anisotropic eikonal equation was solved at each node in both geometries using the fast iterative method, with additional modifications to extract AT, CV magnitude, and direction.

The simplest mesh used was a 2D square sheet with dimensions of 20 mm by 20 mm, composed of triangular elements, and the bottom left corner positioned at (0,0). This mesh contained 128 nodes and 1422 elements, with an average edge length of 218 µm. Cardiomyocyte orientation was uniformly set, with vectors aligned parallel to the x-axis. The longitudinal CV was held constant at 1000 mm/s across the entire sheet, and the anisotropy ratio (the ratio of longitudinal to transverse CV) was uniformly set to 2. Initial conditions were imposed on the node located at (0,0), with an activation time of 0 ms.

The second geometry was a 2D manifold representing the left atrium, generated from electroanatomical mapping of a patient. This mesh consisted of 12965 nodes and 25635 triangular elements, with an average edge length of 1306 µm. The preferential cardiomyocyte orientation was assigned using a rule-based method, as described in Azzolin et al. [94]. Both the longitudinal CV and the anisotropy ratio were set to constant values of 1000 mm/s and 2, respectively, across the entire geometry. Initial conditions were applied to a single node in the lower region of the posterior wall of the left atrium.

After running the simulations, the result obtained in the last iteration for each node from Equation 5.9 was considered the ground truth for the CV direction, $\hat{v}_{\text{true}}$. This term is a normalized vector that points in the true direction of propagation of the excitation wave. Similarly, the value obtained in the last iteration for each node from Equation 5.10 was considered the ground truth for the CV magnitude, v_{true}. This is a scalar value that denotes the true speed of propagation at a given node.

5.2.4 Assessment of Conduction Velocity Estimates

The obtained ATs in the eikonal simulations were used as input for the RBF method to estimate both CV magnitude and direction. These RBF-based estimates were then compared to the ground truth provided also by the FIM. Although the RBF is typically used as a global method, in this case, it was applied locally. An other important distinction between the works of Mase and Ravelli and the current study is that their RBF method is designed to interpolate scattered data [92]. In contrast, the specific adaptation of RBF employed in this study focuses on interpolating from neighboring nodes to the AT of the central node to manage error measurements, rather than interpolating AT at new locations where data is lacking. For instance, the eikonal simulation generates ATs for all nodes within the geometry, and this complete set of ATs values is utilized in the CV estimation. For each node, a neighborhood of surrounding nodes was used to estimate the CV. This neighborhood was defined as all nodes within 4 mm of the central node. If fewer than 10 nodes were within this radius, the 10 closest nodes were selected instead.

A Gaussian function was used as the radial basis function, R, defined as:

$$R(\|X - X_p\|) = e^{-c^2(\|X-X_p\|)^2}, \tag{5.11}$$

where c controls the decay of the Gaussian and was set to 0.01 mm^{-1}. The point X is the central node and X_p is a point in the neighborhood. A linear system was then solved to find the coefficients α_i (Equation 5.1), and the CV was calculated as described in Section 5.2.1. The estimated CV magnitude, denoted as $v_{\text{est}} = \|\overrightarrow{v}\|$, was obtained from the norm of the vector in Equation 5.3. The estimated CV direction was given by normalizing this vector, $\hat{v}_{\text{est}} = \frac{\overrightarrow{v}}{\|\overrightarrow{v}\|}$.

Then to assess this method to estimate CV values, E_{mag}, error of CV magnitude estimation and E_{dir} error of CV direction estimation were calculated. To evaluate the accuracy of the CV magnitude estimates, E_{mag} was defined as the root mean square error (RMSE) and was computed across all nodes by comparing the true CV magnitude with the RBF estimates:

$$E_{\text{mag}} = \sqrt{\frac{1}{M}\sum_{i=1}^{M}(v_{\text{true}}(X_i) - v_{\text{est}}(X_i))^2}, \tag{5.12}$$

where $v_{\text{true}}(X_i)$ and $v_{\text{est}}(X_i)$ represent the true and estimated CV magnitudes at node $X_i \in \Omega$, and M is the total number of nodes in the geometry under analysis. To assess the quality of the CV direction estimation, its error was quantified as the mean angle between the true and estimated CV directions at each node. Let $\hat{v}_{\text{true}}(X_i)$ and $\hat{v}_{\text{est}}(X_i)$ represent the true and estimated CV directions, respectively, at node $X_i \in \Omega$. The angle θ_i between these two vectors at each node is given by the arccosine of their dot product, as follows:

$$\theta_i = \cos^{-1}\left(\hat{v}_{\text{true}}(X_i) \cdot \hat{v}_{\text{est}}(X_i)\right), \tag{5.13}$$

This angle is assume to be always positive and both vectors lie in the plan perpendicular to the normal direction at X_i. The mean angular error across all M nodes is then calculated as:

$$E_{\text{dir}} = \frac{1}{M}\sum_{i=1}^{M}\theta_i. \tag{5.14}$$

5.3 Results

Figure 5.1 illustrates the results from the eikonal simulation in the 2D sheet, which employs a simple horizontal preferential orientation of cardiomyocytes. A radial pattern of electrical activation can be observed, originating from the bottom left corner and spreading throughout the sheet. Due to the faster propagation along the preferential orientation, the bottom right corner is activated in just 20 ms, while the upper left corner takes 40 ms to activate. Overall, the total activation time for the entire geometry is approximately 45 ms. The isochrones take the shape of a quarter of an ellipse, reflecting the anisotropic nature of the propagation. Additionally, it is noteworthy that the CV direction is not always aligned with the normal of the wavefront, further demonstrating anisotropy. The true CV magnitude map indicates that the speed reaches its maximum value of 1000 mm/s near the inferior border, where the propagation aligns with the preferential orientation. In contrast, along the left border, where propagation occurs perpendicular to the preferential orientation, the CV magnitude drops to its minimum value of 500 mm/s, reflecting the anisotropy ratio set at 2.

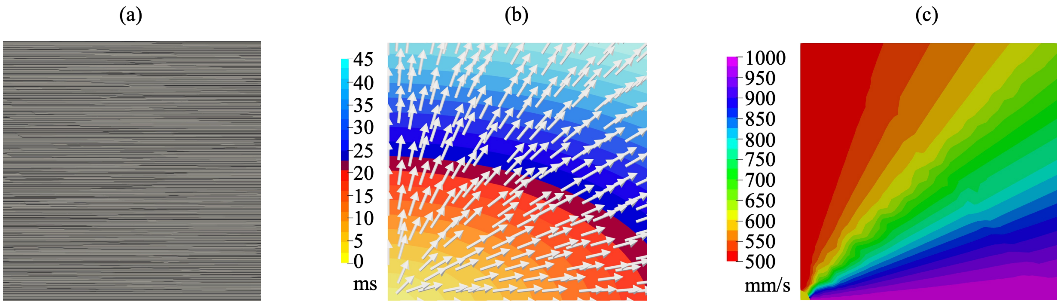

Figure 5.1: Eikonal simulation results in 2D sheet. **a)** Preferential cardiomyocyte orientation parallel to the horizontal axis. **b)** Activation times and vector field with true conduction velocity (CV) direction. **c)** True CV magnitude.

The results from the RBF estimation are presented in Figure 5.2. The estimation of both CV magnitude and direction is more accurate near the inferior and left borders, while the largest errors occur around the stimulated node, particularly in the area above and to its right. The true CV magnitude consistently exceeded the estimated CV magnitude, resulting in positive differences. Additionally, regions with larger CV magnitude discrepancies also correspond to areas with greater angular deviation between the estimated and true CV direction. The RMSE in CV magnitude, E_{mag}, was 108.14 mm/s, while the mean angular error, E_{dir}, between the estimated and true CV direction was 25.31° for all the nodes in the 2D sheet. the estimates respected the upper boundary, never exceeded 1000 mm/s but fell below the lower limit of the ground truth, indicating a meaningful underestimation of the true values.

Figure 5.3 presents the results for the left atrium obtained from the eikonal simulations. The preferential cardiomyocyte orientation was determined using the rule-based method [94],

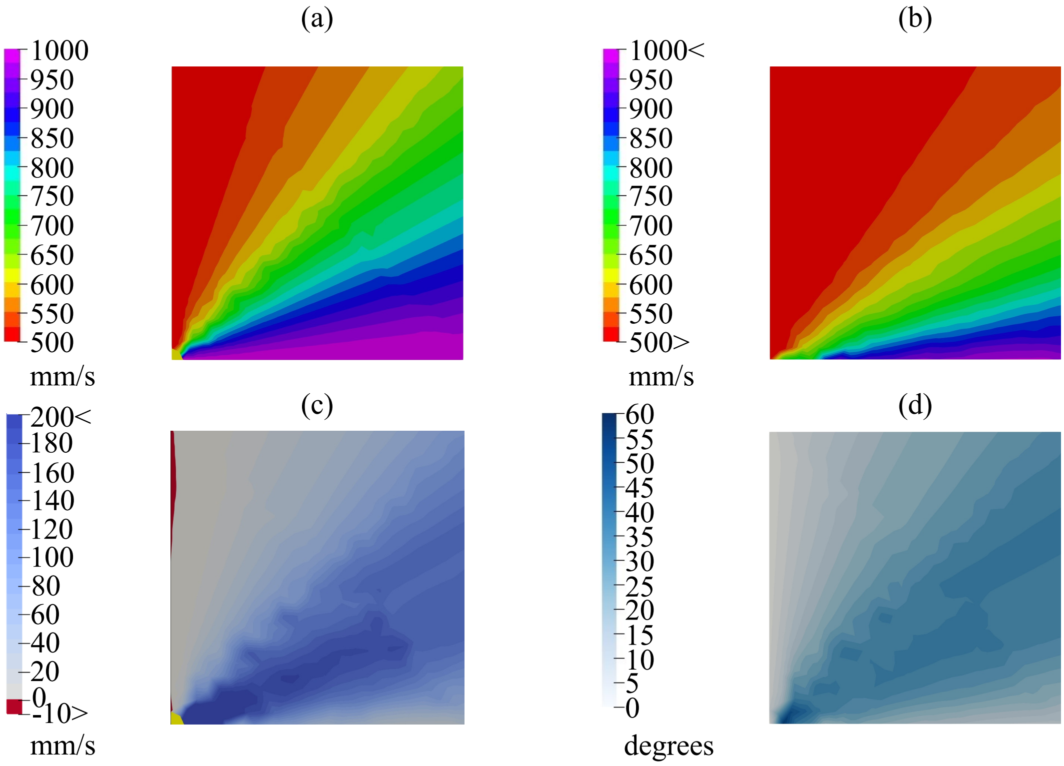

Figure 5.2: Evaluation of RBF estimates for conduction velocity (CV) in the 2D sheet. **a)** Ground truth for CV magnitude as obtained from the eikonal model. **b)** RBF-estimated CV magnitude. **c)** Error map of CV magnitude with the difference between true and estimated CV magnitudes. **d)** Angular error visualization, illustrating the angular discrepancies between true CV direction and estimated CV direction.

representing an endocardial fiber alignment. The total activation time for the atrium was approximately 150 ms, with the pulmonary veins being the last regions to activate. The activation wave propagation was parallel to the fibers in the central region of the posterior wall, where the CV reached 1000 mm/s. In contrast, in the lateral areas, the propagation was more perpendicular, reducing the CV to 500 mm/s.

Evaluation of the estimated values obtained by the RBF in the left atrium are illustrated in Figure 5.4. In these results, areas with slow estimated CV magnitude (i.e., regions in red) are more widespread compared to the true CV magnitude map. Similar to the 2D sheet experiments, regions with the lowest errors corresponded to areas where the true CV magnitude reached either its minimum or maximum values. Even though some correlation between regions with high CV direction error and high CV magnitude error remained, this relationship was less pronounced than in the simplified geometry. The RMSE in CV magnitude, E_{mag}, was 235.71 mm/s, while the mean angular error, E_{dir}, between the estimated and true CV direction was 29.21° for the nodes in the left atrium. Compared to the 2D sheet experiments, the estimation errors E_{mag} and E_{dir} for CV magnitude and direction increased in the more complex left atrial geometry. It was observed that the estimated values for CV magnitude can exceed the defined limits of the ground truth, suggesting that estimations may

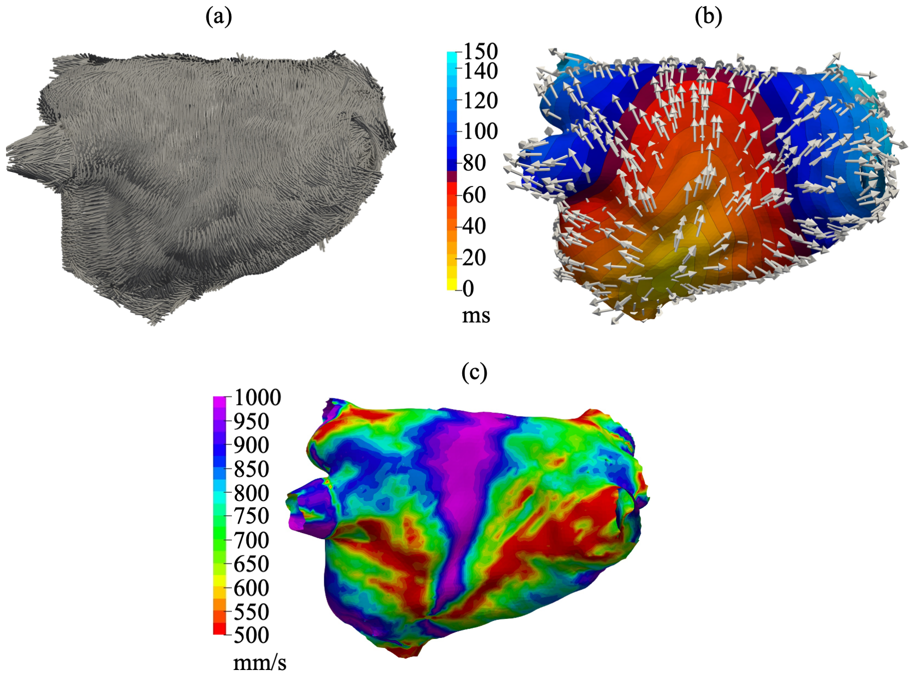

Figure 5.3: Eikonal simulation results in the left atrium. **a)** Preferential cardiomyocyte orientation. **b)** Activation times and vector field with true conduction velocity (CV) direction. **c)** True CV magnitude.

fall outside the expected range. This indicates a potential for meaningful overestimation or underestimation relative to the true values.

5.4 Discussion

The results of this study show the importance of considering anisotropy when estimating CV and demonstrate a potential application of the eikonal model. Specifically, RBF and similar methods tend to overlook anisotropy in their CV calculations, leading to important estimation errors. Simulations assessing RBF with a modified FIM to solve the eikonal equation at physiological levels of anisotropy and longitudinal CV revealed substantial inaccuracies and a tendency to underestimate CV magnitude. This underestimation occurs because the assumption that propagation direction strictly follows the gradient of activation overlooks the complex interaction between two key factors: the activation times of neighboring nodes and the angle between the preferential cardiomyocyte orientation and the edge connecting the central and neighboring nodes. The propagation direction is influenced by these factors. When the neighboring nodes that are better aligned with the preferential orientation activate earlier than others, the propagation direction aligns more closely with the preferential orientation, resulting in a CV closer to its maximum possible value. In such cases, the gradient normal to the wavefront has a different orientation, leading to a slower CV in that direction.

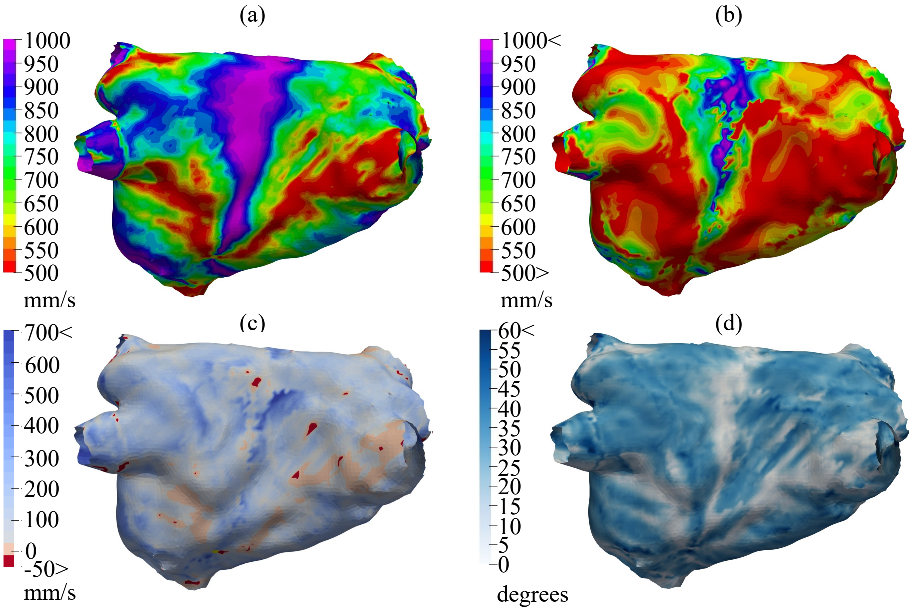

Figure 5.4: Evaluation of RBF estimates for conduction velocity (CV) in the left atrium. **a)** Ground truth for CV magnitude as obtained from the eikonal model. **b)** RBF-estimated CV magnitude. **c)** Error map of CV magnitude with the difference between true and estimated CV magnitudes. **d)** Angle between true CV direction and estimated CV direction.

This effect is more pronounced in situations where the wavefront is curved and travels at a non-zero angle to the preferential orientation, causing greater underestimation. Conversely, in cases where the wavefront is strictly planar and moves in alignment with the preferential orientation, the underestimation of CV is minimized or even eliminated. Additional errors arise from the fact that the RBF method utilize Euclidean distance as input to interpolate the AT, which may explain why the estimations occasionally exceed the ranges established by the ground truth. Employing a distance measure that accounts for anisotropy could potentially address this limitation in regions with relatively constant preferential cardiomyocyte orientation. However, it may introduce further challenges in areas characterized by high heterogeneity of orientations within the selected neighborhood.

Previous work utilized the eikonal model to assess methods for estimating CV [91, 95]. In the study by Nagel et al., the isotropic eikonal equation was solved using the fast marching method, demonstrating good accuracy in the results obtained from the RBF method [91]. In contrast, the current study employs the FIM to solve the anisotropic eikonal equation, highlighting the potential for significant estimation errors. Notably, this study focuses solely on errors arising from neglecting anisotropy, without accounting for inaccuracies in measurements or the calculation of AT. This omission suggests that errors in estimating CV using these methods in clinical practice may be even more severe.

Grandits et al. addressed CV estimation by using the anisotropic eikonal equation and the FIM, which particularly well-suited for managing anisotropic conditions [74, 95]. Similarly, the study in this thesis employs the anisotropic eikonal equation and utilizes the FIM as well.

However, the present work differs from their approach in its primary objective: calculating the optimal trajectory or characteristic direction of propagation, with less focus on the anisotropic tensor or longitudinal CV. Furthermore, while Grandits et al. proposed a method to estimate CV magnitude from AT maps, this thesis aims to provide ground truth data for evaluating such methods and emphasizes the importance of accurately accounting for anisotropy. In their related work, they employed the anisotropic eikonal equation to compute the CV wavefront propagation based on the actual CV direction using a modified version of the FIM. In contrast, this study adopts a version of the FIM that is closer to its classic form [96].

The approach of this thesis offers additional utility beyond parameter fitting in computer modeling, as it accounts for the effective CV of the wavefront in relation to each patient's personalized propagation sequence. This method may help identify areas of slow CV not only due to scar tissue but also because of abnormal propagation that occurs perpendicular to the preferential cardiomyocyte orientation.

The results of this work underscore that neglecting anisotropy is inadvisable in clinical practice, as it can lead to remarkable underestimations of CV magnitude and considerable errors in CV direction. Such misrepresentation may falsely indicate areas of slow CV, potentially resulting in incorrect ablation sites if clinical decisions were made based solely on these estimations. The modified FIM could serve as a valuable tool for quantifying these errors and enhancing the accuracy of RBF and other methods.

However, this study has some limitations. Notably, it did not consider multiple geometries to further validate the impact of anatomical variability. This study also neglected wall thickness, which can significantly influence conduction properties [97–99]. Future studies could investigate how various methods, particularly the more sophisticated methods incorporating machine learning, account for anisotropy [95, 100]. Furthermore, this study did not evaluate the robustness of AT measurements to errors, which is one of the advantages of the RBF method [91, 92, 98, 101]. Another important characteristic that should be considered in the future is the heterogeneity of CV, which was assumed homogeneous in the current study. Moving forward, the updated output from the eikonal model could be leveraged to assess new methods for estimating CV.

5.5 Conclusion

This study highlights the importance of accounting for anisotropy when estimating CV magnitude and direction. Assuming that propagation occurs perpendicular to the wavefront can lead to prominent underestimations of CV magnitude, potentially resulting in inappropriate clinical treatments. Nonetheless, this assumption can hold true in certain cases, such as for planar wavefronts moving in the direction of the preferential cardiomyocyte orientation, where the propagation is perpendicular to the wavefront. However, in more complex scenarios, such as those involving high anisotropy or curvatures, the propagation direction can deviate significantly from the gradient of activation times. Furthermore, incorporating the true CV direction, which represents the optimal trajectory of conduction, provides valuable insights into patient-specific activation sequences. This is particularly relevant in cases where abnormal rhythms favor propagation that deviates from the preferential cardiomyocyte orientation, such as in atrial fibrillation. Future research should aim to extend the application of this work by developing more advanced models that integrate anisotropy, machine learning, and robustness to measurement errors. Improving these methods can significantly enhance the characterization of patients at risk of arrhythmia, ultimately contributing to more effective and personalized therapeutic strategies.

PART III

DIFFUSION REACTION EIKONAL ALTERNANT MODEL

Chapter 6

Implementation of the Diffusion Reaction Eikonal Alternant Model

This chapter is dedicated to the implementation of the diffusion reaction eikonal alternant model (DREAM). This model combines the advantages of the eikonal model with an approximated reaction diffusion (RD) model to allow for reentries in anisotropic media while using the new cyclical FIM (cycFIM) to solve the eikonal equation. The first manuscript introduces the basic elements of the DREAM using a simple anatomical reentry to benchmark the first version of the DREAM with the monodomain model. In the second manuscript of this chapter, conduction velocity (CV) restitution is added to the DREAM to allow for functional reentry. The second version of the DREAM is further compared to the monodomain model in additional experiments including multiple stimulations, functional reentries in 2D sheets and in realistic left atrium geometries represented with a 2D-manifold.

The content of this chapter has been adapted from two manuscripts that have been previously published. The content has been quoted verbatim from these publications [22, 102]. The first manuscript was a conference paper presented at the Computing in Cardiology 2022 conference. The second manuscript is a journal paper that has been accepted for publication in Engineering with Computers. The author of this thesis, as the first author of these manuscripts, played a significant role in multiple steps of this research, as detailed in the author contributions section. Additionally, he was responsible for writing most of the code for the model, which was integrated into the publicly available openCARP framework. This integration not only made the model publicly available but also includes comprehensive documentation and tutorials to foster research and collaboration among scientists in the field [103, 104].

Diffusion Reaction Eikonal Alternant Model: Towards Fast Simulations of Complex Cardiac Arrhythmias

Cristian Barrios Espinosa[1], Jorge Sánchez[1,2], Olaf Dössel[1], Axel Loewe[1]

[1] Institute of Biomedical Engineering, Karlsruhe Institute of Technology (KIT), Karlsruhe, Germany
[2] ITACA Institute, Universitat Politècnica de València, Valencia, Spain

Abstract

Reaction-diffusion (RD) computer models are suitable to investigate the mechanisms of cardiac arrthymias but not directly applicable in clinical settings due to their computational cost. On the other hand, alternative faster eikonal models are incapable of reproducing reentrant activation when solved by iterative methods. The diffusion reaction eikonal alternant model (DREAM) is a new method in which eikonal and RD models are alternated to allow for reactivation. To solve the eikonal equation, the fast iterative method was modified and embedded into DREAM. Obtained activation times control transmembrane voltage courses in the RD model computing, while repolarization times are provided back to the eikonal model. For a planar wave-front in the center of a 2D patch, DREAM action potentials (APs) have a small overshoot in the upstroke compared to pure RD simulations (monodomain) but similar AP duration. DREAM conduction velocity does not increase near boundaries or stimulated areas as it occurs in RD. Anatomical reentry was reproduced with the S1-S2 protocol. This is the first time that an iterative method is used to solve the eikonal model in a version that admits reactivation. This method can facilitate uptake of computer models in clinical settings. Further improvements will allow to accurately represent even more complex patterns of arrhythmia.

1. Introduction

Reaction-diffusion (RD) computer models are suitable to investigate the mechanisms of cardiac arrhythmias but not directly applicable in clinical settings due to their computational cost. For instance, The monodomain equation correspond to one of the RD models in which equal extra and intracellular anisotropy ratios are assumed:

$$\beta C_\mathrm{m} \frac{\partial V_\mathrm{m}}{\partial t} = \nabla \cdot \sigma_\mathrm{m} \nabla V_\mathrm{m} - \beta (I_\mathrm{ion}(V_\mathrm{m}, \eta)) \qquad (1)$$

where β is the surface-to-volume ratio, C_m is the capacitance per unit area, V_m is the transmembrane voltage, σ_m is twice the harmonic mean of the extra and intracellular conductivities and, I_ion is the current density passing through the ionic channels that depends on state variables η.

Alternatively, numerical solutions of the eikonal equation are significantly faster than RD equations due to the simplicity of the eikonal equation and the relaxed mesh resolution requirements:

$$\sqrt{\nabla T^\top M \nabla T} = 1 \; , \qquad (2)$$

where M is the squared conduction velocity (CV) tensor and T is the mapping function between nodes' coordinates and their activation times (AT). The eikonal model provides a close approximation of electrical wave propagation under healthy conditions if only one activation cycle is represented. However, standard eikonal methods do not account for repolarization or reactivation of the cardiomyocytes. This limitation prevents the simulation of reentry, which is a major limitation in the context of complex arrhythmia. To overcome this problem, Pernod et al. and Gassa et al. introduced new methods based on a modified version the Fast Marching Method (FMM) to allow reactivation of the nodes while solving the eikonal equation [1, 2]. Nonetheless, numerical errors can appear when using single pass methods because the characteristics of the anisotropic Eikonal equation do not align with the gradient vector of its viscosity solution [3]. These numerical errors are more relevant in areas where the gradient of the wave-front does not match the characteristic of T. These errors do not decrease numerical stability and then can be unnoticed. Alternative methods have been proposed to solve the anisotropic eikonal equation such as the Fast Iterative Method (FIM) [4] and the Buffered Fast Marching Method [5].

There are two factors that hinder reproducing reentry with iterative solution methods. First, ATs can change several times while solving the eikonal equation iteratively unlike in single pass methods. Second, ATs and repolarization times (RTs) have a mutual dependency. The RT of every node in a given cycle depends on the effective refractory period and AT in the same cycle. Similarly, the AT depends on whether repolarization from the activation in previous cycle happens before or after an activation attempt. These two conditions are challenging for the calculation of the AT in the next cycle given that the AT from the first cycle is constantly being updated. Normally, the final converged ATs are only known at the end of the simulation. However, ATs are required earlier in the algorithm when simulating reentry. In this work, DREAM is introduced as a novel method to overcome this major limitation.

2. Methods

DREAM is a mixed model in which the RD model and the eikonal model are combined and alternated in time. The goal of this model is to accurately simulate reactivation patterns in low-resolution meshes where the RD model would fail (i.e. element size of 800 µm). DREAM is inspired by the reaction eikonal model [6] and the multi-frontal Fast Marching Method [1]. The FIM is used to solve the anisotropic eikonal equation.

Figure 1 shows the steps involved in DREAM. First, the FIM is iterated until the minimum AT of the nodes in the active list is greater than a given period of time τ_e (Figure 1, Step 1). Then, the calculated ATs are used to compute I_diff that approximates the diffusion current of a planar wavefront on a high resolution patch (element size of 200 µm) solved with the pure monodomain model [2]. I_diff is defined as a triple Gaussian function with parameters optimized to decrease the error between I_diff and the diffusion current in a high resolution mesh (Figure 2). Then, the RD model is computed by adding I_diff to the right hand side of the parabolic equation of the system (Figure 1, Step 2):

$$\beta C_\mathrm{m} \frac{\partial V_\mathrm{m}}{\partial t} = I_\mathrm{diff} - \beta(I_\mathrm{ion}(V_\mathrm{m}, \eta)) \tag{3}$$

similar to the RE$^-$ version of the reaction eikonal model [6].

To avoid conflict due to the constant updates of the ATs, the RD model is only computed until $t = \tau_\mathrm{e} - \tau_\mathrm{s}$, where τ_s is a ”safety margin” in time to assure that the nodes with ATs that belong to the interval $[0, \tau_\mathrm{e} - \tau_\mathrm{s}]$ are not affected by following iterations (Figure 1, Step 3). While the RD model is running, RTs are defined as the time points when the transmembrane voltage of an activated node X crosses the threshold $\nu_{th} = -70\,\mathrm{mV}$) to more negative values (Figure 1, Step 4).

It is possible that some activated nodes do not cross that threshold in the interval $[0, \tau_\mathrm{e} - \tau_\mathrm{s}]$. Nonetheless, their RTs are required to know whether they can be reactivated in the next FIM iteration. To solve this issue, the ionic model is used to approximate the V_m to obtain approximated RT ($\tilde{RT}$). The ionic model is run for $t \in [\tau_\mathrm{e} - \tau_\mathrm{s}, \min(\tilde{\mathrm{RT}}, 2\tau_\mathrm{e})]$. Once all the nodes are assigned with real or approximated RTs, the eikonal model runs again until the minimum AT of the nodes in the active list is greater than $2\tau_\mathrm{e}$. This process is repeated by alternating models until t reaches the end of the simulation time (Figure 1, Steps 5, 6, 7 and 8).

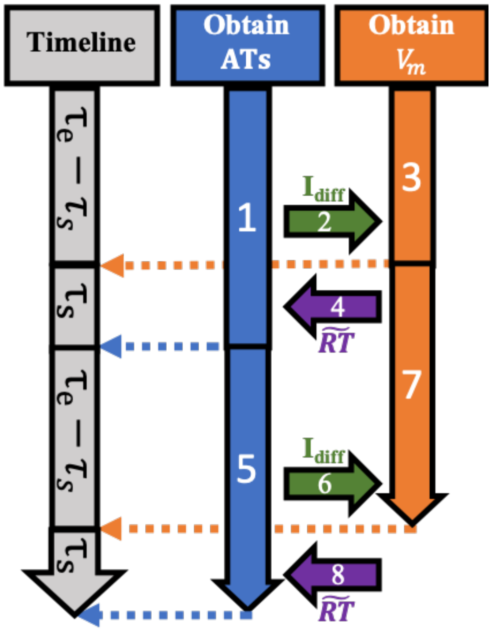

Figure 1. Steps of DREAM algorithm: Eikonal and RD models alternate to calculate ATs and V_m, respectively. ATs calculated with FIM are used to compute I_diff needed in the RD model. V_m calculated with the RD model is used to get real or approximated RTs needed in the FIM to solve eikonal equation. Numbers indicate the order in which DREAM runs every step, τ_e is the time period calculated by FIM every iteration, and τ_s is the safe margin of time to avoid conflicts between cycles

To test the model, two experiments were performed the first in a 2D patch and the second in a 3D ring. The 2D patch consisted of a triangular mesh of $5 \times 5\,\mathrm{cm}$ and resolutions of 200 µm and 800 µm for the RD model and DREAM, respectively. The planar waves were produced by stimulating one edge of the patch. The second stimulus was applied 400 ms after the first stimulus at the same location. The monodomain model was selected as the RD model. CV for DREAM was $1000\,\mathrm{mm\,s^{-1}}$ and the conductivities were tuned accordingly for the RD model. We chose the human atrial cell model suggested by Courtemanche et al. [7]. For the anatomical reentry in a 3D mesh, a ring-shaped mesh of tetrahedral elements was used. The average resolution in the ring was 576 µm) for both mod-

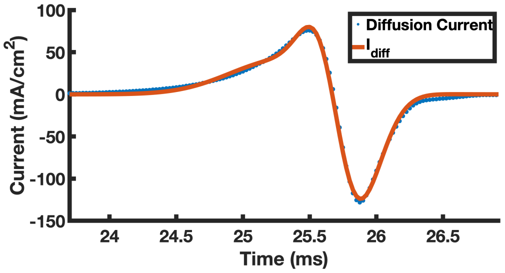

Figure 2. I_{diff} fitted to the diffusion current obtained from pure monodomain simulation of a planar wave on a high-resolution mesh. A triple Gaussian is used to approximate the diffusion current. AT $\approx$ $24\,\mathrm{ms}$.(Sample Frequency: $1\,\mathrm{kHz}$)

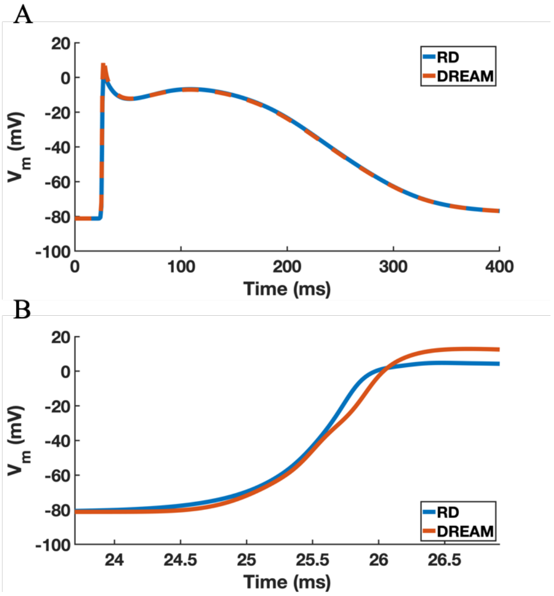

Figure 3. A) Complete APs of RD and DREAM for a node in the center of the mesh. B) AP upstroke (Sample Frequency: $4\,\mathrm{kHz}$).

els. The inner and outer diameters were 20 and $24\,\mathrm{mm}$ respectively. The CV in the longitudinal direction was $200\,\mathrm{mm\,s^{-1}}$ with an anisotropy ratio of 3. Monodomain conductivities were tuned to match these velocities. An S1-S2 protocol was used to induce unidirectional block followed by reentry. The first stimulus was applied at approximately 60° from the first stimulus and $328\,\mathrm{ms}$) later. The sample frequency was $1\,\mathrm{kHz}$ unless stated otherwise. All tissue simulations were performed using openCARP [8].

3. Results

In the RD model, wave propagation in the 2D high-resolution patch was accelerated close to the stimulated edge and the opposing mesh boundary. DREAM in the 2D low-resolution patch kept a constant CV everywhere. Figure 3 compares action potentials (APs) in both models. Action potential durations (APDs) difference between models was smaller than $1\,\mathrm{ms}$ (Figure 3A) and the upstroke was closely matching with a small overshoot in DREAM (Figure 3B). The CV after the second stimulus in DREAM model did not change while the APD shortened. In the RD model both APD and CV decreased as expected. If the time period between stimulus was prolonged to $1000\,\mathrm{ms}$, CV and APD did not change in both models (data not shown).

The experiment in the ring produced an anatomical reentry in both models. Figure 4 shows the maps of the last AT for each node at $850\,\mathrm{ms}$ in both models and the difference map between the two models. The reentry cycle length was $\approx$$320\,\mathrm{ms}$ at that moment. The cycle length in DREAM simulation remained constant over time while the cycle length in the RD model prolonged over time due to CV restitution. In the RD model (Figure 4A), these differences were smaller and the wave-front was almost perpendicular to the boundaries. In DREAM (Figure 4B), nodes located at the inner boundary had earlier ATs than the nodes located at the outer boundary at the same angle due to the shorter geodesic distance to the stimulus location. The difference map (Figure 4C) shows that propagation in the RD model accelerated at the outer boundary and slowed down at the inner boundary.

4. Discussion

DREAM features several characteristics from previously implemented eikonal models [1, 2, 6]. The novelty of this model lies in incorporating node reactivation while solving the eikonal equation with an iterative method. The FIM has the advantage of being more suitable for propagation in anisotropic media than single pass methods as FMM [4]. Additionally, the FIM can parallelize which would further increase computational speed in the future. The DREAM requires slightly longer computational times than the RD model when compared on the same mesh. However, computational speed is gained from the possibility to use the DREAM in coarse meshes in which the RD models diverge.

Our results show that reactivation patterns such as prepacing a 2D patch and anatomical reentries are possible. To reproduce physiological reentries, it is necessary to incorporate at least the influence of the diastolic interval on the CV [2, 9]. Nonetheless, additional factors (i.e. wall thickness, wave-front curvature, source-sink mismatch effects) that markedly affect CV should also be incorporated to accurately reproduce diseased conditions.

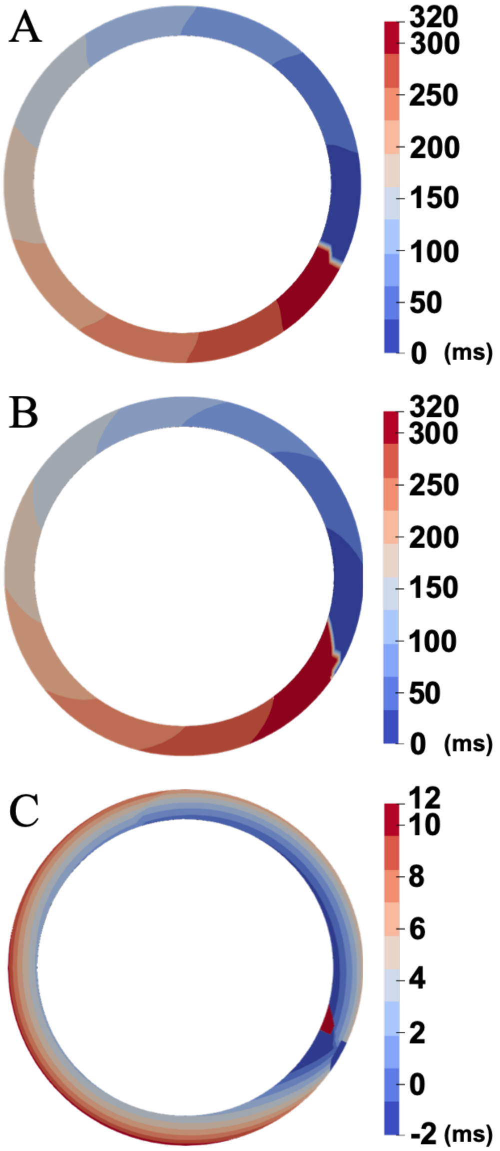

Figure 4. Anatomical reentry: A) ATs in the RD model (AT_{RD}). B) ATs in DREAM (AT_{DREAM}). C) Error map AT_{DREAM} - AT_{RD}.

Acknowledgments

This Project has received funding from the European Union's Horizon research and Innovation programme under the Marie Skłodowska-Curie grant agreement No. 860974. This work was supported by the European High-Performance Computing Joint Undertaking EuroHPC under grant agreement No 955495 (MICROCARD) co-funded by the Horizon 2020 programme of the European Union (EU), the French National Research Agency ANR, the German Federal Ministry of Education and Research, the Italian ministry of economic development, the Swiss State Secretariat for Education, Research and Innovation, the Austrian Research Promotion Agency FFG, and the Research Council of Norway.

References

[1] Pernod E, Sermesant M, Konukoglu E, Relan J, Delingette H, Ayache N. A multi-front eikonal model of cardiac electrophysiology for interactive simulation of radio-frequency ablation. Computers Graphics 2011;35(2):431–440.

[2] Gassa N, Zemzemi N, Corrado C, Coudière Y. Spiral waves generation using an eikonal-reaction cardiac electrophysiology model. In International Conference on Functional Imaging and Modeling of the Heart. Springer, 2021; 523–530.

[3] Sethian JA, Vladimirsky A. Ordered upwind methods for static hamilton–jacobi equations: Theory and algorithms. SIAM Journal on Numerical Analysis 2003;41(1):325–363.

[4] Fu Z, Kirby RM, Whitaker RT. A fast iterative method for solving the eikonal equation on tetrahedral domains. SIAM Journal on Scientific Computing 2013;35(5):C473–C494.

[5] Cristiani E. A fast marching method for hamilton-jacobi equations modeling monotone front propagations. Journal of Scientific Computing 2009;39(2):189–205.

[6] Neic A, Campos FO, Prassl AJ, Niederer SA, Bishop MJ, Vigmond EJ, Plank G. Efficient computation of electrograms and ecgs in human whole heart simulations using a reaction-eikonal model. Journal of Computational Physics 2017;346:191–211.

[7] Courtemanche M, Ramirez RJ, Nattel S. Ionic mechanisms underlying human atrial action potential properties: insights from a mathematical model. American Journal of Physiology Heart and Circulatory Physiology 1998;275(1):H301–H321.

[8] Plank G, Loewe A, Neic A, Augustin C, Huang YL, Gsell MA, Karabelas E, Nothstein M, Prassl AJ, Sánchez J, et al. The opencarp simulation environment for cardiac electrophysiology. Computer Methods and Programs in Biomedicine 2021;208:106223.

[9] Loewe A, Poremba E, Oesterlein T, Luik A, Schmitt C, Seemann G, Dössel O. Patient-Specific Identification of Atrial Flutter Vulnerability–A Computational Approach to Reveal Latent Reentry Pathways. Frontiers in Physiology 2019; 9:1910.

Address for correspondence:

Cristian Alberto Barrios Espinosa
Karlsruhe Institute of Technology (KIT)
Fritz-Haber-Weg 1, 76131 Karlsruhe, Germany
publications@ibt.kit.edu

A Cyclical Fast Iterative Method for Simulating Reentries in Cardiac Electrophysiology Using an Eikonal-Based Model

Cristian Barrios Espinosa[1], Jorge Sánchez [2],
Stephanie Appel[1], Silvia Becker[1,3], Jonathan Krauß[1],
Patricia Martínez Díaz[1], Laura Unger[1,4], Marie Houillon[1],
Axel Loewe[1]*

[1]Institute of Biomedical Engineering, Karlsruhe Institute of Technology (KIT), Karlsruhe, Germany.
[2]ITACA Institute, Universitat Politècnica de València, Valencia, Spain.
[3]Klinik für Kardiologie und Angiologie, Universitäts-Herzzentrum Freiburg - Bad Krozingen, Bad Krozingen, Germany.
[4]Medizinische Klinik IV, Städtisches Klinikum Karlsruhe, Karlsruhe, Germany.

*Corresponding author(s). E-mail(s): publications@ibt.kit.edu;

Abstract

Background: Computer models for simulating cardiac electrophysiology are valuable tools for research and clinical applications. Traditional reaction-diffusion (RD) models used for these purposes are computationally expensive. While eikonal models offer a faster alternative, they are not well-suited to study cardiac arrhythmias driven by reentrant activity. The present work extends the diffusion-reaction eikonal alternant model (DREAM), incorporating conduction velocity (CV) restitution for simulating complex cardiac arrhythmias.
Methods: The DREAM modifies the fast iterative method to model cyclical behavior, dynamic boundary conditions, and frequency-dependent anisotropic CV. Additionally, the model alternates with an approximated RD model, using a detailed ionic model for the reaction term and a triple-Gaussian to approximate the diffusion term. The DREAM and monodomain models were compared, simulating reentries in 2D manifolds with different resolutions.

Results: The DREAM produced similar results across all resolutions, while experiments with the monodomain model failed at lower resolutions. CV restitution curves obtained using the DREAM closely approximated those produced by the monodomain simulations. Reentry in 2D sheets yielded similar results in vulnerable window and mean reentry duration for low CV in both models. In the left atrium, most inducing points identified by the DREAM were also present in the high-resolution monodomain model. DREAM's reentry simulations on meshes with an average edge length of 1600 µm were 87x faster than monodomain simulations at 200 µm.

Conclusion: This work establishes the mathematical foundation for using the accelerated DREAM simulation method for cardiac electrophysiology. Cardiac research applications are enabled by a publicly available implementation in the openCARP simulator.

Keywords: Fast Iterative Method, Reaction Diffusion, Cardiac Electrophysiology, Reentries

1 Introduction

Computer models have provided meaningful contributions to better understand the mechanisms of cardiac arrhythmia [1, 2]. An emerging application of cardiac modeling are tissue-level simulations to guide treatments such as ablation procedures [3]. Tissue-level simulations can be performed using reaction diffusion (RD) or eikonal models [4, 5]. RD models accurately capture the complex interplay between ion channels, cellular, and tissue-level behavior [4, 6]. However, they often require significant computing time, even on high performance computing systems [2]. Therefore, these models are hardly compatible with clinical time frames for intraprocedural decision support. Eikonal models are an alternative to investigate cardiac arrhythmias [5, 7–9]. They can be 3 orders of magnitude faster than RD models and thus better suited for use in clinical settings (e.g. planning ablation procedures) or uncertainty quantification [10, 11]. However, various eikonal-based models encounter distinct challenges that impede their ability to accurately simulate cardiac arrhythmias. These challenges include the absence of repolarization and reactivation phenomena, inadequate representation of conduction velocity (CV) and action potential duration (APD) restitution (i.e., their dependence on activation frequency), and the utilization of numerical methods unsuitable for anisotropic propagation [5, 10, 12]. While not all eikonal-based models face all these limitations, a model capable of addressing these challenges simultaneously could provide a more suitable tool for studying arrhythmia compatible with clinical time frames.

Numerical solutions for the eikonal equation are computationally inexpensive due to its simple formulation and the low mesh resolution requirements. The simplest formulations of the eikonal model are only capable of simulating one activation per node. Consequently, these versions do not account for recovery or reactivation of the cardiomyocytes [10, 13]. This shortcoming hinders the simulation of reentrant activity, which is a major limitation in the context of simulating arrhythmia. To overcome this problem, Pernod et al. modified the fast marching method (FMM) to allow reactivation of the nodes while solving the eikonal equation [5]. Later, Gassa et al. extended the method to enable the simulation of rotors [14]. Nonetheless, when simulating anisotropic propagation in cardiac tissue using single pass methods like the regular FMM, numerical errors can arise because the gradient directions of the eikonal equation solution do not align with the characteristic directions (i.e., the optimal trajectories). This discrepancy affects the accurate depiction of anisotropic wave propagation dynamics, particularly in regions where these directions do not lie within the same simplex in the mesh discretization. Further limitations of single pass methods like FMM in anisotropic media are addressed in more detail by Sethian and Vladimirsky [15]. Alternative methods have been proposed to solve the anisotropic eikonal equation such as the fast iterative method (FIM), the buffered FMM, and the anisotropic FMM [5, 16, 17].

Neic et al. used the FIM to develop the reaction eikonal (RE) model, which incorporates repolarization by linking the eikonal equation with a detailed ionic model [10]. However, it lacks the capability to simulate reactivation and reentry. Later, Campos et al. employed the RE model in virtual induction and treatment of arrhythmias (VITA), a method to investigate ventricular tachycardia [18]. While VITA can identify areas in the heart susceptible to isthmus-dependent reentry, it can only simulate the first reentry cycle and disregards CV restitution and functional reentry.

Iterative methods to solve the anisotropic eikonal equation are challenging when simulating reactivation and reentry phenomena. There are 2 main factors hindering the accurate simulation of reentries using iterative solution methods. First, activation times (ATs) can undergo multiple changes while solving the eikonal equation iteratively unlike in single pass methods. Second, ATs and repolarization times (RTs), i.e. the time after which a node can be reactivated, have a mutual dependency. The RT of every node in a given activation cycle depends on the effective refractory period (ERP) and the AT in the same activation cycle. Similarly, the AT depends on whether a node has fully recovered from the previous cycle's activation before the next activation attempt. Managing these conditions becomes intricate when computing the AT for the next activation cycle while constantly updating the AT from the previous activation cycle. Another important factor to reproduce physiological reentries is to incorporate CV restitution. This phenomenon adds additional complexity as CV becomes dependent on the previous AT, rather than remaining constant. Therefore, a way to calculate the frequency-dependent CV in the eikonal model must be included in the method. This can be achieved by taking the diastolic interval (DI) of previous activation cycles in the node that is being activated, or by considering the DI of the neighboring nodes [12].

This study builds on an initial version of the diffusion reaction eikonal alternant model (DREAM) enabling reactivation in anisotropic media through the solution of the eikonal equation using the FIM [19]. The DREAM introduced a new strategy that alternates between the eikonal and RD models. In the proposed update of the DREAM, a novel approach to CV restitution ensures a coherent set of CV, DI, and AT values for each revised node during the present activation cycle. This work extends the DREAM by CV restitution properties while preserving the model's other advantages.

2 Propagation Models

2.1 Monodomain Model

RD models faithfully represent the propagation of the electrical wavefront through the cardiac tissue [20–22]. These models are the most detailed because they incorporate more physiological mechanisms than other available models. However, numerical methods used to solve the RD equations rely on high resolution meshes, which is the main cause for their high computational cost [4, 23]. The most common examples of RD models are the bidomain and the monodomain models [24]. In this work, the latter is used as control to benchmark the DREAM.

Derived from the bidomain equations, the monodomain model assumes equal intracellular and extracellular anisotropy ratios and is, therefore, computationally more efficient. This assumption does not hold true particularly in scenarios such as the simulation of defibrillation, where the dynamics in the extracellular space play a significant role [25]. However, for the majority of cardiac electrophysiology simulations, the monodomain model proved to be adequate due to its ability to capture various electrophysiological mechanisms accurately, such as source-sink mismatch effects [4, 24]. The equations of the bidomain model are condensed to the monodomain equation:

$$\beta C_\mathrm{m}\frac{\partial V_\mathrm{m}}{\partial t} = \nabla\cdot(\boldsymbol{\sigma}_\mathrm{m}\nabla V_\mathrm{m}) - \beta(I_\mathrm{ion}(V_\mathrm{m},\overrightarrow{\eta}) - I_\mathrm{s}) \qquad \text{on } \Omega\subset\mathbb{R}^3, \quad (1)$$

$$(\boldsymbol{\sigma}_\mathrm{m}\nabla V_\mathrm{m})\cdot\overrightarrow{n}_\mathrm{surf} = 0 \qquad \text{on } \delta\Omega, \quad (2)$$

where β is the surface-to-volume ratio, while C_m denotes the membrane capacitance. The transmembrane voltage is indicated by V_m and $\boldsymbol{\sigma}_\mathrm{m}$ represents the tissue conductivity tensor. The ionic transmembrane current density, denoted as I_ion, depends on V_m and the state variables $\overrightarrow{\eta}$, which determine the behavior of the ion channels in the cell membrane and the sarcoplasmic reticulum. Additionally, I_s is the transmembrane stimulus current density. The myocardium is represented by Ω. There is a non-flux boundary condition at $\delta\Omega$, the boundary of the domain Ω. The outward surface normal vector is represented by $\overrightarrow{n}_\mathrm{surf}$.

2.2 Eikonal Model

The anisotropic eikonal model, based on the macroscopic kinetics of wavefront propagation, seeks to determine the activation time (AT) of points within the myocardium through the following equation: [21, 22]:

$$\sqrt{\nabla T(X)^\top \mathbf{M}(X)\nabla T(X)} = 1 \qquad \forall X\in\Omega, \quad (3)$$

$$T(X) = T_i \qquad \forall X\in\Gamma_i\subset\Omega, \quad (4)$$

where $T:\Omega\to\mathbb{R}_{\geq 0}\cup\{\infty\}$, maps every point in the myocardium to its corresponding AT. Moreover, Γ_i denotes the subset of points in the myocardium where the i-th stimulus is applied at time $T_i\in\mathbb{R}_{\geq 0}$, for $i = 1,\ldots,n_s$, with $n_s\in\mathbb{N}$ representing the total number of stimuli. Additionally, if $T_i = T_j$ then $i = j$. $\mathbf{M} : \Omega \rightarrow \mathbb{R}^{3\times 3}$ maps points in the myocardium to their tensor of squared CV defined as:

$$\mathbf{M}(X) = (v_\mathrm{l}^2(X))\,\overrightarrow{l} \otimes \overrightarrow{l} + (v_\mathrm{t}^2(X))\,\overrightarrow{t} \otimes \overrightarrow{t} + (v_\mathrm{n}^2(X))\,\overrightarrow{n} \otimes \overrightarrow{n}. \tag{5}$$

Here, $\overrightarrow{l}$, $\overrightarrow{t}$, and $\overrightarrow{n}$ form an orthonormal system of vectors in the longitudinal, transversal, and sheet-normal directions, respectively. Importantly, $\overrightarrow{l}$ is aligned with the local preferential myocyte orientation. Furthermore, $v_\mathrm{l}, v_\mathrm{t}, v_\mathrm{n} : \Omega \rightarrow \mathbb{R}_{\geq 0}$ assign the CV values in their respective directions at X.

The FIM is an effective approach for solving the anisotropic eikonal equation as this algorithm is particularly suited for unstructured meshes and anisotropic local CV functions [16]. The single-thread version of the FIM is presented in Algorithm 1. Multi-thread versions are also available [16, 26, 27]. For this work, Ω is considered to be a 2D manifold embedded in $\mathbb{R}^3$. For this reason, it is assumed that $v_\mathrm{n} = v_\mathrm{t}$, however the effect of the normal component is small since most of the characteristic directions (i.e., optimal trajectories) are almost perpendicular to $\overrightarrow{n}$. To numerically approximate the viscosity solution of the eikonal equation, a triangulation $\mathcal{T} \subset \mathcal{P}(\Omega_\mathcal{T})$ is defined over a finite set of points $\Omega_\mathcal{T} \subset \Omega$, such that the convex hull of $\Omega_\mathcal{T}$ (i.e., the union of all triangles in $\mathcal{T}$) approximates Ω. The FIM approximates the viscosity solution of the eikonal equation only at the vertices of the triangles in $\mathcal{T}$ (i.e., points in $\Omega_\mathcal{T}$). When mentioning a node $X \in \Omega_\mathcal{T}$, we refer to both a vertex in the triangulation and its position in $\mathbb{R}^3$. This notation should not cause confusion, as each simulation in this work uses only a single mesh and coordinate system.

In the first step of the FIM, the boundary conditions of the system are defined by the AT of the source nodes (Eq. 4). Then, the neighbors of the nodes that belong to any Γ_i (for $i = 1, \ldots, n_s$) are included in a set of active nodes $L \subset \Omega_\mathcal{T}$, that is initialize as $\emptyset$, which contains the list of nodes that are being updated by the local solver. This local solver is referred to as the UPDATE() function. As soon as L is not empty, the list iteration begins. For each iteration, every node X in L is updated and the previous solution for its AT is replaced. If the difference between the old and the new solution is smaller than a certain threshold ε, the node is then removed from L and each of its neighbors, that are not presently in L, is analyzed. For each neighbor, a tentative new solution is calculated and only replaces the old solution if the new solution is smaller (i.e., earlier) than the old solution. If this condition is fulfilled, this neighbor is added to L. This process is repeated until L is empty.

When solving the eikonal equation on a triangular mesh, the local solver aims to determine the smallest AT that fits the eikonal equation at a specific node X. For this purpose, a tentative AT is calculated for every triangle containing X. Let (X, Y, Z) be a triangle in $\mathcal{T}$, with vertices $X, Y, Z \in \Omega_\mathcal{T}$:

Algorithm 1 Fast Iterative Method

```
$L = \emptyset$
for $X \in \Omega_{\mathcal{T}}$
    $T(X) \leftarrow \infty$
    for $i \in 1, \ldots, n_s$
        if $X \in \Gamma_i$
            $T(X) \leftarrow T_i$
            for adjacent neighbor $X_{\mathrm{NB}}$ of $X$
                add $X_{\mathrm{NB}}$ to $L$
            end for
        end if
    end for
end for
while $L \neq \emptyset$
    for $X \in L$
        $p \leftarrow T(X)$
        $q \leftarrow \mathrm{UPDATE}(X)$
        $T(X) \leftarrow q$
        if $|p - q| < \varepsilon$
            for adjacent neighbor $X_{\mathrm{NB}}$ of $X$
                if $X_{\mathrm{NB}}$ is not in $L$
                    $p \leftarrow T(X_{\mathrm{NB}})$
                    $q \leftarrow \mathrm{UPDATE}(X_{\mathrm{NB}})$
                    if $p > q$
                        $T(X_{\mathrm{NB}}) \leftarrow q$
                        add $X_{\mathrm{NB}}$ to $L$
                    end if
                end if
            end for
            remove $X$ from $L$
        end if
    end for
end while
```

$$
\begin{aligned}
T_{Y,Z}(X) &= \min_{\lambda \in [0,1]} \left(\lambda T(Y) + (1-\lambda) T(Z) + \frac{\sqrt{\overrightarrow{X_\lambda X}^\top \mathbf{D}(X)^{-1} \overrightarrow{X_\lambda X}}}{v_{\mathrm{l}}(X)} \right), \\
\overrightarrow{X_\lambda X} &= \lambda \overrightarrow{YX} + (1-\lambda) \overrightarrow{ZX}, \\
\mathbf{D}(X) &= \mathbf{M}(X) \cdot v_{\mathrm{l}}(X)^{-2},
\end{aligned}
\tag{6}
$$

where $T_{Y,Z}(X)$ is the tentative AT that is obtained if the characteristic direction lies within the triangle (X, Y, Z). Additionally, $\mathbf{D}(X)$ is a tensor that holds information about the anisotropy of conduction, and $v_\mathrm{l}(X)$ is the CV along the longitudinal direction at node X. Finally, UPDATE(X) is set as the minimum AT among all the tentative ATs calculated from each triangle containing X:

$$\mathrm{UPDATE}(X) = \min_{(X,Y,Z)\in\mathcal{T}} T_{Y,Z}(X). \tag{7}$$

2.3 Diffusion Reaction Eikonal Alternant Model (DREAM)

The DREAM is a mixed model combining an approximation of the RD model and the eikonal model. The goal of this model is to simulate reactivation patterns on meshes with lower resolutions than required for comparable simulations with RD models, thereby increasing computational efficiency. The DREAM is inspired by the RE model [10] and the multi-frontal FMM [5]. A modified version of the FIM, named cyclical FIM (cycFIM), was implemented to solve the anisotropic eikonal equation allowing reactivations by alternating with the approximated RD model (Section 2.3.1).

Fig. 1 shows a schematic representation of the steps involved in the DREAM. A single DREAM cycle encompasses the execution of steps A, B, C, and D where subscript indices represent the DREAM cycle's number. It is crucial to differentiate between the DREAM cycle, comprising steps A, B, C, and D as shown in Fig. 1b), and the concept of the activation cycle in cardiac tissue. Within a DREAM cycle, each call of the cycFIM is regarded as a cycFIM cycle, which computes one AT value per node for a subset of nodes. However, it is important to note that not every review of a node will result in an activation cycle for that node, as propagation failures can occur. Additionally, not more than one AT is calculated per DREAM cycle per node.

At first, the cycFIM applies the first stimulus (i.e., computes the first boundary condition) and iteratively reviews every node in L and updates the AT of each node by solving the eikonal equation. A list iteration refers to the process where each node in L is visited once. Therefore, every cycle encompasses one or more list iterations. At the end of each list iteration, t_min is the smallest absolute AT among all nodes in L. A parameter τ_inc is defined to limit the increment of t_min throughout the list iterations of a cycFIM. Once the total increment of t_min during a cycFIM cycle exceeds τ_inc, the cycFIM cycle ends (Fig. 1a), step A_1, Section 2.3.1). Hereby, τ_inc represents the increment of t_min each time cycFIM is called. Then, the determined ATs are used to calculate I_diff, which approximates the diffusion current expressed in the parabolic equation of the RD model. Then, I_diff triggers an action potential (AP) (Fig. 1a), step B_1 and Section 2.3.2), which allows to compute V_m in a low resolution mesh. The approximated RD model uses I_diff to compute V_m in all nodes of the mesh until $t = t_\mathrm{min} - \tau_\mathrm{s}$ (Fig. 1a), step C_1 and Section 2.3.3). τ_s is a safety margin in time, ensuring that only cells with converged ATs are stimulated by I_diff. Thereby, a reliable identification of repolarization times (RTs) is enabled. RTs are defined as the time points when V_m of an activated node X crosses the threshold of $-40\,\mathrm{mV}$ with a negative slope. If V_m in an activated node does not reach this threshold before $t = t_\mathrm{min} - \tau_\mathrm{s}$, the ionic model is run independently for that node to determine its RT (Fig. 1a), step D_1

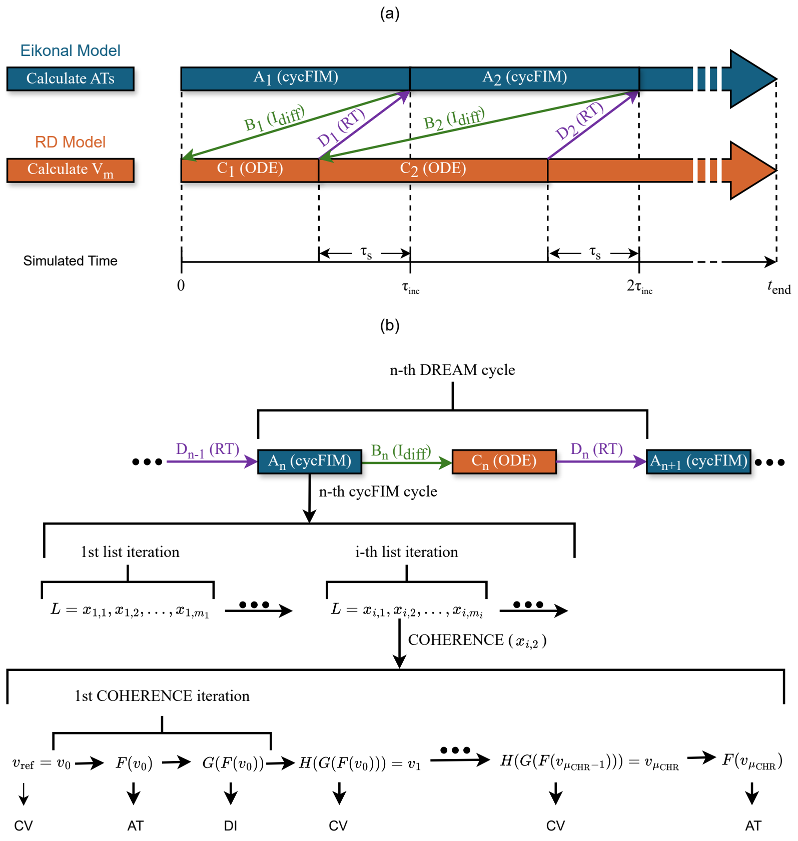

Fig. 1 **a)** Steps of the diffusion reaction eikonal alternant model (DREAM) algorithm in simulated time: eikonal model and approximated reaction diffusion (RD) model alternate to calculate activation times (ATs) and transmembrane voltages (V_m), respectively. The cyclical fast iterative method (cycFIM) is used to calculate ATs (steps A_n). These ATs are utilized to compute I_diff needed in the RD model (steps B_n). The approximated RD model determines V_m by solving the ODE system of the ionic model and incorporating I_diff (steps C_n). V_m is used to get the repolarization times (RT) needed in the cycFIM to allow for reactivation when solving the eikonal equation (steps D_n). The subscript index n represents the cycle number in the sequence. The parameter τ_inc represents the increment of t_min (minimum AT of the nodes in L) with each cycFIM cycle. If L is never empty between stimuli, t_min tends to align approximately with multiples of τ_inc. The parameter τ_s is the temporal safety margin to avoid conflicts between DREAM cycles. **b)** Steps of the DREAM algorithm, showing the sequence of a DREAM cycle. In step A_n, each call of the cycFIM is a cycFIM cycle, containing several list iterations. $x_{i,j}$ is the j-th node among m_i nodes in L at the start of the i-th iteration. Visiting a node calls COHERENCE(), leading to multiple COHERENCE() iterations. In each iteration, functions F, G, and H calculate AT, DI, and CV, respectively. After μ_CHR iterations, or upon convergence, the final output $F(v_{\mu_\mathrm{CHR}})$ is used by the cycFIM.

and Section 2.3.4). To start the next cycle in step A_2, the cycFIM iterates again until $t_{\text{min}} > t_{\text{min,init}} + \tau_{\text{inc}}$, where $t_{\text{min,init}}$ is the last calculated t_{min} of step A_1. Hereby, the previously calculated RTs are considered by cycFIM to check whether a node can be reactivated. Then, steps B_2, C_2, and D_2 are performed in the same manner as steps B_1, C_1, and D_1. This process is repeated until t reaches t_{end}, corresponding to the end of the simulation time. Table 1 shows the variables and parameters of the DREAM including their meaning and values used in this work. The code to run simulations using the DREAM is available in the openCARP simulator [28]. In the next sections, each of the steps is explained in more detail.

Table 1 DREAM parameters and variables: Absolute times denote specific time points, with values spanning over the entire duration of the simulation. Relative times, fixed and typically smaller, constrain the occurrence of absolute times within specified intervals. Maximum permitted iteration parameters set limits for iterative processes within the cyclical FIM.

Absolute times

Variable	Meaning	Value
t_{min}	Minimum AT of nodes in L at the end of each list iteration	(-)[1]
$t_{\text{min,init}}$	Last t_{min} from the previous DREAM cycle	(-)[1]
t	Current time step in RD model	(-)[1]
Parameter	**Meaning**	**Value**
t_{end}	End of simulation	(-)[2]

Relative times

Parameter	Meaning	Value
τ_{inc}	Maximum allowed increment of t_{min} in every DREAM cycle	100 ms
τ_{max}	Maximum allowed difference of AT values among nodes in L	10 ms
τ_{s}	Minimum allowed difference between t_{min} and t	10 ms
ε	Threshold of convergence	0.01 ms

Maximum iterations

Parameter	Meaning	Value
μ_{L_1}	Maximum number of list iterations per node per entry into L	50
μ_{L_2}	Maximum number of node returns to L per activation	50
μ_{CHR}	Maximum number of COHERENCE() iterations per node per call	50

[1] Variable values change throughout the simulation.

[2] t_{end} changes across experiments.

2.3.1 Cyclical Fast Iterative Method

The cycFIM is called in step A_n of the DREAM algorithm with $n \in \mathbb{N}$ representing the number of the cycle. Algorithm 2 describes this cycFIM. Some modifications were made to the single-thread FIM to allow alternation between the eikonal and RD models.

Firstly, the boundary conditions for the eikonal equation need to be dynamically applied as their effect on the system varies depending on the refractory state of the nodes receiving the stimuli. Secondly, list iterations should handle RT and manage multiple ATs per node. Thirdly, the local solver must ensure coherence among the CV, DI, and AT for each node. If L is emptied before all the boundary conditions are computed, further aspects must be considered since $t_{\min}$ does no longer align with multiples of τ_{inc}(see Section 2.3.5).

Dynamic Boundary Conditions

Dynamic boundary conditions handle stimuli applied to specific areas of the tissue. These conditions vary dynamically as they depend on the refractory state of stimulated nodes when stimuli are applied. Unlike conventional eikonal models where boundary conditions are computed a priori irrespective of their timing, the cycFIM computes boundary conditions (i.e, stimuli) progressively during the simulation. For this reason, to compute boundary conditions in the cycFIM the order in which stimuli are applied must be considered. Let $T_1 < T_2 < \ldots < T_{n_s}$ be the times when stimuli are applied, and let $\Gamma_1, \ldots, \Gamma_{n_s} \subset \Omega_{\mathcal{T}}$ be the respective subsets of nodes where this stimuli are applied. At the beginning of the n-th cycFIM cycle, let T_s, for $s \in \mathbb{N}$ and $1 \leq s \leq n_s$, be the time of the $s - th$ stimulus such that $T_1, \ldots, T_{s-1}$ have already been computed during the previous cycFIM cycles. Moreover, assume that $T_s, \ldots, T_{n_s}$ have not yet been computed. Therefore, T_s denotes the time of the earliest stimulus that has yet to be processed. Boundary conditions might be computed in 2 scenarios: at the beginning of each cycle if L is empty, or at the beginning of each list iteration if L is not empty.

In the first case, L can be empty for 2 reasons: the simulation has just started and $n = s = 1$ (i.e., the first stimulus must be computed during the first cycFIM cycle), or all activation times (ATs) associated with activation waves triggered by stimuli applied before T_s have converged, and L was emptied during the $(n-1)$-th cycFIM cycle. To incorporate new nodes into L and start a new list iteration, the s-th stimulus must be computed. In the second case, L is not empty and new stimuli might be applied. For instance, if T_s falls within the range of allowed activation times (ATs) for the nodes in L during this cycFIM cycle (i.e., $T_s \in [t_{\min,\text{init}}, t_{\min,\text{init}} + \tau_{\text{inc}} + \tau_{\max}]$), then the s-th stimulus can be computed. The parameter $\tau_{\max}$ which imposes an upper limit on the ATs of nodes in L will be explained in greater detail in the following subsection. Additionally, all the subsequent stimuli which times $T_{s+1}, T_{s+2}, \ldots$ are within this range, can be computed together.

To compute the s-th stimulus in both aforementioned cases, each node where the stimulus is applied is considered independently. Let $X \in \Gamma_s$ be a node where the s-th stimulus is applied at time T_s, and let $T(X)$ and $R(X)$ be its last computed AT and RT, respectively. Then, T_s is assigned to $T(X)$ if one of the following conditions is fulfilled:

$$(T(X) < R(X) < T_s) \vee (R(X) < T_s < T(X)) \,. \tag{8}$$

In the first condition, the calculation for the present activation of X has not yet begun and that is the reason why $T(X) < R(X)$. In that case, the solution $T(X)$ is replaced if $T_s > R(X)$, indicating that at T_s, the node has already recovered from the previous activation and is ready to be activated again. In the second condition, $R(X) <$

$T(X)$, i.e., the calculation for the present activation for X has already begun and it is still converging. The solution is updated if $R(X) < T_s$ signifying that the node X is ready to be activated at T_s and $T_s < T(X)$, which means T_s is a better (i.e., earlier) solution. The nodes with replaced ATs are removed from L, while their neighbors are added to L. To faithfully represent occurrence of unidirectional propagation, nodes that are successfully activated by a given stimulus cannot continue to activate nodes where an activation by this stimulus was unsuccessful before.

List Iteration

The variable $t_{\text{min,init}}$ represents the minimum AT among the nodes in L reached at the end of the previous DREAM cycle. When L is not empty after computing the first stimulus, $t_{\text{min,init}}$ is initialized to 0 during the first call of cycFIM in the first cycle, or adjusted to the value of t_{min} calculated at the end of step A_{n-1} if $n > 1$. Additionally, $t_{\text{min,init}}$ serves as a reference to be compared to t_{min}, the smallest AT in L at the end of the previous cycFIM cycle. L undergoes multiple iterations until $t_{\text{min}} > t_{\text{min,init}} + \tau_{\text{inc}}$. Then, the function COHERENCE() (see next subsection) is applied to each node in L. Let X be the node that is being revised and $T(X)$ and $R(X)$ its last computed AT and RT, respectively. Then, a new solution q is computed by COHERENCE(X) to potentially replace $T(X)$. If the difference between the old and new AT is smaller than the threshold ε, or either the old or the new solution is infinite, then X is removed from L. To avoid that a node is activated twice in the same iteration of the list, an upper bound τ_{max} is applied to the difference between the maximum AT of the nodes in L and t_{min}. If a certain node has a calculated AT above the maximum allowed AT for a given iteration of cycFIM, i.e., $q > t_{\text{min,init}} + \tau_{\text{inc}} + \tau_{\text{max}}$, then this node will not be removed from L and its neighbors will not be visited yet.

When a node is removed from L, its neighbors that are not in L are revised as well. Let X_{NB} be a neighbor of X with last computed AT and RT being $T(X_{\text{NB}})$ and $R(X_{\text{NB}})$, respectively. If X_{NB} is not in L and a new solution q_{NB} is computed, one of the following conditions (similar to those for stimuli) must be fulfilled for q_{NB} to replace $T(X_{\text{NB}})$:

$$(T(X_{\text{NB}}) < R(X_{\text{NB}}) < q_{\text{NB}}) \vee (R(X_{\text{NB}}) < q_{\text{NB}} < T(X_{\text{NB}}))\,. \tag{9}$$

In the first condition, the calculation for the present activation of X_{NB} has not yet begun. In that case, the solution is replaced (i.e., q_{NB} is assigned as a new tentative AT for X_{NB}) if $q_{\text{NB}} > R(X_{\text{NB}})$, meaning that the node has recovered at q_{NB}. In the second condition, $R(X_{\text{NB}}) < T(X_{\text{NB}})$, i.e., calculation of the present activation has already started for X_{NB} and is still converging. The solution is replaced if $\text{RT}_{X_{\text{NB}}} < q_{\text{NB}} < T(X_{\text{NB}})$, which means that the node is ready to be activated at q_{NB} and q_{NB} is a better (i.e., earlier) solution. If q_{NB} satisfies either of these two conditions and replaces $T(X_{\text{NB}})$, then X_{NB} is added to the list of active nodes, L. Regardless of the previous conditions, if q_{NB} is infinite or smaller than t, X_{NB} will not be added to L. When all the nodes in L and the neighbors of converging nodes have been revised, t_{min} is recalculated to decide whether further iterations are required in step A_n. To reduce the computational cost and to prevent nodes from indefinitely exiting and returning to L or iterating inside of L, 2 limits were defined: μ_{L_1} and μ_{L_2}. The parameter μ_{L_1} represents the maximum number of list iterations per node per entry into L, and μ_{L_2}, denotes the maximum number of returns to L per node per activation.

Algorithm 2 Cyclical Fast Iterative Method within the n-th DREAM cycle

```
if $L = \emptyset$
    Compute boundary conditions
end if
if $n = 0$
    $t_{\mathrm{min,init}} = 0$
else
    $t_{\mathrm{min,init}} = t_{\mathrm{min}}$
end if
repeat
    Compute boundary conditions
    for $X \in L$
        $p \leftarrow T(X)$
        $q \leftarrow$ COHERENCE($X$)
        $T(X) \leftarrow q$
        if $|p - q| < \varepsilon$
            for adjacent neighbor $X_{\mathrm{NB}}$ of $X$
                if $X_{\mathrm{NB}}$ is not in $L$
                    $p \leftarrow T(X_{\mathrm{NB}})$
                    $q_{\mathrm{NB}} \leftarrow$ COHERENCE($X_{\mathrm{NB}}$)
                    if $(p < R(X_{\mathrm{NB}}) < q_{\mathrm{NB}} \lor R(X_{\mathrm{NB}}) < q_{\mathrm{NB}} < p) \land (t < q_{\mathrm{NB}} < \infty)$
                        $T(X_{\mathrm{NB}}) \leftarrow q_{\mathrm{NB}}$
                        add $X_{\mathrm{NB}}$ to $L$
                    end if
                end if
            end for
            remove $X$ from $L$
        end if
    end for
    $t_{\mathrm{min}} = \min\{T(X) | X \in L\}$
until $L = \emptyset$ OR $(t_{\mathrm{min}} - t_{\mathrm{min,init}}) \geq \tau_{\mathrm{inc}}$
```

Coherence Between Conduction Velocity, Diastolic Interval and Activation Time

The local solver for the DREAM seeks to calculate the AT for each node. Unlike the standard eikonal model, the DREAM accounts for the CV restitution at each node in each activation cycle instead of a fixed CV. To implement CV restitution, the function UPDATE() in Algorithm 1 is replaced by a new function COHERENCE() in

Algorithm 2. The CV restitution is incorporated in the model by providing a template restitution curve, for example calculated from monodomain model simulations or inferred from clinical data [7]. To integrate this CV restitution phenomenon into the DREAM, the feedback loop among AT, CV, and DI must be acknowledged. This feedback loop means that calculating the AT depends on the CV, which relies on the DI, which in turn is influenced by the AT.

When applying the COHERENCE() function to a given node X, the reference CV of X, the RT of X from the previous activation, and ATs of the neighboring nodes in the present activation are known. The reference CV corresponds to the maximum possible CV, i.e. $v_l(X)$ when the DI is sufficiently long and CV becomes unaffected by restitution effects. Restitution curves with biphasic behavior, where the maximum CV is reached at intermediate DIs instead of long DIs, are excluded from this method. If an initial AT is estimated using the highest value of the reference CV, this AT will have the smallest (i.e., earliest) possible value, resulting in the shortest possible DI. If this DI is short, when applying the restitution curve, this leads to a slower CV than the reference CV and therefore in a higher (i.e., later) AT than the initially estimated AT. To calculate a tentative AT for X, the COHERENCE() function is utilized to iteratively recalculate CV, DI, and AT until a stable state of coherence between these 3 variables is reached. Note that these temporary values of the 3 variables are referring to the present activation of X. These 3 values are recalculated in each COHERENCE() iteration (not to be confused with list iteration see Fig. 1b). Each application of the local solver involves one or more COHERENCE() iterations, starting with the reference CV and ending with a tentative value for $T(X)$ to be used in cycFIM. Additionally, the term CV can refer to the speed of the wavefront itself, the longitudinal CV when the wavefront moves in the preferential cardiomyocyte orientation, or the transversal CV when the wavefront moves perpendicularly to this orientation. Although the COHERENCE() function utilizes the longitudinal CV (i.e., $v_l(X)$) for its computation and equilibrium is reached among AT, DI, and longitudinal CV, this equilibrium also extends to the wavefront's CV.

COHERENCE() calculates the tentative AT of X using the functions F, G and H. Each of these functions also depends on X. To simplify notation, X as an argument of these functions will be omitted. Let $F : \mathbb{R}_{\geq 0} \to \mathbb{R}_{\geq 0} \cup \{\infty\}$ be the function that computes the AT from the CV:

$$F(v^*) = t^*, \tag{10}$$

where v^* is a temporary value for $v_l(X)$ and t^* is a temporary solution to the eikonal equation (Eq. 3) at node $X \in \Omega$ providing a tentative AT for this node. To solve the eikonal equation, Eq. 6 is used to collect all tentative candidates for t^*. The function F is similar to the UPDATE() function of FIM but considers additional conditions. Propagation block can occur in cycFIM, implying that $v = 0$, thus $F(0) = \infty$. On the other hand, when taking into account the neighboring nodes Y and Z for Eq. 6, the triangle XYZ is not considered if $R(Y) > T(Y)$ or $R(Z) > T(Z)$. This implies that the ATs for these nodes are not yet computed for the present activation cycle and, therefore, must be excluded from the calculation of t^*. Figure 2a shows a schematic representation of function F()'s morphology.

Now, let $G : \mathbb{R}_{\geq 0} \cup \{\infty\} \rightarrow \mathbb{R}_{\geq 0} \cup \{\infty\}$ be the function that computes the DI from t^*:

$$G(t^*) = d^* = t^* - R(X), \tag{11}$$

where $R(X)$ is the RT of node X from the previous activation cycle and d^* is a temporary value for DI in the present activation cycle. Figure 2b shows a schematic representation of function G()'s morphology.

Finally, let $H : \mathbb{R}_{\geq 0} \cup \{\infty\} \rightarrow \mathbb{R}_{\geq 0}$ be the function that computes the new temporary CV v^* from the temporary DI d^*:

$$H(d^*) = v^* = \begin{cases} v_{\text{ref}} \cdot \left(1 - \rho \cdot e^{-\frac{\log(\rho)}{\psi}(d^* + \kappa)}\right) & \text{if } d^* > \theta, \\ 0 & \text{if } d^* \leq \theta. \end{cases} \tag{12}$$

Here, v_{ref} represents the reference CV, while ρ, κ, θ, and ψ are predefined parameters chosen to fit restitution curves for example obtained from monodomain simulations. The formulation in Eq. 12 allows expressing the steepness of the restitution curve in terms of ρ, the shift in the x-axis (i.e., DI) in κ and the shortest propagating DI in θ. Figure 2c shows a schematic representation of function H()'s morphology.

A recursive sequence (v_i) can be defined using the composition of the functions H, G and F:

$$\begin{aligned} v_0 &= v_{\text{ref}}, \\ v_{n+1} &= H(G(F(v_n))). \end{aligned} \tag{13}$$

The COHERENCE() function approximates the AT that corresponds to the CV value which is the limit of the sequence defined in Eq. 13:

$$\text{COHERENCE}(X) \approx F(\lim_{n \to \infty} v_n). \tag{14}$$

Since we cannot calculate this limit analytically, the function is defined as:

$$\text{COHERENCE}(X) = F(v_m) \text{ such that } |F(v_m) - F(v_{m-1})| < \varepsilon \text{ OR } m = \mu_{\text{CHR}}, \tag{15}$$

where μ_{CHR} is the maximum number of COHERENCE() iterations allowed per call. Fig. 2 illustrates an example of one COHERENCE() call with 3 iterations. The input and first element of the sequence is $v_0 = v_{\text{ref}}$, and the final output is $F(v_3)$, representing the AT calculated with v_3, corresponding to the CV obtained in the third iteration. This ensures that $|F(v_3) - F(v_2)| < \varepsilon$. The function typically converges quickly, often within 2 iterations, but an extreme case close to propagation failure was chosen in the example to demonstrate the convergence process more clearly. Moreover, the example was chosen to ensure that the function F has its simplest form, $t^* = a + \frac{b}{v^*}$, where a is the minimum AT among the neighbors of X, and b is the minimum possible value for $(\overrightarrow{X_\lambda X}^\top \mathbf{D}^{-1} \overrightarrow{X_\lambda X})^{\frac{1}{2}}$ in Eq. 6 among all triangles in $\mathcal{T}$ containing X and all $\lambda \in [0, 1]$ (Fig. 2a). If $\mathbf{D}$ is the identity matrix (i.e, in the isotropic case), then b is the minimum Euclidean distance between X and the perimeter of the polygon formed from the union of all triangles containing X. In this example, the function F is monotonically decreasing, continuous, and differentiable within $(0, +\infty)$. For this to occur, the neighboring node with the minimum AT must belong to the triangle where the minimum $(\overrightarrow{X_\lambda X}^\top \mathbf{D}^{-1} \overrightarrow{X_\lambda X})^{\frac{1}{2}}$ is found. In the general case where this condition is not necessarily met, the function F remains monotonous and continuous but may not be differentiable everywhere. Additionally, $F(v^*)$ tends to $+\infty$ as v^* approaches 0, and $F(v^*)$ tends to a as v^* approaches $+\infty$ for any situation.

The proof of convergence of the sequence described in Eq. 13 is based on the idea that the sequence can be partitioned into 2 converging subsequences: one increasing (v_{2n}) and the other decreasing (v_{2n+1}). Furthermore, these subsequences are bounded between v_0 and v_1, and the difference between v_n and v_{n+1} diminishes as n approaches infinity. In some cases, the sequence might need to take values of the DI below the parameter θ before converging. Therefore, when computing COHERENCE(), DI values below θ are allowed as long as the final DI is larger than θ, otherwise COHERENCE$(X) = \infty$.

2.3.2 Approximation of the Diffusion Current

To allow for V_m calculation in coarse meshes, a current I_diff was introduced following the idea of the RE model [10]. In step B_n, I_diff is computed by approximating $\nabla \cdot (\boldsymbol{\sigma}_\mathrm{m} \nabla V_\mathrm{m})$ in Eq. 1. A similar approach is used in the eikonal model by Gassa et al. [14]. In the DREAM, I_diff is defined as a triple Gaussian function:

$$\nabla \cdot (\boldsymbol{\sigma}_\mathrm{m} \nabla V_\mathrm{m})\Big|_X \approx I_\mathrm{diff}(X) = \sum_{i=1}^{3} \alpha_i \exp\left(-\frac{(t - T(X) - \beta_i)^2}{\gamma_i^2}\right), \tag{16}$$

where the parameters α_i, β_i and, γ_i are optimized to reduce the difference between I_diff and the diffusion current specific to the used ionic model. A high-resolution mesh (i.e., average edge length 200 µm) was used to run a monodomain simulation in the optimization process. A planar wavefront was simulated by stimulating at the mesh border. The conductivities were adjusted to obtain a CV of 1000 mm/s. The diffusion current was calculated at a node located far from the boundaries and the stimulus location. I_diff serves as a trigger for an AP, regardless of whether the activation is initiated directly by a stimulus or through diffusion from neighboring nodes. Figure 3 presents the fit of the triple Gaussian model, using the parameters listed in Table 2, to the diffusion current obtained from the monodomain simulation as described above. Since the ionic models by Courtemanche et al. and Bueno-Orovio et al. yield AP and diffusion currents with similar morphology, the same set of parameters was used for I_diff with both models.

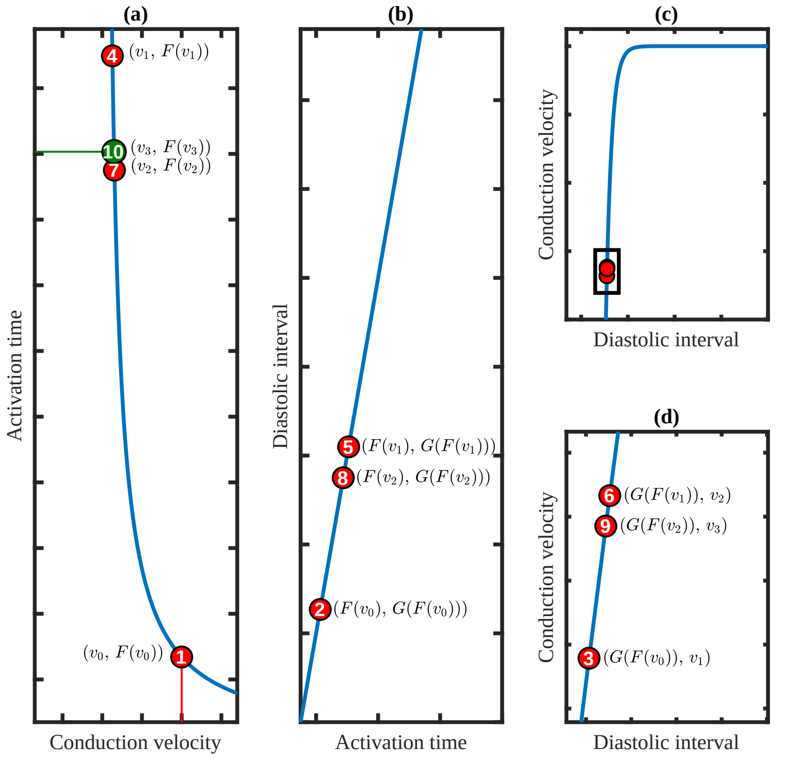

Fig. 2 COHERENCE() call with 3 iterations. Numbers indicate the sequence in which activation times (ATs), diastolic intervals (DIs), and conduction velocities (CVs) are calculated. Red circles correspond to temporary values and the green circle indicates the final output. **a)** Function F mapping CV to AT. The vertical red line marks the initial input of COHERENCE() (i.e., $v_{\text{ref}} = v_0$) on the horizontal axis. The green red line marks the final output of COHERENCE() (i.e, $F(v_3)$) on the vertical axis, **b)** Function G mapping AT to DI, **c)** Function H mapping DI to CV, **d)** Zoom-in of the boxed area in **c)**, illustrating temporary DI and CV values.

2.3.3 Approximated Reaction Diffusion Model

After the n-th cycFIM cycle is finished and I_{diff} is computed, the approximated RD model will run (i.e., step C_n). The time interval for this step is: $[t_{\text{min,init}} - \tau_{\text{s}}, \min(t_{\text{min}} - \tau_{\text{s}}, t_{\text{end}})]$ ensuring that the nodes that trigger an AP during this step have converged ATs. The diffusion term in the parabolic equation of the RD system is replaced by I_{diff}:

$$\beta C_{\text{m}} \frac{\partial V_{\text{m}}}{\partial t} = I_{\text{diff}} - \beta I_{\text{ion}}(V_{\text{m}}, \overrightarrow{\eta}). \tag{17}$$

In this case, the diffusion current is approximated by I_{diff} and only the reaction (ODE) part of the RD system remains to be solved. Solving this ODE system independently for each node in $\Omega_{\mathcal{T}}$ will yield the values for V_{m} within the interval $[t_{\text{min,init}} - \tau_{\text{s}}, \min(t_{\text{min}} - \tau_{\text{s}}, t_{\text{end}})]$.

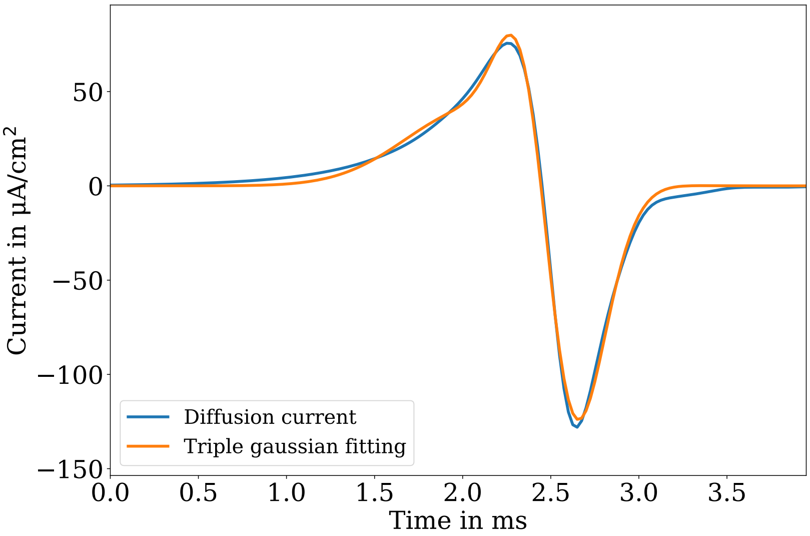

Fig. 3 I_{diff} fitted to the diffusion current obtained from a pure monodomain simulation of a planar wave on a high-resolution mesh. A triple Gaussian was used to approximate the diffusion current. Adapted from [19].

Table 2 Diffusion parameters I_{diff} for the models by Courtemanche et al., Bueno-Orovio et al., and Mitchell & Schaeffer used in the DREAM simulations, corresponding to each of the three Gaussian indices i.

Parameter	i	Courtemanche et al./Bueno-Orovio et al.	Mitchell & Schaeffer
α_i (µA/cm^2)	1	149.5	17.59
	2	41.2	-228.91
	3	-192.2	218.50
β_i (ms)	1	2.383	4.92
	2	2.07	5.19
	3	2.56	5.08
γ_i (ms)	1	0.22	0.49
	2	0.56	0.92
	3	0.29	0.92

2.3.4 Identification of Repolarization Times

Before the $(n+1)$-th cycFIM cycle starts, it is important to identify which nodes and when are available for reactivation. Ideally, V_{m} of every activated node would reach its RT during step C$_n$. However, recently activated nodes will not have recovered at the end of this RD iteration (i.e., at $t_{\min} - \tau_{\mathrm{s}}$). The aim in step D$_n$ is to compute RTs of these nodes. To obtain these times, the ODEs of the single cell models are integrated in time until the threshold $-40\,\mathrm{mV}$ is crossed:

$$C_{\mathrm{m}} \frac{\mathrm{d}V_{\mathrm{m}}}{\mathrm{d}t} = -I_{\mathrm{ion}}(V_{\mathrm{m}}, \overrightarrow{\eta}). \tag{18}$$

This process is implemented for each node that was depolarized but not yet repolarized in the previous step. The initial conditions are defined by the state variables at $t = t_{\mathrm{min}} - \tau_{\mathrm{s}}$ for each node. After the RT is calculated, V_{m} and $\overrightarrow{\eta}$ are reset to the values they had at $t = t_{\mathrm{min}} - \tau_{\mathrm{s}}$.

2.3.5 Considerations for Empty List Scenarios

Additional considerations are required if L is empty but not all the boundary conditions have been computed. Let T_s be the time when the next stimulus will be applied, then V_{m} is computed until $t = T_s - \tau_{\mathrm{s}}$. After identifying the RTs, the stimulus at T_s must be computed before iterating cycFIM again as detailed in Section 2.3.1. If L is not empty after computing the stimulus, cycFIM iterates until $t_{\mathrm{min}} > T_s + \tau_{\mathrm{inc}}$. Given that the list was empty at the end of the previous cycle, it is no longer feasible to establish $t_{\mathrm{min,init}}$. Hence, T_s is employed as the reference $t_{\mathrm{min,init}}$ to monitor the increment of t_{min}. If all nodes in Γ_s (i.e., the region in which the s-th stimulus is applied) are in the refractory period at time T_s, the list will remain empty. In that case, V_{m} is computed until $t = T_{s+1} - \tau_{\mathrm{s}}$, where T_{s+1} is the time of the $(s+1)$-th stimulus. If necessary, subsequent boundary conditions (i.e., stimuli applied at times $T_{s+2}, \ldots, T_{n_s}$) are computed until the list L gain nodes or $t = t_{\mathrm{end}}$.

3 Benchmarking

To assess the DREAM, it was compared with the monodomain model in 3 numerical experiments. First, multiple simulations were run on a 2D rectangular tissue mesh, each with 2 consecutive planar wavefronts per pacing cycle length (PCL) (i.e., interval between wavefronts). The PCL was varied across simulations to analyze CV restitution curves. In the second numercial experiment, functional reentry was examined in absence of structural abnormalities, i.e. their occurrence attributed solely to slow CVs and short ERPs. These reentries were induced using an S1-S2 protocol in a 2D square mesh. In the third numerical experiment, the pacing at the end of the effective refractory period (PEERP) protocol was used to investigate reentry in a realistic geometry of a left atrium [29]. These 3 numerical experiments were conducted using meshes composed of triangular elements with 4 different resolutions. The average edge lengths were 200, 400, 800, and 1600 µm. To facilitate the comparison between different meshes, each node in the lower resolution meshes was mapped to a corresponding node at the same position in the higher resolution meshes. To execute monodomain simulations, tissue conductivities were adjusted to match the CV values desired for each scenario [30, 31]. Anisotropy ratios were set to 4 and 2 for tissue conductivity and CV respectively. The Courtemanche et al. model with standard parameters was used to represent the healthy ionic behavior of atrial cardiomyocytes in the three numerical experiments [32]. On the other hand, atrial fibrillation (AF) was modeled by modifying ion channel conductances of the Courtemanche et al. model [33].To additionally assess the compatibility of the DREAM with different ionic models, the first numerical experiment (i.e., 2D rectangular tissue mesh) was also computed utilizing the simplified ionic models of Bueno-Orovio et al. [34] and Mitchell & Schaeffer [35]. These ionic models were originally developed for ventricles. Therefore, their parameters were adapted for atrial tissue to reflect cellular behavior of healthy and AF remodeled cardiomyocytes. The Bueno-Orovio et al. model was modified as proposed by Lenk et al. [36] providing parameter sets for both conditions. The Mitchell & Schaeffer ionic model was adjusted according to Gassa et al. [14] for healthy atrial cardiomyocytes and case 3 in Corrado et al. [37] for AF remodeled cardiomyocytes.

CV restitution curve parameters ρ, κ, and θ (Eq. 12) were tuned to align the CV restitution curve of the DREAM with either healthy or AF in monodomain simulations. This adjustment was based on the CV restitution curves obtained from monodomain simulations in a mesh with an average edge length of 200 µm (i.e., high resolution mesh) with 2 planar wavefronts resulting in the parameters in Table 3.

The Crank-Nicolson method was used to solve the parabolic equation of the monodomain model. Moreover, the methods described in Section 2.3 were used to solve the eikonal equation and approximate the diffusion current in the DREAM. The ODEs of the ionic model were solved using the forward Euler method for V_m and the Rush-Larsen method for the gating variables in both the monodomain model and the DREAM.

Sheet geometries were created using Gmsh [38] and processed with ParaView [39], Meshmixer [40] and MeshLab [41]. openCARP [30] was used to run simulations with both the DREAM and monodomain model. Plots were generated using the Python library matplotlib [42].

Specifically, the optimization of I_diff parameters was performed using MATLAB, utilizing the curve fitting toolbox. The optimization of the CV restitution parameters was conducted in Python, employing the *minimize* function from SciPy's optimize package [43]. In both optimization processes, the root mean square error was used as a loss function.

3.1 Multiple Stimulations and CV Restitution

To assess the DREAM's ability to faithfully replicate CV restitution, we initially examined its capacity to simulate paced beats across a range of frequencies specific for each condition. These experiments were conducted in a rectangular mesh of 50 mm × 10 mm × 0 mm, with the centroid of the mesh located at (0 µm, 0 µm, 0 µm) for each of the 4 resolutions. Preferential cardiomyocyte orientation was set as constant everywhere in the geometry and aligned with the x-axis (i.e., $\overrightarrow{l} = (1, 0, 0)$). Each experiment involved pre-pacing at a single-cell level for 50 activation cycles at a cycle length of 250 ms. For monodomain simulations, conductivities were tuned to match the target CV of 1000 mm/s.

In this numerical experiment, 2 planar wavefronts were generated for each PCL by stimulating the left side of the mesh with different frequencies. For monodomain simulations, the stimulus was applied as a transmembrane current density with an amplitude of 300 µA/cm^2 for a duration of 2 ms. For the healthy atrial electrophysiology condition with the ionic model of Courtemanche et al., the PCL was decreased in 50 ms intervals from 950 ms to 400 ms, then in 10 ms intervals from 390 ms to 320 ms,

Table 3 Conduction velocity restitution parameters for function H() in healthy and atrial fibrillation (AF) cases for ionic models by: Courtemanche et al., Bueno-Orovio et al. and Mitchell & Schaeffer, used in the DREAM simulations.

	Courtemanche et al.		Bueno-Orovio et al.		Mitchell & Schaeffer	
Parameter	Healthy	AF	Healthy	AF	Healthy	AF
ρ (−)	811	100000	55.13	100000	4.41	2.90
κ (ms)	53	116.41	138.14	118.16	161.47	151.75
θ (ms)	137	66.28	139.73	70.64	129.30	103.12
ψ (ms)	159	159	159	159	159	159

and finally in 1 ms intervals from 320 ms to 318 ms. The different intervals were chosen to cover critical changes in electrophysiological behavior, as CV and ERP drastically decrease towards the last propagating PCL. For the ionic models of Bueno-Orovio et al. and Mitchell & Schaeffer, also shorter PCLs propagated on the mesh. Therefore, the PCL was further decreased in 1 ms intervals to 250 ms. In the AF condition, the PCL was decreased for all ionic models from 950 ms to 200 ms in 50 ms intervals, and from 199 ms to 118 ms in 1 ms intervals. The considered PCL values varied across conditions due to differences in the restitution curves, requiring a range of PCL values tailored to each condition.

After the experiments, the CV restitution curves were determined. To calculate the CV, the ATs of the mesh points (–15000 µm, 0 µm, 0 µm) and (15000 µm, 0 µm, 0 µm) were used. CV was normalized over v_{ref}. The ERP was defined as the time difference between ATs and RTs from the second activation cycle plus θ from Eq. 12 (i.e., shortest propagating DI).

3.2 Reentry in 2D Sheets

To evaluate the impact of mesh resolution on reentry properties in both models, a 2D sheet geometry was subjected to S1-S2 protocols. The geometry was represented by squared unstructured meshes of size 51.2 mm × 51.2 mm × 0, with the centroid of the mesh located at (25600 µm, 25600 µm, 0 µm) for each of the 4 resolutions. Preferential cardiomyocyte orientation was set as constant everywhere in the geometry and aligned with the x-axis (i.e., $\overrightarrow{l} = (1, 0, 0)$). Experiments were conducted for homogeneous reference CV values of 200, 600 and 1000 mm/s. The Courtemanche et al. ionic model was pre-paced at 250 ms PCL for 50 activation cycles. The tissue was pre-paced 5 times with planar stimuli (S1) from the left border of the sheet. Subsequently, a single cross-field stimulus (S2) was applied in the bottom left quadrant at various times to induce reentry. After each simulation, it was assessed whether S2 was applied too early and got completely blocked, applied too late and propagated to all directions without any block, or if unidirectional block occurred as a prerequisite to induce reentry. Reentry duration was defined as the period from S2 application to the last AT in the simulation. ΔS was defined as the difference between the times when S2 and the last S1 were applied. The vulnerable window duration was determined as the difference between the earliest and latest ΔS values that induced reentry. The sample frequency for ΔS values was 1 ms. The mean and standard deviation of the local reentry cycle length were calculated at 4 nodes, each located at the same coordinates in all 4 mesh resolutions: $P_{\text{left}} = (12800\,\mu\text{m},\ 25600\,\mu\text{m},\ 0\,\mu\text{m})$, $P_{\text{down}} = (25600\,\mu\text{m},\ 12800\,\mu\text{m},\ 0\,\mu\text{m})$, $P_{\text{right}} = (38400\,\mu\text{m},\ 25600\,\mu\text{m},\ 0\,\mu\text{m})$, and $P_{\text{up}} = (25600\,\mu\text{m},\ 38400\,\mu\text{m},\ 0\,\mu\text{m})$. To calculate the local reentry cycle length, reentries were induced using DREAM and monodomain simulations with a reference conduction velocity (CV) of 200 mm/s and a stimulus interval (ΔS) of 225 ms in the 4 resolutions. The local reentry cycle length was defined as the difference between the ATs corresponding to 2 consecutive activation cycles of the same node after reentry was induced. To evaluate the long-term stability beyond 1 s of reentry, the simulation was run until the total simulated time reached 60 s. For each of the 438 cycles within this period, the mean and standard deviation of the local cycle length across all nodes were calculated.

3.3 Reentry in the Left Atrium

The PEERP method [29] was used to induce reentries in a realistic human left atrial geometry from a publicly available dataset [44]. This realistic geometry is derived from an instance of a statistical shape model [45]. Preferential cardiomyocyte orientation was assigned using a rule-based method [46]. The endocardial surface was extracted and remeshed at 4 different resolutions to achieve the desired average edge lengths. To benchmark the DREAM on coarse meshes, the adaptations detailed below were introduced; the remaining parameters were sourced from Azzolin et al. [29]. Modifications were applied equally to both DREAM and monodomain experiments. From the coarsest mesh (1600 µm average edge length), 21 points that were evenly spaced approximately 2 cm apart were selected. Since the lower resolution meshes were embedded in the higher resolution ones, each of the 21 points were located at positions where each of the 4 meshes had a corresponding node. The reference CV was reduced to 200 mm/s, and the conductances of the ionic model were adapted to represent AF to increase the likelihood of inducing reentry without the need for an additional arrhythmogenic substrate. Pre-pacing on single cell and tissue level was performed for 50 and 5 activation cycles, respectively, at a PCL of 250 ms. From the APs triggered by the last tissue pre-pacing, the RT was calculated and the ERP was defined as RT+θ. Afterwards, the tissue was stimulated at the end of the ERP to try to induce reentry at each of the 21 chosen locations. Stimulation comprised all nodes within a 5 mm-radius sphere centered at this location. Stimulations were stopped if a reentry was induced or the maximum number of 4 stimuli per location was reached.

3.4 Computing Times

The simulations were executed on a 2023 MacBook Pro, equipped with a 11-Core Apple M3 Pro processor and 16 GB 6.4 GHz LPDDR5 memory. Computing times were benchmarked in 2 experiments across 4 different resolutions using the AF remodeled ionic model of Courtemanche et al. and a CV of 200 mm/s. In the first experiment, one single planar wavefront was stimulated in each of the 2D sheets described in Section 3.2. The computing time was measured from the onset of the stimulus until 500 ms of simulated time thereafter. The selected duration encompassed the repolarization phases of all nodes. In the second experiment, a reentry was induced using the S1-S2 protocol presented in Section 3.2. The computing time was measured starting 200 ms of simulated time after delivering the S2 stimulus and ending 300 ms of simulated time after delivering the S2 stimulus, i.e., in the interval [S2+200 ms, S2+300 ms].

4 Results

4.1 Multiple Stimulations and CV Restitution

Fig. 4 shows the comparison of CV and ERP restitution curves between the DREAM and monodomain models at resolutions of 200, 400, 800, and 1600 µm. The analysis reveals distinct characteristics for both the healthy and AF cases. Specifically, the ionic model of Courtemanche et al. was used for the healthy and AF remodeled case, whereas the AF remodeled case employed the ionic models of Bueno-Orovio et al. and Mitchell & Schaeffer. Table 4 shows the root mean square error (RMSE) of CV and ERP restitution curves for all considered ionic models with both healthy and AF conditions. Monodomain simulations on meshes with an average edge length 200 µm were used as reference solution to calculate RMSE. Addressing simulations with the Courtemanche et al. ionic model, DREAM and monodomain model exhibited similar steepness across all resolutions for the healthy case in both restitution curves (Fig. 4a and Fig. 4b), with RMSEs below 8.85 mm/s and 1.52 ms respectively. In the AF case (Fig. 4c and Fig. 4d), both propagation models maintained similar steepness and shortest propagating DI across resolutions. However, the DREAM notably did not represent the temporary raise of CV during intermediate DIs, while the monodomain model showed varying levels of biphasic restitution across resolutions, with lower resolutions having a higher maximum CV at intermediate DIs. The monodomain model demonstrated smaller last propagating cycle lengths, indicating the shortest possible DIs before propagating failure occurred. A more discernible difference arose in the CV resulting from each propagation model at this minimal DI. The DREAM demonstrated a higher minimum CV compared to the monodomain model (Fig. 4c). The ranges of both restitution curves obtained with DREAM and monodomain model for the Bueno-Orovio et al. ionic model resemble those for the Courtemanche et al. ionic model. The CV and ERP restitution curves (shown for the AF case in Fig. 4e and Fig. 4f) showed similar steepness. Similar to simulations with the DREAM and Courtemanche et al., the biphasic CV restitution obtained with the monodomain model and Bueno-Orovio et al. was not reproduced with the DREAM and Bueno-Orovio et al. The restitution curves for the ionic model of Mitchell & Schaeffer (shown for the AF remodeled case in Fig. 4g) and Fig. 4h) showed higher last propagating cycle lengths for the DREAM compared to the monodomain model. Pacing cycle length and DI for the last possible propagation were about 173 ms and 107 ms, respectively, longer for the DREAM compared to the monodomain models. Despite the absence of biphasic behavior in the monodomain CV restitution curve, the RMSE values were consistently higher across resolutions for the DREAM compared to Courtemanche et al. ionic model. Monodomain simulations resulted in smaller errors for both restitution curves under both conditions for resolutions without propagation failure. Moreover, DREAM simulations showed a tendency towards higher errors for ionic models with reduced

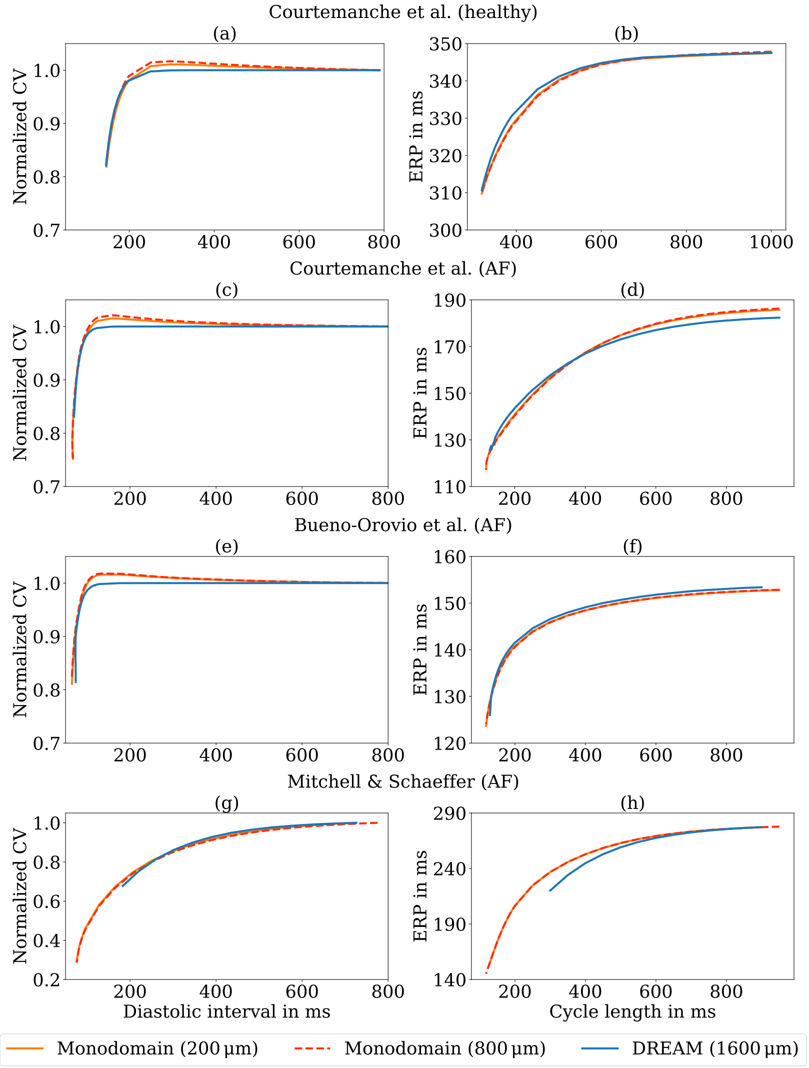

Fig. 4 Restitution curves for conduction velocity (CV) and effective refractory period (ERP) obtained from experiments using meshes with average element edge lengths of 200 µm and 800 µm for the monodomain model, and 1600 µm for the DREAM, with the healthy and AF remodeled Courtemanche et al. ionic model, as well as the AF remodeled ionic models of Bueno-Orovio et al. and Mitchell & Schaeffer. Results for the monodomain model with an edge length of 400 µm are not shown due to negligible differences compared to the 200 µm results, and the monodomain model with 1600 µm edge length is excluded due to propagation failure. Finer resolutions for the DREAM (i.e., 200 µm, 400 µm, and 800 µm) are not displayed as they are mostly indistinguishable from the 1600 µm results. **a, c, e, g)** CV restitution curves normalized to the reference CV, $v_{\text{ref}} = 1000\,\text{mm/s}$ and **b, d, f, h)** ERP restitution curves for the Courtemanche et al. ionic model representing healthy and AF remodeled behavior, as well as the AF remodeled ionic models of Bueno-Orovio et al. and Mitchell & Schaeffer, respectively.

levels of detail. Simulations across different resolutions for the DREAM showed similar RMSEs for each condition and ionic model. For instance, differences in RMSEs among resolutions in DREAM simulations were smaller than 5.46 mm/s and 0.5 ms for the CV and ERP restitution curves respectively per condition and ionic model.

Table 4 Root mean square error of conduction velocity (CV) restitution and effective refractory period (ERP) restitution for healthy and atrial fibrillation (AF) conditions, in DREAM and monodomain model with Courtemanche et al., Bueno-Orovio et al., and Mitchell & Schaeffer embedded ionic models at various resolutions indicated by average edge length, compared to the restitution obtained with the monodomain model at 200 µm.

			CV (mm/s)		ERP (ms)	
Ionic model	Propagation Model	Resolution (µm)	Healthy	AF	Healthy	AF
Courtemache et al.	DREAM	200	8.85	7.19	1.52	2.39
		400	8.74	7.14	1.52	2.39
		800	8.47	7.14	1.50	2.39
		1600	8.01	7.26	1.49	2.38
	Monodomain[1]	200	0.00	0.00	0.00	0.00
		400	0.63	2.60	0.36	0.09
		800	5.88	5.17	0.25	0.46
		1600	(-)	(-)	(-)	(-)
Bueno-Orovio et al.	DREAM	200	7.21	15.95	1.03	1.11
		400	6.62	13.60	1.09	1.12
		800	6.48	11.49	1.02	1.12
		1600	7.07	12.08	1.05	1.17
	Monodomain[1]	200	0.00	0.00	0.00	0.00
		400	0.98	0.30	0.49	0.08
		800	14.36	4.13	1.53	0.18
		1600	(-)	(-)	(-)	(-)
Mitchell & Schaeffer	DREAM	200	17.36	10.82	7.09	6.38
		400	18.21	8.01	7.21	6.44
		800	17.65	7.03	7.22	6.46
		1600	19.28	7.76	7.24	6.46
	Monodomain[1]	200	0.00	0.00	0.00	0.00
		400	2.80	0.30	0.54	0.03
		800	2.20	5.33	0.52	0.04
		1600	(-)	(-)	(-)	(-)

[1] Propagation failure at 1600 µm average edge length.

4.2 Reentry in 2D Sheets

Fig. 5 shows the reentry duration for ΔS values within the vulnerable window for each of the resolutions at a CV of 200 mm/s. The DREAM produced similar results across all resolutions. In contrast, the monodomain results failed to propagate during pre-pacing for coarser resolutions (800 and 1600 µm average edge length). For higher resolutions (200 and 400 µm average edge length), both models showed reentries that

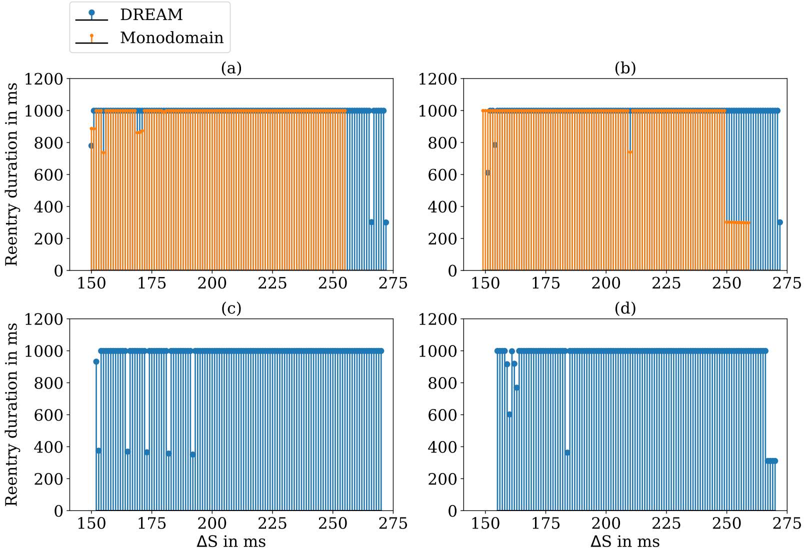

Fig. 5 Reentry duration at a conduction velocity of 200 mm/s for different mesh resolutions. Average edge length: **a)** 200 µm, **b)** 400 µm, **c)** 800 µm, **d)** 1600 µm. Monodomain simulations for coarser resolutions are not shown due to propagation failure in **c)** and **d)**). The horizontal axis shows ΔS (time difference between S2 and S1). The vertical axis shows reentry duration.

lasted 1000 ms (i.e., until the simulation reached t_{end}) for most of the tested ΔS values. However, monodomain simulations produced a few reentries that stopped before 1000 ms for less than 10 ΔS values sparsely distributed across the vulnerable window. Moreover, vulnerable windows were shorter for the monodomain model mainly because it did not induce reentries for the longest ΔS values. For higher CVs, the monodomain model produced reentries that terminated before the end of the simulation, whereas simulations with the DREAM yielded a unidirectional block but did not reactivate the nodes where the S2 stimulus was applied.

Fig. 6a), Fig. 6b) and Fig. 6c) show the vulnerable window duration for the 2 models at each of the 4 resolutions at different reference CVs. The vulnerable window duration was defined as the time between the earliest and the latest S2 time that induced a unidirectional block. Monodomain simulations on the mesh with an average edge length of 200 µm were taken as ground truth. The DREAM kept a stable error as mesh resolution decrease, performing equally even at the coarsest resolution of 1600 µm. Vulnerable windows were longer for all CVs and all the resolutions in the DREAM simulations. These differences in vulnerable window duration between DREAM simulations in all resolutions and monodomain simulation at finer resolutions did not increase in simulations with higher reference CV. Fig. 6d), Fig. 6e) and Fig. 6f) show the reentry duration (mean±std) for the same reference CVs. For the slowest CV both models produced longer reentries at most of ΔS values. In faster CV, both models resulted in shorter durations for all resolutions. The DREAM simulations resulted in reentry duration errors across all resolutions that increased with higher

CVs. The discrepancy is grounded in the fact that the monodomain simulations produced self-terminated shorter reentries with a few turns within the 2D sheet at higher reference CV in this particular experiment. The DREAM simulations, on the other hand, resulted in propagation patterns with unidirectional blocks that were incapable of completing a full turn due to the lack of source-sink mismatch representation.

Table 5 presents the mean and standard deviation of local reentry cycle lengths observed in DREAM and monodomain simulations across various resolutions at nodes P_{left}, P_{down}, P_{right}, and P_{up}. In monodomain simulations with average edge lengths of 200 µm, mean local reentry cycle lengths ranged from 136 to 157 ms, with standard deviations varying from 17 to 28 ms. DREAM simulations consistently showed comparable mean and standard deviation values across different resolutions, ranging from 137 to 164 ms and from 9 to 46 ms, respectively. Notably, most of mean local reentry cycle lengths from DREAM simulations were closer to those observed in monodomain simulations at 200 µm than in simulations at 400 µm.

In the long-term stability analysis, the qualitative behavior of the reentry remained stable beyond the initial 1000 ms, continuing consistently until the simulation reached 60 seconds. However, after 13 seconds, small areas of the sheet began to show artifacts and activation discordance with the rest of the sheet, though this did not affect the overall behavior of the reentry. The mean local cycle length across nodes decreased from an initial value of 182 ms in the first cycle to 138 ms by the seventh cycle, remaining steady around this value until the 426th cycle, where it measured 137 ms. Similarly, the standard deviation of the local cycle length dropped from 27.1 ms to 0.8 ms between the first and seventh cycles, but then increased to 13 ms by the 426th cycle.

Table 5 Mean ± standard deviation of the local reentry cycle length in ms at 4 points P_x across various mesh resolutions, indicated in average edge lengths in µm, for both the DREAM and monodomain models.

Propagation Model	Resolution	P_{left}	P_{down}	P_{right}	P_{up}
DREAM	200	154 ± 45	137 ± 11	151 ± 28	161 ± 45
	400	156 ± 46	138 ± 10	153 ± 28	163 ± 44
	800	158 ± 40	143 ± 9	154 ± 22	164 ± 38
	1600	157 ± 33	149 ± 10	154 ± 20	162 ± 32
Monodomain[1]	200	136 ± 28	157 ± 26	152 ± 28	146 ± 17
	400	162 ± 15	174 ± 24	174 ± 19	168 ± 24
	800	(-)	(-)	(-)	(-)
	1600	(-)	(-)	(-)	(-)

[1] Propagation failure at 800 and 1600 µm.

4.3 Reentry in the Left Atrium

Fig. 7 shows the number of inducing points of the 21 stimulation points in the left atrium per experiment. Monodomain experiments at higher resolutions (average edge lengths 200 and 400 µm) showed the same number of inducing points. On the other

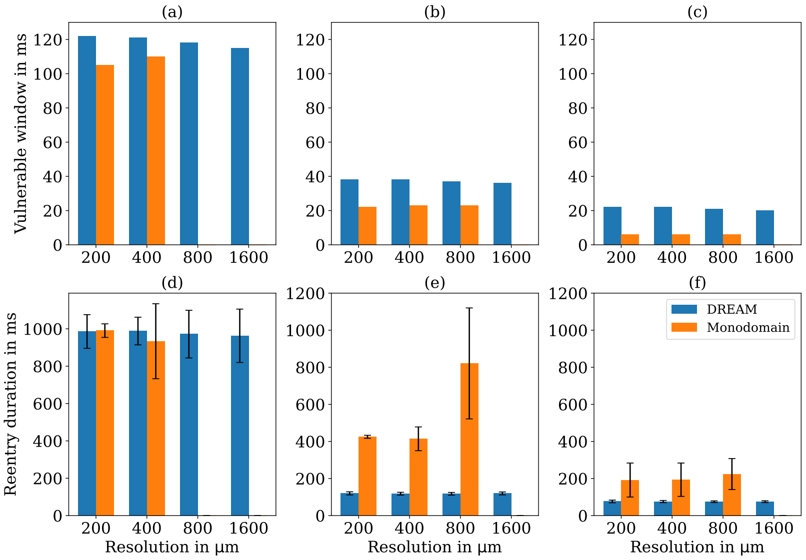

Fig. 6 (**a**) Vulnerable window at different mesh resolutions for a conduction velocity (CV) of 200 mm/s, (**b**) 600 mm/s and (**c**) 1000 mm/s. (**d**) Reentry duration (mean±std) for a CV of 200 mm/s, (**e**) 600 mm/s, (**f**) and 1000 mm/s.

hand, monodomain simulations failed to induce any reentry at lower resolutions (average edge lengths 800 and 1600 µm) due to propagation failure. DREAM experiments showed a lower number of inducing points compared to monodomain experiments. However, DREAM experiments showed a similar amount of inducing points across all resolutions. For some experiments, both models showed similar mechanisms of reentry at the same inducing point. For example, Fig. 8 shows simulations in the same inducing point in which both the DREAM and monodomain model produced a figure-of-eight reentry. Despite this example showing the same mechanism of reentry, the one induced by the DREAM lasted longer time. Fig. 9 shows an example where the DREAM shows a figure-of-eight reentry while the monodomain model shows a spiral reentry. This difference arose from the lack of source-sink mismatch representation in the DREAM. In both cases, the reentries were sustained for the full 1000 ms simulated. Table 6 provides sensitivity and specificity of both models in the resolutions that did not have propagation failure running the PEERP protocol. Monodomain results at the highest resolution (i.e., average edge length of 200 µm) were used as ground truth. DREAM simulations exhibited better specificity than sensitivity, as most inducing points identified by the DREAM were also found by the monodomain model, whereas not all points found by the monodomain model were captured by the DREAM. On the other hand, DREAM performance was consistent across all resolutions, except for a significant drop in specificity for the coarsest resolution (i.e., average edge length of 1600 µm) to 50 %.

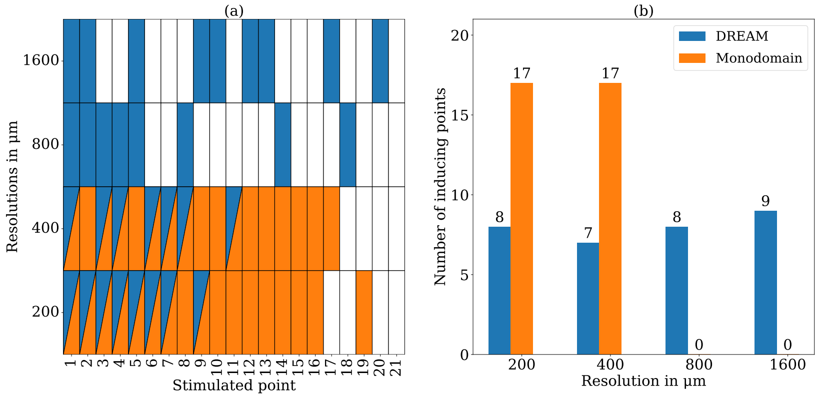

Fig. 7 Inducing points identified by the PEERP protocol. **a)** Distribution of points that induced reentry in experiments with the DREAM, the monodomain model or both at different mesh resolutions (average edge length of 200, 400, 800, or 1600 µm). Each row represents an experiment, and each column represents one of the 21 stimulated points. The square's color indicates points that produced reentry with the DREAM, monodomain model, or both. **b)** Number of inducing points per model and resolution.

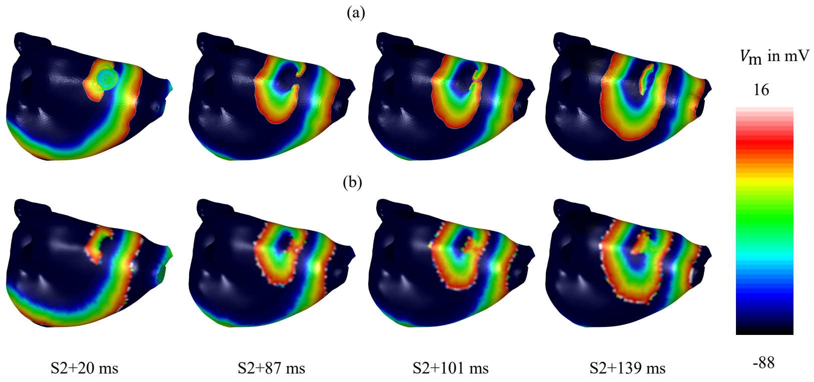

Fig. 8 Left atrium posterior view of transmembrane voltage maps of induced reentries at different time points after S2 , stimulated at a point close to the roof. **a)** Monodomain model with 200 µm average edge length **b)** DREAM with 1600 µm average edge length.

4.4 Computing Times

Fig. 10 illustrates the computing times that the DREAM and monodomain model took for simulating a planar wavefront and reentry across different mesh resolutions. The proportion of computing time for the different steps of both models remained consistent across resolutions. Therefore, the detailed computing times for each step are mentioned only for simulations on a mesh with an average edge length of 200 µm.

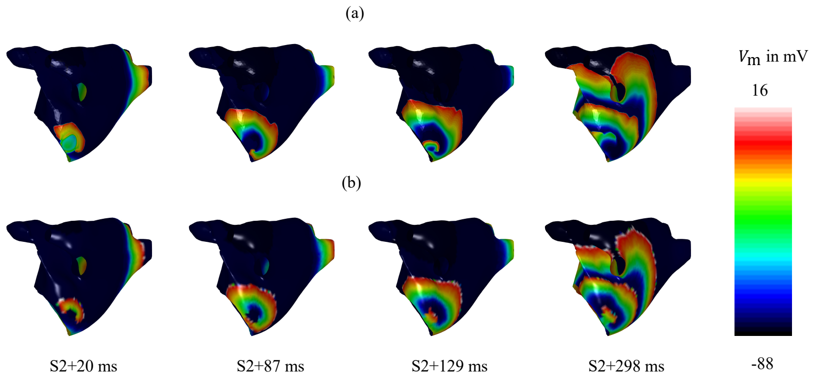

Fig. 9 Left atrium posterolateral view of transmembrane voltage maps of induced reentries at different time points after S2, stimulated at a point near the mitral valve, **a)** Monodomain model with 200 µm average edge length **b)** DREAM with 1600 µm average edge length.

Table 6 Sensitivity and specificity for the DREAM and monodomain model at different mesh resolutions, expressed in average edge length in µm, considering monodomain experiments at 200 µm as the ground truth.

Propagation Model	Resolution	Sensitivity (%)	Specificity (%)
DREAM	200	47	100
	400	41	100
	800	41	75
	1600	41	50
Monodomain[1]	200	100	100
	400	94	75
	800	(-)	(-)
	1600	(-)	(-)

[1] Propagation failure at 800 and 1600 µm.

In both the planar wavefront and reentry experiment, for all resolutions, simulations with the DREAM were faster than those with the monodomain model. DREAM simulations on coarser resolution meshes (1600 µm) were 122 times faster in the planar wavefront experiment and approximately 87 times faster in the reentry experiment than monodomain simulations on finer mesh resolutions (200 µm).

In the DREAM simulations for the planar wavefront, the majority of the computing time was spent solving the ionic model equations (Fig. 1 step C), which took 83 s. The second most time-consuming step was calculating recovery times (Fig. 1 step D), which took 6 ms, followed by iterating the cycFIM (Fig. 1 step A), which took 5 s. Computing I_{diff} (Fig. 1 step B) required 2.5 s. In the same scenario, the monodomain model spent 80 s computing the ionic model and 138 s solving the parabolic equation.

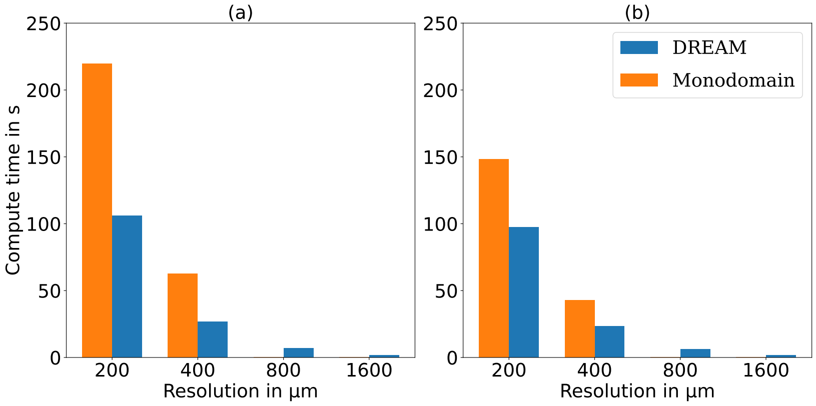

Fig. 10 Computing time: **a)** planar wavefront, **b)** reentry.

When simulating the reentry with the DREAM, the majority of computing time was spent in step C, followed by steps A, D, and B, taking 51, 22, 16, and 2 s respectively (See Fig. 1). Given the significant role of diffusion currents in reentries, the monodomain simulations devoted most of their time to solving the parabolic equation (97 s), with only 51 s spent on computing the ionic current.

5 Discussion

5.1 Advantages and Novel Aspects of the DREAM

The DREAM benefits from the consistency of the eikonal model across mesh resolutions. Across all experiments, it was possible to obtain similar results with all tested resolutions. Unlike the monodomain model that requires fine mesh resolutions, hence more computational effort, the DREAM yields similar results at lower resolutions. This characteristic allows the DREAM to perform faster simulations.

Most of the eikonal models that have attempted to incorporate reentry phenomena use the FMM as a numerical method [5, 14] and implementations are not publicly available. Moreover, the regular FMM struggles with anisotropic propagation because this algorithm assumes the characteristic direction to be always colinear with the wavefront gradient, which is not true for anisotropic cases [15]. To address this limitation, Pernod et al. developed the anisotropic FMM, which incorporates an additional “CHANGED” list to enable recursive corrections [5]. Similarly, Cristiani proposed a similar method, introducing the “BUFFER” list with the same recursive correction concept [17]. In his study, he conducted various tests comparing the buffered FMM against the regular FMM, focusing on anisotropy problems. His findings revealed that the regular FMM calculated incorrect solutions with varying degrees of error across different anisotropic scenarios and resolutions. For instance, in an experiment with an anisotropy ratio of approximately 5 on a 2D grid of varying resolutions, the regular FMM was evaluated for its accuracy in solving the anisotropic eikonal equation, which in our case corresponds to finding ATs. The errors in the solution of the eikonal equation were 40 to 50 times larger compared to those of the buffered FMM, with the fast sweeping method, which is a classical iterative method, used as the reference solution [47].

Another constraint of the regular FMM is the inability to simulate reentry and reactivation. Pernod et al. also developed the multifrontal FMM, integrating a REFRACTORY list to include reentry [5]. However, this adaptation omitted the "CHANGED" list essential for managing anisotropic propagation, thereby compromising its efficacy in such scenarios. Although no reason for this omission is provided, it is possible that they faced similar challenges to those motivating this work. Specifically, changes in the solution of the eikonal equation make it difficult to determine definitive ATs for calculating RTs. Gassa et al. later incorporated ideas from the multifrontal FMM, the Dijkstra's algorithm and the Mitchell & Schaeffer membrane model, reproducing spiral reentries in the atria [9, 12, 14, 35]. Notably, this adaptation neglected the use of recursive corrections or any other mechanism for better handling of anisotropy, possibly due to similar challenges encountered in Pernod et al.'s work.

The numerical solution of the anisotropic eikonal equation with regular FMM-based methods without recursive corrections does not lose stability under grid refinement [15]. The error from neglecting recursive corrections can be small, especially in experiments with small geometries, low anisotropy, and homogeneous properties [15, 17] and errors may be less apparent due to the stability of the solution [15]. However, arrhythmia simulations of multiple reentry cycles in realistic geometries with heterogeneous properties and high anisotropy may deviate significantly from the viscosity solution. For these complex cases, some of the adaptations made in the DREAM might be particularly useful.

The FIM is better suited to solve systems with anisotropic conditions [16]. However, the iteration process hinders the implementation of reactivation patterns and reentry. The DREAM uses the cycFIM framework to manage anisotropic propagation through correction mechanisms. The DREAM also addresses reentry by incorporating a "safety margin in time" τ_s, allowing for corrections before calculating RT based on a reliable AT. This approach could potentially also be applied for merging the anisotropic FMM and the multifrontal FMM, leveraging the strengths of both methods [5]. However, the computational cost of buffered FMM and the anisotropic FMM can exceed that of iterative methods in worst-case scenarios with high anisotropy. This is due to the increase in the "BUFFER" and "CHANGED" list sizes, respectively [5, 17]. Additionally, an FIM-based algorithm is more favorable because it can be parallelized more easily while maintaining computational density [16, 26, 27, 48]. The DREAM is the first model to use an iterative method such as cycFIM, ionic models and CV restitution to simulate functional reentry to the best of our knowledge.

Another method that uses the FIM in an alternative approach is the VITA method. This method employs the RE method based on the FIM approach [10, 16, 18]. Initially intended for studying ventricular tachycardia, VITA explores reentries using the FIM. While VITA relies on scar tissue with an isthmus to simulate anatomical reentry, the DREAM is capable of simulating reentry in the absence of structural abnormalities, including functional and anatomical reentries. Additionally, the cycFIM within the DREAM framework can simulate multiple ATs per node per reentry, considering CV restitution and ERP values to analyze reentry maintenance and average cycle length. Conversely, VITA does not compute multiple ATs per node during reentry. Instead, VITA calculates 2 types of ATs using the eikonal-based model. The first AT map identifies isochrone splitting and merging points, revealing isthmus exits where then elements are decoupled to induce unidirectional block for the second activation. This unidirectional block does not consider the electrophysiological properties at that location during repolarization. Subsequently, a second AT map is calculated for each isthmus exit, stimulating where the elements were decoupled. This second AT is the only one calculated during reentry. Then, the round-trip time (RTT) is defined as the time the wavefront takes to go around and reach the isthmus exit again. The RTT serves as a surrogate marker for possible ablation targets if its value is longer than 50 ms. One argument for using RTT as a surrogate instead of personalized CV restitution and ERP values is that the latter are rarely available in clinical settings. While most in silico studies do not personalize these variables but rather rely on literature references, some clinical and in silico studies have explored the effect of personalized CV restitution and ERP values on reentry patterns [49–52]. The DREAM in contrast can incorporate personalized CV restitution and ERP values extracted from patient measurements when available by adjusting parameters in the embedded ionic model and the COHERENCE() function.

While implementing τ_s allows to have reentries with multiple activation cycles in iterative methods, it also entails a new challenge successfully addressed by the DREAM. The cycFIM in step $\mathrm{A_n}$ of the n-th DREAM cycle and the RD portion in step C_{n-1} of the $(n-1)$-th DREAM cycle operate within different, non-overlapping time windows. Consequently, in scenarios such as reentry, it is common for the AT of a node to be calculated in step A_n without the previous RT for that node having been calculated by the RD model during step C_{n-1}, as required by the cycFIM. The DREAM overcomes this limitation in step D_{n-1} by briefly running the ionic model on the activated nodes until the voltage threshold is reached. This enables the ERP restitution to be directly obtained from the ionic model instead of relying on provided phenomenological curves [5, 7, 53].

This study also demonstrated how the DREAM could adapt to different ionic models by adjusting the corresponding parameters. This adaptability allows for the selection of the most suitable ionic model for a specific research question, depending on the required levels of computational speed and physiological detail. For instance, the Courtemanche et al. model is ideal when detailed biophysical information is needed, although it comes at the cost of computational speed [32]. In contrast, the simplified Bueno-Orovio et al. model, which includes the main ionic currents that modify the AP morphology and basic calcium dynamics, offers intermediate complexity with improved computational efficiency [34]. At the other end of the spectrum, the simplified model of Mitchell & Schaeffer combines fast inward and outward currents to represent basic AP dynamics, providing higher computational speed [35]. The DREAM was able to reproduce restitution behaviors very similar to the monodomain model when reducing the level of detail in the embedded ionic model for the sake of computational efficiency, as shown in the comparison between the Courtemanche et al. and Bueno-Orovio et al. ionic models. This demonstrates that the DREAM is flexible enough to be used in various research scenarios where computational resources are a constraint without significantly compromising on accuracy.

Another novel aspect of the DREAM lies in its approach to incorporate CV restitution. Previous methods typically involved incorporating the DI at every node from the previous activation cycle or the DI of neighboring nodes in the present activation cycle [7, 12]. In this study, CV is calculated using the DI of the present activation cycle, allowing for better adaptation to sudden changes in activation frequency and DI. Furthermore, as CV is assigned per node rather than per element, the minimization of AT is facilitated using analytical formulas such as Eq. 6. This eliminates the need for the Dijkstra's algorithm and additional pathways within the triangles can be considered [9]. In contrast, Corrado et al. proposed incorporating the DI within the Dijkstra's algorithm [12] which considers trajectories solely along the edges.

5.2 Limitations and Future Work

Several attempts have been made to incorporate additional properties such as curvature and diffusion effects into the pure eikonal model [54–57]. However, existing eikonal models still struggle to accurately represent complex activation patterns, such as multi-wavelet reentry, which are influenced by high wavefront curvatures, bath loading, wave collisions, and other source-sink mismatch effects. These properties are typical of propagation in fibrotic and heterogeneous tissue, a key factor in sustaining reentry [55]. To simulate these complex activation patterns accurately, it is necessary to accurately model diffusion and curvature effects, as well as reactivation and repolarization.

In this work, the approximation of the diffusion current was incorporated as a function that depends solely on the ATs with constant amplitude and duration. This function is unaffected by electrophysiological properties of the surrounding tissue. This limitation implies that the DREAM at this moment does not consider source-sink mismatch effects in the diffusion current and in the CV. Most of the differences observed between the DREAM and monodomain model in the experiments regarding reentries can be attributed to this phenomenon. In the RE$^+$ model described by Neic et al., I_{foot} (analogous to I_{diff} in the DREAM) is added to the parabolic portion of the RD model. On the other hand, the RE$^-$ model replaces the diffusion term $\nabla \cdot (\boldsymbol{\sigma}_\text{i} \nabla V_\text{m})$ with I_{foot}. By doing this, the RE$^+$ model managed to obtain similar repolarization phases as those obtained in the RD models when the tissue had heterogeneous APD. In the DREAM, I_{diff} is implemented as in the RE$^-$ model, resulting in sharp repolarization gradients that preserve the APD differences between neighboring cells. The primary reason for the sharp repolarization gradients is that I_{diff} does not account for the diffusion currents during the repolarization phase. Neglecting these diffusion currents during the repolarization phase can lead to the appearance of artifacts in localized regions during extended simulations. When implementing the RE$^+$ approach in the DREAM, one needs to ensure that the RD wavefront is never ahead of the eikonal wavefront to prevent major artifacts in the membrane models and their refractory behavior. This is more difficult for complex activation patterns with spatially heterogeneous curvature than for planar or radial excitation spread. For instance, during the repolarization phase, new activations (i.e., not predicted by the eikonal model) occurred when there was a strong gradient between cells with short APD and neighboring cells with longer APD. Since I_{diff} was calibrated using monodomain simulations with fixed conductivity values to obtain a CV of 1000 mm/s without considering restitution at shorter cycle lengths, this might result in small differences in AP amplitude.

In the present formulation of the DREAM, changes in sodium channel conductance are not explicitly linked to CV and I_{diff}. However, in the approach used to model AF in this manuscript, upstroke velocity changes are not critical for the dynamics under study [33]. While this approach may be less suitable for conditions where sodium channel dysfunction or block leads to a significant reduction in CV, we believe that CV can still be accurately fitted to patient-specific data or obtained from small-scale monodomain simulations for use in the DREAM model. In future work, further personalization of I_{diff} and CV to account for conductivity variations, I_{diff} restitution, and changes in ionic model conductances may enhance the model's accuracy.

While this paper is limited to triangles, the DREAM algorithm can be executed in tetrahedra by employing a similar approach as described in [16] and by implementing DREAM's adaptations to the tetrahedra equation within the local solver, as performed in Eq. 6. Nevertheless, further analysis of the computational efficiency is required for DREAM simulations in volumetric meshes. While the simulations in this paper were conducted in serial code, parallelization can further enhance the efficiency of the DREAM.

Another promising improvement to decrease the computing time of the DREAM would be to increase the integration time step when calculating the RT in cases where they were not yet provided by the ionic model. Currently, RTs are calculated twice at some nodes. In the first calculation, the membrane potential V_{m} is determined asynchronously for each cell, but only the RT is saved and passed to the eikonal model, without storing V_{m}. In the second calculation, the membrane potential V_{m} is computed in a synchronized manner across all nodes (i.e., each time step is calculated for all nodes simultaneously), and the V_{m} values are stored. The need for synchronizing the nodes for storing purposes is the reason why the state variables and V_{m} states are reset between the first and second calculation. Since diffusion currents during the repolarization phase are neglected in the latest version of the DREAM, this redundancy does not introduce discrepancies, as the same calculations are being repeated. However, future improvements could focus on optimizing the process to avoid redundant RTs calculations. Additionally, new considerations will be needed when diffusion currents during the repolarization phase are incorporated.

In this work, atrial cell models and CV values were tested in the context of AF. Nonetheless, other atrial or ventricular models can also be used with the DREAM as long as the parameters of CV restitution and AP properties are tuned accordingly. Investigating the tissue effects of additional changes in ionic models, such as pharmacological effects or channel mutations, represents another valuable area for exploration. On the other hand, the DREAM with the embedded ionic model of Mitchell & Schaeffer demonstrated challenges in reproducing the restitution behavior at short pacing cycle lengths observed in the corresponding monodomain model. Therefore, a better adjustment of the DREAM parameters is required to further improve the faithful representation of CV restitution curve and simulation of reentrant scenarios.

More systematic analysis of the new parameters introduced in the DREAM is required to further understand the optimal tuning that allows for a good balance between accuracy and computational efficiency. We expect that τ_{s} should increase when the anisotropy ratio increases as more changes are required. On the other hand, τ_{inc} must be smaller than the sum of the longest possible APD and the minimum DI, i.e., parameter θ in Eq. 12. Moreover, further investigation of the COHERENCE() function could enhance the approximation of CV restitution, particularly near propagation failure.

The cycFIM embedded in the DREAM could potentially also be used as an alternative method to simulate other applications of RD models. In this case, changing the ionic model according to the reaction part of the probable application would be necessary. Potential use cases include the RD model simulating cyclical phenomena like the Belousov-Zhabotinsky reaction, which can also exhibit spiral propagation patterns [58].

5.3 Conclusion

The DREAM presents several advancements in simulating cardiac arrhythmias compared to existing eikonal-based models while retaining their main advantages and making it accessible as part of the openCARP simulator [30]. By inheriting consistency across mesh resolutions from the eikonal model, the DREAM achieves faster computing times compared to RD models for a given desired accuracy. Additionally, the DREAM faithfully represents functional reentry without the need for structural abnormalities like scar tissue. The use of cycFIM enables multiple ATs per node, allowing for better analysis of reentry patterns in anisotropic media. Moreover, the DREAM permits modification of CV restitution and ERPs, enhancing the personalization of cardiac computer models. Ongoing work aims to overcome limitations in representing source-sink balance. Overall, the DREAM offers promising prospects for advancing our understanding and improving treatments of cardiac arrhythmias compatible with clinical time frames. Finally, the cycFIM may find applications beyond cardiac modeling in simulating cyclical phenomena.

Acknowledgments. This work was supported from the European Union's Horizon research and Innovation programme under the Marie Skłodowska-Curie grant agreement No. 860974, by the Leibniz ScienceCampus "Digital Transformation of Research" with funds from the programme "Strategic Networking in the Leibniz Association", the European High-Performance Computing Joint Undertaking EuroHPC under grant agreement No 955495 (MICROCARD) co-funded by the Horizon 2020 programme of the European Union (EU) and the German Federal Ministry of Education and Research (BMBF), by the Deutsche Forschungsgemeinschaft (DFG, German Research Foundation) – Project-ID 258734477 – SFB 1173 and LO 2093/6-1 (SPP 2311) and – Project-ID 394433254 (LU 2294/1-1, DO 637/23-1, WA 4259/1-1), and by the MCIN\AEI and the European Union NextGenerationEU\RTR under grant PLEC2021-007614.

Authors Contributions. Conceptualisation: CBE, AL. Data curation: CBE, PMD. Formal Analysis: CBE, SA, SB. Funding Acquisition: AL. Investigation: CBE,

SA, LU, SB. Methodology: CBE, JS, SA, AL. Project administration: CBE, AL. Software: CBE, JS, MH, SB, LU, SA, PMD, AL. Supervision: AL. Validation: JS, SB, SA. Visualization: CBE, SA, JK. Writing – original draft: CBE, SA. Writing – review and editing: CBE, JS, MH, LU, PMD, JK, SB, AL, SA.

Data availability. No original data was used for this work

Code availability. The repository with all the original code is publicly available in the openCARP repository (https://git.opencarp.org/openCARP).

Conflict of interest. The authors declare no competing interests

References

[1] Grandi, E., Dobrev, D., Heijman, J.: Computational modeling: What does it tell us about atrial fibrillation therapy? International Journal of Cardiology **287**, 155–161 (2019) https://doi.org/10.1016/j.ijcard.2019.01.077

[2] Trayanova, N.A., Lyon, A., Shade, J., Heijman, J.: Computational modeling of cardiac electrophysiology and arrhythmogenesis. Physiological Reviews (2023) https://doi.org/10.1152/physrev.00017.2023

[3] Jacquemet, V.: Lessons from computer simulations of ablation of atrial fibrillation. The Journal of Physiology **594**(9), 2417–2430 (2016) https://doi.org/10.1113/JP271660

[4] Nagel, C., Barrios Espinosa, C., Gillette, K., Gsell, M.A.F., Sanchez, J., Plank, G., Dossel, O., Loewe, A.: Comparison of propagation models and forward calculation methods on cellular, tissue and organ scale atrial electrophysiology. IEEE Transactions on Biomedical Engineering **70**(2), 511–522 (2023) https://doi.org/10.1109/tbme.2022.3196144

[5] Pernod, E., Sermesant, M., Konukoglu, E., Relan, J., Delingette, H., Ayache, N.: A multi-front eikonal model of cardiac electrophysiology for interactive simulation of radio-frequency ablation. Computers & Graphics **35**(2), 431–440 (2011) https://doi.org/10.1016/j.cag.2011.01.008

[6] Bishop, M.J., Plank, G.: Bidomain ecg simulations using an augmented monodomain model for the cardiac source. IEEE Transactions on Biomedical Engineering **58**(8), 2297–2307 (2011) https://doi.org/10.1109/TBME.2011.2148718

[7] Loewe, A., Poremba, E., Oesterlein, T., Luik, A., Schmitt, C., Seemann, G., Dössel, O.: Patient-specific identification of atrial flutter vulnerability–a computational approach to reveal latent reentry pathways. Frontiers in Physiology **9**(Article 1910) (2019) https://doi.org/10.3389/fphys.2018.01910

[8] Jacquemet, V.: An eikonal-diffusion solver and its application to the interpolation and the simulation of reentrant cardiac activations. Computer Methods and Programs in Biomedicine **108**(2), 548–558 (2012) https://doi.org/10.1016/j.cmpb.2011.05.003

[9] Wallman, M., Smith, N.P., Rodriguez, B.: A comparative study of graph-based, eikonal, and monodomain simulations for the estimation of cardiac activation times. IEEE Transactions on Biomedical Engineering **59**(6), 1739–1748 (2012) https://doi.org/10.1109/TBME.2012.2193398

[10] Neic, A., Campos, F.O., Prassl, A.J., Niederer, S.A., Bishop, M.J., Vigmond, E.J., Plank, G.: Efficient computation of electrograms and ecgs in human whole heart simulations using a reaction-eikonal model. Journal of Computational Physics **346**, 191–211 (2017) https://doi.org/10.1016/j.jcp.2017.06.020

[11] Niederer, S.A., Lumens, J., Trayanova, N.A.: Computational models in cardiology. Nature Reviews Cardiology **16**(2), 100–111 (2019) https://doi.org/10.1038/s41569-018-0104-y

[12] Corrado, C., Zemzemi, N.: A conduction velocity adapted eikonal model for electrophysiology problems with re-excitability evaluation. Medical Image Analysis **43**, 186–197 (2018) https://doi.org/10.1016/j.media.2017.11.002

[13] Pullan, A.J., Tomlinson, K.A., Hunter, P.J.: A finite element method for an eikonal equation model of myocardial excitation wavefront propagation. SIAM Journal on Applied Mathematics **63**(1), 324–350 (2002) https://doi.org/10.1137/S0036139901389513

[14] Gassa, N., Zemzemi, N., Corrado, C., Coudière, Y.: Spiral waves generation using an eikonal-reaction cardiac electrophysiology model. In: International Conference on Functional Imaging and Modeling of the Heart, pp. 523–530 (2021). https://doi.org/10.1007/978-3-030-78710-3_50 . Springer

[15] Sethian, J.A., Vladimirsky, A.: Ordered upwind methods for static hamilton–jacobi equations: Theory and algorithms. SIAM Journal on Numerical Analysis **41**(1), 325–363 (2003) https://doi.org/10.1137/S0036142901392742

[16] Fu, Z., Kirby, R.M., Whitaker, R.T.: A fast iterative method for solving the eikonal equation on tetrahedral domains. SIAM Journal on Scientific Computing **35**(5), 473–494 (2013) https://doi.org/10.1137/120881956

[17] Cristiani, E.: A fast marching method for hamilton-jacobi equations modeling monotone front propagations. Journal of Scientific Computing **39**(2), 189–205 (2009) https://doi.org/10.1007/s10915-008-9257-x

[18] Campos, F.O., Neic, A., Costa, C.M., Whitaker, J., O'Neill, M., Razavi, R., Rinaldi, C.A., Niederer, S.A., Plank, G., Bishop, M.J., *et al.*: An automated

near-real time computational method for induction and treatment of scar-related ventricular tachycardias. Medical Image Analysis **80**, 102483 (2022) https://doi.org/10.1016/j.media.2022.102483

[19] Espinosa, C.B., Sánchez, J., Dössel, O., Loewe, A.: Diffusion reaction eikonal alternant model: Towards fast simulations of complex cardiac arrhythmias. Computing in Cardiology **498**, 1–4 (2022) https://doi.org/10.22489/CinC.2022.054 . IEEE

[20] Tung, L.: A bi-domain model for describing ischemic myocardial dc potentials. PhD thesis, Massachusetts Institute of Technology (1978)

[21] Franzone, P.C., Pavarino, L.F., Scacchi, S.: Mathematical Cardiac Electrophysiology. Springer (2014)

[22] Keener, J., Sneyd, J.: Mathematical physiology 1: Cellular physiology. Springer (2009)

[23] Vigmond, E., Dos Santos, R.W., Prassl, A., Deo, M., Plank, G.: Solvers for the cardiac bidomain equations. Progress in Biophysics and Molecular Biology **96**(1-3), 3–18 (2008) https://doi.org/10.1016/j.pbiomolbio.2007.07.012

[24] Potse, M., Dubé, B., Vinet, A., Cardinal, R.: A comparison of monodomain and bidomain propagation models for the human heart. In: 2006 International Conference of the IEEE Engineering in Medicine and Biology Society, pp. 3895–3898 (2006). https://doi.org/10.1109/IEMBS.2006.259484 . IEEE

[25] Kandel, S.M.: The electrical bidomain model: a review. Sch. Acad. J. Biosci **3**, 633–639 (2015)

[26] Fu, Z., Jeong, W.-K., Pan, Y., Kirby, R.M., Whitaker, R.T.: A fast iterative method for solving the eikonal equation on triangulated surfaces. SIAM Journal on Scientific Computing **33**(5), 2468–2488 (2011) https://doi.org/10.1137/100788951

[27] Jeong, W.-K., Whitaker, R.T.: A fast iterative method for eikonal equations. SIAM Journal on Scientific Computing **30**(5), 2512–2534 (2008) https://doi.org/10.1016/j.procs.2014.05.170

[28] openCARP Eikonal. GitLab. https://git.opencarp.org/openCARP/openCARP/-/tree/openCARP_DREAM

[29] Azzolin, L., Schuler, S., Dössel, O., Loewe, A.: A reproducible protocol to assess arrhythmia vulnerability in silico: pacing at the end of the effective refractory period. Frontiers in Physiology **12**, 656411 (2021) https://doi.org/10.3389/fphys.2021.656411

[30] Plank, G., Loewe, A., Neic, A., Augustin, C., Huang, Y.-L.C., Gsell, M., Karabelas, E., Nothstein, M., Sánchez, J., Prassl, A., Seemann, G., Vigmond, E.: The openCARP simulation environment for cardiac electrophysiology. Computer Methods and Programs in Biomedicine **208**, 106223 (2021) https://doi.org/10.1016/j.cmpb.2021.106223

[31] Costa, C.M., Hoetzl, E., Rocha, B.M., Prassl, A.J., Plank, G.: Automatic parameterization strategy for cardiac electrophysiology simulations, 373–376 (2013). IEEE

[32] Courtemanche, M., Ramirez, R.J., Nattel, S.: Ionic mechanisms underlying human atrial action potential properties: insights from a mathematical model. American Journal of Physiology-Heart and Circulatory Physiology **275**(1), 301–321 (1998) https://doi.org/10.1152/ajpheart.1998.275.1.H301

[33] Loewe, A.: Modeling Human Atrial Patho-electrophysiology from Ion Channels to ECG-substrates, Pharmacology, Vulnerability, and P-waves vol. 23. KIT Scientific Publishing, Karlsruhe (2016)

[34] Bueno-Orovio, A., Cherry, E.M., Fenton, F.H.: Minimal model for human ventricular action potentials in tissue. Journal of Theoretical Biology **253**(3), 544–560 (2008) https://doi.org/10.1016/j.jtbi.2008.03.029

[35] Mitchell, C.C., Schaeffer, D.G.: A two-current model for the dynamics of cardiac membrane. Bulletin of Mathematical Biology **65**(5), 767–793 (2003) https://doi.org/10.1016/S0092-8240(03)00041-7

[36] Lenk, C., Weber, F.M., Bauer, M., Einax, M., Maass, P., Seeman, G.: Initiation of atrial fibrillation by interaction of pacemakers with geometrical constraints. Journal of Theoretical Biology **366**, 13–23 (2015) https://doi.org/10.1016/j.jtbi.2014.10.030

[37] Corrado, C., Whitaker, J., Chubb, H., Williams, S., Wright, M., Gill, J., O'Neill, M.D., Niederer, S.A.: Personalized models of human atrial electrophysiology derived from endocardial electrograms. IEEE Transactions on Biomedical Engineering **64**(4), 735–742 (2016) https://doi.org/10.1109/TBME.2016.2574619

[38] Geuzaine, C., Remacle, J.-F.: Gmsh: A 3-d finite element mesh generator with built-in pre-and post-processing facilities. International Journal for Numerical Methods in Engineering **79**(11), 1309–1331 (2009)

[39] Ahrens, J., Geveci, B., Law, C.: ParaView: An End-User Tool for Large Data Visualization

[40] Schmidt, R., Singh, K.: meshmixer: an interface for rapid mesh composition. In: ACM SIGGRAPH 2010 Talks. SIGGRAPH '10. Association for Computing Machinery, New York, NY, USA (2010). https://doi.org/10.1145/1837026.

1837034

[41] Cignoni, P., Callieri, M., Corsini, M., Dellepiane, M., Ganovelli, F., Ranzuglia, G.: MeshLab: an Open-Source Mesh Processing Tool. https://doi.org/10.2312/LocalChapterEvents/ItalChap/ItalianChapConf2008/129-136

[42] Hunter, J.D.: Matplotlib: A 2d graphics environment. Computing in Science & Engineering **9**(3), 90–95 (2007) https://doi.org/10.1109/MCSE.2007.55

[43] Virtanen, P., Gommers, R., Oliphant, T.E., Haberland, M., Reddy, T., Cournapeau, D., Burovski, E., Peterson, P., Weckesser, W., Bright, J., van der Walt, S.J., Brett, M., Wilson, J., Millman, K.J., Mayorov, N., Nelson, A.R.J., Jones, E., Kern, R., Larson, E., Carey, C.J., Polat, İ., Feng, Y., Moore, E.W., VanderPlas, J., Laxalde, D., Perktold, J., Cimrman, R., Henriksen, I., Quintero, E.A., Harris, C.R., Archibald, A.M., Ribeiro, A.H., Pedregosa, F., van Mulbregt, P., SciPy 1.0 Contributors: SciPy 1.0: Fundamental Algorithms for Scientific Computing in Python. Nature Methods **17**, 261–272 (2020) https://doi.org/10.1038/s41592-019-0686-2

[44] Azzolin, L., Eichenlaub, M., Nagel, C., Nairn, D., Sánchez, J., Unger, L., Doessel, O., Jadidi, A., Loewe, A.: 29 Atrial Models Created with a Patient-specific Augmented Atrial Model Generation Tool (AugmentA). https://doi.org/10.5281/zenodo.5589289

[45] Nagel, C., Schuler, S., Dössel, O., Loewe, A.: A bi-atrial statistical shape model for large-scale in silico studies of human atria: model development and application to ecg simulations. Medical Image Analysis **74**, 102210 (2021) https://doi.org/10.1016/j.media.2021.102210

[46] Azzolin, L., Eichenlaub, M., Nagel, C., Nairn, D., Sánchez, J., Unger, L., Arentz, T., Westermann, D., Dössel, O., Jadidi, A., *et al.*: Augmenta: patient-specific augmented atrial model generation tool. Computerized Medical Imaging and Graphics **108**, 102265 (2023) https://doi.org/10.1016/j.compmedimag.2023.102265

[47] Qian, J., Zhang, Y.-T., Zhao, H.-K.: A fast sweeping method for static convex hamilton–jacobi equations. Journal of Scientific Computing **31**(1-2), 237–271 (2007) https://doi.org/10.1007/s10915-006-9124-6

[48] Capozzoli, A., Curcio, C., Liseno, A., Savarese, S.: A comparison of fast marching, fast sweeping and fast iterative methods for the solution of the eikonal equation. In: 2013 21st Telecommunications Forum Telfor (TELFOR), pp. 685–688 (2013). https://doi.org/10.1109/TELFOR.2013.6716321 . IEEE

[49] Unger, L.A., Azzolin, L., Nothstein, M., Sanchez, J., Luik, A., Seemann, G., Yeshwant, S., Oesterlein, T., Doessel, O., Schmitt, C., *et al.*: Cycle length statistics during human atrial fibrillation reveal refractory properties of the underlying

substrate: a combined in silico and clinical test of concept study. EP Europace **23**(Supplement_1), 133–142 (2021) https://doi.org/10.1093/europace/euaa404

[50] Deng, D., Murphy, M.J., Hakim, J.B., Franceschi, W.H., Zahid, S., Pashakhanloo, F., Trayanova, N.A., Boyle, P.M.: Sensitivity of reentrant driver localization to electrophysiological parameter variability in image-based computational models of persistent atrial fibrillation sustained by a fibrotic substrate. Chaos: An Interdisciplinary Journal of Nonlinear Science **27**(9) (2017) https://doi.org/10.1063/1.5003340

[51] Corrado, C., Williams, S., Karim, R., Plank, G., O'Neill, M., Niederer, S.: A work flow to build and validate patient specific left atrium electrophysiology models from catheter measurements. Medical Image Analysis **47**, 153–163 (2018) https://doi.org/10.1016/j.media.2018.04.005

[52] Martínez Díaz, P., Dasí, A., Goetz, C., Unger, L., Haas, A., Luik, A., Rodríguez, B., Dössel, O., Loewe, A.: Impact of effective refractory period personalization on arrhythmia vulnerability in patient-specific atrial computer models. medRxiv, 2024–06 (2024) https://doi.org/10.1101/2024.06.06.24308556

[53] Serra, D., Romero, P., Garcia-Fernandez, I., Lozano, M., Liberos, A., Rodrigo, M., Bueno-Orovio, A., Berruezo, A., Sebastian, R.: An automata-based cardiac electrophysiology simulator to assess arrhythmia inducibility. Mathematics **10**(8), 1293 (2022) https://doi.org/10.3390/math10081293

[54] Sermesant, M., Coudière, Y., Moreau-Villéger, V., Rhode, K.S., Hill, D.L., Razavi, R.: A fast-marching approach to cardiac electrophysiology simulation for xmr interventional imaging. In: Medical Image Computing and Computer-Assisted Intervention–MICCAI 2005: 8th International Conference, Palm Springs, CA, USA, October 26-29, 2005, Proceedings, Part II 8, pp. 607–615 (2005). https://doi.org/10.1007/11566489_75 . Springer

[55] Gander, L., Krause, R., Weiser, M., Sahli Costabal, F., Pezzuto, S.: On the accuracy of eikonal approximations in cardiac electrophysiology in the presence of fibrosis. In: International Conference on Functional Imaging and Modeling of the Heart, pp. 137–146 (2023). Springer

[56] Colli Franzone, P., Guerri, L., Rovida, S.: Wavefront propagation in an activation model of the anisotropic cardiac tissue: asymptotic analysis and numerical simulations. Journal of Mathematical Biology **28**, 121–176 (1990) https://doi.org/10.1007/BF00163143

[57] Keener, J.P.: An eikonal-curvature equation for action potential propagation in myocardium. Journal of Mathematical Biology **29**(7), 629–651 (1991) https://doi.org/10.1007/BF00163916

[58] Keener, J.P., Tyson, J.J.: Spiral waves in the belousov-zhabotinskii reaction.

Physica D: Nonlinear Phenomena **21**(2-3), 307–324 (1986) https://doi.org/10.1016/0167-2789(86)90007-2

Chapter 7

Investigating Conduction Velocity Restitution Using the Diffusion Reaction Eikonal Alternant Model

This chapter shows the an application of the diffusion reaction eikonal alternant model (DREAM) investigating the effects of conduction velocity (CV) restitution properties on the dynamics of reentry events.

The work presented in this chapter is based on research conducted during the master's thesis of M.Sc. Silvia Becker, which was supervised and guided by the author of this thesis [105].

7.1 Introduction

Atrial fibrillation (AF) remains a significant public health issue worldwide, primarily due to the incomplete understanding of its underlying pathophysiological mechanisms [106]. Among the extensively studied factors, changes in CV have been identified as key contributors to increased AF risk. Slow and heterogeneous CV is a well-established mechanism linked to AF vulnerability [87, 88]. Additionally, CV restitution plays a crucial role in promoting reentry mechanisms, further increasing the risk of AF [107]. Despite its importance, CV restitution has not been fully investigated. A deeper understanding of the relationship between CV and pacing frequency could enhance knowledge of AF mechanisms and offer new insights into patient assessment. These new insights can enable new pharmacological or ablation targets to improve the treatment and prevention of AF episodes.

Several numerical studies have offered initial understanding into the influence of CV restitution on arrhythmia vulnerability, factors modifying CV restitution, and methods to assess restitution in patients. Qu et al. provide insights into the mechanisms underlying cardiac arrhythmias by analyzing how preexisting gradients in refractoriness affect the vulnerable window for unidirectional conduction block caused by premature extrasystoles. They highlight that a critical action potential duration gradient, influenced by CV restitution and gap junction conductance, is essential for understanding the risk of lethal arrhythmias [108, 109]. They further demonstrate that discordant action potential duration (APD) alternans, driven by steep APD and CV restitution properties, increases the dispersion of refractoriness and the susceptibility to reentrant arrhythmias, suggesting potential strategies for antiarrhythmic interventions through the modulation of electrical restitution properties. Xie et al. discuss the impact of electrotonic coupling between fibroblasts and myocytes on CV restitution, showing that this coupling significantly alters CV restitution, promotes spatially discordant alternans, and affects APD, which plays a crucial role in arrhythmogenesis in fibrotic cardiac tissue [110]. Additionally, Nothstein et al. presented the CVAR-Seg pipeline, which automates the analysis of S1-S2 protocols, delivering accurate evaluations of CV and restitution curves in atrial tissue, even under challenging noise conditions, thus enhancing the characterization of AF risk [107].

This study aims to expand the understanding of CV restitution by exploring how its morphology affects arrhythmia vulnerability and maintenance. The DREAM is used to simulate and analyze the vulnerable window and reentry duration under different CV restitution parameters. This approach provides insights into the relationship between CV restitution dynamics and the risk of arrhythmias.

7.2 Methods

The methods section starts by presenting the patient data collected to obtain parameters for the numerical simulations. Next, the computational tools used are outlined followed by definition, and parametrization of the restitution curve that was fed into the DREAM. The process of tuning the ionic model within DREAM for conducting in-silico experiments is then be described. Afterwards, the experiments conducted to assess vulnerability with different scenarios are detailed. Finally, the methods for data analysis are presented.

7.2.1 Patient Data

This study included 13 patients with persistent AF, with an average age of 67 ± 8 years, of whom 8 were female. Each patient underwent electroanatomical mapping and a decremental pacing protocol at Städtisches Klinikum Karlsruhe. Two mapping catheters were used: the Constellation basket catheter and the Orion mini-basket catheter (both from Boston Scientific Corporation), each equipped with 64 electrodes. The study was approved by the Institutional Review Board, and all participants provided informed written consent prior to their involvement.

First, the Orion mini-basket catheter was used to identify the atrial geometry. Following this, the decremental pacing protocol was performed. This protocol involved pacing from the coronary sinus at progressively shorter intervals, starting with longer intervals and decreasing until AF was induced. The pacing triggered an excitation wave, which activated the atrial myocardium. One of the mapping catheters was then used to measure the time between pacing and the activation detected by each electrode, defined as the post pacing interval (PPI).

The pacing cycle lengths (PCLs) ranged from 600 ms to 180 ms. Initially, the pacing intervals decreased by 50 ms increments until reaching 300 ms, and then by 10 ms steps until 180 ms or until AF was induced. An exemplary pacing protocol for one of the patients is illustrated in Figure 7.1. The PCL, that ultimately induced AF, is referred to as the last propagating PCL in this study. It is important to clarify that the CV at each PCL was not directly estimated in this study. Specifically, the CV was not derived from the activation time (AT) recorded during each PCL.

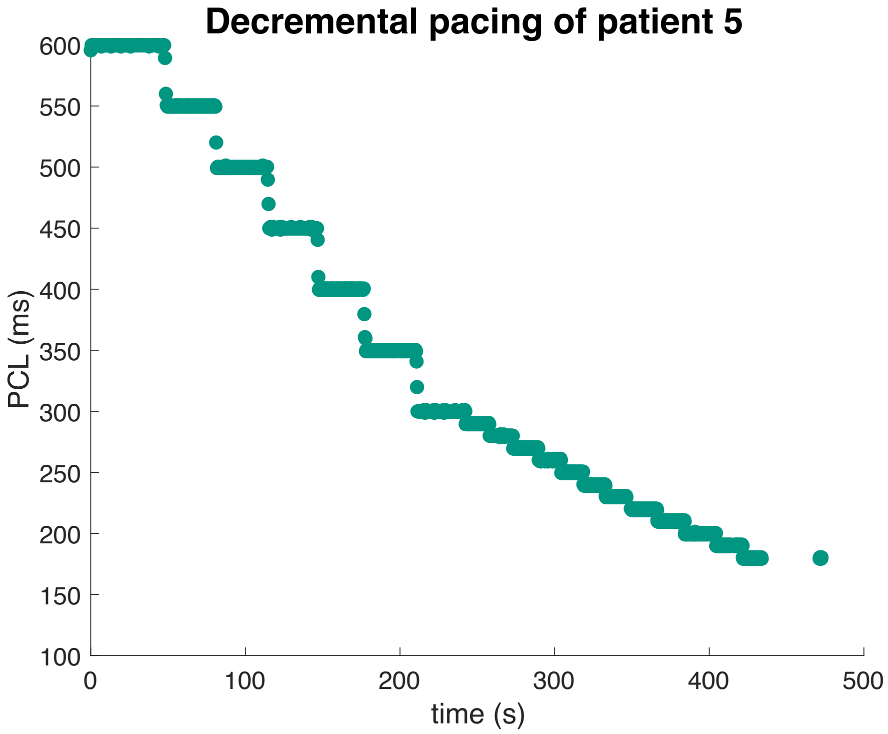

Figure 7.1: Decremental pacing. The pacing cycle length started at 600 ms and was progressively reduced over time until 180 ms was reached. The gap at the end of the protocol results from measurement errors caused by poor contact.. Figure reproduced from [105].

7.2.2 Software Tools

This section outlines the software tools used in this study for statistical analysis, data visualization, and electrophysiological simulations of cardiac tissue. MATLAB was employed for statistical analysis, data visualization, and importing clinical data [111]. Electrophysiological simulations were conducted using openCARP, a freely available cardiac electrophysiology simulator [103], with the DREAM selected for performing the in-silico experiments [22, 104]. Python [112] was used to integrate the carputils package, execute the simulations, and handle data processing and visualization.

7.2.3 Conduction Velocity Restitution Curve

This section defines and explains the parametrization of the CV restitution curve, which is fed into the DREAM. First, the formula used to parametrize the restitution curve is introduced, followed by an explanation of its parameters. The remainder of this work assumes that the restitution of CV is independent of propagation speed (i.e., v_{ref}), and monodomain simulations are conducted to validate this assumption. Finally, the process of fitting the CV restitution formula to patient data is explained. Each set of data obtained from an electrode is fitted with a separate curve, resulting in one restitution curve per electrode measurement for each patient.

Conduction Velocity Restitution Formula To represent the shape of the CV restitution curve as a continuous function, a formula was developed that defines the CV as a function of the PCL. This formula differs from the restitution curve outlined in the DREAM manuscript, as it uses PCL as the independent variable instead of the diastolic interval (DI) (refer to Equation 12 in [22], Chapter 6).

$$CV_{\text{PCL}} = \begin{cases} v_{\text{ref}} \left(1 - \rho \cdot e^{-(\text{PCL}+\kappa)\frac{\log(\rho)}{\psi}}\right) & \text{for PCL} \geq \theta \\ 0 & \text{for PCL} < \theta \end{cases} \tag{7.1}$$

This formula was designed to be straightforward, with parameters that are easy to interpret and each affecting a specific characteristic of the curve. The parameter ρ controls the steepness of the curve and is dimensionless, while κ represents a shift of the curve along the x-axis measured in ms. Figures 7.2 and 7.3 illustrate a sensitivity analysis of ρ and κ, respectively.

The last propagating PCL is denoted by θ also measured in ms. If the PCL is less or equal to θ, the excitation wave cannot propagate, resulting in a CV of 0 mm/s. Since the minimum PCL in the decremental protocol was 180 ms, θ is set to this value in the sensitivity analyses in Figures 7.2 and 7.3. These curves are cropped due to the presence of negative CV values at low PCLs, which is deemed unrealistic. For simplicity, the value of ψ was initially determined empirically and fixed at 67 ms, with its variability not being considered in this study. The reference CV when there are no restitution effects (i.e., at large PCL) is denoted v_{ref}. In the figures depicting the sensitivity analyses, v_{ref}, the maximal longitudinal CV, was normalized. The following experiments are designed to demonstrate that the CV restitution is independent of the reference CV v_{ref}.

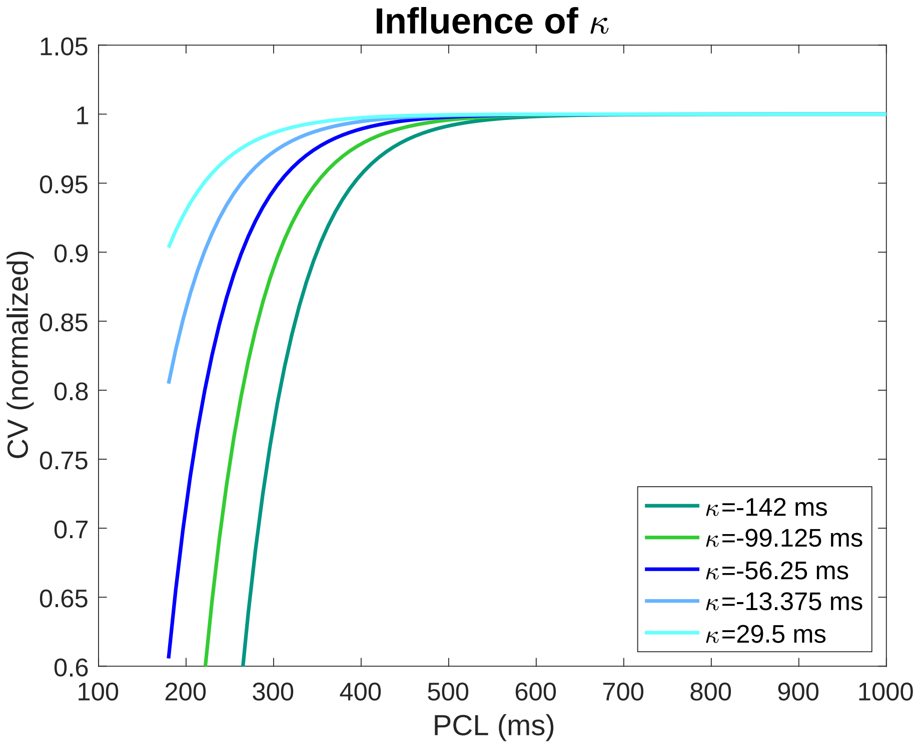

Figure 7.2: Conduction velocity restitution curves of varying parameter κ with ρ fixed at 3. Figure reproduced from [105].

Monodomain Simulations An important assumption made for this study was that the effects of CV restitution are independent of the reference CV. To verify this, a series of monodomain simulations were conducted to obtain CV restitution curves under different scenarios. A simple rectangular mesh geometry of 10 mm by 1 mm was used for this purpose, containing triangular elements with an average edge length of approximately 200 µm. Figure 7.4 shows a representation of the geometry used for these simulations. Courtemanche et al.'s model was selected as the ionic model with the original parameters for the healthy scenario, and the conductances were adjusted based on Loewe's work to simulate AF [66, 113].

To generate the restitution curves, an in-silico S1-S2 protocol was performed on the geometry. First, five planar wavefronts (S1) were initiated by stimulating the left border of the mesh at a PCL of 250 ms. The next stimulus, S2, was used to trigger the sixth planar wavefront by stimulating the same region on the left border. Separate simulations were carried out for each S1-S2 interval, ranging from 1000 ms down to 130 ms, with 200 ms decrements between 1000 ms and 400 ms, 20 ms decrements between 400 ms and 200 ms, and finally 10 ms decrements from 200 ms to 130 ms. The protocol was stopped when the PCL reached 130 ms or when the S2 stimulus failed to propagate through the mesh.

To calculate the CV, two nodes positioned in the center of the geometry were selected, ensuring a distance of 2 mm between them. These nodes were placed sufficiently far from the boundaries to minimize any boundary effects. Figure 7.4 illustrates the location of these

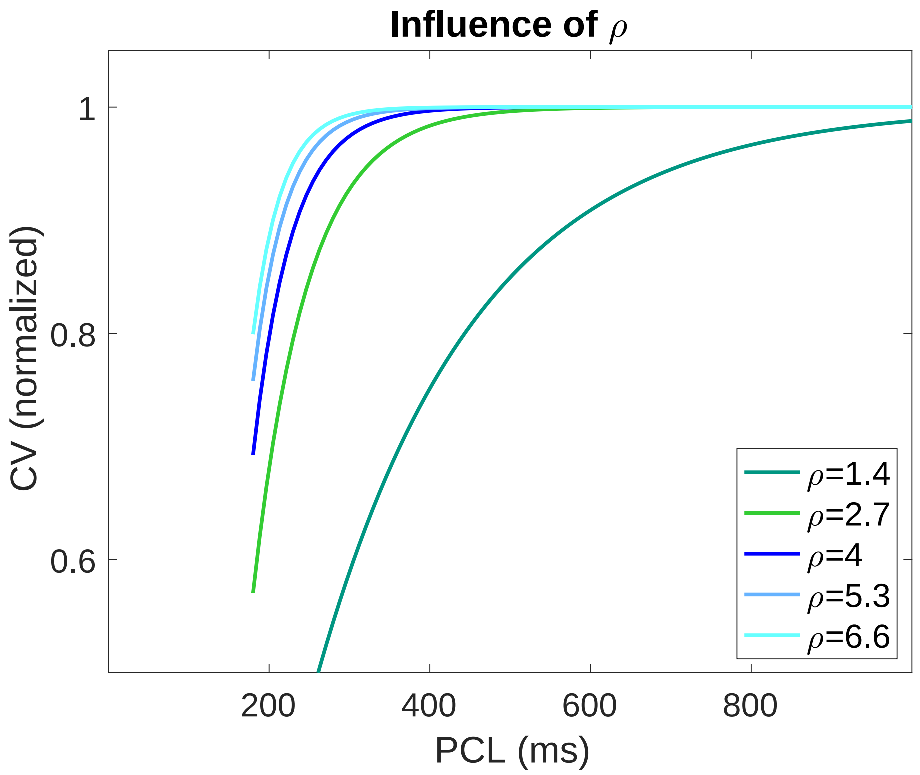

Figure 7.3: Conduction velocity restitution curves of varying parameter ρ with κ fixed at -56 ms. Figure reproduced from [105].

nodes. The CV was computed by dividing the 2 mm distance by the difference in the ATs recorded at the two nodes following the S2 stimulus.

The CV restitution curve was generated by associating each PCL with its corresponding calculated CV. This restitution curve was derived for the healthy and the AF scenario, with reference CV values of 300 mm/s, 500 mm/s, 700 mm/s, and 1000 mm/s. To achieve these target reference CV values, tissue conductivities were adjusted using the tuneCV function from openCARP, following the approach described by Costa et al. [103, 114].

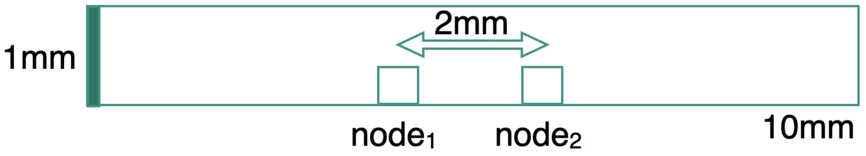

Figure 7.4: Mesh for conduction velocity (CV) restitution curves. This mesh was used to obtain CV restitution curves from monodomain simulations, with dimensions of 10 mm x 1 mm and two central nodes separated by 2 mm for CV calculation. The thickened edge on the left represents the stimulated area. Figure reproduced from [105].

Personalization of Parameters ρ and κ Once the independence between the reference CV and CV restitution was confirmed, CV restitution curves for the patient data were fitted. Although CV was not directly measured, the restitution curves could still be estimated. This was done by assuming that the factor responsible for prolonging the PPI (i.e., time interval between the pacing in the coronary sinus and the activation of a given electrode) as the PCL shortens is the inverse of the factor that causes the CV to decrease when the PCL is shortened. For each electrode and patient, the PPI dataset across all PCL values was inverted and normalized to create the target data for fitting the CV restitution formula. The parameters ρ and κ were then adjusted to minimize the root mean square error (RMSE) between the observed data and the restitution formula. As a result, one pair of ρ and κ values was obtained for each electrode for every patient. The reference CV was not calculated per electrode since the restitution curve was assumed independent from v_{ref}.

Outliers caused by measurement errors in the clinical setting were identified by examining the parameters ρ and κ. Any parameter with a value greater than three scaled median absolute deviations from the median was flagged as an outlier. If either ρ or κ in a pair was classified as an outlier, the entire pair was removed from the dataset. To assess potential sex bias, advanced statistical tests were employed to examine differences in the ρ and κ parameters between men and women. A generalized linear mixed-effects model was applied to account for variations across different patients, which was essential to properly handle the multiple measurements taken per patient.

Ionic Model Tuning to Last Propagating Cycle Length Since the decremental pacing protocol in patients was stopped after AF was induced, it was not possible to assign an individual last propagating PCL to each electrode. Instead for all the electrodes within the same patient the last propagating PCL was assumed to be the PCL when AF was induced. On the other hand, in the DREAM, the last propagating PCL is an explicit parameter in the model (i.e., parameter θ). To avoid inconsitencies between the parameter θ and the ionic model, the conductance values of the ionic model were tuned to match the desired last propagating PCL.

To tune the conductances, it was assumed that the conductances derived from Loewe's model yield the shortest possible last propagating PCL under maximum remodeling conditions. Conversely, the healthy parameters were expected to provide the longest last propagating cycle length and the minimum level of remodeling. A linear interpolation was then defined between the sets of conductance values for the healthy case and the AF case.

To facilitate this, a factor $x \in [0,1]$ was defined, and each factor x is mapped to a set of conductances of the ionic model. In this mapping, $x = 0$ is assigned to the set of parameters for the healthy case, and $x = 1$ corresponds to the set of parameters for the AF case. For any given $x \in [0,1]$ and any ion X, the conductance for its channel $g_X(x)$ is defined as:

$$g_X(x) = (1-x) \cdot g_X(0) + x \cdot g_X(1) \tag{7.2}$$

where $g_X(0)$ and $g_X(1)$ are the conductance values for the healthy and AF scenarios, respectively.

A series of 16 values for x, distributed between 0 and 1, was used to create 16 sets of conductance values representing varying levels of remodeling. A restitution curve was generated using the monodomain model, as previously described, to obtain the last propagating PCL for each set of conductances. Each factor x was then paired with its corresponding last propagating PCL, denoted as θ.

A polynomial fit was established to predict the factor x based on the given θ. The parameters of a cubic polynomial function were optimized to minimize the RMSE between the 16 obtained data points and the polynomial fit.

7.2.4 Vulnerability Assessment

Once the parameters ρ, κ, and θ were obtained for each electrode and patient, excluding outliers, simulations were conducted to assess the vulnerability of a representative set of CV restitution parameters. Specifically, DREAM simulations were performed to replicate the S1-S2 protocol and induce reentries. For this step, a 2D sheet measuring 50 mm by 50 mm, composed of triangular elements with an average edge length of approximately 800 µm, was utilized.

Similar to the S1-S2 protocol used to obtain the restitution curve, five S1 stimuli were applied to the left border of the mesh to generate five sequential planar wavefronts. Subsequently, an S2 stimulus was applied in the lower left quarter of the mesh as a cross-field stimulus to attempt to induce reentry. Figure 7.5 illustrates the geometry used for the simulations and the location where the stimuli were applied. For each valid set of parameters ρ, κ, and θ, a reference CV of either 200 mm/s, 400 mm/s, or 600 mm/s was selected to run the protocol.

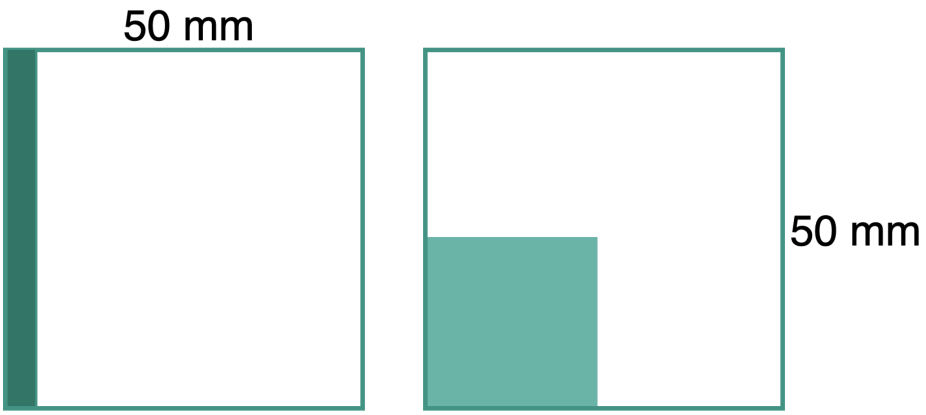

Figure 7.5: Mesh for inducing reentries using the DREAM. The mesh is 50 mm x 50 mm. S1 pacing starts from the thickened left edge, while the S2 location is shown by the light green area in the right image. Figure reproduced from [105].

In this study, a single experiment is defined as a set of simulations in which the S1-S2 protocol was executed for a specified set of parameters ρ, κ, θ, and v_{ref} to identify the time intervals between the S1 and S2 stimuli that induce reentry. In these experiments, the four parameters defining the CV restitution and reference CV were assigned homogeneously across the entire geometry.

Additional experiments were conducted to assess heterogeneous CV restitution by assigning a fixed to the mean value for parameter ρ and a constant v_{ref} across the entire geometry, while applying the minimal and maximal κ values observed for the mean parameter ρ to the left and right halves of the geometry. The experiments were then repeated by fixing κ and using the minimal and maximal ρ values observed for the mean parameter κ.

For each experiment, after running the S1-S2 protocols, two key outputs were analyzed: the vulnerable window and the average reentry duration. The vulnerable window was defined as the difference between the longest and shortest S1-S2 interval that induced reentry. The duration of a reentry was defined as the time interval between the application of the S2 stimulus and the last AT (AT) in the simulation. If the reentry did not self-terminate, a maximum duration was set, defined as the total simulation time of 2000 ms minus the difference between S1 and S2. The average reentry duration was calculated as the mean duration of reentry across all S1-S2 intervals that induced reentry during a given experiment.

7.3 Results

7.3.1 Conduction Velocity Restitution Parameters

Figure 7.6 presents the CV restitution curves from monodomain simulations for both healthy and AF tissue at varying baseline v_{ref} values. Each curve has been normalized to its corresponding reference CV, allowing for a clear comparison. Notably, after normalization, the restitution curves align closely across all scenarios, demonstrating minimal variation regardless of their absolute values.

After confirming that variations in conductivities did not influence the restitution effects, the data from each electrode was fitted to the restitution curve formula, obtaining the parameters ρ, κ, and θ for each measurement. Figure 7.7 illustrates the restitution curves generated from these fitted parameters, along with the simulated curves using the monodomain model for different conductance sets: AF from Loewe and the healthy case [105, 113]. Notably, most patient-derived restitution curves and all θ values fall between the AF model of Loewe and the healthy restitution curve. Among all the potential modelling strategies for AF, Loewe was chosen for its particularly low last propagating PCL. Figure 7.8 shows all the clinical set of normalized parameters ρ and κ in a scatter plot. A grid of 12 points uniformly distributed was located inside the sample space. The closest 12 pairs of ρ and κ to the points in the grid that also had the information for θ available were chosen to run simulations to assess arrhythmia vulnerability. The statistical analysis revealed no significant sex differences for

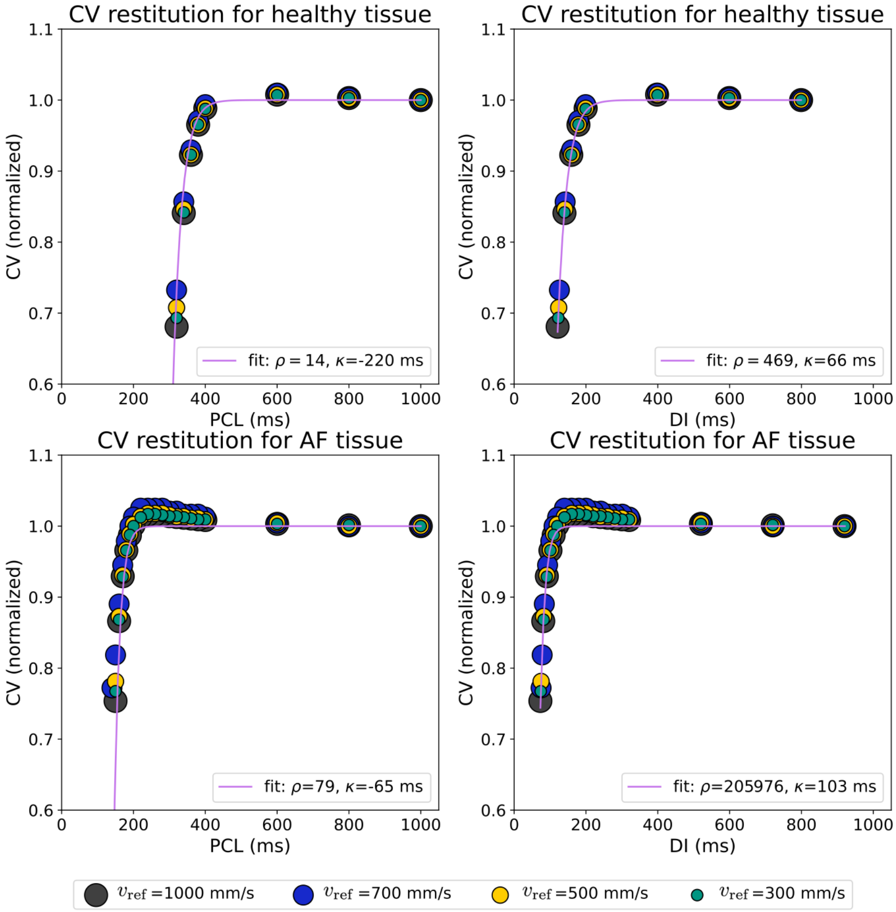

Figure 7.6: Conduction velocity restitution curves from monodomain simulations for healthy and AF tissue and different v_{ref} values. The various colors denote different v_{ref} values, ranging from 300 mm/s to 1000 mm/s. The size of the points was only chosen to visualize overlapping points and does not have additional meaning. The fitted curve is depicted in violet. Healthy tissue was simulated with the conductance values of the Courtemanche model and atrial fibrillation tissue with the conductance values of Loewe [113]. Restitution is estimated based on pacing cycle length (left) or diastolic interval (right). Figure reproduced from [105].

any parameter after controlling for the batch effect, considering that data were collected from 13 patients, each with multiple electrodes contributing to the parameter analysis.

Figure 7.9 displays the simulation data points relating the factor $x \in [0,1]$ to the last propagating PCL, represented by the parameter θ. To minimize the RMSE, a third-degree polynomial was fitted to the data. Using this regression, the conductance values of the ionic model could be freely adjusted to any desired last propagating PCL. The resulting parameter optimization yielded the regression in Equation 7.3.

$$x = c_1\theta^3 + c_2\theta^2 + c_3\theta + c_4, \tag{7.3}$$

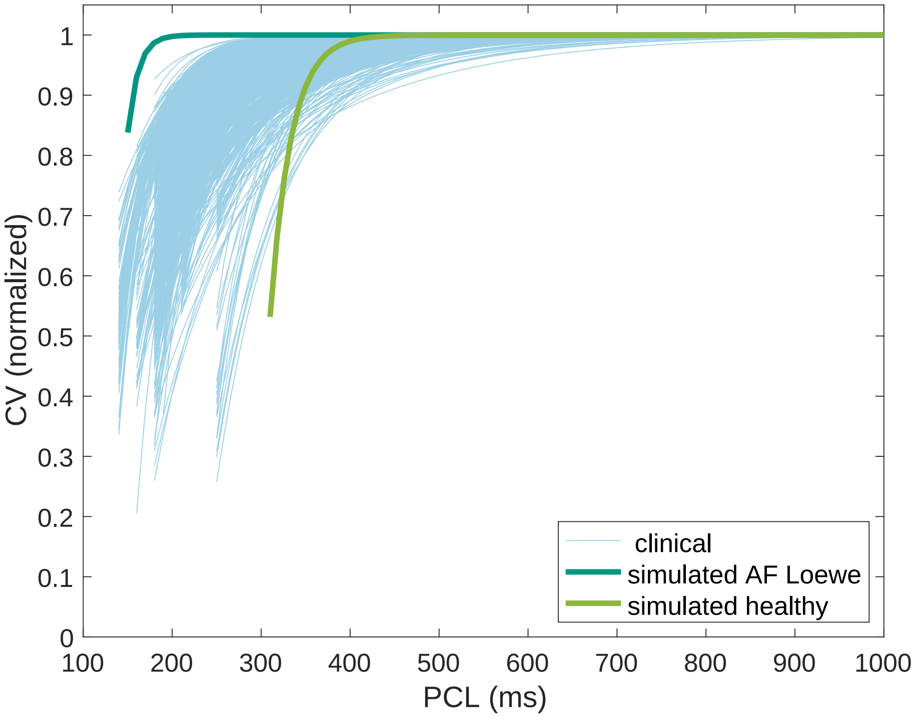

Figure 7.7: Simulated and Clinical conduction velocity Restitution Curves. Clinical conduction velocity restitution curves are shown in blue, while simulated curves are in red, orange, and green. The light green line represents healthy simulations using Courtemanche model conductance values. The dark green line corresponds to atrial fibrillation simulations with conductance values from Loewe [113]. Figure reproduced from [105].

where the coefficients are optimized to the following values:

$$
\begin{aligned}
c_1 &= 52.67 \cdot 10^{-6}\,\mathrm{ms}^{-3},\\
c_2 &= 38.82 \cdot 10^{-5}\,\mathrm{ms}^{-2},\\
c_3 &= -97.82 \cdot 10^{-3}\,\mathrm{ms}^{-1}\\
c_4 &= -869.9(-).
\end{aligned}
$$

7.3.2 Vulnerability Assessment

In Figure 7.10, the results from four experiments are shown, each conducted with a different set of parameters. The data illustrate that slower conduction velocities result in a wider vulnerable window and longer reentry durations. In the upper left, the experiment uses parameter values of $\rho = 4$, $\kappa = \text{-}24\,\mathrm{ms}$, $\theta = 140\,\mathrm{ms}$, and $v_{\mathrm{ref}} = 200\,\mathrm{mm/s}$. In this case, the vulnerable window was 114 ms. The reentry duration varied across different S1-S2 intervals without showing a dominant trend. Initially, a stable baseline duration was observed, followed by a slightly elevated baseline. Additionally, sporadic episodes of significantly longer reentry durations appeared between these baseline phases. In the top right, a similar experiment with

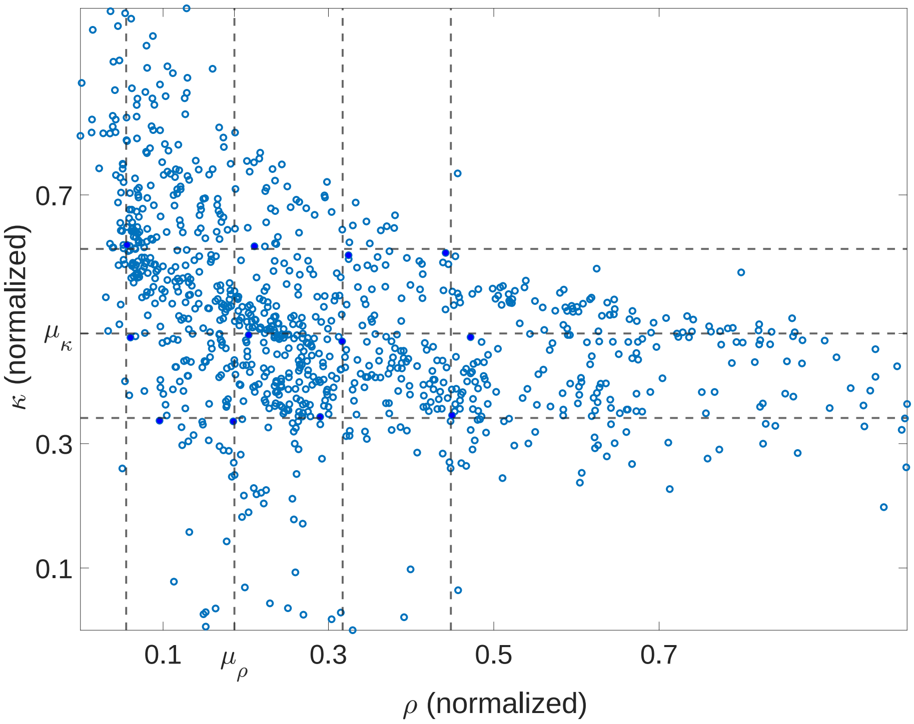

Figure 7.8: Clinically measured and normalized ρ and κ values for all patients are shown. The grid is derived from the mean values with variations of multiple standard deviations. The points closest to the grid points with information about θ are filled in blue. These combinations of ρ and κ were utilized for the reentry experiments. Outliers are not shown. Figure reproduced from [105].

the same v_{ref}, $\kappa = 22$ ms, a smaller ρ ($\rho = 2$), and a higher θ shows a comparable pattern. Reentry durations varied, with stable baselines interrupted by occasional longer reentry episodes. The vulnerable window in this case was 180 ms. In the left bottom corner, the depicted experiments with $v_{\text{ref}} = 600$ mm/s. The other parameters were $\rho = 4$, $\kappa = 57$ ms, and $\theta = 160$ ms. Here, the vulnerable window was much shorter, only 45 ms, with shorter reentry durations and no intermittently longer reentries. Finally, the bottom right experiment, conducted with $v_{\text{ref}} = 600$ mm/s, and values of $\rho = 2$, $\kappa =$ -55 ms, and $\theta = 210$ ms, showed similar qualitative behavior to the previous example, with a vulnerable window of 54 ms.

Figures 7.11 and 7.12 illustrate the relationship between the average vulnerable window and the average duration of reentries as a function of the parameter ρ. In Figure 7.11, the black dots represent the results of individual experiments, while the bars indicate the average vulnerable windows for different reference CVs (v_{ref}) of 200 mm/s (dark green), 400 mm/s (light green), and 600 mm/s (blue). It is evident that as ρ increases (i.e., the restitution curve is steeper), the average vulnerable window decreases, particularly for lower conduction velocities. It is also possible to see how the vulnerable window is greater for slower conduction velocities. Similarly, Figure 7.12 presents the average duration of reentries, with results showing a consistent trend across the different reference conduction velocities. The black dots indicate individual experimental results, while the bars represent the averages, demonstrating that longer average reentry durations correspond to lower values

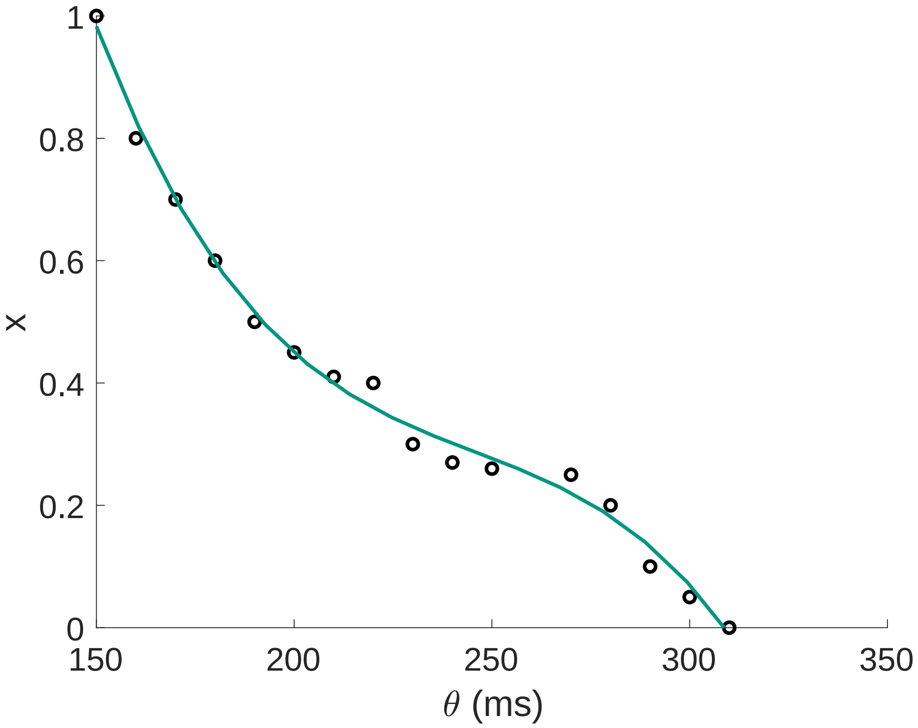

Figure 7.9: Cubic polynomial fit used to approximate factor x from patient-derived θ (i.e., last propagating PCLs). The circles are measurements obtained by simulations in the monodomain model to obtain the polynomial fit. The green line shows the fitted cubic function, see Equation 7.3. Figure reproduced from [105].

for the parameter ρ (i.e., less steep curve), especially at lower conduction velocities. Both figures highlight that the smaller values for the parameter ρ have higher risk of vulnerability and stable reentry. Regarding the heterogeneous simulations, the simulations showed that heterogeneous ρ values were associated with a greater vulnerable window and shorter average duration. There were not clear patterns or trends for the variations in parameters ρ and θ for the analysed dataset.

7.4 Discussion

The primary advantage of this study is the ability to utilize a rare clinical dataset. It is quite challenging to obtain clinical data where a decremental protocol has been measured across multiple patients and electrodes, particularly in patients where all have persistent AF. The investigation of this clinical data was supported by numerical simulations conducted using a monodomain model and the DREAM [22].

One of the initial tested hypotheses was to examine whether the restitution effects on CV are independent of the reference CV. Therefore, variations in conductivity in the monodomain model yield similar restitution effects. The simulations showed that the hypothesis was true

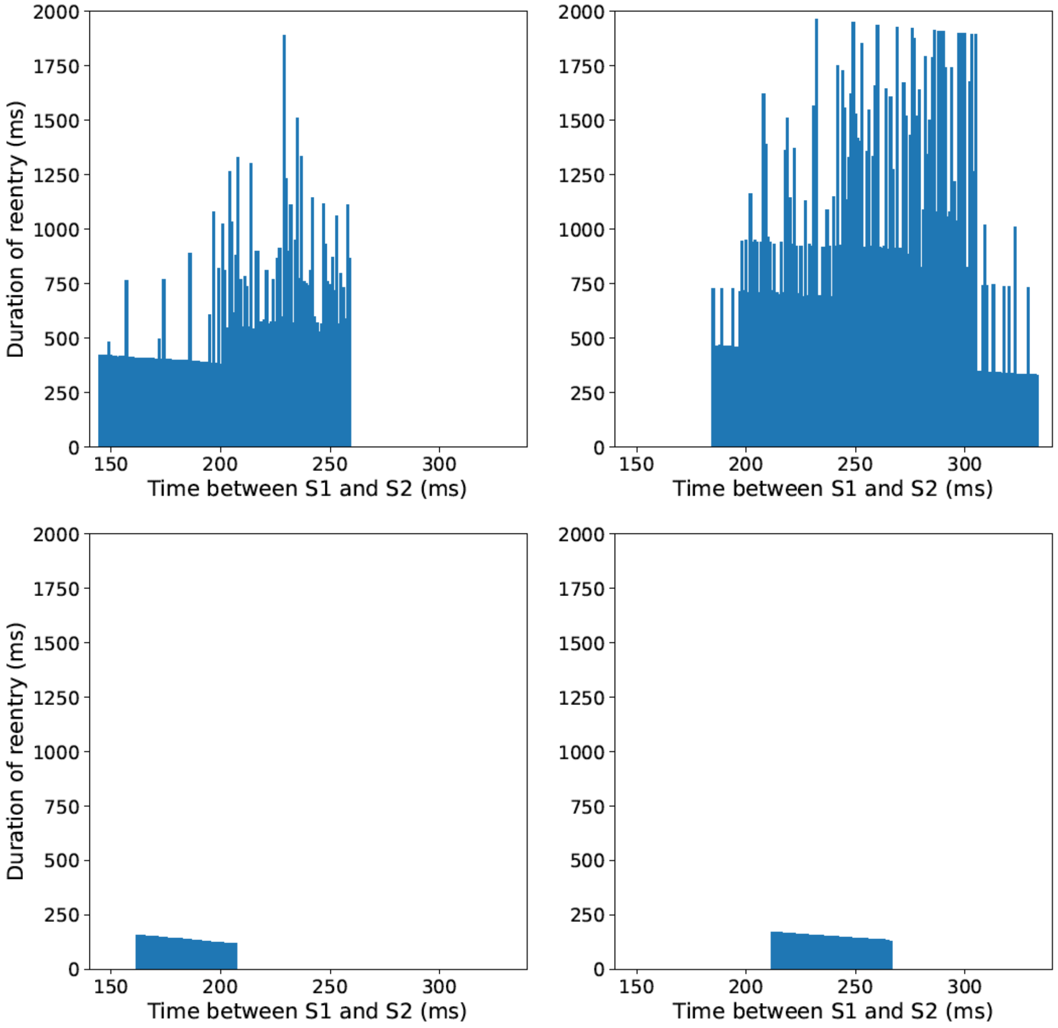

Figure 7.10: Results of Single Experiments with Steep and Shallow conduction velocity Restitution Curves. Results of four simulations with varying S2 timings (horizontal axis) and reentry durations (vertical axis). The top left plot has parameters $v_{\text{ref}} = 200\,\text{mm/s}$, $\rho = 4$, $k = -24\,\text{ms}$, $\theta = 140\,\text{ms}$; the top right $v_{\text{ref}} = 200\,\text{mm/s}$, $\rho = 2$, $\kappa = -22\,\text{ms}$, $\theta = 180\,\text{ms}$. The bottom left shows the results for $v_{\text{ref}} = 600\,\text{mm/s}$ with $\rho = 4$, $\kappa = -57\,\text{ms}$, $\theta = 160\,\text{ms}$, and the bottom right for $\rho = 2$, $\kappa = -55\,\text{ms}$, $\theta = 210\,\text{ms}$. Figure reproduced from [105].

since varying conductivities showed only small differences in normalized CV restitution obtained from monodomain simulations.

Another important advantage of combining numerical models with the clinical dataset is the ability to fit the conductance values of the ionic model to the last PCL. By utilizing a regression model and a cubic polynomial function, the parameters of this polynomial were adjusted to match the data generated from monodomain simulations. This approach provided the flexibility to perform DREAM simulations with restitution curves derived from real patient data.

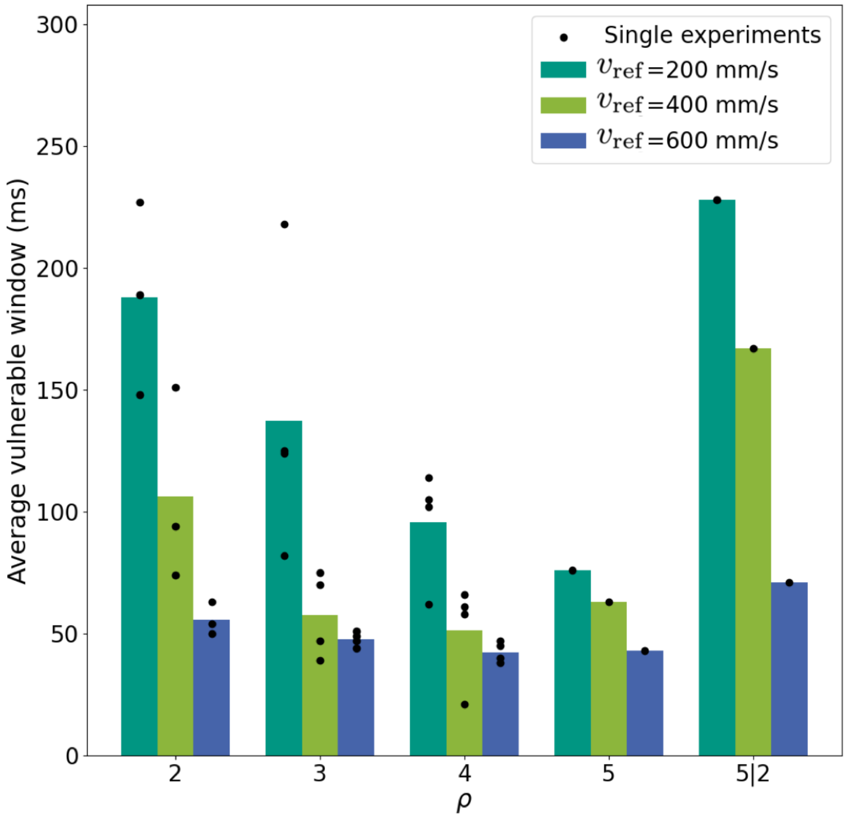

Figure 7.11: Average vulnerable window over ρ. The black dots show the results of the single experiments. The bars show the average over those results. In dark green the results for a v_{ref} of 200 mm/s, in light green of 400 mm/s and in blue for 600 mm/s are shown. The last entry on the horizontal axis represents the heterogeneous experiment for ρ. Figure reproduced from [105].

A benefit of the dataset was the sex balance, which included a significant amount of female patients. Although the population size was small, each patient provided signals from multiple electrodes. This allowed for a statistical analysis of sex differences in the parameters of the restitution curve. After accounting for the batch effect, the differences in parameters between genders were not significant. For this reason, there was no need to disaggregate the data per sex for the remainder of the study.

This study demonstrated one of the primary use cases of the DREAM: the ability to personalize CV restitution for patients. This flexibility allows for the tuning of the restitution curve as needed, enabling simulations that provide new insights into vulnerability and the risk of reentry and arrhythmia. One of the main insights from this study was that the steepness of the restitution curve, represented by parameter ρ, plays a considerable role in modulating the average duration of reentry and the vulnerable window. Additionally, heterogeneous ρ across the geometry also increases the vulnerable window but renders it more unstable. The decreasing average vulnerable window with increasing ρ can be explained by the fact

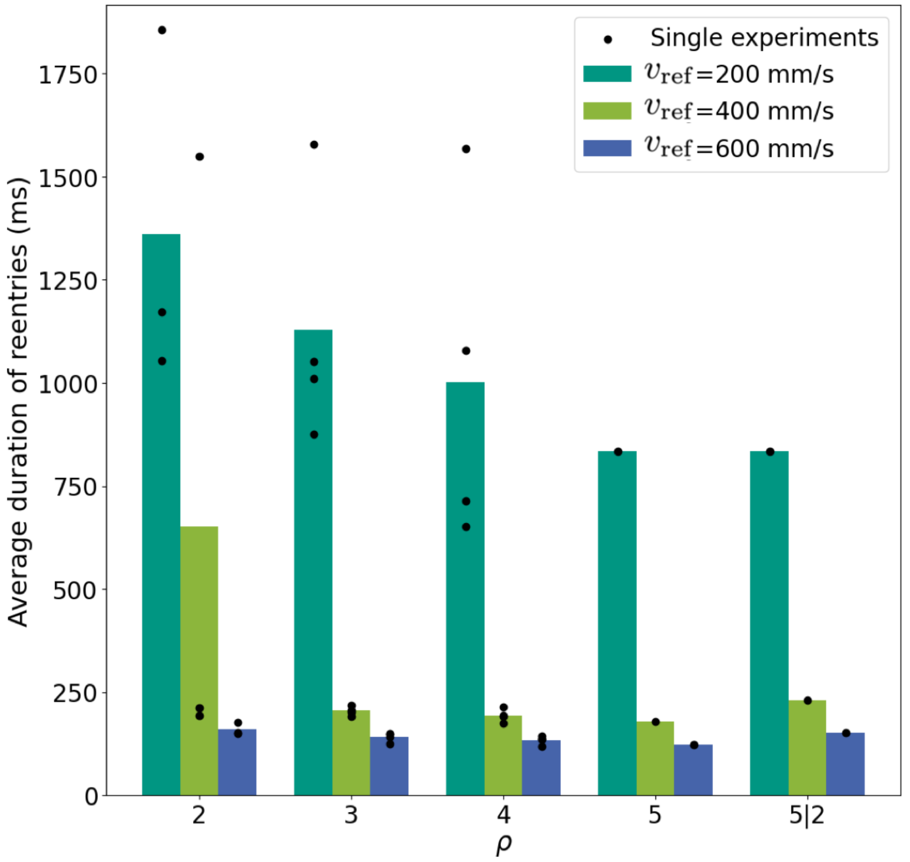

Figure 7.12: Average duration of reentries over ρ. The black dots show the results of the single experiments. The bars show the average over those results. In dark green the results for a v_{ref} of 200 mm/s, in light green of 400 mm/s and in blue for 600 mm/s are shown. The last entry on the horizontal axis represents the heterogeneous experiment for κ. Figure reproduced from [105].

that a steep conduction CV restitution curve (indicated by a greater value for parameter ρ) corresponds to a narrower range of PCL for which restitution occurs. In this scenario, a wave can either propagate, be slowed down over a few PCLs, or be completely blocked. Conversely, a less steep CV restitution curve has a broader range of PCLs where restitution is effective, allowing for more PCLs to slow the wave without causing a block. The results provided in this study align with what was shown in previous study about the important role of CV restitution especially regarding the steepness of the curve [108].

One of the main limitations of this study, compared to the DREAM as described in the original manuscript, is that the restitution curve uses PCL as the independent variable, whereas the DREAM manuscript employs the DI. This choice has the disadvantage of overlooking variations in CV due to fluctuations in action potential duration. In future work, it may be possible to replace the PCL with an approximated DI [115]. The reason the PCL was chosen over the DI for this study was that it is more readily obtainable from the clinical dataset, while measuring the real DI is currently quite challenging with existing mapping systems. Another limitation directly connected to the DREAM is the lack of explicit representation of the CV alternants which might be introduced in future work.

Another noteworthy limitation is the absence of region-specific last propagating PCL. Instead, a global parameter θ was selected for each patient, representing the PCL at which AF was induced. Regionalizing the parameter θ across different areas of the atria could enhance the model's personalization. However, acquiring these parameters with current technology presents a considerable challenge.

It is important to interpret these results with caution, as the absence of source-sink mismatch in the DREAM may influence the dynamics of reentry. Additionally, the lack of observable trends for different values of κ and θ can be attributed to the limited selection of parameter sets used in the experiments. Future work should consider a more systematic analysis of the parameter space, along with a thorough sensitivity analysis. Furthermore, the next logical step is to analyze arrhythmia vulnerability using 3D simulations in realistic geometries.

7.5 Conclusion

The findings of this study offer new insights into the impact of CV restitution properties on the dynamics of reentry and arrhythmia vulnerability. This was achieved by leveraging a rare clinical dataset from decremental pacing in patients with persistent AF and conducting numerical simulations using the DREAM. The results revealed that the steepness of the restitution curve significantly influences both the average duration of reentry and the vulnerable window, with decreasing steepness leading to higher values for both outputs. Future work should address the limitations of this study and the DREAM, such as incorporating source-sink mismatch effects and utilizing the DI instead of PCL. Nonetheless, the current study highlights the potential applications of the DREAM, particularly in personalizing restitution curves while maintaining lower computational costs due to the use of coarse meshes.

PART IV

IMPLEMENTING SOURCE-SINK MISMATCH IN THE EIKONAL MODEL

Chapter 8

Influence of Wall Thickness and Tissue Curvature on Conduction Velocity

This chapter studies the significance of wall thickness and tissue curvature in influencing conduction velocity (CV). It explains how the eikonal model can be extended to account for these characteristics of the atrial tissue to improve its accuracy and reduce the numerical errors in simulating electrical wave propagation in cardiac tissue.

The work presented in this chapter is based on research conducted during the bachelor's thesis of B.Sc. Nils Skupien, which was supervised and guided by the author of this thesis [116].

8.1 Introduction

As discussed in earlier chapters, computer models are valuable tools for studying cardiac arrhythmias and could aid clinical applications. However, commonly used reaction-diffusion models are computationally expensive, often requiring supercomputers [19, 20]. Eikonal models offer a more efficient alternative but neglect important electrophysiological mechanisms, such as source-sink mismatch, wavefront curvature, and tissue structure effects on CV, limiting their accuracy [19–21]. This trade-off between efficiency and accuracy remains a key challenge for clinical use.

Wall thickness and wall curvature, in particular, have a considerable influence on CV in cardiac tissue. This is closely related to the source-sink mismatch effects, where CV increases when the excited area is larger than the area to be excited and decreases when the excited area is smaller. For instance, when the wavefront propagates through a curved wall, the CV tends to be faster on the outer wall compared to the inner wall 8.1. As wall thickness increases, the compensation required to maintain synchronization between the epicardial and endocardial wavefronts becomes more pronounced, amplifying these effects [19, 97].

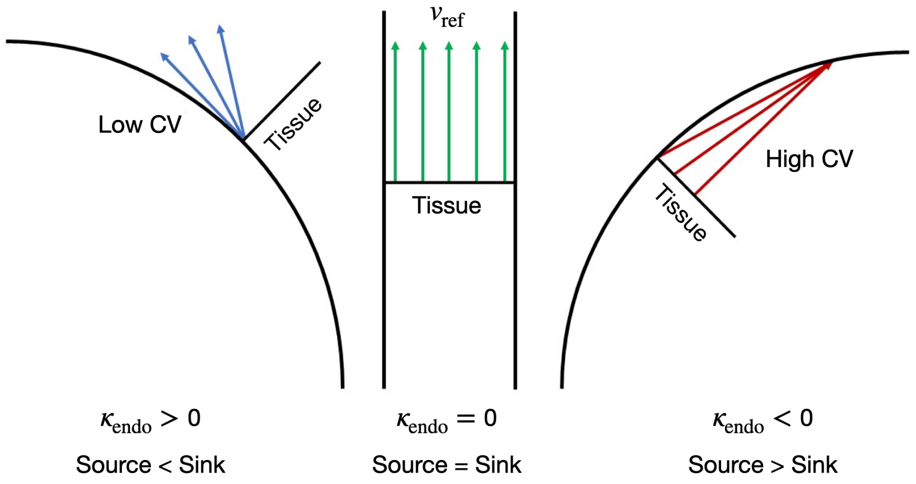

Figure 8.1: The impact of tissue curvature on CV, where the lines in the right and left panels represent the endocardium, while the middle panel depicts both the endocardium and epicardium. This analysis assumes a wavefront propagating perpendicularly to the endocardium of the curved tissue, considering source-sink mismatch effects. For positive curvatures (κ_{endo} is the reciprocal of the osculating circle of the endocardial side), the sink is relatively large, resulting in a decrease in CV. Conversely, for negative curvatures, the sink is comparatively small, leading to an increase in CV. Figure reproduced from [116].

In standard eikonal models, CV often neglects the influences of the wall thickness and tissue curvature. When the input CV is kept constant across the wall, the wavefront travels a shorter distance along the inner surface compared to the outer surface, resulting in a delay between the activation of the endocardium and the epicardium. This can lead to artificial endo-epicardial dissociation, where areas on the endocardial surface are activated before their corresponding epicardial regions. This discrepancy arises because the model fails to account for source-sink mismatch effects and geometrical factors such as wall thickness and tissue curvature. As a result, artificial trans-mural breakthroughs can appear in simulations, leading to false arrhythmia predictions, which could prompt unnecessary and potentially risky clinical interventions when the eikonal model is used to support clinical decision, [19, 102].

Studies in animals, such as goats, and in humans have demonstrated that epicardial fibrosis can exacerbate endo-epicardial dissociation [48, 49, 117]. When this dissociation becomes sufficiently severe, it can lead to transmural breakthroughs, which have been identified as a new mechanism for atrial fibrillation (AF). This mechanism is particularly relevant in patients with persistent AF [50]. Therefore, it is critical that when computer models are used to predict the risk of arrhythmia in patients, endo-epicardial dissociation is accurately represented, as transmural breakthroughs could be a potential mechanism that triggers or maintains AF.

In the work by Rossi et al., the bidomain model was used to study the effects of wall thickness and wall curvature on CV across the inner and outer walls [97]. The researchers utilized a 2-dimensional rectangular mesh, where the left border represented the endocardium and the right border represented the epicardium. The mesh was modified to simulate different wall thicknesses by altering its width, and various curvatures were introduced. Negative curvature was defined as the mesh curving to the right, while positive curvature was defined as the mesh curving to the left.

The mesh was stimulated from the inferior border, and CV was measured along the right border. Through these simulations, they investigated how wall thickness and curvature affected CV. It was observed that when the wall thickness was minimal (i.e., 0.05 mm), curvature had little to no effect on the CV of the inner wall. However, as wall thickness increased, the influence of curvature on CV became more pronounced (See Figure 8.2a). Another important conclusion from their analysis was that the effects of curvature were not influenced by changes in tissue conductivity or anisotropy ratio. This indicates that variations in baseline CV or the degree of anisotropy did not alter the impact of wall curvature on CV. Notably, the effect of curvature on CV remained consistent, even in isotropic propagation (See Figure 8.2b and c).

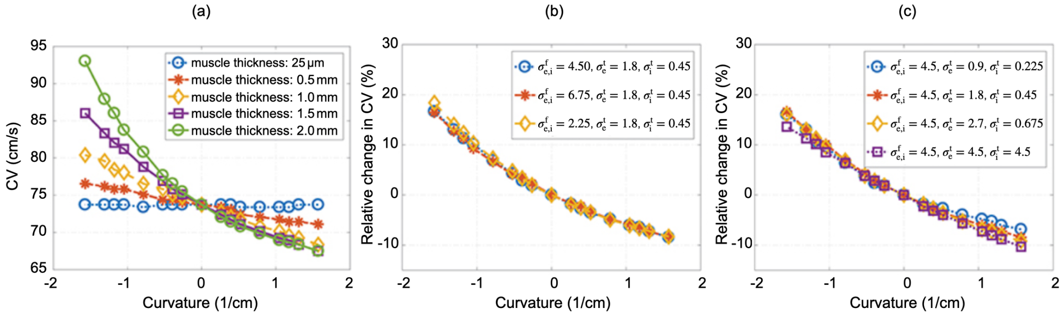

Figure 8.2: (a) Endocardial conduction velocities (CVs) as a function of curvature for various wall thicknesses without bath-loading. Negative curvatures increase CVs, while positive curvatures slow them. (b) Relative change in CVs (compared to flat muscle) for different longitudinal conductivities at fixed muscle thickness (1.5 mm). Longitudinal conductivities have minimal impact. (c) Relative change in CVs for different transversal conductivities. Even in isotropic conditions, curvature affects endocardial CVs. Adapted from [97] and licensed under Creative Commons Attribution License (CC BY).

To extend the capabilities of eikonal model, this work aims to incorporate critical geometrical factors, such as wall thickness and tissue curvature, into the CV input of the eikonal model. To achieve this, the findings from the work of Rossi et al. are used to create regression models that fit CV data, which is then incorporated as inputs into the eikonal model before running simulations. While this approach may not fully address the limitations posed by the lack of source-sink mismatch effects, accounting for these geometrical influences can significantly improve the accuracy of eikonal models in simulating arrhythmia mechanisms. By enhancing the eikonal-based models' accuracy, this refinement could make these models a more reliable and practical tool for clinical use, reducing the risk of false positives and unnecessary interventions. It is important to clarify that when discussing the refinement of the eikonal model, this does not imply the use of finer resolution meshes. Instead, "refinement" refers to the enhancement or improvement of the eikonal model after integrating the regression model.

8.2 Methods

8.2.1 Tissue Mesh Generation

To generate the mesh used in this study, the aim was to replicate, as closely as possible, the framework from Rossi et al.'s work to enable a direct comparison between the bidomain and eikonal simulations [97]. The mesh was designed to represent a transverse cross-section of the cardiac wall. The geometry is a rectangle where the width represents the actual wall thickness, denoted as ℓ_m. The mesh is located in the domain $\Omega_m = [0\,\mathrm{cm}, \ell_m] \times [-0.3\,\mathrm{cm}, 2\,\mathrm{cm}]$. The lower boundary extends from $-0.3\,\mathrm{cm}$ to $2\,\mathrm{cm}$ in the vertical direction, allowing for the application of different curvatures in the upper part of the mesh. The left border is defined as the endocardial side and the right border as the epicardial side. In Figure 8.3, an illustration of the mesh used in this work can be observed.

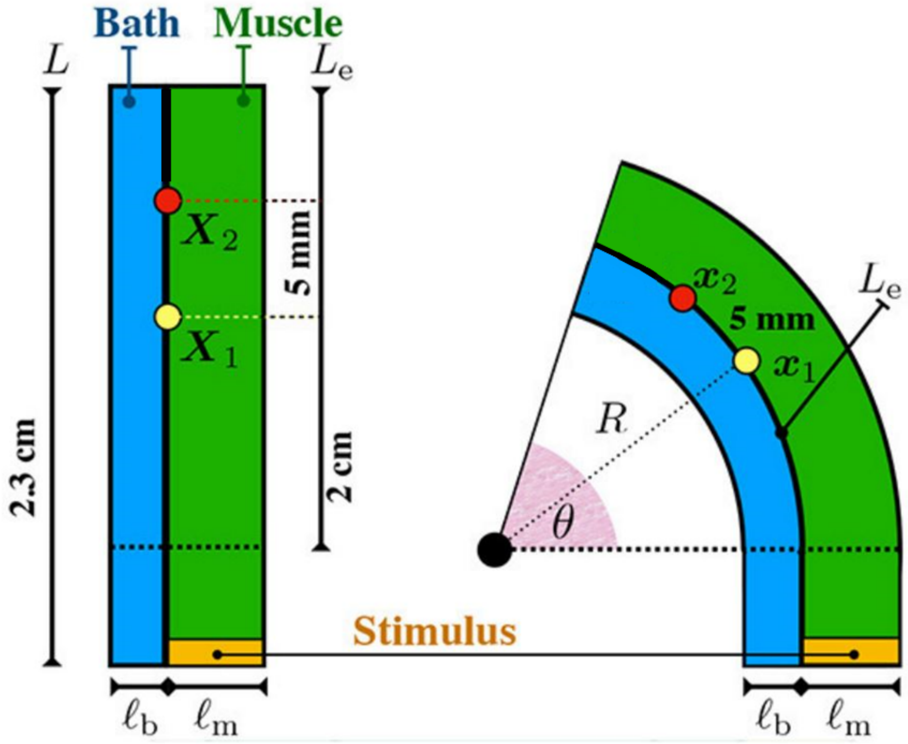

Figure 8.3: Idealized model of cardiac tissue. The tissue is represented by the green area and it's length L_e is fixed at 2 cm in the endocardium (left side), where as the length of the epicardium (right side) changes depending on the tissue's curvature. The curvature is equal to the inverse of the radius in the endocardium and is applied to the upper 2 cm of the tissue. The tissue has a thickness of ℓ_m. An endocardial bath (blue) borders the muscle with a thickness of ℓ_b. The parameters tissue curvature κ_{endo} and tissue thickness ℓ_m are varied to investigate their effect on CV. Bath-loading ℓ_b is set to 0 mm for all the experiments in this study. The points X_1 and X_2 are relevant for the CV measurement. Taken from [97] and licensed under Creative Commons Attribution License (CC BY).

The height of the rectangle consists of two parts: the lower section is 3 mm, and the upper section is 2 cm, resulting in a total mesh height of 2.3 cm. Despite the work of Rossi et al., who conducted some experiments investigating bath-loading (as shown in the Figure 8.3 illustrating the geometry used in their study), bath-loading effects are disregarded in this work. All data extracted from Rossi's research come from experiments where bath-loading was not present. [97]. The mesh contains triangular elements with an edge length of 25 µm in the horizontal direction and 50 µm in the vertical direction.

Additionally, the lower 0.3 cm of the mesh remains flat, without any curvature, while the upper 2 cm are curved in different directions and with varying degrees of curvature. To apply the curvature to the upper part of the mesh, the coordinates of a point in the flat mesh are labeled as (X,Y), where X is the horizontal axis and Y is the vertical axis. The transformation applied to curve the mesh is based on an angle θ in the interval $(0,\pi]$.

The transformation to obtain the desired coordinates for the curved mesh follows a specific formula that induces curvature with angle θ, allowing for the generation of different curvature profiles in the upper section of the mesh:

$$x = \begin{cases} X & Y \leq 0 \\ -c \cdot (R_{\text{endo}} - R cos(\theta \frac{Y}{Y_{\max}})) & Y > 0 \end{cases} \tag{8.1}$$

$$y = \begin{cases} Y & Y \leq 0 \\ R sin(\theta \frac{Y}{Y_{\max}}) & Y > 0 \end{cases} \tag{8.2}$$

The transformation parameter c represents the direction of the curvature. If $c = 1$, the curvature bends to the left, and if $c = -1$, the curvature bends to the right. The length of 2 cm on the endocardial side of the straight mesh remains unchanged after applying curvature, while the arc length on the epicardial side varies depending on the degree of curvature applied. The radius of the endocardium is determined by $R_{\text{endo}} = \frac{Y_{\max}}{\theta}$, where $Y_{\max}$ is the maximum Y-coordinate, set to 2 cm. Using R_{endo}, the radius at any point in the tissue is defined as $R = R_{\text{endo}} + cX$. The curvature at the endocardium is given by $\kappa_{\text{endo}} = \frac{1}{R_{\text{endo}}}$, which is the reciprocal of the radius of the osculating circle.

The preferential cardiomyocyte orientation was incorporated into the mesh by assigning a normalized vector to each node, representing the preferential cardiomyocyte orientation. For $\kappa_{\text{endo}} = 0$ (i.e.,the initial straight mesh), the preferential cardiomyocyte orientation is set to $f = [0,1]$ at each node, parallel to the y-axis. When curvature is applied, the preferential orientations should remain aligned with the endocardium and epicardium. To achieve this, the x- and y-components of the preferential orientation vector were derived by differentiating equations 8.1 and 8.2 with respect to X.

The x- and y-components of the preferential orientation vector are then given by:

$$f_x = \begin{cases} 0 & Y \leq 0 \\ -c \cdot \sin\left(\theta \frac{Y}{Y_{\max}}\right) & Y > 0 \end{cases} \tag{8.3}$$

$$f_y = \begin{cases} 1 & Y \leq 0 \\ c \cdot \cos\left(\theta \frac{Y}{Y_{\max}}\right) & Y > 0 \end{cases} \tag{8.4}$$

Finally, the preferential orientation vectors above the x-axis are normalized to have a uniform magnitude of 1:

$$f_{\text{normalized}} = \frac{f}{\|f\|} = \frac{f}{\sqrt{f_x^2 + f_y^2}} \tag{8.5}$$

In 3D models, preferential cardiomyocyte orientation defines a local coordinate system with longitudinal, transversal, and normal orientations. However, the 2D muscle tissue model in this work includes only two directions: longitudinal and transversal. Unlike the usual notation, the endocardium-to-epicardium direction is referred to as transversal rather than normal for this study.

8.2.2 Development of Regression Models

The objective of this step is to develop a regression model that helps assigning CV values to each node in the mesh, taking into consideration wall thickness and tissue curvature prior to executing the eikonal model. Figure 8.2A illustrated the variation of absolute CVs across different curvatures and wall thicknesses. The absolute CVs were processed to obtain relative CVs, using the absolute CV without tissue curvature (73.89 cm/s) as a reference. The relative change in CV was defined as follows:

$$\text{CV}_{\text{rel}} = \frac{\text{CV} - 73.89\,\text{cm/s}}{\text{CV}} \tag{8.6}$$

In the regression model, the dependent variable was the relative change in CV, while the independent variables were the curvature of the tissue and wall thickness. The values for wall thickness of 0.05 mm were neglected for being unrealistic and to facilitate the fitting of the regression model. Then to calculate the CV of any node in the endocardium the following formula was applied:

$$\text{CV}_{\text{rel}}(\kappa_{\text{endo}}) = a \cdot e^{-b \cdot \kappa_{\text{endo}}} - a \tag{8.7}$$

where a and b are parameters that depend on ℓ_{m} (i.e., the wall thickness) which require additional regression fitting with the following formulas:

$$a(\ell_{\text{m}}) = p_1 \cdot \ell_{\text{m}} + p_2 \tag{8.8}$$

$$b(\ell_{\text{m}}) = p_3 \cdot e^{p_4 \cdot \ell_{\text{m}}} \tag{8.9}$$

Combining Equations 8.6, 8.8 and, 8.9, the resulting multivariable model is:

$$\text{CV}_{\text{rel}}(\kappa_{\text{endo}}, \ell_{\text{m}}) = (p_1 \cdot \ell_{\text{m}} + p_2) \cdot e^{-p_3 \cdot e^{p_4 \cdot \ell_{\text{m}}} \cdot \kappa_{\text{endo}}} - (p_1 \cdot \ell_{\text{m}} + p_2) \tag{8.10}$$

where parameters p_1, p_2, p_3 and, p_4 are optimized to reduce the root mean square error (RMSE) between the predicted CVs and the relative CVs obtained from processing the data collected from Rossi et al. [97]. Utilizing the optimized parameters and the reference CV, it is then possible to calculate the absolute CV:

$$\mathrm{CV}(\kappa_{\mathrm{endo}}, \ell_{\mathrm{m}}, v_{\mathrm{ref}}) = v_{\mathrm{ref}} \cdot \left(1 + (p_1 \cdot \ell_{\mathrm{m}} + p_2) \cdot e^{-p_3 \cdot e^{p_4 \cdot \ell_{\mathrm{m}}} \cdot \kappa_{\mathrm{endo}}} - (p_1 \cdot \ell_{\mathrm{m}} + p_2)\right) \tag{8.11}$$

8.2.3 Refinement of the Eikonal Model

The refining of the eikonal model is based on recalculating the CV accounting for wall thickness, tissue curvature, and the reference CV. Once the upgraded CV is obtained it is use as input in the eikonal model. In the previous section, a regression model was used to help recalculating this value. In this section explains how every node in the mesh is assigned with a CV value. First, if the wall thickness and the curvature of the endocardium is known, then the formula in Equation 8.11 can be used to calculate the CV in this node. For nodes in the epicardium the same formula can be applied but the curvature of the epicardium κ_{epi} must be inferred from the wall thickness and the curvature of the endocardium:

$$\kappa_{\mathrm{epi}} = \frac{1}{R_{\mathrm{epi}}} = -\frac{1}{\frac{1}{\kappa_{\mathrm{endo}}} + \ell_{\mathrm{m}}} \tag{8.12}$$

where R_{endo} and R_{epi} are the radii of the osculating circles for the endocardium and epicardium, respectively. Notably, the curvatures of the epicardium and endocardium have opposite signs, except when the mesh is flat, in which case both curvatures are $0\,\mathrm{cm}^{-1}$. The CV at any node within the wall is interpolated from the corresponding epicardial and endocardial nodes that share the same Y-coordinates in the original unbent mesh.

$$\mathrm{CV} = \mathrm{CV}_{\mathrm{endo}} + \frac{\mathrm{CV}_{\mathrm{epi}} - \mathrm{CV}_{\mathrm{endo}}}{\ell_{\mathrm{m}}} \cdot X \tag{8.13}$$

Here, $X \in [0, \ell_{\mathrm{m}}]$ represents the distance of a node from the endocardium in the bent mesh or the original X-coordinate of the node in the unbent mesh.

8.2.4 Assessment of the Eikonal Model Refinement

Similar to the approach by Rossi et al., the conductivities for the bidomain model were based on the work of Roth et al. [97, 118], with adjustments made to achieve a CV of 100 cm/s while maintaining the same intra- and extracellular conductivity ratios as well as anisotropy ratios. The conductivity tensors were defined using these scalar values, along with the vectors specified in Equations 8.3 and 8.4. A stimulus was applied at the bottom of the mesh to generate a planar wavefront, and no-flux Neumann boundary conditions were enforced at the mesh boundaries. As previously mention, no bath-loading effects were included in the bidomain simulations. The finite element method was used to solve the bidomain equations.

For the eikonal simulations, CV was evaluated both before and after applying a regression-based refinement model. The anisotropy ratio for CV was defined as the square root of the anisotropy ratio of the conductivities used in the bidomain model. Boundary conditions were similarly applied at the bottom of the mesh to initiate the planar wavefront. The reference CV of 100 cm/s was used as longitudinal CV everywhere before the refinement. The output of the regression model on each node was used as longitudinal CV after the refinement. Same preferential cardiomyocyte orientation was used as in the bidomain model to compute the anisotropic tensor. The fast iterative method (FIM) was used to solve the eikonal equation.

The comparisons were conducted across 24 different meshes, created by combining 6 values of tissue curvature: $\pi/2$, 1, $\pi/4$, $-\pi/4$, -1, and $-\pi/2$ cm/s with 4 wall thickness values: 0.5, 1, 1.5, and 2 mm. For each mesh, a comparison was made between the bidomain and eikonal models, both before and after the refinement of the eikonal model.

The activation time (AT) from the simulations were used to calculate the RMSE, quantifying the differences in AT at each node between the two models. The error was calculated following this formula:

$$\mathrm{RMSE} = \sqrt{\frac{\sum_{i=1}^{N}(\mathrm{LAT}_{\mathrm{eik},i} - \mathrm{LAT}_{\mathrm{bi},i})^2}{N}}, \tag{8.14}$$

where $\mathrm{LAT}_{\mathrm{eik},i}$ and $\mathrm{LAT}_{\mathrm{bi},i}$ are the AT obtained from the eikonal and bidomain simulation respectively, for the ith node in the mesh and N is the total number of nodes in the mesh.

Furthermore, the effect of mesh resolution was assessed by comparing the eikonal model results on the original 24 meshes with an edge length of 50 µm to those on lower resolution meshes with an edge length of 100 µm. These differences were also calculated before and after refinement to determine whether the refinement preserved the minimal error introduced by changes in mesh resolution, which is a key advantage of the eikonal model. To facilitate the mesh comparison, the nodes of the coarse mesh were aligned with a subset of nodes in the high-resolution mesh. The error for this comparison was computed using the following formula:

$$\mathrm{RMSE} = \sqrt{\frac{\sum_{i=1}^{M}(\mathrm{LAT}_{\mathrm{fine},i} - \mathrm{LAT}_{\mathrm{coarse},i})^2}{M}}, \tag{8.15}$$

where $\mathrm{LAT}_{\mathrm{coarse},i}$ and $\mathrm{LAT}_{\mathrm{fine},i}$ are the AT obtained from the eikonal model in the coarse and fine meshes, respectively, for the i-th node in both meshes, and M is the total number of nodes in the coarse mesh. It is assumed in this equation that the i-th node of the fine mesh and the i-th node of the coarse mesh share the same location.

8.2.5 Software Tools

The simulations were implemented using a variety of software tools. Myokit [119] was employed as a data extractor to obtain data from figures in Rossi et al.'s work [97]. Several MATLAB toolboxes [111] were utilized: the Partial Differential Equation toolbox was used for mesh creation, the Curve Fitting toolbox for developing a regression model to match the extracted data, and the Optimization toolbox's lsqnonlin function to optimize the parameters of the regression formula. MATLAB [111] was also used to run the eikonal simulations, while openCARP [103] was employed for running bidomain simulations.

8.3 Results

8.3.1 Regression Model Performance

The results of the regression model were presented to evaluate its effectiveness in optimizing the eikonal model. The data from Rossi et al. were used to optimize the parameters of the regression formula, aiming to predict relative changes in CV based on wall thickness and tissue curvature. Qualitatively, the regression model accurately captured the influence of curvature: for negative curvature (bending to the right of the mesh), CV increased on the endocardium, while for positive curvature (bending to the left), CV decreased. This behavior was further intensified by greater wall thickness, aligning with the trends observed in Rossi et al.'s bidomain simulations.

Quantitatively, the fit of the regression model was highly accurate, with errors smaller than 1 %. However, for a wall thickness of 0.05 mm, the model's accuracy diminished. Since this value is not physiologically realistic, it was excluded from the study to maintain simplicity. As a result, the rest of the study and the benchmark of the eikonal model focused on more realistic wall thicknesses, with the regression model achieving a small error across all other cases and without adding complexity to the regression formula. The comparison between the results of the regression model and the extracted bidomain simulation data from Rossi et al. is elucidated in Figure 8.4. It highlights how the regression model's predictions of relative changes in CV for different curvatures and wall thicknesses align closely with the bidomain simulation data.

8.3.2 Eikonal vs. Bidomain Comparison

The eikonal and bidomain models were compared both before and after refinement. The initial eikonal simulations, prior to refinement, displayed differing behavior compared to the bidomain model simulations. Specifically, they exhibited artificial endocardial-epicardial action potential (AP) dissociation, as expected, due to the varying distances traveled by the AP across the endocardial and epicardial surfaces. This dissociation was dependent on the curvature and wall thickness, being more pronounced with higher curvature or thicker walls. As shown in Figure 8.5, the initial simulations with the standard eikonal model, without the regression model, produced ATs with substantial discrepancies across different curvatures, due to the constant longitudinal CV applied across the nodes.

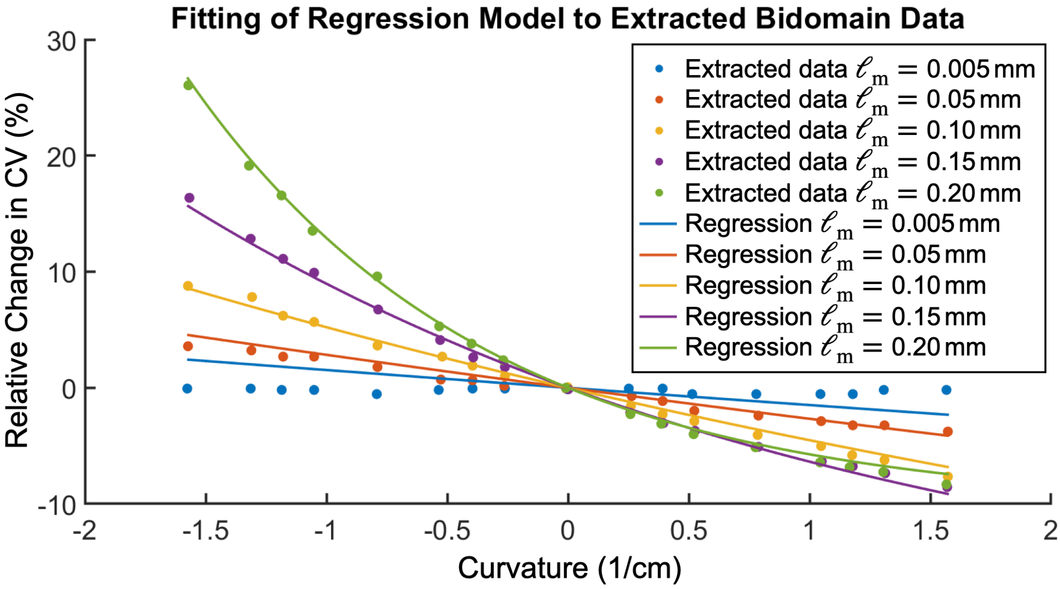

Figure 8.4: The relative changes in CV for different curvatures and tissue thicknesses are compared for the results of the regression formula (lines) and the extracted bidomain simulation data (points) from Rossi et al. [97]. Each colour represents a certain tissue thickness according to the legend on the right top. Figure reproduced from [116].

In contrast, bidomain simulations, as demonstrated by Rossi et al., showed that the wavefront propagation was more perpendicular to both the epicardial and endocardial surfaces [97]. This alignment likely results from the source-sink mismatch effects being properly accounted for in bidomain model.

After refining the eikonal model to incorporate wall thickness and tissue curvature effect on CV, the wavefront propagation became significantly more similar to the bidomain simulations. To assess this, the RMSE between the eikonal and bidomain models was measured, and the results indicated that the refinement improved the simulation accuracy for all 24 cases of varying wall thickness and curvature. The improvement of RMSE after refinement for all 24 geometries can be observed in Table 8.2 This improved behavior can be observed in Figure 8.6.

Table 8.1: RMSE of AT eikonal - AT Bidomain before and after the implementation of the regression model for 24 different geometries in terms of muscle thickness ℓ_m and curvature κ.
RMSE in ms before regression $\rightarrow$ RMSE in ms after regression.

ℓ_m (mm) κ_endo (1/cm)	0.5	1	1.5	2
$\pi/2$	0.32 →0.057	0.54 →0.065	0.62 →0.170	0.60 →0.34
1	0.20 →0.051	0.33 →0.057	0.40 →0.110	0.40 →0.18
$\pi/4$	0.16 →0.047	0.27 →0.055	0.32 →0.085	0.24 →0.23
$-\pi/4$	0.18 →0.051	0.31 →0.069	0.39 →0.067	0.43 →0.14
-1	0.22 →0.058	0.37 →0.071	0.46 →0.100	0.50 →0.24
$-\pi/2$	0.35 →0.081	0.58 →0.110	0.70 →0.270	0.74 →0.71

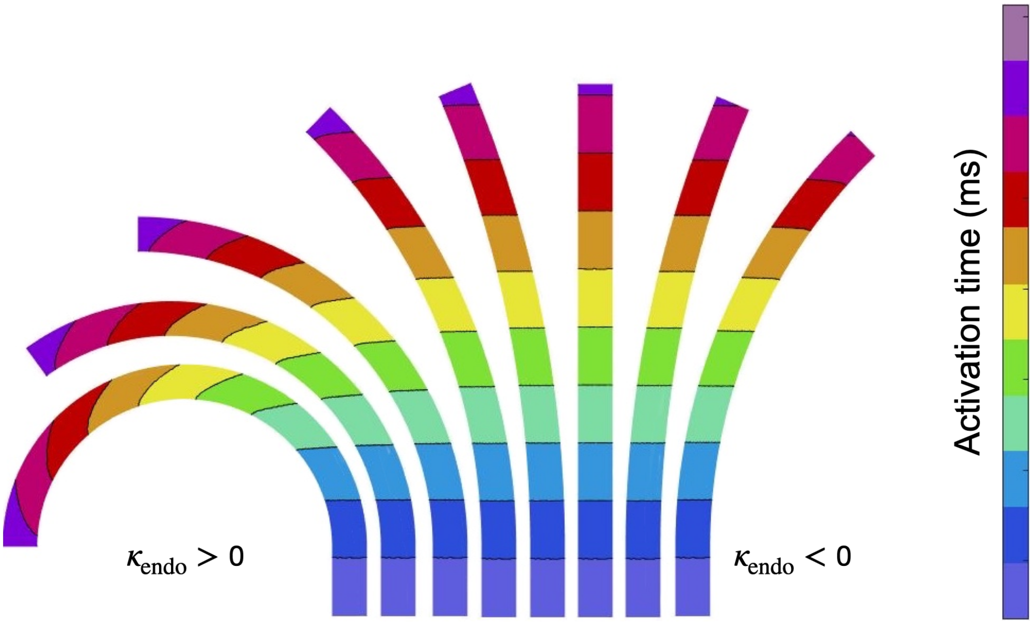

Figure 8.5: AT at different endocardial curvatures for a muscle thickness of 1.5 mm without bath-loading conditions. Achieved by eikonal simulations without the regression model implemented and thus a constant value in the longitudinal CV of every node. Figure reproduced from [116].

8.3.3 Mesh Resolution Impact

The differences between high- and low-resolution meshes were analyzed for the eikonal model both before and after refinement. Specifically, the ATs were compared across different mesh resolutions. Before incorporating the regression model, the eikonal model showed minimal variation in activation times between fine and coarse meshes, highlighting its well-known insensitivity to mesh resolution. After incorporating the regression model, this insensitivity remained, with even smaller differences in activation times between high- and low-resolution simulations. This demonstrates that the refined model maintains the robustness of the original eikonal model, with consistent propagation patterns and activation times across both mesh configurations.

8.4 Discussion

This study provides additional benefits to the eikonal model, particularly by incorporating wall thickness and curvature effects on CV. An important advantage of this approach is that it maintains the computational efficiency of the standard eikonal model. The proposed method requires minimal pre-processing where the regression models are incorporated, allowing for easy integration into existing eikonal simulations. The simplicity of this step, applying the

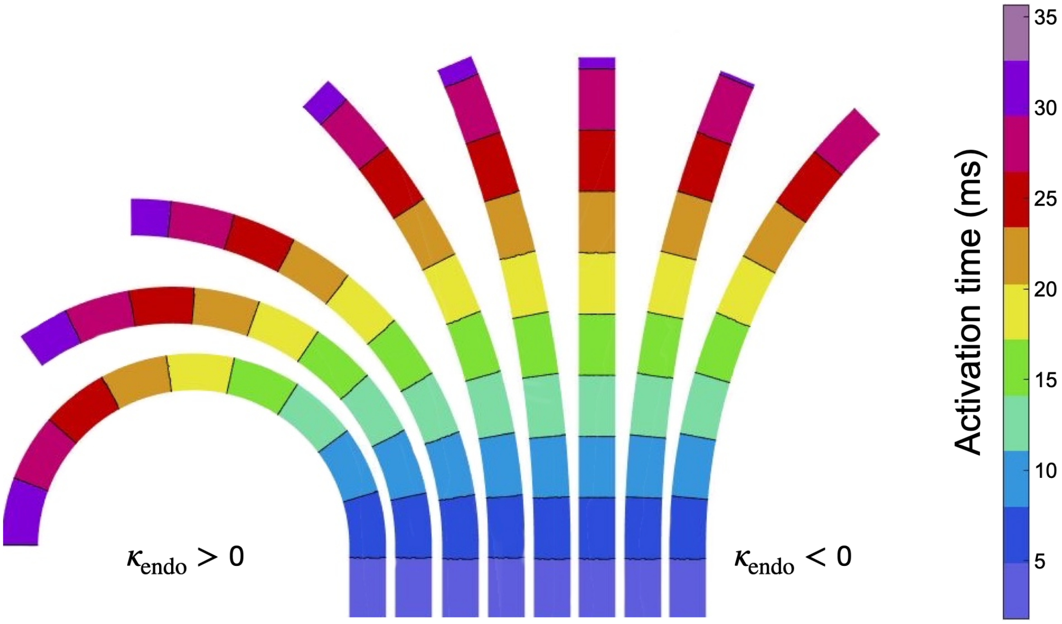

Figure 8.6: AT at different endocardial curvatures for a muscle thickness of 1.5 mm without bath-loading conditions. Achieved by eikonal simulations with the regression model implemented and thus the longitudinal CV of every node was calculated by the regression formula. Figure reproduced from [116].

Table 8.2: RMSE between the high- and the low-resolution mesh according to Equation 8.15 before and after the implementation of the regression model for 24 different geometries in terms of tissue thickness ℓ_{m} and curvature κ. The high-resolution mesh has an average element size of 50 µm and the low-resolution mesh has an average element size of 100 µm.
RMSE in ms before regression $\rightarrow$ RMSE in ms after regression.

ℓ_{m} (mm) / κ_{endo} (1/cm)	0.5	1	1.5	2
$\pi/2$	0.017 →0.0075	0.023 →0.0068	0.027 →0.0054	0.034 →0.016
1	0.012 →0.0074	0.015 →0.0062	0.017 →0.0050	0.022 →0.013
$\pi/4$	0.011 →0.0075	0.012 →0.0061	0.012 →0.0049	0.018 →0.013
-$\pi/4$	0.010 →0.0073	0.011 →0.0056	0.012 →0.0051	0.017 →0.013
-1	0.012 →0.0072	0.014 →0.0057	0.016 →0.0053	0.020 →0.013
-$\pi/2$	0.016 →0.0072	0.026 →0.0059	0.026 →0.0061	0.030 →0.014

regression model to account for variations in CV, makes it a practical and fast solution for enhancing the eikonal model, while keeping low computational cost.

Moreover, the study demonstrates the potential to reduce the artificial endocardial-epicardial AP dissociation that is commonly introduced by the standard eikonal model. Traditional models assume constant CV across the wall, neglecting the crucial effects of tissue curvature and wall thickness [19, 102]. This oversight could lead to unrealistic wave propagation behaviors. Eikonal simulations in this and other studies suggest the potential for false transmural breakthroughs due to artificial endo-epicardial dissociation [19, 102]. However, eikonal-based models that simulate reentry have not yet fully explored the occurrence of these breakthroughs [21, 23]. Further investigation is required to verify these findings and to validate the significance of this approach using an eikonal-based model capable of simulating reentry in volumetric geometries with wall thickness. This will help determine if the technique reduces the risk of simulating artificial transmural breakthroughs, which could otherwise be misinterpreted as the maintenance or initiation of atrial fibrillation. Nonetheless, by incorporating these geometrical factors (i.e., tissue curvature and wall thickness), the proposed method provides a more accurate representation of wavefront propagation, which is essential for realistic simulations of cardiac electrical activity. The incorporation of wall thickness and curvature not only enhances the fidelity of the model but will also allow for a better understanding of how these factors interact with reentry dynamics during arrhythmia such as AF.

Another remarkable advantage of the eikonal model is its insensitivity to mesh resolution [20]. This study has shown that the eikonal simulations remain accurate even when coarse meshes are used, preserving a comparable level of performance despite reduced spatial resolution. This characteristic is particularly valuable in large-scale simulations where computational resources may be limited. The ability of the eikonal model to maintain accuracy under various mesh conditions makes it an appealing choice for researchers seeking to balance computational efficiency with model fidelity. The refinement introduced in this study conserves this robustness, ensuring that the eikonal model remains viable for more complex but coarse geometries that may involve varying anatomical features or patient-specific geometries.

While the study offers valuable enhancements to the eikonal model, there are limitations that must be addressed. The regression model used is relatively simple and may not fully account for very thin wall thicknesses. Although this may not pose a critical limitation for the physiological scenarios analyzed, it underscores the need for further refinement when working with extremely thin tissue layers. Additionally, the wave propagation produced in the simplified mesh differs significantly from more complex propagation patterns observed in simulations of reentry in realistic geometry by the bidomain model. This discrepancy suggests that additional considerations may be necessary in future work to better align the model with real-world cardiac dynamics and behavior.

Looking ahead, an important next step is to extend this approach to 3-dimensional curvatures, similar to those seen in more complex anatomical measures. The use of an osculating sphere provides a simple method for estimating curvature in volumetric geometries. This approach offers a more practical alternative to calculating the more complex Gaussian curvature. Furthermore, this study focused primarily on atria, using physiologocal atrial ranges for CV, and wall thickness. It is likely that the effects observed are even more pronounced in ventricular tissue, where wall thickness is significantly greater. Adapting the regression model for ventricular parameters could provide valuable insights and deserves further exploration of the ventricles' specific electrical properties.

8.5 Conclusion

This work addresses limitations of the eikonal model by incorporating the effects of wall thickness and tissue curvature on CV, reducing artificial discrepancies such as endo-epi dissociation and false transmural breakthroughs. The refined model enhances the accuracy of simulations by accounting for these structural factors, bridging the gap between simplified models and more complex propagation dynamics.

The approach presented here paves the way for further advancements in the eikonal model by introducing a practical, computationally efficient method. These developments offer the potential to enhance the model's applicability in more complex and clinically relevant scenarios while maintaining computational efficiency. Continued refinement and integration of these methods could enhance simulation accuracy while maintaining efficiency in broader applications, such as 3D atrial models.

Chapter 9

Effects of Source-Sink Mismatch and Restitution on Diffusion Current

This chapter explores how various factors influence the diffusion current (DC) generated in the monodomain model under different conditions, such as pacing frequency and source-sink mismatch effects. It also examines how regression techniques can be used to predict DC amplitude based on the activation time (AT) of neighboring nodes. Additionally, the chapter provides new insights into how this understanding can help address the limitations of eikonal-based models, such as diffusion reaction eikonal alternant model (DREAM), by improving their accuracy in modeling cardiac electrical activity.

The work presented in this chapter is based on research conducted during the bachelor's thesis of B.Sc. Lisa Keller, which was supervised and guided by the author of this thesis [120].

9.1 Introduction

One of the main limitations of the eikonal-based models, which also simulate transmembrane voltage, is their insufficient representation of DCs [20, 22, 23]. Although outstanding advancements have been made to extend eikonal-based models from merely calculating ATs to simulating transmembrane voltage dynamics, these models often struggle to capture essential phenomena such as bath-loading, waveform curvature, wave collision dynamics, and similar effects. The reaction-eikonal (RE) model is one of the eikonal-based models that has made outstanding progress in incorporating the dynamics of transmembrane voltage. In the RE^{+} version of the RE model, the DC is accounted for, which reduces the repolarization gradients. However, it is not capable of simulating reactivations of the cells, which hinders the inclusion of frequency effects [20]. Other studies, such as those by Gassa et al. and the DREAM, are capable of simulating reactivation [22, 23]. However, their representation of DCs does not account for DCs restitution or source-sink mismatch effects.

Several mechanisms explain why source-sink mismatch effects are important for reentry dynamics, as they can lead to functional block. One mechanism occurs when scar tissue creates channels that cause the wavefront to transition abruptly from a small area of activation to a significantly larger area at the exit of an ithsmus [121]. Disparities in electrical properties, particularly with reduced or impaired gap junctions, can further exacerbate this issue [122]. Additionally, the orientation of the wavefront in relation to the preferential cardiomyocyte orientation and the presence of scar tissue can also contribute to functional block [123]. All the events described above promote the formation and maintenance of reentry due to source-sink mismatch.

One of the main challenges in understanding and incorporating source-sink mismatch is the lack of an appropriate technique to quantify this effects. While qualitative behaviors have been identified, such as a greater source than sink in colliding wavefronts or a smaller source in very curved wavefronts, these insights do not provide a quantitative measure applicable to any node at any time under various scenarios [124, 125]. Lawson et al. addressed this challenge by quantitatively assessing time delays in bifurcated geometries [125]. In the context of integrating source-sink mismatch effects to enhance the eikonal model, this quantification must rely on variables and parameters that are readily available during eikonal simulations, which adds complexity to the problem. Examples of these variables include ATs, diastolic intervals (DIs), node coordinates, and element edge length [22].

Additionally, restitution plays an important role in various aspects of cardiac electrophysiology, referring to changes in specific properties based on pacing frequency or cycle length. Examples of variables that exhibit restitution include action potential duration (APD), CV, and calcium transients [107, 126, 127]. The behavior of restitution in these variables is crucial for modulating different reentry dynamics and mechanisms of cardiac arrhythmias. However, the restitution of DCs remains an area that has not yet been investigated.

The lack of an accurate representation of DCs might pose a barrier to the clinical application of the eikonal model, as it currently fails to adequately describe DCs in various scenarios, such as highly curved wavefronts, wave collisions, or varying pacing frequencies [20, 23]. Therefore, it is crucial to develop more precise representations of these currents within the eikonal model while avoiding substantial computational costs in simulations. To achieve this, further investigation into the behavior of DCs under diverse conditions using the monodomain model can provide valuable insights into their dynamics. Analyzing this behavior can improve the approximation of these currents in various eikonal-based models.

Diffusion currents associated with the propagation of electrical waves throughout heart tissue consist of both the depolarization and repolarization phases. Although the repolarization phase of the DC have an important role in cardiac electrophysiology, this work focuses primarily on the depolarization phase as an initial step [20]. The depolarization phase features a positive initial component followed by a decrease in normal planar wavefront propagation [22]. However, the characteristics of the DC, such as amplitude, duration, and frequency decomposition, are affected differently when the propagation dynamics vary [120]. This study specifically examines the variation of the extrema of DCs under different scenarios, i.e., their maximum and minimum values.

The objective of this study is to explore the behavior of the DCs, particularly their extreme values, under varying pacing frequencies. Additionally, the impact of source-sink mismatch effects on these currents is investigated. To facilitate this, source-sink mismatch is quantified for use in regression analysis within this work. By examining these factors, improved methods for approximating DCs may be developed while accounting for more complex physiological phenomena. Ultimately, this could enhance the applicability and accuracy of the eikonal model without sacrificing computational efficiency, paving the way for its integration into clinical settings.

9.2 Methods

In this section, the overall methods used in this study are outlined. First, the general simulation setup for the monodomain simulations employed to analyze DCs is presented. The effect of pacing frequency on the extrema of DCs is described, starting with an explanation of the relevant monodomain simulations, followed by a description of how the regression model is developed to predict these extrema. Next, the methods for investigating the impact of source-sink mismatch effects on the extrema of DCs is explained, including the simulation setup for analyzing its effects. A new method for quantifying source-sink mismatch based on eikonal variables is also introduced, along with an explanation of how to create a regression model that correlates the quantification of source-sink mismatch with the extrema of the DC.

9.2.1 General Simulation Setup

The simulations were conducted using the monodomain model with the Courtemanche ionic model to represent cell electrophysiology, utilizing healthy parameters unless otherwise specified [66]. Rectangular meshes with triangular elements, averaging an edge length of 200 µm, were employed. Conductivities were adjusted to achieve the desired CV value of 600 mm/s, with the preferential orientation of cardiomyocytes aligned along the x-axis set to (1,0,0) everywhere [114]. The Crank-Nicolson method was used to solve the parabolic equation of the monodomain model [128]. The sampling frequency was set to 10 kHz to capture rapid changes in DCs, with an integration step of 10 µs. Diffusion currents were inferred from transmembrane voltage calculations, similarly to the method described in the work of Gassa et al. [23]. Briefly explained, the difference in transmembrane voltage at each node before and after applying the Crank-Nicholson method was calculated, divided by the integration time step, and this value represented the DC. Only the depolarization phase was considered, defined as the DC within the time interval from the first to the last instance when the current crossed the 1 µA/cm² threshold. The extrema were calculated as the minimum and maximum values of the DC within this interval.

9.2.2 Pacing Frequency

A 2-dimensional rectangular mesh measuring 10 mm x 1 mm was generated. A rectangular stimulus was applied along the left boundary of the mesh, covering all outermost nodes on the left edge, with uniform strength of 250 µA/cm² and duration of 2 ms. The experiments were conducted using pacing cycle length (PCL) of 110 ms, 120 ms, 130 ms, 140 ms, 150 ms, 160 ms, 170 ms, 180 ms, 190 ms, 200 ms, 220 ms, 240 ms, 260 ms, 280 ms, 300 ms, 320 ms, 340 ms, 360 ms, 380 ms, 400 ms, 600 ms, 800 ms, 1000 ms, 1500 ms, and 2000 ms. These PCLs were selected based on the pacing protocols used during ablation therapy for patients with atrial fibrillation (AF) [129]. For each PCLs, six stimuli were applied, with the second and sixth stimuli selected for analysis. The DC during the depolarization phase of the central node was extracted from these stimuli. Additionally, the DI for this node was calculated as the difference between the recovery time, defined as the moment when the transmembrane voltage crosses the -40 mV threshold with a negative slope in the previous cycle, and the AT, which is defined as the moment when the transmembrane voltage crosses the 35 mV threshold with a positive slope in the analyzed cycle.

To establish a correlation between the DC and various pacing frequencies, the DI, which is often linked to different pacing cycle lengths, was selected as the variable of interest. The CV follows a restitution curve [130], and by investigating the relationship between DC characteristics and DI, the aim is to determine if a similar correlation exists. The DI represents the period during which a node is excitable but not yet excited.

The behavior of the DC extremes in relation to the DI was analyzed using the following fitting function:

$$w_{\mathrm{ex}} = \left(1 - k_0 \cdot \exp(-(DI + k_1) \cdot \frac{\log k_0}{k_2})\right) \cdot \gamma, \tag{9.1}$$

where k_i for $i = \{0, 1, 2\}$ are the curve-fit parameters, and γ represents the value towards which the function converges for large DI values. For better comparison between the extremes, the absolute value was used for the minimum.

9.2.3 Source-Sink Dynamics

To investigate the influence of source-sink mismatch effects, reentry was induced using the S1-S2 protocol. Tissue vulnerability was increased by adjusting the conductivity to simulate AF, following the model proposed by Loewe [113]. Five S1 stimuli were applied to the left edge of the mesh, generating five planar wavefronts. Subsequently, an S2 cross-field stimulus was delivered to the lower left quadrant to induce reentry. After collecting ATs, DIs, and DCs at each node, a regression model was developed to predict the extrema of the DC based on the ATs and DIs. To construct the regression model, it is essential to define the method for quantifying the source-sink mismatch.

Figure 9.1 illustrates the quantification of the source-sink mismatch. The node at the center of this analysis located at $\overrightarrow{s_0}$, is refered as the central node. The perimeter of the polygon formed by the union of all triangles containing the central node is denoted as P. For this quantification, the ATs of the neighboring nodes, as well as the AT of the central node and the coordinates of all these nodes, are taken into account. The key steps involved include:

1. **Normalization of the perimeter**: A bijective mapping function assigns a unique point $\overrightarrow{s_j} \in P$ for any scalar in $s_j \in [0,1)$, ensuring that the proportion of each edge relative to the entire perimeter remains within the interval $[0,1)$. In other words, the green line in Figure 9.1a is transformed into the x-axis of Figure 9.1b. It is important to note that the interval $[0,1)$ is semi-open to maintain the injective property, as both 0 and 1 would be assigned to the same point in P.
2. **Interpolation of ATs**: The ATs of neighbors are linearly interpolated for any $\overrightarrow{s_j} \in P$, with the equation:
$$AT_j = AT_i + (AT_{i+1} - AT_i)\frac{s_j - s_i}{s_{i+1} - s_i}, \tag{9.2}$$
where $\overrightarrow{s_i}$ and $\overrightarrow{s_{i+1}}$ are the extremes points of the edge containing $\overrightarrow{s_j}$.
3. **Shift of ATs**: The function $h_{\mathrm{AT}}()$ is defined to account for varying distances from the stimulus, ATs are shifted:
$$h_{\mathrm{AT}}(s_j) = AT_j^* = AT_j - AT_{\min}, \tag{9.3}$$
where $AT_{\min}$ is the minimum AT among the nodes in P
4. **Computation of propagation times**: propagation time (PT) for a wave to travel from a point in P to the central node is calculated considering anisotropy tensor D:
$$PT_{\mathrm{j}} = \frac{\sqrt{(\overrightarrow{s_0} - \overrightarrow{s_j})^\top D^{-1} (\overrightarrow{s_0} - \overrightarrow{s_j})}}{CV} \tag{9.4}$$
5. **Source-sink distinction**: The AT of the central node is identified as the minimum of the function g (sum of shifted ATs and PTs), distinguishing sources (nodes activated before the central node) and sinks (activated after the central node).

Two new variables, the source area A_{source} and sink ratio r_{sink}, are computed. The source area is defined by:

$$A_{\mathrm{source}} = \int_{\ell} g(b)\,\mathrm{d}s \quad \text{for} \quad \ell = \{\overrightarrow{s_j} \in P : h_{\mathrm{AT}}(s_j) < AT_0^*\} \tag{9.5}$$

The sink ratio is given by:

$$r_{\mathrm{sink}} = \frac{\int_{\ell^*} 1\,\mathrm{d}s}{\int_P 1\,\mathrm{d}s} \tag{9.6}$$

where $\ell^* = P - \ell$. A_{source} influences the upstroke amplitude of the DC, and r_{sink} affects its downstroke. To fit the maximum DC, the following polynomial function is used:

$$u_{\max} = \alpha_0 \cdot A_{\mathrm{source}}^3 + \alpha_1 \cdot A_{\mathrm{source}}^2 + \alpha_2 \cdot A_{\mathrm{source}} + \alpha_3 \tag{9.7}$$

For the minimum DC, a hyperbolic fit is applied:

$$v_{\min} = \frac{\eta_0}{r_{\text{sink}} - \eta_1} + \eta_2 \tag{9.8}$$

In Figure 9.1(a), the propagation of a planar wavefront is illustrated, while the parametrization of the mesh segment is presented in Figure 9.1(b). By calculating the interpolated AT and the propagation time for each point on the perimeter surrounding the central node, the time it takes for the wave to reach the central node from these points can be determined. This process allows us to quantify the areas of points classified as sinks and those identified as sources.

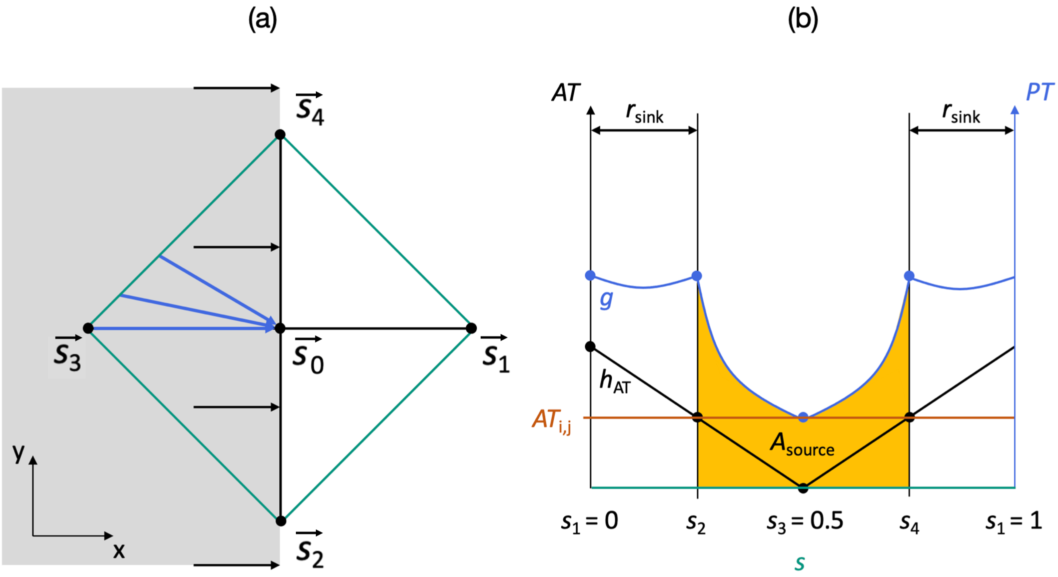

Figure 9.1: Variables of source-sink mismatch. In (a), the considered scenario is depicted. A planar wavefront (gray) propagates in the x-direction (black arrows), which is also the preferential myocyte orientation, through a segment in a mesh. The ATs of neighboring points on the perimeter (green) are represented in (b) as the function h_{AT} (black). The sum of PTs of the neighbors and h_{AT} results in the function g (blue), where the PT describes the time interval during which a wave propagates from a neighbor or a point on the perimeter to the central node. The minimum of this function g represents the AT of the central node, where neighboring points activated prior are denoted as source and those activated afterward are referred to as sinks. The source area A_{source} (yellow) indicates the area under function g for neighboring points identified as sources. The sink ratio r_{sink} is the portion of the perimeter that constitutes part of the sink. Figure reproduced from [120].

9.2.4 Software Tools

The simulations investigating electrical signal propagation patterns were conducted using the openCARP cardiac electrophysiology simulation environment, integrated with the carputils toolbox in Python for streamlined experiment management. Conductivity tuning was performed using the tuneCV function, while mesher was employed to create meshes and meshalyzer for visualization [103]. Post-processing was carried out using Python and MATLAB to analyze the results and optimize computational performance [111, 112].

9.3 Results

9.3.1 Pacing Frequency

Figure 9.2 presents the data points extracted from the monodomain simulation, showing the correlation between the DI and the extrema of the DC. The regression fit accurately captured the restitution behavior for both the second and sixth stimuli. Tables 9.1 and 9.2 show the fitted parameters used to optimized the regression. Interestingly, the absolute minima are consistently higher than the absolute maxima for both stimuli and across all DI values. The restitution behavior for the second and sixth stimuli is quite similar, though the sixth stimulus tends to reach lower absolute extrema values for shorter DI values before propagation failure.

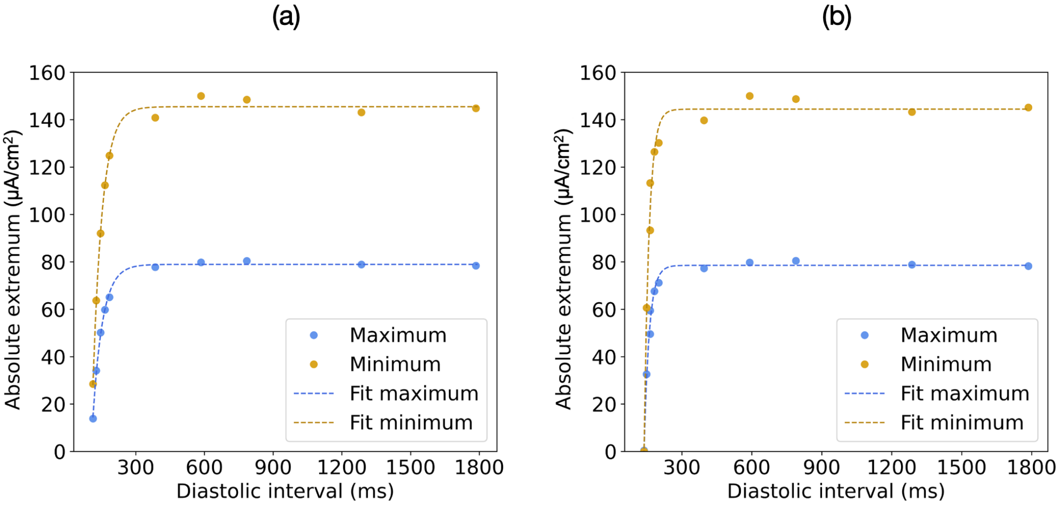

Figure 9.2: Restitution curve for the upstroke and downstroke of the DC. The maximum of the DC, representing the upstroke, is shown in blue, while the absolute value of the minimum of the DC, representing the magnitude of the downstroke, is shown in red. Six stimuli, each forming a planar wavefront, were applied at a CV of 600 mm/s. In (a), the behavior of the DC characteristics for the second stimulus is displayed, while (b) represents this behavior for the sixth stimulus. Figure reproduced from [120].

Table 9.1: Fitting parameters of the restitution curve for the maxima of the DC. Table reproduced from [120].

	k_0 (–)	k_1 (ms)	k_2 (ms^{-1})	γ(mA/cm^2)
Second stimulus	35.3	48.2	152.6	78.9
Sixth stimulus	28.8	-62.1	75.5	78.5

Table 9.2: Fitting parameters of the restitution curve for the minima of the DC. Table reproduced from [120].

	k_0 (–)	k_1 (ms)	k_2 (ms^{-1})	γ(mA/cm^2)
Second stimulus	12.7	1.22	105.3	145.4
Sixth stimulus	51.7	-53.6	84.1	144.4

9.3.2 Source-Sink Mismatch

Figures 9.3a and 9.4a show the interpolated ATs for two scenarios: colliding wavefronts and a highly curved wavefront reaching the central node, respectively. In Figures 9.3b and 9.4b, the corresponding areas representing the interpolated ATs along the perimeter and the propagation time areas are shown. Two distinct patterns emerge in each case. In the colliding waves scenario, most of the nodes along the perimeter contribute to A_{source}, where the blue region does not reach the yellow line. Conversely, for the curved wavefront scenario, the blue area mostly surpasses the yellow region, indicating that most perimeter nodes contribute to r_{sink}.

By quantifying this for every node in reentries, where colliding waves and curved wavefronts occur at different times and locations, it becomes clear, as seen in Figure 9.5, that A_{source} versus the extrema of the DC cluster together. This clustering reveals that a nonlinear regression can be developed to approximate the extrema of the DC based on A_{source}, which is derived from parameters available in eikonal-based models. A cubic fit was selected for A_{source} versus the maximum values, while a hyperbolic fit was chosen for the r_{sink} versus the minimum values. The histograms show that most data points for the maximum of the DC are concentrated in regions with large source areas. Using Equation (9.7), the data points for these nodes were fitted with a polynomial function. The fit parameters for the maximum, denoted by u_{max}, are provided in Table 9.3.

For the correlation between the minimum of the DC and the sink ratio, a similar fit was performed using Equation (9.8). The resulting fit parameters for the minimum of the DC are presented in Table 9.4. According to the histograms, most data points cluster around a sink ratio of 0.5. The standard deviation for differences for the curve fitting is 5.46 mA/cm^2 for the maximum and 65.2 mA/cm^2 for the minimum, with mean values of 5.49 mA/cm^2 and 29.3 mA/cm^2, respectively.

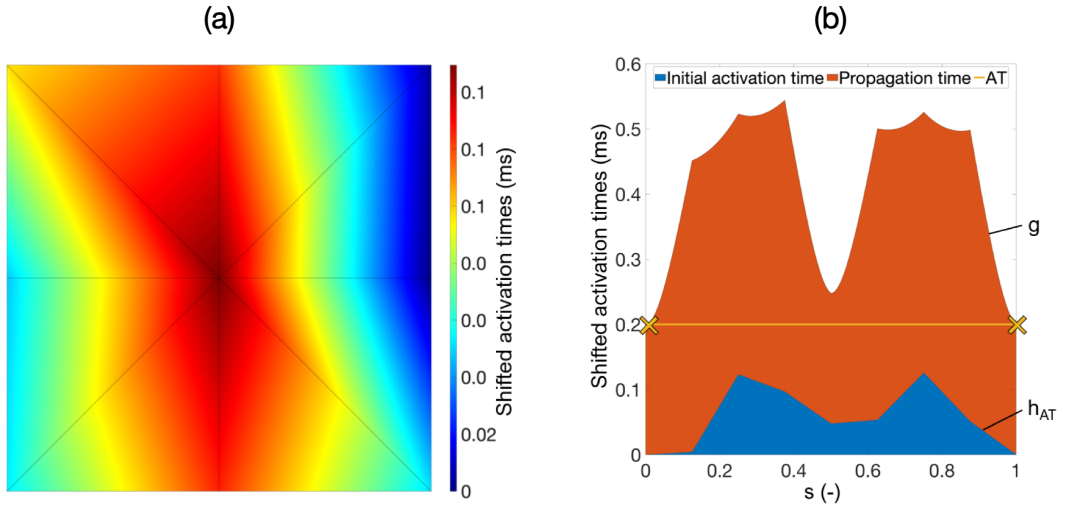

Figure 9.3: Parameterization of colliding waves. In (a), the propagation pattern of two colliding waves is depicted, where stimuli were applied at the left and right mesh boundaries, inducing the propagation of two converging waves. Activation times were calculated for nine nodes, each located at the corners, the center, and along the edges of the rectangle. In (b), this scenario is parametrized for the mesh segment shown in (a). s represents a point on the perimeter of the polygon formed by the union of all triangles containing the central node, and it is assigned a number in the interval $[0, 1)$.ATs of neighboring nodes are represented in blue, while the PT, indicating the time a wave takes to propagate from a neighboring node to the observed node, is shown in orange. The function's minimum corresponds to the action potential (AP) of the observed node, illustrated in yellow. Figure reproduced from [120].

Table 9.3: Fitting parameters of the correlation between the maximum of the DC and the source area.

α_0 $(\mathrm{mA/(ms^3 \cdot cm^2)})$	α_1 $(\mathrm{mA/(ms^2 \cdot cm^2)})$	α_2 $(\mathrm{mA/(ms \cdot cm^2)})$	α_3 $(\mathrm{mA/cm^2})$
-31.2	63.01	-59.85	85.3

Table 9.4: Fitting parameters of the correlation between the minimum of the DC and r_{sink}.

η_0 $(\mathrm{mA/cm^2})$	η_1 (–)	η_2 $(\mathrm{mA/cm^2})$
3.067	0.4645	-170.3

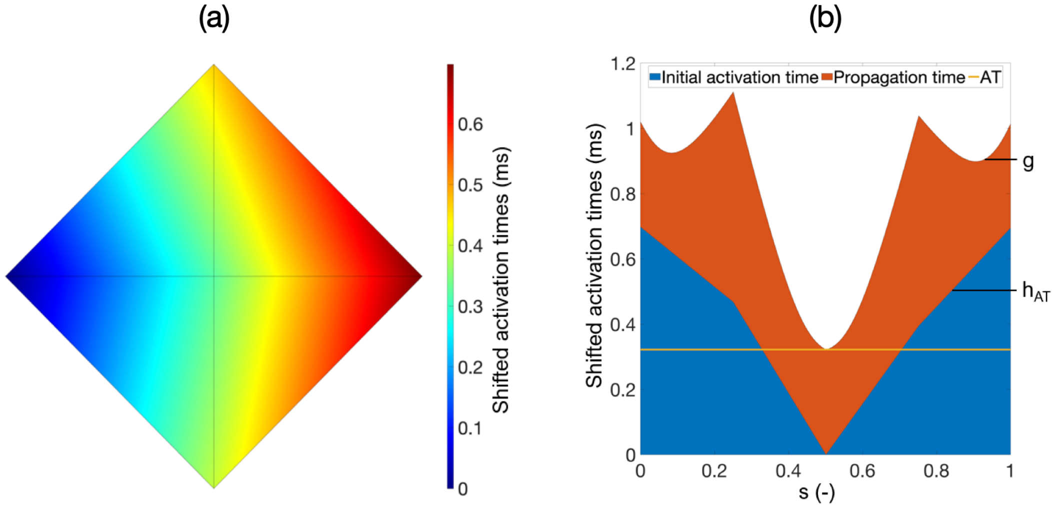

Figure 9.4: Parameterization of a convexly curved wavefront. In (a), the propagation pattern of a convexly curved wavefront is illustrated. A node at the left mesh boundary was stimulated, leading to the formation of a curved wavefront. Activation times were calculated for nine nodes, each located at the corners, and along the edges of the rectangle. In (b), this scenario is parameterized for the mesh segment shown in (a). s represents a point on the perimeter of the polygon formed by the union of all triangles containing the central node, and it is assigned a number in the interval $[0, 1)$. ATs of neighboring nodes are represented in blue, while the PT, indicating the time a wave takes to propagate from a neighboring node to the observed node, is shown in orange. The function's minimum corresponds to the action potential (AP) of the observed node, illustrated in yellow. Figure reproduced from [120].

9.4 Discussion

This study provides valuable insights into the behavior of DCs under different conditions, offering a pathway for incorporating these effects into eikonal-based models. To achieve this, regression models were developed based on monodomain simulations to predict the extreme values of DCs. The results showed that both pacing frequency and source-sink mismatch effects significantly affect the maximum and minimum values of the DC.

The findings offer a deeper understanding of how DCs behave in various scenarios, emphasizing key parameters, such as frequency and the relationship between source and sink regions, that must be considered when modeling these phenomena. The regression models were designed with independent variables that are readily available in eikonal-based models, facilitating their integration. In the DREAM, the I_{diff} function is applied only after the cyclical FIM (cycFIM) has determined the final solution of the eikonal equation for the central node (see Equation 17 in [22] in Chapter 6). As a result, the solver's iterative process does not interfere with the approximation of the DC extreme values.

Importantly, this study also demonstrates how regression models can be used to predict some of the critical features of DCs, such as their amplitude and extrema, without necessitating a prominent increase in model complexity. This is a crucial finding, as one of the

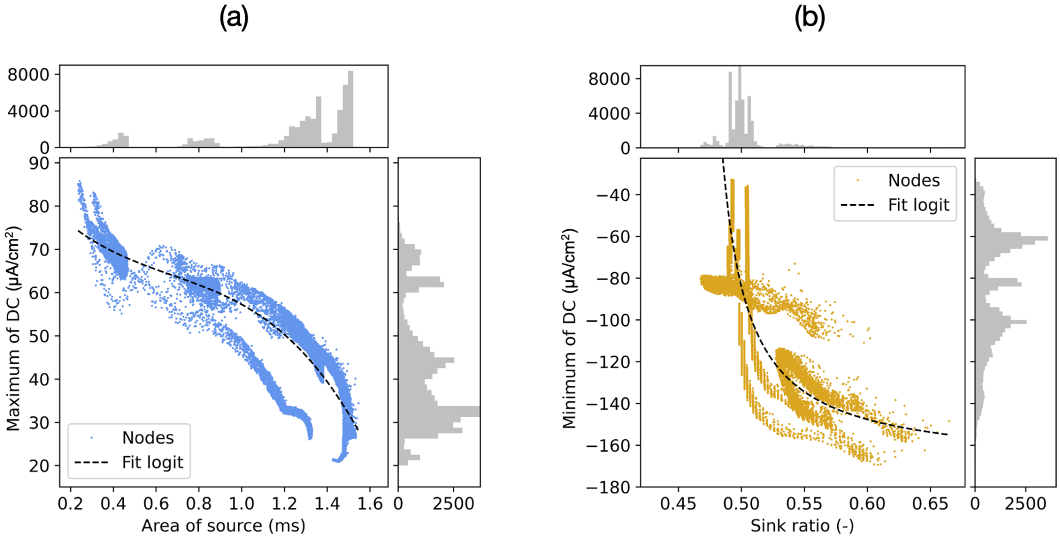

Figure 9.5: Histograms and correlations between the maximum and minimum of the DC and the source area and sink ratio. In (a), a correlation between the maximum of the DC and the source area is shown. The histograms indicate that most data points have a large source area. A correlation is represented by a polynomial function. For the minimum in (b), a correlation for the sink ratio was found through a hyperbolic function. Since the data points for very low sink ratios constitute a very small portion of the overall data, they were not considered for this fit. Figure reproduced from [120].

goals of this research is to maintain computational efficiency in eikonal-based models while improving their physiological accuracy.

One of the key advantages of eikonal-based models is their computational efficiency, making them suitable for large-scale simulations. It is therefore crucial that any enhancements to these models do not introduce computationally expensive steps. By utilizing relatively simple regression models to predict the extrema of DCs, the added computational complexity remains minimal. This is a critical point, as one of the primary goals of this research is to preserve the computational speed of eikonal-based models while simultaneously improving their physiological accuracy.

Another key innovation in this work is the development of a novel method to quantify source-sink mismatch. Two new variables were introduced: the area of source and the ratio of sink, which effectively represent the balance between source and sink around each node. These variables are computed using information readily available in eikonal models, such as ATs and node coordinates. This method not only has the potential to enhance eikonal-based models but could also serve as a valuable tool for directly investigating source-sink mismatch effects across various applications. Additionally, using the same metric to research their impact directly in CV could be a meaningful contribution.

Several limitations of this study must be acknowledged. An important one is the exclusion of repolarization currents, which are critical for understanding arrhythmic behavior and reentry dynamics. Future research should focus on incorporating DCs during the repolarization phase, particularly those occurring during reentry, to enhance the accuracy of eikonal-based models. This study mainly focused on developing regression models to predict maximum and minimum DC values, which may limit broader applicability. Future work should also explore sub-clustering the scatter plots in Figure 9.5, which are likely influenced by factors such as the number of neighboring nodes or the distance to a boundary within the geometry. Additionally, other influential factors should be explored, such as frequency decomposition or wave duration in the context of highly curved or colliding wavefronts. Investigating these elements could improve understanding of action potential (AP) propagation in complex geometries. The increased complexity associated with these metrics may necessitate the use of machine learning approaches for more accurate predictions.

While considerable insights were gained in this study to better understand DCs and develop regression models for their incorporation into eikonal-based models, it is essential to implement these models and examine the details of their integration. Several regression models have previously been used to incorporate physiological effects into eikonal-based models, such as the DC in the work of Gassa et al., the DREAM for the restitution curve of CV, and the restitution curve of APD in the multifrontal fast marching method [21–23]. Similarly, the regression model for approximating the extrema of DCs could adopt a comparable approach.

9.5 Conclusion

This study marks an important step toward improving the integration of DCs into eikonal-based models of AP propagation. It highlights how factors like pacing frequency and source-sink mismatch effects influence DCs, while demonstrating that regression models can predict key features without adding unnecessary complexity. Additionally, a novel method for quantifying source-sink mismatch was introduced, which could be valuable not only for enhancing eikonal-based models but also for investigating source-sink mismatch effects in reaction diffusion (RD) models. However, certain limitations remain, such as the exclusion of repolarization currents and the focus on predicting only the extrema of the DC. These areas present opportunities for future improvement. Despite these limitations, this work lays a foundation for further refinement of eikonal-based models, aiming to increase their accuracy without compromising computational efficiency. Such advancements could enhance the applicability of eikonal models in both research and clinical contexts.

PART V

SUMMARY

Chapter 10

Outlook

10.1 Future Research Directions and Limitations

Despite the advancements made in this work, several gaps in the literature remain that require further investigation. An important direction for future research is the exploration of more complex geometries and volumetric models. While the methodologies employed in this study primarily utilized simple 2D meshes and 2D manifolds in 3D space, extending this work to incorporate variable geometries and fully account for wall thickness will be crucial. To facilitate this, the parallelization of the code, particularly concerning the diffusion reaction eikonal alternant model (DREAM) framework, could significantly enhance computational efficiency and broaden the scope of potential applications. Another relevant aspect for future research is the translation of the techniques developed in this work to ventricular pathologies. This involves tuning geometrical features, conduction velocity (CV) ranges, and ionic models to apply the eikonal-based model advancements to the ventricles. Such efforts could foster a deeper understanding of ventricular arrhythmias and their underlying mechanisms, while also guiding patient stratification and treatment recommendations

The DREAM has been utilized within this work to study the effects of CV restitution curves on arrhythmia vulnerability. However, its applications extend beyond this context. For instance, the DREAM can facilitate large in silico studies that assess arrhythmia vulnerability by varying patient geometries. Additionally, it holds significant potential for exploring ablation treatments and pharmacological applications, further enhancing its value in the field of cardiac electrophysiology.

Moreover, integrating machine learning into the development of eikonal-based models presents a promising path for future exploration. By leveraging insights from the eikonal model alongside machine learning techniques, researchers could significantly enhance the estimation of CV derived from electroanatomical recordings. Furthermore, machine learning could help address limitations associated with source-sink mismatch and the absence of diffusion currents during the repolarization phase. These techniques may simplify the complexities of diffusion current (DC) phenomena and improve predictions of key features related to source-sink mismatch effects. Such advancements could result in the development of more accurate and robust eikonal-based models, ultimately enhancing their clinical applicability.

Several limitations of this study must be acknowledged. First, the simulations were restricted to simple atrial geometries and 2D sheets, neglecting volumetric meshes. This limitation may affect the generalizability of the results to more complex anatomical structures. Most experiments relied on a single instance from a statistical shape model or a single patient's geometry for each setup. This approach limited the incorporation of variations from a broader range of patient data and the diversity of the statistical shape model. While the study focused on atrial tissue, including its specific geometry, CV ranges, and ionic models, the findings may not fully translate to other regions of the ventricles.

Another limitation of this study is the lack of a robust representation of source-sink mismatch, which remains a significant challenge for the eikonal model. Although some progress was made in addressing this issue through the integration of regression models that account for factors like wall thickness and tissue curvature, these approaches do not fully capture the complexities of physiological interactions that occur within cardiac tissue. As a result, the eikonal model's accuracy is constrained by this shortcoming, particularly when predicting arrhythmia dynamics, where source-sink interactions are critical in influencing conduction patterns and stability. The inability to accurately model these interactions can lead to discrepancies in simulations that affect treatment strategies for patients with cardiac arrhythmias. Therefore, future research should prioritize the development of more sophisticated techniques to accurately represent these phenomena.

Additionally, a technical limitation of the study was the absence of parallelization in the computational models. Most experiments were conducted sequentially, which, while not critical for the specific use cases examined, hinders computational efficiency and restrict the ability to scale simulations to larger or more detailed anatomical structures. Furthermore, the diffusion current during repolarization, an essential factor for electrophysiological accuracy, was not thoroughly explored in this work and should be a focus of future investigations. Most approaches developed in these studies to address the limitations of source-sink mismatch and improve representation of diffusion currents primarily focused on the depolarization phase, neglecting the phenomena occurring during repolarization.

10.2 Challenges and Opportunities

Advancing research in eikonal-based models presents both challenges and opportunities. One major challenge is convincing clinicians of the importance of computer models. Achieving this requires thorough validation and clinical trials to demonstrate the efficacy and potential benefits of these models, not only for clinicians but also for patients, healthcare companies, and policymakers.

Technologically, computational cost remains a significant barrier. Like many models, eikonal-based frameworks face the ongoing struggle between achieving high accuracy and managing resource consumption. Ideally, these models should provide substantial clinical value while efficiently utilizing available hospital resources.

Looking to the future, there are significant opportunities for advancement in this field. As technology progresses, improvements in segmentation techniques for anatomical features and parameter measurement, such as CV estimation and sex-specific parameters, will enhance the results generated by eikonal-based models. This evolution could lead to better predictive capabilities and more personalized patient assessments, ultimately broadening the applicability of these models in clinical practice.

Another promising opportunity lies in the increasingly interdisciplinary nature of research. Collaborative efforts among mathematicians, engineers, clinicians, biologists, and other disciplines can provide diverse insights to improve the methodology. While this work primarily involves mathematical and technical methods, the contributions from clinicians and biologists, derived from patient studies and in vitro experiments, will play an increasingly vital role in adapting and refining computer models.

Chapter 11

Conclusion

11.1 Summary of Key Findings

This study aimed to enhance the eikonal model and expand its applications in cardiac electrophysiology, with a specific focus on the research, diagnosis, and treatment of atrial arrhythmias. The key objectives were: evaluating the performance of the standard eikonal model by comparing it with reaction diffusion (RD) models, using it to assess methods for estimating conduction velocity (CV) in atrial tissue, extending its capabilities by integrating it with other models to reproduce reentry, and reducing its limitations related to the representation of source-sink mismatches.

The findings revealed both strengths and limitations in the current use of the eikonal model. The standard eikonal model performed well in simulating sinus rhythm. The results were sufficiently accurate, when compared to RD models, especially in simulations of a single heartbeat in atrial geometry without fibrosis. However, the model's accuracy declined significantly when fibrosis was introduced. This decline was largely due to its inability to represent source-sink mismatches, which led to discrepancies in simulations of more complex arrhythmias.

This study assessed methods to estimate CV. It was found that with minor adjustments to the eikonal solution, and by utilizing intermediate variables calculated during the fast iterative method, it was possible to provide a ground truth for both CV and activation times (ATs) during wave propagation. When comparing this ground truth from anisotropic simulations to the CV estimates provided by methods like radial basis function, which neglects anisotropy, the results showed a clear underestimation of CV. This underestimation could potentially lead to harmful and unnecessary treatments in clinical settings, highlighting the critical importance of accounting for anisotropy when estimating CV in clinical practice.

One of the major contributions of this study was the development of the diffusion reaction eikonal alternant model (DREAM), which combines the computational efficiency of the eikonal model with the ability of RD models to simulate reentry and reactivation phenomena. This new model successfully replicated key electrophysiological behaviors, such as reentry dynamics and CV restitution, providing a more comprehensive simulation framework. A core component of DREAM is the cyclical FIM (cycFIM), an adaptation of the fast iterative method, which allows for the simulation of reactivations within the eikonal model.

Another significant advantage of the DREAM is its ability to personalize restitution curves of CV using data from clinical patients. By incorporating patient-specific data, DREAM enabled a detailed investigation into the morphology of CV restitution curves and their impact on arrhythmia dynamics. Notably, the study found that the steepness of restitution curves plays a crucial role in modulating the vulnerable window and average duration of reentries. This insight demonstrates the potential of DREAM to not only enhance the accuracy of personalized simulations, but also to provide valuable clinical insights into the mechanisms that predispose patients to reentry and arrhythmias.

Recognizing that the lack of accurate source-sink mismatch representation remains a significant limitation of the eikonal model, two primary methods were proposed to mitigate this issue: (1) incorporating the effects of wall thickness and tissue curvature into the model through a regression approach based on bidomain simulations, and (2) using monodomain simulations to investigate how pacing frequency and source-sink mismatch influence diffusion currents. These methods provided simple regression models that can be integrated into eikonal-based simulations, improving accuracy without significantly compromising computational efficiency.

11.2 Contribution to the Field

The findings of this research provide valuable insights into the utility and limitations of the eikonal model in cardiac electrophysiology. A key contribution of this study is the identification of scenarios in which the eikonal model performs effectively, such as simulating sinus rhythm in the absence of fibrosis. In these contexts, its performance is comparable to that of more detailed RD models. These findings suggest that the eikonal model could be utilized effectively in specific clinical and research settings without significant loss of accuracy, particularly in less complex simulations.

The study also pointed out the importance of accounting for anisotropy when estimating CV. Neglecting anisotropy, as seen in some methods such as radial basis functions, can lead to underestimations of CV, which may have critical implications in clinical settings. This insight has the potential to influence industry approaches to CV mapping tools, highlighting the need for more accurate methods that consider tissue anisotropy appropriately.

Furthermore, by integrating the eikonal model with other models like RD, the study demonstrated that more complex phenomena, such as reentry and reactivation, could be effectively simulated. This broadens the range of applications for eikonal-based models, particularly in investigating arrhythmias, especially with the availability of the DREAM as open-source software. The development of the cycFIM within DREAM illustrated that it is indeed possible to simulate reactivations using the eikonal model while employing iterative techniques that better account for anisotropy. This novel approach to simulating reactivations in anisitropic propagation may have implications beyond the medical field.

Additionally, this research emphasized the lack of source-sink mismatch representation as a significant limitation of the eikonal model. This limitation contributed to discrepancies between RD simulations and eikonal-based simulations, particularly in more complex scenarios. However, the study demonstrated that these limitations could be partially mitigated through straightforward techniques, such as regression models that incorporate factors like wall thickness, tissue curvature, pacing frequency, and the quantification of source-sink mismatch in diffusion current amplitude. The development of new methods to quantify source-sink mismatch using variables available in the eikonal model (e.g., ATs and node coordinates) represents a novel contribution to the field. These methods not only enhance the accuracy of eikonal-based models but also provide tools for investigating source-sink mismatch effects, such as those observed in electroanatomical recordings or detailed RD simulations. By leveraging variables within the eikonal model, this approach paves the way for further exploration of how source-sink mismatch influences wave propagation and arrhythmia dynamics.

11.3 Broader Implications

The development of the cycFIM marks a significant theoretical and practical advancement in the simulation of reactivation waves. This innovative approach may inspire other research groups facing similar challenges, encouraging them to adopt or adapt its principles in their own work. With the DREAM now publicly available through the openCARP platform, it is anticipated that additional research teams will utilize this tool for simulations requiring the computation of reentries at a lower cost. Furthermore, the open-source nature of DREAM allows for collaboration among groups, fostering improvements and enhancements driven by community contributions to the source code and tutorials.

This research also provides valuable insights that could influence future studies in cardiac electrophysiology. One significant finding is that anisotropy should not be ignored for CV estimation. This discovery encourages researchers to develop methods for estimating CV without assuming isotropic propagation, potentially leading to improved estimation techniques that better reflect the patient-specific activation patterns. Additionally, the implementation of regression techniques to reduce the limitations of the eikonal model opens another opportunity for improvement of the model. This approach can inspire other research teams to adopt similar or more sophisticated regression techniques to enhance eikonal-based models, thereby broadening the applicability and accuracy of eikonal-based simulations. Moreover, the lower computing times of eikonal-based simulations can be beneficial in research, enabling large-scale in silico studies and the exploration of a wide range of scenarios efficiently.

On a practical level, the extended eikonal-based models (i.e., the DREAM and the method to provide ground truth for CV magnitude and direction) introduced in this work pave the way for integrating the eikonal model into clinical settings. Although widespread implementation is not yet achievable, progress is being made toward this goal. Once fully developed, these models could significantly enhance patient assessments by providing more accurate estimates of CV and the associated risks of arrhythmias. Additionally, personalized simulations could yield tailored treatment recommendations, ultimately improving both pharmacological and ablation strategies.

As the eikonal-based models continue to evolve, they hold the potential to impact industry practices. It may guide the design of improved mapping systems capable of estimating CV with greater accuracy since they can be tested with computer models. This progress could contribute to the inclusion of computational tools in future clinical guidelines. Moreover, the insights gained from this research could lead to the establishment of new regulatory standards, particularly regarding anisotropic propagation. This would help minimize the risk of underestimating CV and its potential implications for patient care. Furthermore, simulating reentry with eikonal-based models like the DREAM, using personalized anatomical and functional parameters, could enhance decision support systems. The reduced computing times of these eikonal-based models could enable companies to develop products that provide clinicians with personalized treatment recommendations. This will allow for effective patient care based on simulations performed in a very short time.

11.4 Conclusion

In conclusion, this research shows the significant potential of the eikonal model in advancing our understanding and clinical management of cardiac arrhythmias. By offering a computationally efficient alternative to more complex and resource-intensive models, the eikonal framework enables valuable insights into arrhythmia mechanisms, diagnosis, and treatment recommendations. Its computational efficiency makes it particularly appealing for conducting large-scale in silico studies and for the use in clinical settings where computing resources may be limited and quicker results are required. However, it is essential to address the current limitations, especially regarding the accurate representation of source-sink mismatches, which are crucial for understanding conduction dynamics. The findings of this study pave the way for enhanced applications of eikonal-based models in cardiac electrophysiology, ultimately contributing to improved patient outcomes and broader implications that extend beyond the medical field.

References

[1] G. A. Roth, G. A. Mensah, C. O. Johnson, et al., “Global burden of cardiovascular diseases and risk factors, 1990–2019: update from the gbd 2019 study,” *Journal of the American College of Cardiology*, vol. 76, pp. 2982–3021, 2020. doi:10.1016/j.jacc.2020.11.010

[2] R. Luengo-Fernandez, M. Walli-Attaei, A. Gray, et al., “Economic burden of cardiovascular diseases in the european union: a population-based cost study,” *European Heart Journal*, vol. 44, pp. 4752–4767, 2023. doi:10.1093/eurheartj/ehad583

[3] J. N. M. Lui, C. Williams, M. J. Keng, et al., “Impact of new cardiovascular events on quality of life and hospital costs in people with cardiovascular disease in the united kingdom and united states,” *Journal of the American Heart Association*, vol. 12, p. e030766, 2023. doi:10.1161/JAHA.123.030766

[4] M. Borgi, G. Biondi-Zoccai, G. Frati, and M. Peruzzi, “Cardiovascular disease and mental health: a dangerous duo?” pp. 1686–1688, 2023. doi:10.1093/eurjpc/zwad199

[5] E. J. Benjamin, P. Muntner, A. Alonso, et al., “Heart disease and stroke statistics—2019 update: a report from the american heart association,” *Circulation*, vol. 139, pp. e56–e528, 2019. doi:10.1161/CIR.0000000000000659

[6] C. R. Wyndham, “Atrial fibrillation: the most common arrhythmia,” *Texas Heart Institute Journal*, vol. 27, p. 257, 2000.

[7] G. Hindricks, T. Potpara, N. Dagres, et al., “2020 esc guidelines for the diagnosis and management of atrial fibrillation developed in collaboration with the european association for cardio-thoracic surgery (eacts) the task force for the diagnosis and management of atrial fibrillation of the european society of cardiology (esc) developed with the special contribution of the european heart rhythm association (ehra) of the esc,” *European Heart Journal*, vol. 42, pp. 373–498, 2021. doi:10.1093/eurheartj/ehaa612

[8] J. Heijman, J.-B. Guichard, D. Dobrev, and S. Nattel, “Translational challenges in atrial fibrillation,” *Circulation Research*, vol. 122, pp. 752–773, 2018. doi:10.1161/CIRCRESAHA.117.311081

[9] E. Grandi, D. Dobrev, and J. Heijman, “Computational modeling: What does it tell us about atrial fibrillation therapy?” *International Journal of Cardiology*, vol. 287, pp. 155–161, 2019. doi:10.1016/j.ijcard.2019.01.077

[10] A. Dasí, M. T. Pope, R. S. Wijesurendra, et al., “What determines the optimal pharmacological treatment of atrial fibrillation? insights from in silico trials in 800 virtual atria,” *The Journal of Physiology*, vol. 601, pp. 4013–4032, 2023. doi:10.1113/JP284730

[11] M. Mase, “Application of computer models on atrial fibrillation research,” *Minerva Cardioangiologica*, vol. 65, pp. 398–419, 2017. doi:10.23736/S0026-4725.17.04363-8

[12] K. N. Aronis, R. Ali, and N. A. Trayanova, “The role of personalized atrial modeling in understanding atrial fibrillation mechanisms and improving treatment,” *International Journal of Cardiology*, vol. 287, pp. 139–147, 2019. doi:10.1016/j.ijcard.2019.01.096

[13] L. Azzolin, S. Schuler, O. Dössel, and A. Loewe, “A reproducible protocol to assess arrhythmia vulnerability in silico: pacing at the end of the effective refractory period,” *Frontiers in Physiology*, vol. 12, p. 656411, 2021. doi:10.3389/fphys.2021.656411

[14] D. G. Whittaker, M. Clerx, C. L. Lei, D. J. Christini, and G. R. Mirams, “Calibration of ionic and cellular cardiac electrophysiology models,” *Wiley Interdisciplinary Reviews: Systems Biology and Medicine*, vol. 12, p. e1482, 2020. doi:10.1002/wsbm.1482

[15] M. Wallman, N. P. Smith, and B. Rodriguez, “A comparative study of graph-based, eikonal, and monodomain simulations for the estimation of cardiac activation times,” *IEEE Transactions on Biomedical Engineering*, vol. 59, pp. 1739–1748, 2012. doi:10.1109/TBME.2012.2193398

[16] L. Tung, “A bi-domain model for describing ischemic myocardial dc potentials,” PhD thesis, Massachusetts Institute of Technology, 1978.

[17] J. Keener and J. Sneyd, “Mathematical physiology 1: Cellular physiology,” 2009. doi:10.1007/978-0-387-75847-3

[18] P. C. Franzone, L. F. Pavarino, and S. Scacchi, *Mathematical cardiac electrophysiology*, vol. 13. Springer, 2014. doi:10.1007/978-3-319-04801-7

[19] C. Nagel, C. Barrios Espinosa, K. Gillette, et al., “Comparison of propagation models and forward calculation methods on cellular, tissue and organ scale atrial electrophysiology,” *IEEE Transactions on Biomedical Engineering*, vol. 70, pp. 511–522, 2023. doi:10.1109/tbme.2022.3196144

[20] A. Neic, F. O. Campos, A. J. Prassl, et al., “Efficient computation of electrograms and ecgs in human whole heart simulations using a reaction-eikonal model,” *Journal of Computational Physics*, vol. 346, pp. 191–211, 2017. doi:10.1016/j.jcp.2017.06.020

[21] E. Pernod, M. Sermesant, E. Konukoglu, J. Relan, H. Delingette, and N. Ayache, “A multi-front eikonal model of cardiac electrophysiology for interactive simulation of radio-frequency ablation,” *Computers & Graphics*, vol. 35, pp. 431–440, 2011. doi:10.1016/j.cag.2011.01.008

[22] C. B. Espinosa, J. Sánchez, S. Appel, et al., “A cyclical fast iterative method for simulating reentries in cardiac electrophysiology using an eikonal-based model,” *arXiv preprint arXiv:2406.18619*, 2024.

[23] N. Gassa, N. Zemzemi, C. Corrado, and Y. Coudière, “Spiral waves generation using an eikonal-reaction cardiac electrophysiology model,” in *International Conference on Functional Imaging and Modeling of the Heart*. Springer, 2021, pp. 523–530. doi:https://doi.org/10.1007/978-3-030-78710-3_50

[24] L. Mesotten, A. Maes, A.-S. Hambÿe, et al., “Nuclear cardiology, part i: anatomy and function of the normal heart,” *Journal of Nuclear Medicine Technology*, vol. 26, pp. 4–8, 1998.

[25] P. A. Iaizzo, *Handbook of cardiac anatomy, physiology, and devices*. Springer Science & Business Media, 2010. doi:10.1007/978-3-319-19464-6

[26] Z. J. Schoppen, L. C. Balmert, S. White, et al., “Prevalence of abnormal heart weight after sudden death in people younger than 40 years of age,” *Journal of the American Heart Association*, vol. 9, p. e015699, 2020. doi:10.1161/JAHA.120.015699

[27] R. H. Anderson, R. Razavi, and A. M. Taylor, “Cardiac anatomy revisited,” *Journal of Anatomy*, vol. 205, pp. 159–177, 2004. doi:10.1111/j.0021-8782.2004.00330.x

[28] F. G. Pérez, “L. latarjet-ruiz, anatomía humana, tomo ii, médica panamericana, buenos aires (2004),” 2005.

[29] O. College, “Illustration from anatomy & physiology,” 2013. https://commons.wikimedia.org/wiki/File:2008_Internal_Anatomy_of_the_HeartN.jpg

[30] I. Kucybała, K. Ciuk, and W. Klimek-Piotrowska, “Clinical anatomy of human heart atria and interatrial septum—anatomical basis for interventional cardiologists and electrocardiologists. part 1: right atrium and interatrial septum,” *Kardiologia Polska (Polish Heart Journal)*, vol. 76, pp. 499–509, 2018. doi:10.5603/KP.a2017.0248

[31] S. Ciuk, P. Janas, and W. Klimek-Piotrowska, “Clinical anatomy of human heart atria and interatrial septum—anatomical basis for interventional cardiologists and electrocardiologists. part 2: left atrium,” *Polish Heart Journal (Kardiologia Polska)*, vol. 76, pp. 510–519, 2018. doi:10.5603/KP.a2018.0001

[32] S. Y. Ho, J. A. Cabrera, and D. Sanchez-Quintana, “Left atrial anatomy revisited,” *Circulation: Arrhythmia and Electrophysiology*, vol. 5, pp. 220–228, 2012. doi:10.1161/CIRCEP.111.962720

[33] B. Dye and J. Lincoln, “The endocardium and heart valves,” *Cold Spring Harbor Perspectives in Biology*, vol. 12, p. a036723, 2020. doi:10.1101/cshperspect.a036723

[34] A. J. Pope, G. B. Sands, B. H. Smaill, and I. J. LeGrice, “Three-dimensional transmural organization of perimysial collagen in the heart,” *American Journal of Physiology-Heart and Circulatory Physiology*, vol. 295, pp. H1243–H1252, 2008. doi:10.1152/ajpheart.00484.2008

[35] A. M. Gerdes, S. E. Kellerman, J. A. Moore, et al., “Structural remodeling of cardiac myocytes in patients with ischemic cardiomyopathy.” *Circulation*, vol. 86, pp. 426–430, 1992. doi:10.1161/01.cir.86.2.426

[36] A. M. Gordon, A. F. Huxley, and F. J. Julian, “The variation in isometric tension with sarcomere length in vertebrate muscle fibres,” *The Journal of Physiology*, vol. 184, pp. 170–192, 1966. doi:10.1113/jphysiol.1966.sp007909

[37] R. Klabunde, *Cardiovascular physiology concepts*. Lippincott Williams & Wilkins, 2011.

[38] M. Mohamed Elshennawy, “Cardiac sarcomere structure,” 2022. https://commons.wikimedia.org/wiki/File:Cardiac_sarcomere_structure.jpg

[39] S. Y. Ng, C. K. Wong, and S. Y. Tsang, “Differential gene expressions in atrial and ventricular myocytes: insights into the road of applying embryonic stem cell-derived cardiomyocytes for future therapies,” *American Journal of Physiology-Cell Physiology*, vol. 299, pp. C1234–C1249, 2010. doi:10.1152/ajpcell.00402.2009

[40] S. Brandenburg, E. C. Arakel, B. Schwappach, and S. E. Lehnart, “The molecular and functional identities of atrial cardiomyocytes in health and disease,” *Biochimica et Biophysica Acta (BBA)-Molecular Cell Research*, vol. 1863, pp. 1882–1893, 2016. doi:10.1016/j.bbamcr.2015.11.025

[41] A. C. Guyton, *Text book of medical physiology*. Elsevier, 2006.

[42] S. N. Hatem, A. Coulombe, and E. Balse, “Specificities of atrial electrophysiology: Clues to a better understanding of cardiac function and the mechanisms of arrhythmias,” *Journal of Molecular and Cellular Cardiology*, vol. 48, pp. 90–95, 2010. doi:10.1016/j.yjmcc.2009.08.029

[43] PeaBrainC, “Cardiac sarcomere structure,” 2015. https://commons.wikimedia.org/wiki/File:Currents_responsible_for_the_cardiac_action_potential.png

[44] A. D. Elliott, M. E. Middeldorp, I. C. Van Gelder, C. M. Albert, and P. Sanders, “Epidemiology and modifiable risk factors for atrial fibrillation,” *Nature Reviews Cardiology*, vol. 20, pp. 404–417, 2023. doi:10.1038/s41569-022-00820-8

[45] C. Magnussen, T. J. Niiranen, F. M. Ojeda, et al., “Sex differences and similarities in atrial fibrillation epidemiology, risk factors, and mortality in community cohorts: results from the biomarcare consortium (biomarker for cardiovascular risk assessment in europe),” *Circulation*, vol. 136, pp. 1588–1597, 2017. doi:10.1161/CIRCULATIONAHA.117.028981

[46] U. Schotten, S. Verheule, P. Kirchhof, and A. Goette, “Pathophysiological mechanisms of atrial fibrillation: a translational appraisal,” *Physiological Reviews*, vol. 91, pp. 265–325, 2011. doi:10.1152/physrev.00031.2009

[47] S. Tzeis, E. P. Gerstenfeld, J. Kalman, et al., “2024 european heart rhythm association/heart rhythm society/asia pacific heart rhythm society/latin american heart rhythm society expert consensus statement on catheter and surgical ablation of atrial fibrillation,” *Europace*, vol. 26, p. euae043, 2024. doi:10.1093/europace/euae043

[48] A. Gharaviri, E. Bidar, M. Potse, et al., “Epicardial fibrosis explains increased endo-epicardial dissociation and epicardial breakthroughs in human atrial fibrillation.” *Frontiers in Physiology*, vol. 11, p. 68, 2020. doi:10.3389/fphys.2020.00068

[49] J. Eckstein, B. Maesen, D. Linz, et al., “Time course and mechanisms of endo-epicardial electrical dissociation during atrial fibrillation in the goat,” *Cardiovascular Research*, vol. 89, pp. 816–824, 2011. doi:10.1093/cvr/cvq336

[50] N. M. de Groot, R. P. Houben, J. L. Smeets, et al., “Electropathological substrate of longstanding persistent atrial fibrillation in patients with structural heart disease: epicardial breakthrough,” *Circulation*, vol. 122, pp. 1674–1682, 2010. doi:10.1161/CIRCULATIONAHA.109.910901

[51] S. B. Owais, Z. B. Bulwa, and F. El Ammar, “Differences in stroke clinical presentation among sexes,” *Journal of Stroke and Cerebrovascular Diseases*, p. 107807, 2024. doi:10.1016/j.jstrokecerebrovasdis.2024.107807

[52] M. Arrigo, M. Jessup, W. Mullens, et al., “Acute heart failure,” *Nature Reviews Disease Primers*, vol. 6, p. 16, 2020. doi:10.1038/s41572-020-0151-7

[53] J. S. Steinberg, H. O’Connell, S. Li, and P. D. Ziegler, “Thirty-second gold standard definition of atrial fibrillation and its relationship with subsequent arrhythmia patterns: analysis of a large prospective device database,” *Circulation: Arrhythmia and Electrophysiology*, vol. 11, p. e006274, 2018. doi:10.1161/CIRCEP.118.006274

[54] E. Invers-Rubio, I. Hernández-Romero, J. Reventos-Presmanes, et al., “Regional conduction velocities determined by noninvasive mapping are associated with arrhythmia-free survival after atrial fibrillation ablation,” *Heart Rhythm*, 2024. doi:10.1016/j.hrthm.2024.04.063

[55] M. Thind, Q. Lou, E. S. Zado, et al., “Utility of noninvasive electrocardiographic imaging in the localization of nonpulmonary vein triggers of atrial fibrillation determined by pacing common trigger sites,” *Journal of Cardiovascular Electrophysiology*, 2024. doi:10.1111/jce.16347

[56] M. Njeim, B. Desjardins, and F. Bogun, “Multimodality imaging for guiding ep ablation procedures,” *JACC: Cardiovascular Imaging*, vol. 9, pp. 873–886, 2016. doi:10.1016/j.jcmg.2016.03.009

[57] E. Seeram, “Computed tomography: a technical review,” *Radiologic Technology*, vol. 89, pp. 279CT–302CT, 2018.

[58] T. Niendorf, A. Graessl, C. Thalhammer, et al., “Progress and promises of human cardiac magnetic resonance at ultrahigh fields: a physics perspective,” *Journal of Magnetic Resonance*, vol. 229, pp. 208–222, 2013. doi:10.1016/j.jmr.2012.11.015

[59] D. T. Ginat, M. W. Fong, D. J. Tuttle, S. K. Hobbs, and R. C. Vyas, “Cardiac imaging: Part 1, mr pulse sequences, imaging planes, and basic anatomy,” *American Journal of Roentgenology*, vol. 197, pp. 808–815, 2011. doi:10.2214/AJR.10.7231

[60] J. Tonko, A. Lee, N. Mannakkara, et al., “Structural phenotyping in atrial fibrillation with combined cardiac ct and atrial mri: Identifying and differentiating individual structural remodelling types in af,” *Journal of Cardiovascular Electrophysiology*, 2024. doi:10.1111/jce.16357

[61] S. Bugenhagen, N. Kolluri, N. Y. Tan, M. F. Morris, and P. S. Rajiah, “Utility of ct and mri in cardiac electrophysiology,” *RadioGraphics*, vol. 44, p. e230222, 2024. doi:10.1148/rg.230222

[62] J. P. O’Brien, M. B. Srichai, E. M. Hecht, D. C. Kim, and J. E. Jacobs, “Anatomy of the heart at multidetector ct: what the radiologist needs to know,” *Radiographics*, vol. 27, pp. 1569–1582, 2007. doi:10.1148/rg.276065747

[63] M. J. Cluitmans, G. Plank, and J. Heijman, “Digital twins for cardiac electrophysiology: state of the art and future challenges,” *Herzschrittmachertherapie+ Elektrophysiologie*, pp. 1–6, 2024. doi:10.1007/s00399-024-01014-0

[64] A. Dasi, A. Roy, R. Sachetto, J. Camps, A. Bueno-Orovio, and B. Rodriguez, “In-silico drug trials for precision medicine in atrial fibrillation: From ionic mechanisms to electrocardiogram-based predictions in structurally-healthy human atria,” *Frontiers in Physiology*, vol. 13, p. 966046, 2022. doi:10.3389/fphys.2022.966046

[65] B. Amuzescu, R. Airini, F. B. Epureanu, S. A. Mann, T. Knott, and B. M. Radu, “Evolution of mathematical models of cardiomyocyte electrophysiology,” *Mathematical Biosciences*, vol. 334, p. 108567, 2021. doi:10.1016/j.mbs.2021.108567

[66] M. Courtemanche, R. J. Ramirez, and S. Nattel, “Ionic mechanisms underlying human atrial action potential properties: insights from a mathematical model,” *Am J Physiol*, vol. 275, pp. 1522–1539, 1998. doi:10.1152/ajpheart.1998.275.1.H301

[67] C. C. Mitchell and D. G. Schaeffer, “A two-current model for the dynamics of cardiac membrane,” *Bulletin of Mathematical Biology*, vol. 65, pp. 767–793, 2003. doi:10.1016/S0092-8240(03)00041-7

[68] S. Rush and H. Larsen, “A practical algorithm for solving dynamic membrane equations,” *IEEE Transactions on Biomedical Engineering*, pp. 389–392, 1978. doi:10.1109/TBME.1978.326270

[69] M. E. Marsh, S. T. Ziaratgahi, and R. J. Spiteri, “The secrets to the success of the rush–larsen method and its generalizations,” *IEEE Transactions on Biomedical Engineering*, vol. 59, pp. 2506–2515, 2012. doi:10.1109/TBME.2012.2205575

[70] E. Vigmond, R. W. Dos Santos, A. Prassl, M. Deo, and G. Plank, “Solvers for the cardiac bidomain equations,” *Progress in Biophysics and Molecular Biology*, vol. 96, pp. 3–18, 2008. doi:10.1016/j.pbiomolbio.2007.07.012

[71] M. J. Bishop and G. Plank, “Bidomain ECG simulations using an augmented monodomain model for the cardiac source.” *IEEE Transactions on Bio-Medical Engineering*, vol. 58, 2011. doi:10.1109/TBME.2011.2148718

[72] M. Potse, B. Dubé, A. Vinet, and R. Cardinal, “A comparison of monodomain and bidomain propagation models for the human heart,” in *2006 International Conference of the IEEE Engineering in Medicine and Biology Society*. IEEE, 2006, pp. 3895–3898. doi:10.1109/IEMBS.2006.259484

[73] G. Plank, A. Loewe, A. Neic, et al., “The openCARP simulation environment for cardiac electrophysiology.” *Computer Methods and Programs in Biomedicine*, vol. 208, p. 106223, 2021. doi:10.1016/j.cmpb.2021.106223

[74] Z. Fu, R. M. Kirby, and R. T. Whitaker, "A fast iterative method for solving the eikonal equation on tetrahedral domains," *SIAM Journal on Scientific Computing*, vol. 35, pp. C473–C494, 2013. doi:10.1137/120881956

[75] S. Coveney, C. Cantwell, and C. Roney, "Atrial conduction velocity mapping: clinical tools, algorithms and approaches for understanding the arrhythmogenic substrate," *Medical & Biological Engineering & Computing*, vol. 60, pp. 2463–2478, 2022. doi:10.1007/s11517-022-02621-0

[76] J. A. Sethian and A. Vladimirsky, "Ordered upwind methods for static hamilton–jacobi equations: Theory and algorithms," *SIAM Journal on Numerical Analysis*, vol. 41, pp. 325–363, 2003. doi:10.1073/pnas.201222998

[77] N. Tueni, J.-M. Allain, and M. Genet, "On the structural origin of the anisotropy in the myocardium: Multiscale modeling and analysis," *Journal of the Mechanical Behavior of Biomedical Materials*, vol. 138, p. 105600, 2023. doi:10.1016/j.jmbbm.2022.105600

[78] J. E. Saffitz, L. M. Davis, B. J. Darrow, H. Lee Kanter, J. G. Laing, and E. C. Beyer, "The molecular basis of anisotropy: role of gap junctions," *Journal of Cardiovascular Electrophysiology*, vol. 6, pp. 498–510, 1995. doi:10.1111/j.1540-8167.1995.tb00423.x

[79] J. A. Cyr, M. Colzani, S. Bayraktar, et al., "Extracellular macrostructure anisotropy improves cardiac tissue-like construct function and phenotypic cellular maturation," *Biomaterials Advances*, vol. 155, p. 213680, 2023. doi:10.1016/j.bioadv.2023.213680

[80] T. Sano, N. Takayama, and T. Shimamoto, "Directional difference of conduction velocity in the cardiac ventricular syncytium studied by microelectrodes," *Circulation Research*, vol. 7, pp. 262–267, 1959. doi:10.1161/01.RES.7.2.262

[81] M. Valderrábano, "Influence of anisotropic conduction properties in the propagation of the cardiac action potential," *Progress in Biophysics and Molecular Biology*, vol. 94, pp. 144–168, 2007. doi:10.1016/j.pbiomolbio.2007.03.014

[82] C. Cabo, A. M. Pertsov, W. T. Baxter, J. M. Davidenko, R. A. Gray, and J. Jalife, "Wave-front curvature as a cause of slow conduction and block in isolated cardiac muscle." *Circulation Research*, vol. 75, pp. 1014–1028, 1994. doi:10.1161/01.res.75.6.1014

[83] J. P. Kucera, A. G. Kléber, and S. Rohr, "Slow conduction in cardiac tissue, ii: effects of branching tissue geometry," *Circulation Research*, vol. 83, pp. 795–805, 1998. doi:10.1161/01.res.83.8.795

[84] R. M. Shaw and Y. Rudy, "Ionic mechanisms of propagation in cardiac tissue: roles of the sodium and l-type calcium currents during reduced excitability and decreased gap junction coupling," *Circulation Research*, vol. 81, pp. 727–741, 1997. doi:10.1161/01.res.81.5.727

[85] J. J. Gard, K. Yamada, K. G. Green, et al., "Remodeling of gap junctions and slow conduction in a mouse model of desmin-related cardiomyopathy," *Cardiovascular Research*, vol. 67, pp. 539–547, 2005. doi:10.1016/j.cardiores.2005.04.004

[86] M. Strocchi, K. Gillette, A. Neic, et al., "Effect of scar and his–purkinje and myocardium conduction on response to conduction system pacing," *Journal of Cardiovascular Electrophysiology*, vol. 34, pp. 984–993, 2023. doi:10.1111/jce.15847

[87] B. Han, M. L. Trew, and C. M. Zgierski-Johnston, "Cardiac conduction velocity, remodeling and arrhythmogenesis," *Cells*, vol. 10, p. 2923, 2021. doi:10.3390/cells10112923

[88] G. R. Mines, "On dynamic equilibrium in the heart," *The Journal of Physiology*, vol. 46, p. 349, 1913. doi:10.1113/jphysiol.1913.sp001596

[89] J. J. B. Vicera, Y.-J. Lin, P.-T. Lee, et al., “Identification of critical isthmus using coherent mapping in patients with scar-related atrial tachycardia,” *Journal of cardiovascular electrophysiology*, vol. 31, pp. 1436–1447, 2020. doi:10.1111/jce.14457

[90] C. D. Cantwell, C. H. Roney, F. S. Ng, J. H. Siggers, S. J. Sherwin, and N. S. Peters, “Techniques for automated local activation time annotation and conduction velocity estimation in cardiac mapping,” *Computers in Biology and Medicine*, vol. 65, pp. 229–242, 2015. doi:10.1016/j.compbiomed.2015.04.027

[91] C. Nagel, N. Pilia, L. Unger, and O. Dössel, “Performance of different atrial conduction velocity estimation algorithms improves with knowledge about the depolarization pattern,” *Current Directions in Biomedical Engineering*, vol. 5, pp. 101–104, 2019. doi:10.1515/cdbme-2019-0026

[92] M. Masé and F. Ravelli, “Automatic reconstruction of activation and velocity maps from electro-anatomic data by radial basis functions,” in *2010 Annual International Conference of the IEEE Engineering in Medicine and Biology*. IEEE, 2010, pp. 2608–2611. doi:10.1109/IEMBS.2010.5626616

[93] P. V. Bayly, B. H. KenKnight, J. M. Rogers, R. E. Hillsley, R. E. Ideker, and W. M. Smith, “Estimation of conduction velocity vector fields from epicardial mapping data,” *IEEE Transactions on Biomedical Engineering*, vol. 45, pp. 563–571, 1998. doi:10.1109/10.668746

[94] L. Azzolin, M. Eichenlaub, C. Nagel, et al., “Augmenta: patient-specific augmented atrial model generation tool,” *Computerized Medical Imaging and Graphics*, vol. 108, p. 102265, 2023. doi:10.1016/j.compmedimag.2023.102265

[95] T. Grandits, K. Gillette, A. Neic, et al., “An inverse eikonal method for identifying ventricular activation sequences from epicardial activation maps,” *Journal of Computational Physics*, vol. 419, p. 109700, 2020. doi:10.1016/j.jcp.2020.109700

[96] T. Grandits, S. Pezzuto, J. M. Lubrecht, T. Pock, G. Plank, and R. Krause, “Piemap: personalized inverse eikonal model from cardiac electro-anatomical maps,” in *International Workshop on Statistical Atlases and Computational Models of the Heart*. Springer, 2020, pp. 76–86.

[97] S. Rossi, S. Gaeta, B. E. Griffith, and C. S. Henriquez, “Muscle thickness and curvature influence atrial conduction velocities,” *Frontiers in Physiology*, vol. 9, p. 1344, 2018. doi:10.3389/fphys.2018.01344

[98] S. Zahid, T. Malik, C. Peterson, et al., “Conduction velocity is reduced in the posterior wall of hypertrophic cardiomyopathy patients with normal bipolar voltage undergoing ablation for paroxysmal atrial fibrillation,” *Journal of Interventional Cardiac Electrophysiology*, vol. 67, pp. 203–210, 2024. doi:10.1007/s10840-023-01533-9

[99] J. Jang, J. Whitaker, E. Leshem, et al., “Local conduction velocity in the presence of late gadolinium enhancement and myocardial wall thinning: a cardiac magnetic resonance study in a swine model of healed left ventricular infarction,” *Circulation: Arrhythmia and Electrophysiology*, vol. 12, p. e007175, 2019. doi:10.1161/CIRCEP.119.007175

[100] T. Grandits, S. Pezzuto, F. S. Costabal, et al., “Learning atrial fiber orientations and conductivity tensors from intracardiac maps using physics-informed neural networks,” in *International Conference on Functional Imaging and Modeling of the Heart*. Springer, 2021, pp. 650–658. doi:10.1007/978-3-030-78710-3_62

[101] S. Gaeta, T. D. Bahnson, and C. Henriquez, “High-resolution measurement of local activation time differences from bipolar electrogram amplitude,” *Frontiers in Physiology*, vol. 12, p. 653645, 2021. doi:10.3389/fphys.2021.653645

[102] C. B. Espinosa, J. Sánchez, O. Dössel, and A. Loewe, "Diffusion reaction eikonal alternant model: Towards fast simulations of complex cardiac arrhythmias," *Computing in Cardiology*, vol. 498, pp. 1–4, 2022. doi:10.22489/CinC.2022.054

[103] G. Plank, A. Loewe, A. Neic, et al., "The openCARP simulation environment for cardiac electrophysiology," *Computer Methods and Programs in Biomedicine*, vol. 208, p. 106223, 2021. doi:10.1016/j.cmpb.2021.106223

[104] (2024) openCARP eikonal. GitLab. https://git.opencarp.org/openCARP/openCARP/-/tree/openCARP_DREAM

[105] S. Becker, "Influence of conduction velocity restitution on vulnerability to and maintenance of atrial fibrillation," Master's thesis, Institute of Biomedical Engineering, Karlsruhe Institute of Technology (KIT), 2024.

[106] M. Sagris, E. P. Vardas, P. Theofilis, A. S. Antonopoulos, E. Oikonomou, and D. Tousoulis, "Atrial fibrillation: pathogenesis, predisposing factors, and genetics," *International Journal of Molecular Sciences*, vol. 23, p. 6, 2021. doi:10.3390/ijms23010006

[107] M. Nothstein, A. Luik, A. Jadidi, et al., "Cvar-seg: an automated signal segmentation pipeline for conduction velocity and amplitude restitution," *Frontiers in Physiology*, vol. 12, p. 673047, 2021. doi:10.3389/fphys.2021.673047

[108] Z. Qu, A. Garfinkel, P.-S. Chen, and J. N. Weiss, "Mechanisms of discordant alternans and induction of reentry in simulated cardiac tissue," *Circulation*, vol. 102, pp. 1664–1670, 2000. doi:10.1161/01.cir.102.14.1664

[109] Z. Qu, A. Garfinkel, and J. N. Weiss, "Vulnerable window for conduction block in a one-dimensional cable of cardiac cells, 1: single extrasystoles," *Biophysical Journal*, vol. 91, pp. 793–804, 2006. doi:10.1529/biophysj.106.080945

[110] Y. Xie, A. Garfinkel, J. N. Weiss, and Z. Qu, "Cardiac alternans induced by fibroblast-myocyte coupling: mechanistic insights from computational models," *American Journal of Physiology-Heart and Circulatory Physiology*, vol. 297, pp. H775–H784, 2009. doi:10.1152/ajpheart.00341.2009

[111] T. M. Inc., "Matlab version: 9.13.0 (r2022b)," Natick, Massachusetts, United States, 2022. https://www.mathworks.com

[112] G. Van Rossum and F. L. Drake, *Python 3 reference manual*. Scotts Valley, CA: CreateSpace, 2009.

[113] A. Loewe, *Modeling human atrial patho-electrophysiology from ion channels to ECG-substrates, pharmacology, vulnerability, and P-waves*, vol. 23. Karlsruhe: KIT Scientific Publishing, 2016.

[114] C. M. Costa, E. Hoetzl, B. M. Rocha, A. J. Prassl, and G. Plank, "Automatic parameterization strategy for cardiac electrophysiology simulations," *Computing in Cardiology*, pp. 373–376, 2013.

[115] H. Dzindo, "Behavior and transformation of restitution curves of different stimulation protocols under atrial fibrillation conditions."

[116] N. Skupien, "Refining the eikonal model to reproduce the influence of geometrical factors on conduction velocity," Bachelor's thesis, Institute of Biomedical Engineering, Karlsruhe Institute of Technology (KIT), 2021.

[117] S. Verheule, J. Eckstein, D. Linz, et al., "Role of endo-epicardial dissociation of electrical activity and transmural conduction in the development of persistent atrial fibrillation," *Progress in Biophysics and Molecular Biology*, vol. 115, pp. 173–185, 2014, novel Technologies as

Drivers of Progress in Cardiac Biophysics. doi:https://doi.org/10.1016/j.pbiomolbio.2014.07.007

[118] B. J. Roth, “Effect of a perfusing bath on the rate of rise of an action potential propagating through a slab of cardiac tissue,” *Annals of Biomedical Engineering*, vol. 24, pp. 639–646, 1996. doi:10.1007/BF02684177

[119] M. Clerx, P. Collins, E. Lange, and P. Volders, “Myokit: A simple interface to cardiac cellular electrophysiology,” *Progress in Biophysics and Molecular Biology*, vol. 120, pp. 100–114, 2016. doi:10.1016/j.pbiomolbio.2015.12.008

[120] L. Keller, “Influence of electrical propagation patterns on diffusion currents,” Bachelor’s thesis, Institute of Biomedical Engineering, Karlsruhe Institute of Technology (KIT), 2023.

[121] E. J. Ciaccio, J. Coromilas, A. L. Wit, N. S. Peters, and H. Garan, “Formation of functional conduction block during the onset of reentrant ventricular tachycardia,” *Circulation: Arrhythmia and Electrophysiology*, vol. 9, p. e004462, 2016. doi:10.1161/CIRCEP.116.004462

[122] C. Cabo, J. Yao, P. A. Boyden, et al., “Heterogeneous gap junction remodeling in reentrant circuits in the epicardial border zone of the healing canine infarct,” *Cardiovascular Research*, vol. 72, pp. 241–249, 2006. doi:10.1016/j.cardiores.2006.07.005

[123] B. Y. Kogan, W. J. Karplus, B. S. Billett, and W. G. Stevenson, “Excitation wave propagation within narrow pathways: geometric configurations facilitating unidirectional block and reentry,” *Physica D: Nonlinear Phenomena*, vol. 59, pp. 275–296, 1992. doi:10.1016/0167-2789(92)90071-T

[124] E. J. Ciaccio, J. Coromilas, A. L. Wit, N. S. Peters, and H. Garan, “Source-sink mismatch causing functional conduction block in re-entrant ventricular tachycardia,” *JACC: Clinical Electrophysiology*, vol. 4, pp. 1–16, 2018. doi:10.1016/j.jacep.2017.08.019

[125] B. A. Lawson, R. S. Oliveira, L. A. Berg, P. A. Silva, K. Burrage, and R. W. Dos Santos, “Variability in electrophysiological properties and conducting obstacles controls re-entry risk in heterogeneous ischaemic tissue,” *Philosophical Transactions of the Royal Society A*, vol. 378, p. 20190341, 2020. doi:10.1098/rsta.2019.0341

[126] A. Garfinkel, Y.-H. Kim, O. Voroshilovsky, et al., “Preventing ventricular fibrillation by flattening cardiac restitution,” *Proceedings of the National Academy of Sciences*, vol. 97, pp. 6061–6066, 2000. doi:10.1073/pnas.090492697

[127] G.-N. Tseng, “Calcium current restitution in mammalian ventricular myocytes is modulated by intracellular calcium.” *Circulation Research*, vol. 63, pp. 468–482, 1988. doi:10.1161/01.res.63.2.468

[128] N. A. Barnafi, N. M. M. Huynh, L. F. Pavarino, and S. Scacchi, “Robust parallel nonlinear solvers for implicit time discretizations of the bidomain equations with staggered ionic models,” *Computers & Mathematics with Applications*, vol. 167, pp. 134–149, 2024. doi:10.1016/j.camwa.2024.04.014

[129] F. Morady, M. Harvey, S. J. Kalbfleisch, R. el Atassi, H. Calkins, and J. J. Langberg, “Radiofrequency catheter ablation of ventricular tachycardia in patients with coronary artery disease.” *Circulation*, vol. 87, pp. 363–372, 1993. doi:10.1161/01.CIR.87.2.363

[130] F. M. Weber, A. Luik, C. Schilling, et al., “Conduction velocity restitution of the human atrium—an efficient measurement protocol for clinical electrophysiological studies,” *IEEE Transactions on Biomedical Engineering*, vol. 58, pp. 2648–2655, 2011. doi:10.1109/TBME.2011.2160453

List of Publications and Supervised Theses

Journal Articles

- **Barrios Espinosa, C.**, Sánchez, J., Appel, S., Becker, S., Krauß, J., Martínez Díaz, P. & Loewe, A. (2024). *A Cyclical Fast Iterative Method for Simulating Reentries in Cardiac Electrophysiology Using an Eikonal-Based Model.* Accepted for publication in Engineering with Computers. Preprint available at arXiv preprint arXiv:2406.18619.
- Nagel, C., **Espinosa, C. B**., Gillette, K., Gsell, M. A., Sánchez, J., Plank, G., ... & Loewe, A. (2022). *Comparison of propagation models and forward calculation methods on cellular, tissue and organ scale atrial electrophysiology*. IEEE Transactions on Biomedical Engineering, 70(2), 511-522.
- Vila, M., Rivolta, M. W., **Espinosa, C. A. B.**, Unger, L. A., Luik, A., Loewe, A., & Sassi, R. (2023). *Recommender system for ablation lines to treat complex atrial tachycardia. Computer Methods and Programs in Biomedicine*, 231, 107406.

Refereed Conference Articles

- **Espinosa, C. B.**, Sánchez, J., Dössel, O.,& Loewe, A. (2022, September). *Diffusion reaction eikonal alternant model: Towards fast simulations of complex cardiac arrhythmias*. In 2022 Computing in Cardiology (CinC) (Vol. 49). IEEE.
- Becker, S., **Espinosa, C**. B., Unger, L., Haas, A., Luik, A.,& Loewe, A. *Influence of Conduction Velocity Restitution Steepness on Atrial Fibrillation Vulnerability and Maintenance.* In 2024 Computer in Cardiology (CinC).
- Sánchez, J., Ruales, K. A., Macarulla-Rodríguez, M., **Espinosa, C**. B., Loewe, A.,& Guillem, M. S. (2023, October). *Inflammation-Induced Remodeling and Atrial Arrhythmias in Systemic Lupus Erythematosus: In Silico Insights.* In 2023 Computing in Cardiology (CinC) (Vol. 50). IEEE.
- Skupien, N., **Barrios Espinosa, C**., Dössel, O.,& Loewe, A. (2022, September). *Refining the Eikonal Model to Reproduce the Influence of Atrial Tissue Geometry on Conduction*

Velocity. In Current Directions in Biomedical Engineering (Vol. 8, No. 2, pp. 133-136). De Gruyter.

Refereed Conference Abstracts

- **Espinosa, C. B.**, Skupien, N., Kachel, G., Dössel, O.,& Loewe, A. *Influence of Wave-Front and Atrial Tissue Properties on Eikonal Model Simulations.* In **Atrial Signals**. Karlsruhe. 2021

Conference Presentations

- The role of the Eikonan model in personalized cardiac modeling from parameter aquisition to arrythmia simulations in Computational medicine of the heart: towards cardiac digital twins. **International Congress on Industrial and Applied Mathematics.** Tokyo. 2023
- Enhancing Machine Learning Methods for Cardiac Electrophysiology Through the use of Eikonal Simulations. **SIAM Conference on Dynamical Systems.** Portland. 2023
- Using the Eikonal Model to Assess Anisotropic Conduction Velocity in Cardiac Tissue. **The Joint Annual Conference of the Austrian, German and Swiss Societies for Biomedical Engineering.** Innsbruck. 2022
- Diffusion reaction eikonal alternant model: Towards fast simulations of complex cardiac arrhythmias. In 2022 Computing in Cardiology. **Computing in Cardiology.** Tampere. 2022
- Influence of Wave-Front and Atrial Tissue Properties on Eikonal Model Simulations. **Atrial Signals Conference.** Karlsruhe. 2021

Supervised Student Projects

- Silvia Becker, *Influence of Conduction Velocity Restitution on Vulnerability to and Maintenance of Atrial Fibrillation*, Master Thesis, Institute of Biomedical Engineering, Karlsruhe Institute of Technology (KIT), 2024
- Hanish Raval, *The Eikonal-Based Method to Analyze the Regional Changes of Patients with Atrial Fibrillation*, Master Thesis, Hochschule University of Furtwangen, 2023
- Lisa Keller, *Influence of Electrical Propagation Patterns on Diffusion Currents*, Bachelor Thesis, Institute of Biomedical Engineering, Karlsruhe Institute of Technology (KIT), 2023

- Nils Skupien, *Investigating Volumetric Geometrical Factors on Conduction Velocity*, Internship, Institute of Biomedical Engineering, Karlsruhe Institute of Technology (KIT), 2021
- Guillaume Kachel, *Influence of electrical wavefronts collisions and curvature on conduction velocity in atrial tissue*, Intership, Polytech Clermont-Ferrand, 2021
- Nils Skupien, *Refining the Eikonal Model to reproduce the Influence of Geometrical Factors on Conduction Velocity*, Bachelor Thesis, Institute of Biomedical Engineering, Karlsruhe Institute of Technology (KIT), 2021

Awards & Grants

- Best Poster Award. **Atrial Signals Conference.** Karlsruhe 2021
- Financial Support Program for Travel Expenses. **International Congress on Industrial and Applied Mathematics**. Tokyo. 2023